



HAL
open science

Diamond-based multimaterials for thermal management applications

Clio Azina

► **To cite this version:**

Clio Azina. Diamond-based multimaterials for thermal management applications. Material chemistry. Université de Bordeaux; University of Nebraska-Lincoln, 2017. English. NNT : 2017BORD0767 . tel-01699064

HAL Id: tel-01699064

<https://theses.hal.science/tel-01699064>

Submitted on 2 Feb 2018

HAL is a multi-disciplinary open access archive for the deposit and dissemination of scientific research documents, whether they are published or not. The documents may come from teaching and research institutions in France or abroad, or from public or private research centers.

L'archive ouverte pluridisciplinaire **HAL**, est destinée au dépôt et à la diffusion de documents scientifiques de niveau recherche, publiés ou non, émanant des établissements d'enseignement et de recherche français ou étrangers, des laboratoires publics ou privés.

DIAMOND-BASED MULTIMATERIALS FOR
THERMAL MANAGEMENT APPLICATIONS

By

Clio Azina

A DISSERTATION

Presented to the Faculty of

The Graduate College at the University of Nebraska, United States

and

The Graduate College at the University of Bordeaux, France

In Partial Fulfillment of Requirements

For the Degree of Doctor of Philosophy

Major: Engineering (Electrical Engineering)

Major: Chemistry (Physical-Chemistry of Condensed Matter)

Under the Supervision of:

Professor Yongfeng Lu, University of Nebraska-Lincoln

Professor Jean-François Silvain, University of Bordeaux

Lincoln, Nebraska

November, 2017

THÈSE EN COTUTELLE PRÉSENTÉE
POUR OBTENIR LE GRADE DE

DOCTEUR DE
L'UNIVERSITÉ DE BORDEAUX ET DE L'UNIVERSITÉ
DU NEBRASKA

ÉCOLE DOCTORALE DES SCIENCES CHIMIQUES (Université de Bordeaux)

SPÉCIALITÉ : Physico-Chimie de la Matière Condensée

ÉCOLE DOCTORALE DE GENIE ELECTRIQUE (Université du Nebraska)

SPÉCIALITÉ : Génie Electrique

Par **Clio AZINA**

**Optimisation de multi-matériaux à base de diamant pour la
gestion thermique**

Sous la direction de M. Jean-François SILVAIN et M. Yongfeng LU

Soutenu le 21 Novembre 2017

Rapporteurs :

Mme Anne JOULAIN
M. Hansang KWON

Professeur, PDP Institut P', Université de Poitiers
Maître de conférences, Pukyong National University

Examineurs :

M. Jerry HUDGINS
M. Sidy NDAO
M. Pierre-Marie GEFFROY
M. Guillaume LACOMBE

Professeur, ECE, UNL
Maître de conférences, MME, UNL
Chargé de Recherche CNRS, SPCTS, Université de Limoges
Ingénieur Recherche et Développement, Composite Innovation

Invités

M. Natale IANNO
M. Jean-Marc HEINTZ

Professeur, ECE, UNL
Professeur INP Bordeaux, ICMCB, ENSCBP

DIAMOND-BASED MULTIMATERIALS FOR THERMAL MANAGEMENT APPLICATIONS

Clio Azina, Ph.D.

University of Nebraska; University of Bordeaux, 2017

Advisors: Yongfeng Lu, Jean-François Silvain

Today, the microelectronics industry uses higher functioning frequencies in commercialized components. These frequencies result in higher functioning temperatures and, therefore, limit a component's integrity and lifetime. Until now, heat-sink materials were composed of metals which exhibit high thermal conductivities (TC). However, these metals often induce large coefficient of thermal expansion (CTE) mismatches between the heat sink and the nonmetallic components of the device. Such differences in CTEs cause thermomechanical stresses at the interfaces and result in component failure after several on/off cycles.

To overcome this issue, we suggest replacing the metallic heat sink materials with a heat-spreader (diamond film) deposited on metal matrix composites (MMCs), specifically, carbon-reinforced copper matrices (Cu/C) which exhibit optimized thermomechanical properties. However, proper transfer of properties in MMCs is often compromised by the absence of effective interfaces, especially in nonreactive systems such as Cu/C. Therefore, the creation of a chemical bond is ever more relevant.

The goal of this research was to combine the exceptional properties of diamond by means of a thin film and the adaptive thermomechanical properties of MMCs. Carbon-reinforced copper matrix composites were synthesized using an innovative solid-liquid coexistent phase process to achieve designed composition gradients and optimized matrix/reinforcement interface properties. In addition, the lack of chemical affinity

between Cu and C results in poor thermal efficiency of the composites. Therefore, alloying elements were inserted into the material to form carbide interphases at the Cu/C interface. Their addition enabled the composite's integrity to be optimized in order to obtain thermally efficient assemblies. The diamond, in the form of a thin layer, was obtained by laser-assisted chemical vapor deposition. This process allowed action on the film's phase purity and adhesion to the substrate material. Of particular importance was the influence of the interfaces on thermal properties both within the composite material (matrix-reinforcement interface) and within the diamond film-MMC assembly.

This work was carried out within the framework of a Franco-American agreement between the Institute of Condensed Matter Chemistry of the University of Bordeaux in France and the Department of Electrical Engineering at the University of Nebraska-Lincoln, in the United States. Funding, in France, was provided by the Direction Générale de l'Armement (DGA), and by the American equivalent in the United States.

OPTIMISATION DE MULTI-MATERIAUX A BASE DE DIAMANT POUR LA GESTION THERMIQUE

Clio Azina

Université du Nebraska – Université de Bordeaux, 2017

Encadrants : Jean-François Silvain, Yongfeng Lu

De nos jours, l'industrie microélectronique utilise des fréquences de fonctionnement plus élevées dans les composants commercialisés. Ces fréquences entraînent des températures de fonctionnement plus élevées et limitent donc l'intégrité et la durée de vie des composants électroniques. Cependant, les besoins actuels nécessitent des dispositifs miniaturisés et de haute densité de puissance. De ce fait, la dissipation thermique dans les composants microélectroniques s'avère capitale. Ainsi, des drains thermiques sont utilisés pour évacuer la chaleur produite par le fonctionnement du composant. Les drains thermiques actuels sont composés de métaux, tels que le cuivre et l'aluminium, présentant des conductivités et des coefficients de dilatation thermiques élevés. Néanmoins, les coefficients de dilatation thermique des différents matériaux présents dans un circuit peuvent induire des contraintes thermo-mécaniques aux interfaces et engendrer une défaillance des composants après plusieurs cycles de fonctionnement.

Dans ce contexte, nous proposons de remplacer ces drains métalliques par un système composite à matrice cuivre renforcée par du carbone, sur lequel est déposé un diffuseur thermique sous forme de diamant. Ces composites Cu/C présentent des propriétés thermo-mécaniques adaptatives pouvant palier aux contraintes induites durant l'utilisation des composants. Le transfert optimal des propriétés dans les MMC est souvent compromis par l'absence de liaison chimique interfaciale, en particulier dans les systèmes non réactifs tels

que Cu/C. Cependant, pour un assemblage thermiquement efficace, l'interface devrait permettre un bon transfert de charges thermo-mécaniques entre les matériaux.

L'objectif de cette étude est de combiner les propriétés exceptionnelles du diamant et les propriétés thermo-mécaniques adaptatives des MMC. Les composites à matrice de cuivre renforcés au carbone sont synthétisés à l'aide d'un processus dit semi-liquide pour obtenir des gradients de composition et des propriétés optimisées d'interface matrice - renfort. Par conséquent, des éléments d'alliage sont insérés dans le matériau pour former des interphases de carbure à l'interface Cu/C. Le film mince de diamant est obtenu par dépôt chimique en phase vapeur assisté par laser. Cette méthode de dépôt permet d'agir sur la qualité du film ainsi que sur l'adhésion avec le substrat composite. Finalement, une importance particulière est portée à l'influence des interfaces sur les propriétés thermiques tant au sein du matériau composite (interface matrice – renfort), qu'au sein de l'assemblage film diamant – MMC.

Ces travaux ont été menés dans le cadre d'un accord franco-américain de cotutelle de thèse entre l'Institut de Chimie de la Matière Condensée de l'Université de Bordeaux, en France, et le département d'Ingénierie Electrique de l'Université du Nebraska-Lincoln, aux Etats-Unis. Ils ont été financés, en France, par la Direction Générale de l'Armement (DGA), et par l'équivalent Américain aux Etats-Unis.

A ma famille, Christos, Anne,

Alexandre et Nicolas

Στη Γιαγιά, Θεοδούλα

Στον κύριο Σάββα Κελογρηγόρη

*“Don’t give yourselves to these unnatural men.
Machine men with machine minds and machine hearts.
You are not machines.
You are not cattle.
You are men.
You the people have the power to make this life free and beautiful.
To make this life a wonderful adventure.”*

- Charlie Chaplin

ACKNOWLEDGEMENT

My gratitude first goes to my French and American advisors, Dr. Jean-François Silvain from the ICMCB and Pr. Yongfeng Lu from the College of Engineering of the University of Nebraska-Lincoln. Their support and trust, as well as their patience were constant from the very first day of my program and kept along until the very end. Thank you for all the time and effort you put for this work to be accomplished, and thank you for being there for me.

I would like to thank the Direction Générale de l'Armement and its American equivalent for financial support at the University of Bordeaux and at the University of Nebraska-Lincoln, respectively. I would also like to give particular thanks to Dr. Bruno Mortaigne for his support throughout this program. In addition, I would like to thank Dr. Mario Maglione, Director of the ICMCB, for welcoming me to his lab.

I would also like to thank Professors Jerry L. Hudgins, Natale Ianno, and Sidy Ndao from the University of Nebraska-Lincoln, as well as Pr. Hansang Kwon from Pukyong National University in Busan, Korea, Pr. Anne Joulain from the Institut Pprime of Poitiers, Dr. Pierre-Marie Geffroy from the SPCTS in Limoges, Pr. Jean-Marc Heintz from the ICMCB of Bordeaux, and Dr. Guillaume Lacombe from Composite Innovation SAS for being part of my supervisory committee and for agreeing to judge my work.

I would also like to thank Pr. Jean-Luc Battaglia and Pr. Andrzej Kusiak from the I2M in Bordeaux, for their great contribution to the work presented in this manuscript. I am honored to have spent so much time with you and to have been able to learn and discover a new area, which is oh so interesting and challenging for me. Thank you for 'adopting' me at the I2M and I look forward to our future collaborations. I would also like to acknowledge Pr. Jérôme Roger for his time and help with everything related to thermodynamics, Dr. Pierre-Marie Geffroy for the COMSOL simulations, Professors Anne Joulain and Vincent Mauchamp for the TEM and EELS analyzes.

Crossing the Atlantic Ocean repeatedly for a dual PhD is far from being the most convenient way to get a doctorate, but it is a very exciting, challenging, and enriching human and scientific experience. I am particularly honored to be part of this collaboration, and to have contributed to enrich this strong academic partnership between our two universities. I would like to thank all the people in Bordeaux and Lincoln who made me feel at home in both places.

My lab mates in Lincoln, former and current: Dawei, Xi, Lei, Yutian, Raif, Leimin, Zhe, Ying, Yao, Qiming, Chenfei, Lisha, Wei, Wenjia, Mengxiao, Jun, Lydia, and Dr. Zhou. I also want to thank Dr. Lanping Yue, Xingzhong (Jim) Li, and Ehsan Rezaei, of the NCMN for their help with the AFM, NanoSEM and nanoindentation, respectively. Special thanks to Pr. Dennis R. Alexander for giving me access to his lab's SEM, and to Pr. Eva Schubert for her amazing classes and conversations regarding thin films. I would also like to thank Dr. Jack Campbell for his time and long conversations about networking and his valuable advice.

I could not have made it in the US without the help of Ms Cheryl Whemhoff, Teresa Ryans, and Joyce Ore who were able to answer all my questions with a smile. Also, my repeated travels!) would have been way more difficult without the help of Ms Pamela Weise and Stevie Woodrum. I would also like to thank Dr. Eva Bachman and the ISSO Staff for making sure I was correctly enrolled at UNL and able to maintain my VISA status!

Finally, my stays in Lincoln would not have been the same without the friends that I have made. Therefore, I would like to mention Hossein, Dicle, Amir, Behrooz, Luigi, Mohsen (and Cosmo),

Jamie, Nazanin, and more particularly Mengmeng, Lijia and Kamran for being there to pick me up at the airport and listen to me moan about everything. Thank you guys, for being there and I wish you all the best, while hoping we will get to see each other again.

Je souhaiterais tout d'abord remercier les personnes qui ont contribué, de façon non-négligeable, à ce travail de thèse, notamment les multiples stagiaires qui ont souffert sous ma 'direction' : Loic Constantin, Ana Belén Moral, Iñaki Cornu, Marine Lechartier, Lucas Villate, et Jérôme Biran. Merci à vous pour votre patience, votre motivation et beau travail.

Je voudrais aussi remercier Thomas Guillemet, qui a été le premier impliqué dans cette collaboration entre Bordeaux et Lincoln, pour ses travaux sur lesquels je me suis souvent basée. Merci aussi d'avoir simplifié toutes les procédures administratives, car « It's like Thomas' PhD », a résolu tous mes problèmes !

Un grand merci aux membres du 'greuh 4' (anciens et actuels) Benji, qui tient toujours le coup, Nabil Choupinou et ses cheveux dorés, Samy et Tadhg pour nos discussions au caes et les soirées films, Diaa pour sa solidarité féminine dans le bureau, Guigui même si il se réfugiait en haut pour nous éviter (!) Vola, Maël l'héritier, Guillaume Le Padre, Adrien, Jonat, Eliane, Waldemir, et Zhengyan, Guy-Marie, Marianne, Alexis, Samuel C., Jean-Marc, Jean-Louis, Amélie, Christophe, Mythili, Sylvie, Mohamed, Angéline, et Sophie. Merci pour leur bonne humeur, les longues discussions qu'on a pu avoir pendant les pauses café et surtout merci de m'avoir supporté !

Je voudrais aussi remercier les personnes des différents services et groupes avec qui j'ai pu interagir : Mathieu Duttine, Alexandre Fargues, Phong, Fougou, Alain Demourgues, Glenna Drisko, Samuel Marre, Patrick Rosa, la team Placamat (Marion, Philou, Nico, Pascale), U-Chan Chung, Rodolphe Decourt, Dominique Denux, et j'en oublie. Je tiens à remercier plus particulièrement Eric Lebraud et Stan Pechev pour leur patience et leur aide précieuse avec la DRX. Grand merci à Stéphane Toulain pour tous les bouquins que j'ai pu emprunter et à Cyril Dufour qui m'a toujours dépanné en cas de problème informatique. Petite mention spéciale pour Lionel Teule-Gay et ses séances de psychanalyse les vendredis après-midi. Et un GRAND merci à Carole Malburet d'avoir eu une oreille attentive à chaque fois que je voulais me plaindre et pour tous ses encouragements !

Je n'oublie pas non plus les personnes qui ont facilité mon séjour à l'ICMCB, mes missions et mes commandes, à commencer par Frédérique Bonnet, Christine Sanz, Matthieu Renaudin, Abderrahman Salhi et Liva Razanakolona. Un grand merci à Sandrine Quillateau et au reste du service infra, pour leur bonne humeur et les milliers de réservations de salles que j'ai pu faire.

Je souhaite aussi remercier les non-permanents pour la bonne ambiance au labo et surtout pour les chouffes : Alexandra, Marie C., Marie D., Mathias, Cyril, Baptiste, Jean-Charles, Aimery, Christopher, Damien, Vincent, Juan, Béatrice, Arnaud, Elodie, Thomas V., Fan, Anthony, Guillaume G., Louisiane, Céline, Lucas F., Sergey, Rui, Samantha, Toto, Jakub, Timothée, Maxime, Quentin, Clément, Face de Basque, Stéphanie, Jojo, et la mafia italienne : Aliche, Lorenzo, Giulio, Maria, Alberto, et Guilio.

Je tiens aussi à mentionner les survivants du master CPCM et Pinou !

Finalement, je tiens à remercier mes parents, Anne et Christos, et mes frères, Alexandre et Nicolas, ainsi que Rocky, pour leur amour, leur soutien et leur patience. Je n'aurais pu arriver au bout de cette thèse sans vous à mes côtés. Promis maintenant que c'est fini, je rentrerais à Chypre plus souvent !

RESUME DES TRAVAUX DE THESE

L'essor de la microélectronique a permis de nombreuses avancées dans des domaines aussi variés que le traitement/transfert/stockage de l'information, les transports, la médecine et l'énergie. Cette technologie ne cesse d'évoluer grâce à l'augmentation des puissances échangées par des composants de plus en plus miniaturisés. Ce confinement entraîne cependant des contraintes thermomécaniques fortes. Il est estimé que 80 % des pannes des composants et/ou des systèmes électroniques sont liées à une mauvaise dissipation de la chaleur produite en fonctionnement. Afin d'augmenter leur fiabilité et leur durée de vie, il est impératif de développer des drains thermiques performants en synthétisant des matériaux aux propriétés physiques exceptionnelles et en les intégrant au cœur des composants. Dans ce contexte, ce projet vise à créer de nouveaux matériaux dits composites par l'association judicieuse de deux matériaux aux propriétés complémentaires : i) le diamant, une variété cristallographique rare du carbone, pour son excellente conductivité thermique et son isolation électrique ; ii) des métaux pour leurs caractères malléables offrant une flexibilité pour la mise en forme et l'absorption des contraintes thermomécaniques. L'obtention de matériaux composites aux propriétés thermiques et thermomécaniques adaptatives implique de contrôler et moduler finement la répartition des deux phases au sein de micro-architectures de matrices métalliques serties de particules de diamants.

Depuis quelques années, la miniaturisation des systèmes électroniques à hautes performances connaît une baisse de développement. Tandis que les efforts du secteur en termes de recherche et de développement ont permis à ces tendances de se poursuivre sans

discontinuer, les niveaux de densité de chaleur atteints actuellement par les circuits constituent un obstacle majeur aux améliorations futures.

Ce projet de thèse comprend deux parties. L'une est dédiée à des films micrométriques de diamant obtenus par dépôt chimique en phase vapeur (CVD) assisté laser. L'intérêt de cette partie est d'étudier l'effet du substrat (propriété physique et morphologie de surface) sur l'adhésion du film ainsi que sur sa qualité. En effet, les films de diamant déposés sont obtenus par un procédé qui comprend une torche à combustion qui peut être utilisée sous air. Les films obtenus via ce procédé présentent souvent des impuretés, notamment à l'interface avec le substrat, ou on retrouve une couche d'épaisseur non-négligeable de carbone amorphe. Afin de palier à ce problème, le procédé de torche à combustion est couplé à un faisceau induit par un laser infrarouge (IR). Le faisceau laser utilisé permet d'augmenter la dissociation des atomes de carbone et ainsi favoriser la formation de carbone sp^3 . Les travaux portant sur cette première partie ont été effectués au sein du groupe Laser-assisted Nano-engineering du département de Génie Electrique et Informatique à l'Université du Nebraska à Lincoln.

La deuxième partie de ce projet est de concevoir et d'optimiser des drains thermiques, typiquement constitués de métaux (Al, Cu), en adaptant leurs propriétés thermiques et thermomécaniques. Les drains thermiques envisagés sont des matériaux composites à matrice métallique cuivre et renforts particuliers en diamant. Le système Cu-C étant chimiquement inerte, la liaison interfaciale entre le cuivre et les renforts carbonés est uniquement d'ordre mécanique. Cette liaison évolue et se dégrade au cours de la vie du matériau. Afin de créer une liaison chimique forte entre la matrice de Cu et les renforts diamant, des composés capables de réagir avec le carbone, pour générer des

carbures interfaciaux, sont ajoutés au système. Dans cet optique, de tels additifs (X) doivent présenter une forte affinité chimique pour le carbone favorisant ainsi la création de liaisons C-X à travers des interphases de type carbure métallique. Ces travaux ont été effectués au sein du groupe Métallurgie et Matériaux Fonctionnels à l'Institut de Chimie de la Matière Condensée de Bordeaux.

Ce manuscrit de thèse se divise en 4 chapitres. Le premier chapitre explique de manière plus approfondie le contexte à travers une étude bibliographique. Les propriétés du diamant sont introduites, ainsi que les méthodes de synthèse conventionnelles. Les systèmes réactifs et non-réactifs de matériaux composites à matrices métalliques sont présentés et finalement, les propriétés thermiques sont discutées en détail. Le second chapitre, introduit la synthèse et les caractérisations microstructurale, structurale et chimique des matériaux composites obtenus. Le troisième chapitre concerne les dépôts de diamant et plus précisément les effets du substrat et du procédé sur l'adhésion et la qualité des films respectivement. Finalement, le quatrième chapitre présente les propriétés thermiques des matériaux composites obtenus.

Le premier chapitre, après avoir présenté le contexte dans lequel s'inscrit ce travail, et notamment la défaillance de composants microélectroniques due à une mauvaise gestion thermique, explique en détail l'intérêt du diamant en tant que matériau. La suite du chapitre présente ce qu'est un composite à matrice métallique ainsi que les phénomènes de réactivité ou de non réactivité aux interfaces matrice-renforts. L'absence d'affinité chimique entre certains métaux, tels que le Cu, et les renforts de carbone induisent un mauvais transfert de propriétés. Ce phénomène est encore plus marqué pour les propriétés thermiques car la conduction thermique dans les métaux se fait principalement par les électrons,

contrairement au carbone, et surtout dans le cas du diamant, ou la conduction se fait par les phonons. Il est donc important d'assurer le bon transfert entre deux matériaux différents via la création d'une liaison chimique. Ce chapitre conclue sur un bref état de l'art portant sur les matériaux composites Cu/D élaborés en présence d'éléments d'alliages qui après l'élaboration du matériau composite forment des interphases de type carbure.

Le deuxième chapitre présente les matériaux composites Cu/C obtenus via un procédé innovant appelé le « solid-liquid co-existent phase process », ou procédé semi-liquide. Ce procédé a été utilisé dans le cas de matériaux composites à base d'aluminium, cependant il n'a jamais été utilisé, à notre connaissance, dans le cas de matériaux à base de cuivre. En effet, dans le cas de l'aluminium, qui est un élément carburigène, l'insertion d'une faible quantité d'alliage (par ex. AlSi) possédant une température de fusion inférieure à celle de l'aluminium pur, permet la coexistence d'une phase liquide (AlSi) et d'une phase solide (Al et renforts) durant le frittage à une température intermédiaire aux températures de fusion de l'alliage et de l'Al. Ainsi, la phase liquide permet d'augmenter la réactivité de l'Al avec le carbone et de promouvoir la formation du carbure Al_4C_3 . Dans le cas des matériaux synthétisés pour ce travail, l'élément carburigène est ajouté à l'alliage, car la matrice Cu est non-réactive face au carbone. Des poudres d'alliages Cu-Ti et Cu-Zr, aux compositions eutectiques respectives de 27 % at. et 6 % at., sont insérées dans les mélanges composites afin d'obtenir des interphases de TiC et ZrC. Les températures de fusion des alliages Cu-Ti et Cu-Zr sont respectivement 875°C et 966°C.

Le processus semi-liquide est présenté dans la Figure 0.1 Figure. Dans un premier temps, les poudres sont mélangées à l'aide d'un mélangeur 3D puis elles sont insérées dans un moule en graphite. Le frittage a lieu dans une presse à chaud, ou le chauffage est assuré

par une bobine à induction et la pression est appliquée dans une direction uniaxiale. Durant le frittage, à une température intermédiaire aux températures de fusion du Cu et de chaque alliage, l'alliage de cuivre passe en phase liquide et est capable de s'écouler parmi les porosités présentes dans le mélange. La phase liquide a un effet non-négligeable sur la diffusion du Ti et du Zr dans la matrice de Cu et permet aussi d'augmenter la réactivité de ces espèces. A la fin du frittage, un matériau composite dense est attendu dans lequel les renforts de carbone sont revêtus d'une interphase de TiC ou de ZrC, selon le mélange initial.

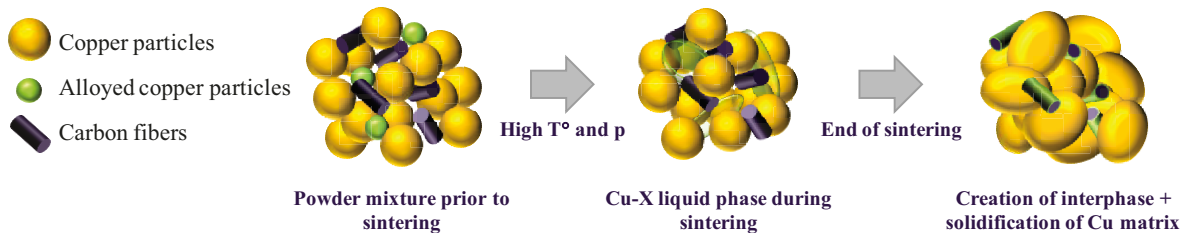


Figure 0.1: Procédé semi-liquide

Les matériaux composites obtenus présentent des interphases continues et homogènes dont l'épaisseur varie selon la quantité d'alliage inséré dans le mélange de poudres. Les micrographies de microscopie électronique à balayage obtenues sont données dans la Figure 0.2.

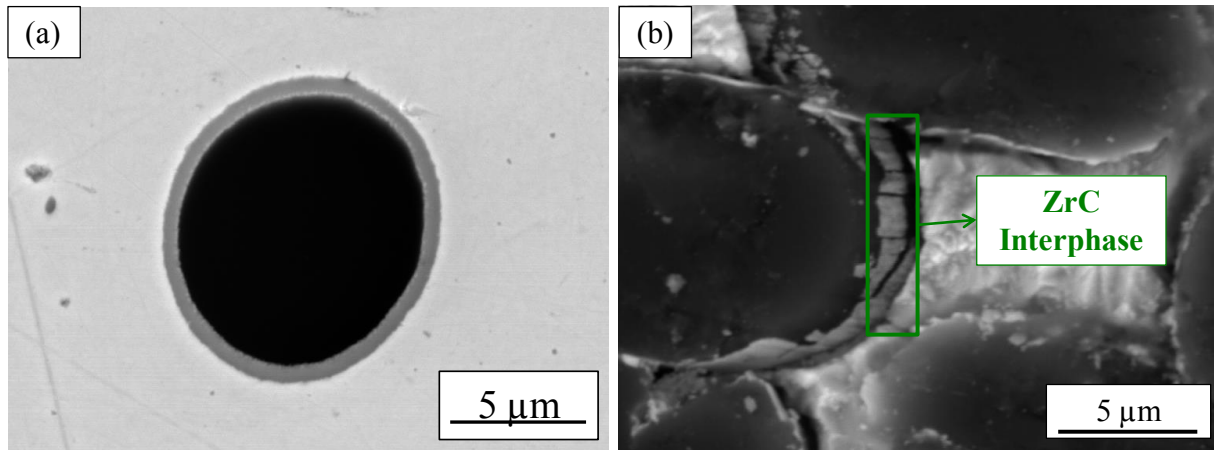


Figure 0.2: Micrographies MEB de la section de (a) un matériau composite avec interphase TiC, et (b) un matériau composite avec interphase ZrC après attaque chimique.

Des simulations thermodynamiques ont permis de prédire la réaction entre les deux éléments et les renforts ainsi que la composition des interphases qui sont comprises entre $\text{TiC}_{0,97}$ et $\text{TiC}_{0,99}$ et $\text{ZrC}_{0,99}$ et ZrC stœchiométrique. Les compositions de TiC ont été confirmées par spectroscopie des pertes d'énergie (EELS).

Des analyses en microscopie électronique à transmission (MET) ont permis la visualisation des microstructures des carbures, sous forme de nanograins pour TiC et de colonnes pour ZrC.

Il a aussi été montré que la phase liquide favorise la purification de la matrice de Cu, à des hautes fractions volumiques de carbone, car elle favorise la diffusion des éléments formant les carbures vers les renforts de carbone. Pour les fractions de faible volume (10% vol.), le potentiel de diffusion du Ti est plus faible, et donc le Ti reste en solution solide dans la matrice de Cu.

La présence de la phase liquide a également permis d'augmenter les densités relatives des matériaux composites pour des fractions de renforts de plus grand volume, par rapport à un simple matériau composite Cu/C.

Enfin, la création des carbures dans les matériaux composites renforcés par des particules de diamants a également été confirmée. La présence de l'interphase conduit à une rupture fragile du diamant (Figure 0.3), lors de la cryofracture, ce qui indique que les liens entre la matrice, les interphases et les renforts sont forts. On s'attend donc à ce que ces interphases améliorent la conductivité thermique des matériaux composites.

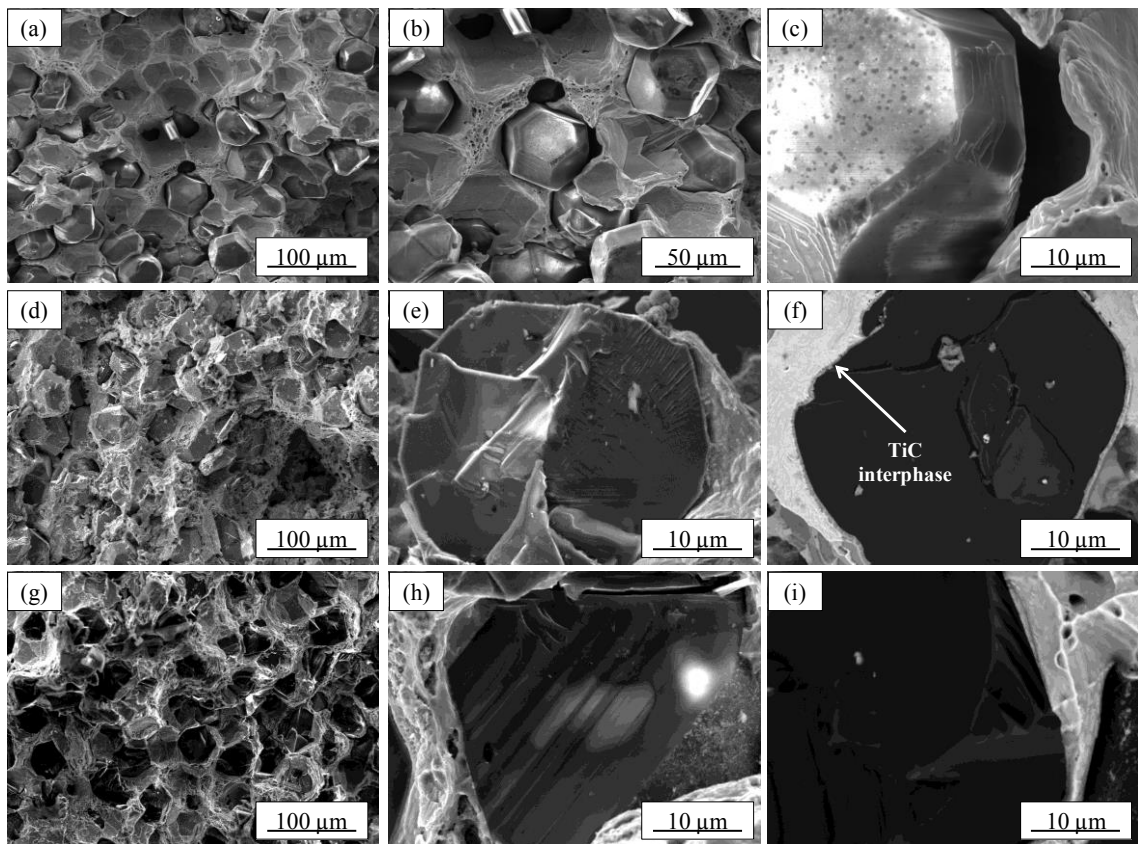


Figure 0.3: Micrographies MEB des sections transverses de matériaux composites Cu/D (a)-(c) sans interphases, (d)-(f) avec interphases TiC, et (g)-(i) interphases ZrC.

Le chapitre 3 résume les travaux menés sur les dépôts de diamants par CVD à combustion assistée laser, l'objectif étant de revêtir des substrats composites cuivre/carbone (Cu/C) avec des films de diamant uniformes et adhérents. Bien que plusieurs procédés CVD existent, le processus de flamme de combustion a été choisi pour cette étude en raison de son fonctionnement à l'air, son faible coût et son taux de dépôt rapide.

L'impact des films de diamant sur la dissipation thermique permet de prédire le comportement d'un film de diamant sur les surfaces composites Cu/C et de prouver leur importance. Les profils de température des substrats composites Cu/CF40% vol. avec et sans un revêtement de diamant sont rapportés sur la Figure 0.4 (a) et (b), respectivement. Plusieurs sources de chaleur sont placées sur le même dissipateur de chaleur. On peut observer que les lignes d'isovaleur de la température sont clairement décalées en raison de l'étalement de chaleur dans le plan induit par le revêtement de diamant, dans le cas de l'assemblage film de diamant/composite. Cette chaleur planaire, qui s'étend à la surface du drain thermique, conduit à une augmentation de la dissipation thermique par conduction à travers le substrat mais également par convection sur la surface du substrat à proximité des sources de chaleur. Ce dernier mode peut avoir un impact important, en particulier lorsque les sources de chaleur sont de petites tailles et que le substrat est épais.

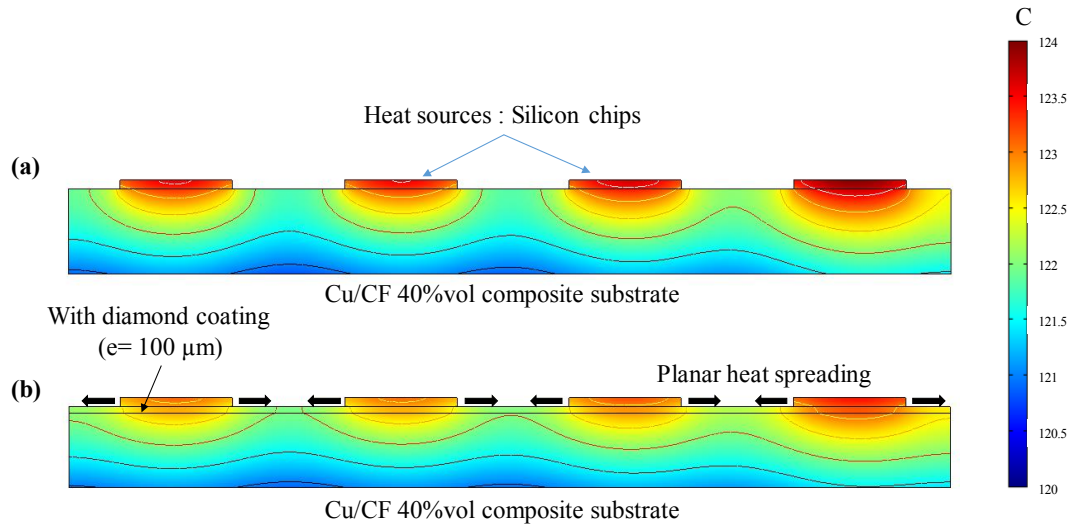


Figure 0.4: Simulation de la dissipation de chaleur par un composite Cu/CF 40% vol. (a) sans et (b) avec un film de diamant de 100 μm d'épaisseur.

Par conséquent, la pertinence d'avoir un film de diamant déposé sur la surface d'un dispositif de dissipation thermique est montrée. Dans le chapitre précédent, l'effet de la teneur en fibres sur le coefficient de dilatation thermique (CTE) des matériaux composites a été discuté. Dans ce chapitre, l'effet du CTE et de la morphologie de surface sur l'adhésion du film de diamant sur le substrat sera démontrée. De plus, une partie de cette recherche visait à modifier les surfaces en faisant varier les géométries des armatures pour favoriser l'encrage mécanique.

Ce chapitre démontre que le dépôt rapide de films diamantés de haute qualité sur des substrats composites Cu/C est possible en utilisant la technique CVD à combustion assistée par laser. Le processus de synthèse présente des avantages par rapport aux voies CVD traditionnelles telles que la flexibilité, le faible coût et les taux de croissance élevés. Le procédé de dépôt multi-énergétique, établi dans des études antérieures, s'est révélé aussi

efficace sur les substrats Cu/C que sur des substrats en Si ou WC, et a permis d'obtenir des films de diamant de hautes qualités (Figure 0.5).

La température optimale du substrat pour le dépôt de diamant a été déterminée comme étant de [700-740] °C. Les températures proches de 740 °C ont donné des cristaux à facettes {100} tandis que des températures plus basses ont favorisé des cristaux orientés de manière aléatoire.

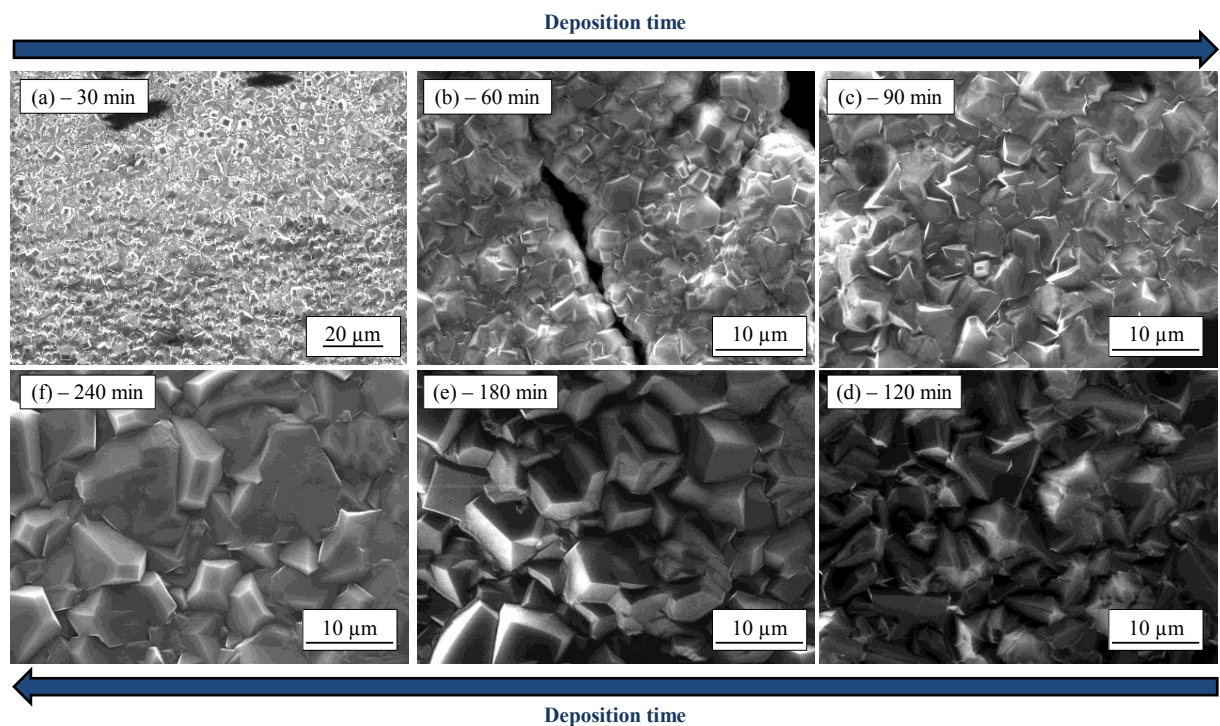


Figure 0.5: Micrographies MEB des surfaces de films de diamants obtenus pour différents temps de dépôts.

La spectroscopie Raman a mis en lumière l'augmentation de la pureté de phase avec l'augmentation de l'épaisseur du film de diamant qui est liée à une augmentation de la taille des grains de diamant. En outre, il a révélé la diminution des contraintes résiduelles totales avec l'augmentation de l'épaisseur du film, indiquant l'augmentation des contraintes

(traction) intrinsèques lors de la croissance du diamant. L'insertion de CF a amélioré les substrats à base de cuivre. Les fibres de carbone ont permis d'adapter le CTE du substrat et de réduire les contraintes thermiques induites à l'interface diamant-substrat.

Les différentes géométries de renfort utilisées ont permis de créer différents sites d'encrage mécanique ce qui a favorisé la germination et assuré une bonne adhérence des films de diamant sur les substrats composites. Cependant, d'autres analyses sont nécessaires pour tirer des conclusions sur l'effet des morphologies des vides sur la pureté de la phase du film de diamant et les contraintes résiduelles.

Les matériaux composites Cu/C présentés dans le chapitre 3 ont été utilisés pour la caractérisation thermique. La conductivité thermique est au centre de ce dernier chapitre car elle est un facteur important dans la bonne performance de ces matériaux composites comme dispositifs de dissipation thermique.

Les matériaux composites présentés ici ont été synthétisés en utilisant un procédé de métallurgie des poudres reposant sur un pressage unidirectionnel à chaud. Cependant, certains de ces matériaux composites ont été fabriqués en utilisant le procédé semi-liquide. Le Ti et le Zr, qui ont été ajoutés au mélange de poudres initial, ont été capables de former des interphases de carbure d'épaisseur nanométrique, d'épaisseur contrôlée, à l'interface Cu/C. Ces interphases devraient améliorer le transfert thermique dans les composites.

Deux systèmes sont présentés, les composites renforcés par CF et les composites renforcés par D. Pour les renforts CF, il faut prendre en compte la distribution et l'orientation des CF car leur forme anisotrope, et donc leurs propriétés thermiques anisotropes, rendent le matériau anisotrope également. En effet, selon la direction

d'analyse, les CF sont soit alignés le long de leur axe principal, soit perpendiculaires à celui-ci. Sachant que la conductivité thermique de la CF est plus élevée le long de son axe primaire, l'analyse dans cette direction entraîne souvent des conductivités thermiques plus élevées. Cependant, les deux directions (parallèle à l'axe de la CF ou perpendiculaire) conduisent à des conductivités thermiques inférieures à la conductivité thermique du Cu. Pour simplifier l'anisotropie, on suppose que le renfort a une conductivité moyenne de 278 W/m.K, qui est inférieure à celle du Cu et donc, réduit la conductivité globale du composite (Figure 0.6).

En outre, il n'est pas trivial de prédire le comportement thermique de matériaux anisotropes avec des modèles analytiques. En effet, la plupart des problèmes proviennent de l'absence de paramètres reliant la distribution, l'orientation, le facteur de forme et les contributions des résistances thermiques interfaciales dans les modèles.

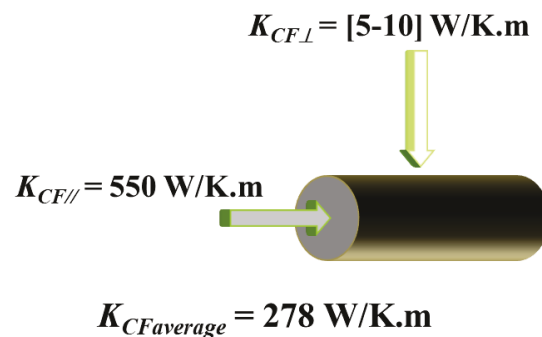


Figure 0.6: Anisotropie de la fibre de carbone (CF).

Les conductivités thermiques des matériaux composites synthétisés en utilisant le procédé semi-liquide, avec Ti et Zr, présentent des conductivités thermiques supérieures à celles des matériaux composites Cu/CF sans interphases, bien que la conductivité thermique globale soit toujours inférieure à celle du Cu pur. Cependant, la présence d'une

interphase de carbure est bénéfique pour le transfert de propriétés dans le matériau composite.

L'impact de la quantité de phase liquide insérée dans le matériau composite, et donc des quantités de Ti ou de Zr, est également indiqué. En effet, il y a une teneur en Zr qui présente la conductivité thermique la plus élevée comme indiqué sur la Figure 0.7.

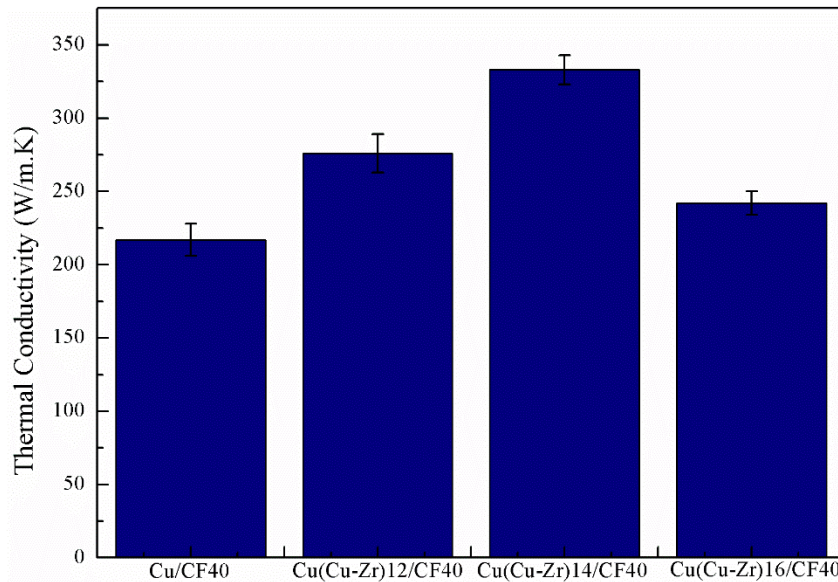


Figure 0.7: Effet de la quantité de Cu-Zr sur la conductivité thermique de composites avec 40 vol. % de CF.

Les caractérisations thermiques réalisées sur les matériaux composites renforcés par des particules de D ont permis d'obtenir une conductivité thermique plus élevée pour le matériau composite que pour le Cu pur. Parallèlement aux analyses expérimentales, des calculs analytiques et numériques ont été effectués pour prédire les résistances thermiques interfaciales et les conductivités thermiques effectives pour les matériaux composites Cu/D, Cu(Cu-Ti)/D et Cu(Cu-Zr)/D. Il a été montré que le modèle DMM, utilisé pour prédire la résistance thermique interfaciale dans un matériau composite Cu/D, n'est pas

assez réaliste car il ne prend en compte aucun aspect morphologique de l'interface, comme la rugosité, les vides et autres défauts.

De plus, la résistance thermique interfaciale dans un matériau composite Cu(Cu-X)/D (avec X = Ti, Zr) inclut la contribution du carbure (terme $e_{TiC \text{ ou } ZrC} / k_{TiC \text{ ou } ZrC}$ dans l'équation 5.6). Le procédé semi-liquide permet d'atteindre des résistances thermiques interfaciales comprises entre $1,5-3,05 \times 10^{-8}$ K.m²/W, ce qui est très faible et surtout comparable à des interfaces du type substrat/couche mince. En effet, un film mince obtenu par pulvérisation cathodique sur des surfaces propres et lisses présente généralement des résistances thermiques de l'ordre de $5-10 \times 10^{-8}$ K.m²/W. Par conséquent, des interphases de qualité de couches minces peuvent être obtenues par un processus qui peut facilement être industrialisé.

L'impact de la taille des particules de diamant sur la conductivité thermique, qui avait été mentionné dans la littérature, a été confirmé. Les conductivités thermiques les plus élevées obtenues pour une fraction volumique donnée de particules de diamant ont été mesurées pour des diamètres de poudre de diamant variant entre 170 à 200 μ m.

De plus, les prédictions de conductivités thermiques pour les matériaux composites qui contiennent du Ti et du Zr sont assez précises, bien que d'autres investigations soient nécessaires pour confirmer et établir une méthodologie.

Enfin, les conductivités thermiques des matériaux composites obtenus par le procédé semi-liquide sont bien situées par rapport à la littérature et aux études antérieures menées à l'ICMCB. A titre de comparaison, la Figure 0.8 rassemble les conductivités thermiques obtenues pour les matériaux composites Cu/D avec les interphases B₄C, Cr₃C₂

et Cu submicroniques ainsi que celles présentées dans ce travail pour les interphases TiC et ZrC.

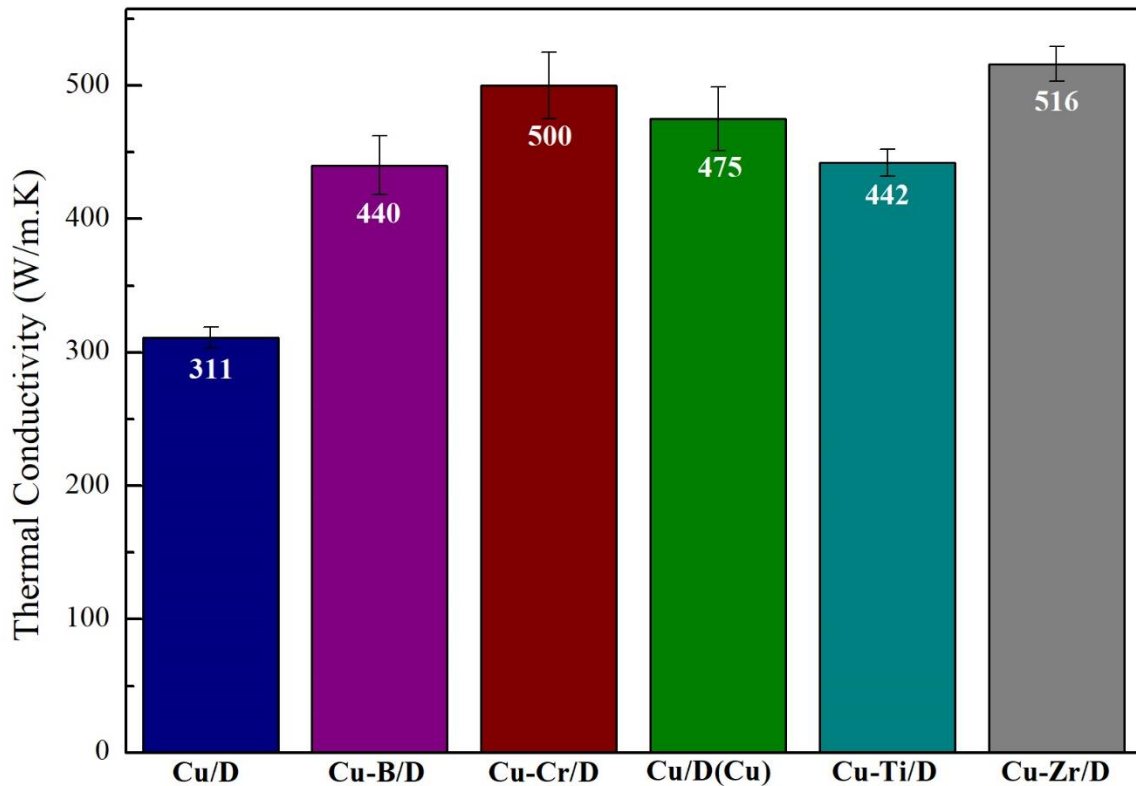


Figure 0.8: Conductivités thermiques obtenues pour des matériaux composites renforcés par des particules de diamant de 60 μm de diamètre dans les études précédentes menées à l'ICMCB et dans ce travail.

En conclusion, le diamant était situé au centre de ce travail de thèse. C'est un candidat très prometteur pour les applications de dissipation thermique en raison de ses propriétés thermiques exceptionnelles. L'objectif était d'utiliser des multi-matériaux à base de diamant pour remplacer les dissipateurs de chaleur dans les composants microélectroniques. En effet, pour améliorer la miniaturisation et la densité de puissance des composants, il faut se concentrer sur la dissipation de la chaleur créée pendant le fonctionnement du composant.

TABLE OF CONTENTS

1. INTRODUCTION.....	17
1.1. Motivations.....	17
1.2. Overview of the Dual Ph.D. Program	22
1.3. Dissertation Outline.....	24
2. BACKGROUND AND REVIEWS	25
2.1. Introduction	25
2.2. Diamond: From Precious Gem to Common Applications	26
2.2.1. Composition and Crystal Structure.....	26
2.2.2. Properties	29
2.2.2.1. Optical Properties	29
2.2.2.2. Mechanical Properties	31
2.2.2.3. Electrical Properties.....	32
2.2.2.4. Thermal Properties	32
2.3. Diamond Synthesis.....	33
2.3.1. High Pressure High Temperature Process.....	34
2.3.2. Chemical Vapor Deposition.....	35
2.3.3. Nucleation.....	36
2.3.4. Growth	37
2.4. Metal Matrix Composites.....	38
2.4.1. The Metal Matrix	39
2.4.2. The Reinforcements	41
2.4.3. The Interface	42
2.4.4. Reactive and Nonreactive Systems.....	44
2.4.4.1. Reactive Systems.....	44
2.4.4.2. Nonreactive Systems	47
2.5. Heat Transfer Phenomena	51
2.5.1. Heat Transfer Across a Metal-Diamond Interface.....	57
2.5.2. Heat Transfer at the Metal–Nonmetal Interface	58

2.5.2.1	The Acoustic Mismatch Model	61
2.5.2.2	The Diffuse Mismatch Model.....	63
2.5.3.	Metal Matrix Composites for Thermal Management	65
2.5.3.1	Analytical and Numerical Models.....	66
2.5.3.2	Experimental Data	69
2.6.	Conclusion.....	72
3.	COPPER/CARBON COMPOSITE MATERIALS	74
3.1	Introduction	74
3.2	The Solid-Liquid Coexistent Phase Process.....	77
3.2.1	Starting Materials.....	80
3.2.1.1	The Copper Matrix	80
3.2.1.2	The Alloyed Copper	82
3.2.1.3	The Carbon Reinforcements	86
3.2.2	Sintering.....	91
3.2.2.1	Mixing	91
3.2.2.2	Cold Compaction.....	92
3.2.2.3	Sintering Mechanism.....	92
3.2.2.4	Experimental Setup.....	94
3.2.3	Thermodynamic Assessments.....	95
3.2.3.1	The Cu-Ti-C System.....	95
3.2.3.2	The Cu-Zr-C system	98
3.3	In Situ Creation of the XC Interphases	101
3.3.1	Cu/C Composite Materials.....	102
3.3.2	Cu(Cu-Ti)/C Composite Materials	106
3.3.3	Cu(Cu-Zr)/C Composite Materials	113
3.3.4	Diamond-Based Composite Materials	119
3.4	Conclusion.....	121
4.	COMBUSTION CVD OF DIAMOND FILMS	123
4.1.	Introduction	123

4.2.	Combustion Synthesis of Diamond Films.....	125
4.2.1	Principle	125
4.2.1.1	Experimental Setup.....	128
4.3.	Diamond Growth on Cu/C Composite Materials.....	130
4.3.1.	First Instance of Diamond Deposition	130
4.3.2.	Diamond Film Microstructure	135
4.3.2.1	Top Surface Microstructure.....	137
4.3.2.2	Cross-Section Microstructure	138
4.3.3.	Diamond Film Phase Purity and Residual Stresses	141
4.3.3.1	Raman Principle and Setup.....	141
4.3.3.2	Phase Purity	145
4.3.3.3	Residual Stresses	148
4.4	. Laser-Assisted Combustion Flame CVD of Diamond Films.....	150
4.4.1	Vibrational excitation of precursor molecules	150
4.4.1.1	Principle.....	150
4.4.1.2	Experimental Setup.....	154
4.4.2	Electronic Excitation of Precursor Molecules	155
4.4.2.1	Principle.....	156
4.4.2.2	Experimental Setup.....	156
4.5.	Laser-Assisted Diamond Growth on Cu/C Composite Materials	157
4.5.1.	Exposed Surfaces	157
4.5.2	Surface Roughness.....	158
4.5.3	Diamond Film Microstructure	160
4.5.4	Diamond Phase Purity and Residual Stresses.....	162
4.6.	Conclusion.....	164
5.	PHYSICAL PROPERTIES	166
5.1.	Introduction	166
5.2.	Experimental Setups.....	168
5.3.	Thermal Characterization of Cu/C Composites	171
5.3.1.	Cu/CF Composites	171

5.3.1.1	Cu/CF Composites With No Interphase	171
5.3.1.2	Cu-Ti Additions.....	176
5.3.1.3	Cu-Zr Additions.....	178
5.3.2.	Cu/D composites.....	181
5.3.2.1	Interfacial Thermal Resistance Dependence	183
5.3.2.2	Interphase Dependence.....	185
5.3.2.3	Particle size dependence.....	191
5.4.	Conclusion.....	193
6.	GENERAL CONCLUSIONS AND OUTLOOKS	197
6.1	General conclusion.....	197
6.2	Future directions.....	200
6.2.1	Diamond deposition.....	200
6.2.2	Thermal evaluation of diamond films.....	201
6.2.3	Thermal evaluation of composites	204
6.2.4	Thermal evaluation of interphases	206
6.2.5	Alternative interphases.....	208

LIST OF FIGURES

Figure 1.1. Moore's law. (a) Initial predictions published in 1965 [3] and (b) evolution up to 2016 [4].....	18
Figure 1.2. Three-dimensional view of a multichip power electronic module [5].....	20
Figure 2.1. Schematic drawing of the diamond crystal structure: (a) the inner crystal, (b) the {111}, and (c) the {100} faces, respectively [12].	27
Figure 2.2. Four types of natural diamonds: a) Type Ia, b) Type Ib, c) Type IIa, and d) Type IIb.	30
Figure 2.3. P-T phase diagram for carbon [22].....	34
Figure 2.4. Simplified form of the atomic C–H–O diagram based on the diagram published by Bachman et al. [25].....	36
Figure 2.5. Types of metal matrix composites. (a) Continuous composite, (b) and (c) discontinuous composites.	42
Figure 2.6. Cross-section of a SCS-6 SiC fiber coated with pyrolytic carbon within a Ti6Al4V matrix [35].....	44
Figure 2.7. Liquid drop on a solid substrate with various contact angles [36], with γ_{sv} , γ_{sl} , γ_{lv} , the interfacial tensions between the solid-vapor, solid-liquid, and liquid-vapor phases, respectively.	45
Figure 2.8. SEM micrograph of the cross-section of an Al-C specimen after 20400 s at 1100 K [37].....	46
Figure 2.9. Optical micrographs showing the reactions that occurred at the interface between the C substrate and the Cu alloys containing (a) 1 at% chromium (Cr), (b) 1 at% Ti, (c) 1 at% tantalum (Ta), and (d) 1 at% Zr [40].....	48
Figure 2.10. Scanning electron microscopy (SEM) micrograph of copper-chromium/carbon fiber composite after sintering and annealing treatment [41].....	49

Figure 2.11. Transmission electron microscopy (TEM) micrographs of a Cu/Coated diamond particle obtained at the ICMCB during T. Guillemet's Ph.D. [5].	51
Figure 2.12. Schematic of the interactions between free electrons and impurities. (a) Free electrons and impurities with no interaction, (b) collision between electrons and impurities, and (c) displaced impurities and electrons after collision.	53
Figure 2.13. Example of a) longitudinal wave and b) transversal wave.	54
Figure 2.14. Schematic of lattice vibrations. (a) No vibration, (b) only one side is heated; therefore, one side of the network starts vibrating, and (c) the entire network vibrates.	55
Figure 2.15: Schematic illustration of the two possible couplings for heat transport. (1) Transfer from electrons from the metal and phonons from the nonmetal through anharmonic interactions, and (2) transfer of the electrons' energy to the phonons in the metal which has a resistance R_{e-p} and then transfer of the phonons' energy to the nonmetal across the interface with a resistance R_{p-p} [50]. The terms T , T_e , T_p , and T'_e stand for the temperature of the nonmetal, the electron and phonon temperatures of the metal, and the equivalent temperature of the metal, respectively.	60
Figure 2.16. (a) Schematic of the possibilities within the framework of AMM for phonons incident on an interface, and (b) incident and transmitted phonon angles, related according to Snell's law [48].	61
Figure 2.17. Comparison of effective thermal conductivity of bimodal distribution of Al_2O_3 filler in a polyethylene matrix (with a filler-to-grain ratio of 65:9 μm) as predicted by various models and experimental points taken from [58].	69
Figure 2.18. Thermal conductivity with respect to the thickness of the Ti coating deposited on diamond particles, from [66].	72
Figure 3.1. Schematic view of how CTE mismatches lead to compressive stresses (yellow arrows) and tensile stresses (green arrows) for $\alpha_{Al_2O_3} < \alpha_{Cu}$.	74
Figure 3.2. Binary phase diagram of the Cu-C system. Closer view of the solubility limit of C in solid Cu at high temperatures.	75

Figure 3.3. Schematic view of (a) a Cu-C nonreactive interface and the (b) presence of an XC carbide interphase.	78
Figure 3.4. Schematic of the solid-liquid coexistent phase process. The initial powder mixture (Cu + Cu-X+ CF) is sintered under load at high temperature. During the sintering plateau, the Cu-X liquid phase is generated. Finally, at the end of the sintering process, the carbon fibers are coated with a XC interphase.....	79
Figure 3.5. SEM micrographs of dendritic copper powders used for the composite matrix.....	81
Figure 3.6. XRD pattern of the dendritic Cu powder.....	81
Figure 3.7: SEM micrographs of (a), (b) Cu-Ti alloy and (c), (d) Cu-Zr alloy powders.....	85
Figure 3.8: High quality XRD patterns of (a) Cu-Ti and (b) Cu-Zr alloyed powders.	86
Figure 3.9. (a) SEM micrograph of a CF and (b) anisotropic thermal conductivity caused by the anisotropy of shape of the CF.	89
Figure 3.10: MBD6 grade diamond particles used as reinforcements in the Cu-D composites. ...	90
Figure 3.11. 3D mixing device used for powder homogenization.....	92
Figure 3.12. The stages of sintering: Stage 1, loose powder; Stage 2, initial stage with contact points between particles; Stage 3, intermediate stage including the creation of "necks" between particles and an increase in the relative density and localization of pores at the trijunctions of adjacent grains; and Stage 4, final stage with a relative density between 91 and 95%, and the pores are now closed [75].....	93
Figure 3.13. (a) Photograph and (b) schematic of the uniaxial hot-press apparatus.....	95
Figure 3.14. Cu-Ti-C system: (a) Cu-rich side of the Cu-Ti phase diagram and (b) isothermal section at 950 °C [79–81].	96
Figure 3.15. Calculated Ti-C binary phase diagram according to the assessment of Dumitrescu et al [81].....	97
Figure 3.16. Equilibrium composition calculations of the five samples at 950 °C: (a) mole and (b) volume fractions of phases.....	98

Figure 3.17. Equilibrium composition calculations of the five samples at 25 °C: (a) mole and (b) volume fractions of phases.....	98
Figure 3.18. Cu-Zr-C system: (a) Cu-rich side of the Cu-Zr phase diagram and (b) isothermal section at 1050 °C.....	99
Figure 3.19. Equilibrium composition calculations of the four samples at 1050 °C: (a) mole and (b) volume fractions of phases.....	101
Figure 3.20: Equilibrium composition calculations of the four samples at 25 °C: (a) mole and (b) volume fractions of phases.....	101
Figure 3.21. Orientation of carbon fibers in the composite (a) cross-section, observation perpendicular to the pressure axis, and (b) surface, observation parallel to the pressure axis.....	103
Figure 3.22. SEM micrographs of Cu-CF composites (a) with 40 vol % and (b) with 60 vol % of CFs.....	105
Figure 3.23. SEM micrograph of a Cu/C composite showing debonded interfaces [83].	106
Figure 3.24. SEM micrographs in backscattered electron (BSE) mode of Cu(Cu-Ti) _x /CF20 composites with (a) 4, (b) 8, and (c) 10 vol% of Cu-Ti alloyed powders.....	107
Figure 3.25: EDS line scan obtained through the cross-section of a CF coated with a Ti-based interphase inside the Cu matrix.....	108
Figure 3.26. High quality XRD pattern obtained from a Cu(Cu-Ti) ₈ /CF20 composite in a 2-Theta range of 30 to 65°.....	109
Figure 3.27. TEM images of Cu(Cu-Ti) ₄ /CF10 composite material. (a) Overall view of a CF, the interfacial zone, and the Cu matrix, (b) enlarged interfacial zone of micrograph (a), where a polycrystalline structure is observed. (c) Electron diffraction patterns of interfacial zone and (d) an area where both the interfacial zone and the Cu matrix are present.	110
Figure 3.28. (a) EELS spectrum collected between 240 and 515 eV in the interphase area of the Cu(CuTi) ₄ /CF10 sample, (b) ELNES at the C K-edge, (c) TEM bright field micrograph (left) and corresponding EDX map at the C-K edge (red), Cu-K edge (yellow), and Ti-K edge (green). ...	112

Figure 3.29: ELNES at the Cu $L_{2,3}$ edge. The Cu edge recorded in the sample (black line) is compared to reference spectra obtained on Cu (blue line), Cu_2O (red line), and CuO (green line), which were taken from [27]. For the sake of clarity, the reference spectra were vertically shifted; and the energy of the Cu edge onset was adjusted to that of the reference spectra.	113
Figure 3.30. SEM micrographs in BSE mode of $Cu(Cu-Zr)_x/CF40$, with (a), (b) 14, and (c) 20 vol% of Cu-Zr alloyed powders.....	114
Figure 3.31. EDS line scan obtained through the cross-section of a CF coated with a Zr-based interphase inside the Cu matrix.....	115
Figure 3.32: SEM micrograph in BSE mode of a $Cu(Cu-Zr)_{20}/CF40$ composite after chemical etching of 2 min in diluted HNO_3	116
Figure 3.33: High quality XRD pattern obtained from a $Cu(Cu-Zr)_{12}/CF40$ composite in a 2Theta range of 30 to 70°.....	117
Figure 3.34: Transmission electron micrographs of $Cu(Cu-Zr)_{14}/CF40$ composite material. (a) Overall view of a CF, the interfacial zone, and the Cu matrix and (b) higher magnification of a similar zone. Electron diffraction patterns of (c) the interfacial zone and (d) an area where both the interfacial zone and the Cu matrix are present.....	119
Figure 3.35: Scanning electron micrographs of fracture surfaces of (a)-(c) Cu/D, (d)-(f) $Cu(Cu-Ti)/D$, and (g)-(i) $Cu(Cu-Zr)/D$ composite materials.	121
Figure 4.1. Simulation of heat dissipation in a Cu/CF 40 vol% substrate and a diamond film-Cu/CF 40 vol% substrate [89].	124
Figure 4.2. Schematic view of the oxyacetylene combustion flame geometry.....	126
Figure 4.3. Evolution of diamond crystal morphology as a function of the facet growth velocity ratio. From left to right, α increases from 1 (cubic) to 3 (octahedron) with a step of 0.25. The arrows indicate the fastest growth direction [98].....	128
Figure 4.4. Schematic diagram of the diamond deposition setup.	129

- Figure 4.5. Cu/CF 40 vol% surface (a) before diamond deposition, (b) after 2 min, (c) after 5 min, and (d) after 15 min of diamond deposition..... 131
- Figure 4.6. Schematic views of the initial surface and the voids left on the surface after the CF consumption. (a) Before diamond deposition, (b) ① closed void (the gap of the void is sufficiently small to trap deposited carbon), and (b) ② open void (the gap of the void is large enough that it cannot trap carbon), after diamond deposition..... 132
- Figure 4.7. SEM micrographs of (a) the surface of a Cu/CF 20 vol% composite after diamond film peel-off and (b) the bottom face of diamond film with ball-like carbon protrusions..... 133
- Figure 4.8. SEM micrographs showing the early stages of diamond deposition in the matrix region. (a) Creation of diamond nuclei in the voids (after 5 min deposition), (b) creation of diamond nuclei on the top surface (after 10 min deposition), and (c) diamond crystal coalescence (after 15 min deposition). 134
- Figure 4.9. SEM micrographs of films deposited on Cu/CF composites after 30 min of deposition at various temperatures. (a) 690 °C, no diamond presence, (b) 720°C, randomly oriented diamond crystals, (c) 755 °C, randomly oriented diamond crystals, and (d) 770 °C, amorphous carbon. 135
- Figure 4.10. SEM micrographs of diamond films after diamond depositions of 30 min. (a) Cu , (b) Cu/CF 10 vol%, (c) Cu/CF 20 vol%, (d) Cu/CF 30 vol%, and (e) Cu/CF 40 vol% substrate. ... 137
- Figure 4.11. SEM micrographs of diamond films deposited on Cu/CF 40 vol% composite substrates for (a) 30, (b) 60, (c) 90, (d) 120, (e) 180, and (f) 240 min..... 138
- Figure 4.12. SEM micrographs of the cross-sections of diamond films deposited for (a) 90, (b) 120, (c) 180, and (d) 240 min. 140
- Figure 4.13. (a) Energy level diagram showing the states involved in Raman spectroscopy. The line thickness is representative of the signal strength. (b) Light-matter interaction processes in Raman spectroscopy..... 142
- Figure 4.14. Typical Raman spectrum of diamond. Sharp peak at 1332 cm⁻¹. 143

Figure 4.15. Typical Raman spectrum of a diamond film deposited through the use of combustion flame CVD.....	144
Figure 4.16. Simplified Raman setup schematic.....	145
Figure 4.17. Raman spectra of diamond films deposited on Cu/CF 40 vol% composites after 90, 120, 180, and 240 min.....	147
Figure 4.18. Schematic of energy storage for a diatomic molecule.....	151
Figure 4.19. OES spectrum, showing the optical absorption of the CO ₂ laser excitation by the combustion flame.....	153
Figure 4.20. (a) Scheme of how the laser excitation at 10.532 μm affects the wagging mode of a C ₂ H ₄ molecule. Photographs of the combustion flame (b) without and (c) with 10.532 μm laser irradiation.....	154
Figure 4.21. Experimental setup for CO ₂ -laser-assisted combustion flame CVD of diamond films.	155
Figure 4.22. Schematic diagram showing electron excitation of carbon atoms.....	156
Figure 4.23. KrF-assisted diamond deposition setup. (a) Schematic and (b) set-up and laser path.	157
Figure 4.24. SEM micrographs of the carbon reinforcements used. (a) Graphite flakes, (b) carbon powder, and (c) carbon fibers.	158
Figure 4.25. SEM micrographs of top surface after 5 min of diamond deposition on surfaces containing (a) GFs, (b) CFs, and (c) CPs.....	159
Figure 4.26. Optical profiler 3D maps of the composite substrates after 5 min of diamond deposition with (a) CFs, (b) carbon powder, and (c) GFs on surfaces.	160
Figure 4.27. SEM micrographs of the top surface of diamond films deposited with no laser excitation on surfaces with (a) CFs, (b) GFs, and (c) CP.	161
Figure 4.28. SEM micrographs of the top surface of diamond films deposited with CO ₂ laser excitation on surfaces with (a) CFs, (b) GFs, and (c) CP.	161

Figure 4.29. SEM micrographs of the top surface of diamond films deposited with KrF laser excitation on surfaces with (a) CFs, (b) GFs, and (c) CP.	162
Figure 5.1. Scanning electron micrographs of Cu/CF composites with (a) TiC interphases, and (b) ZrC interphases (after chemical etching).	167
Figure 5.2. Flash laser apparatus: (a) photograph and (b) schematic of the setup.	169
Figure 5.3. Experimental setup implemented at the I2M.	170
Figure 5.4. (a) Schematic of the thermal diffusivity measurement and (b) thermogram example.	170
Figure 5.5. Micrographs of a Cu/CF composite taken (a) on the cross-section and (b) on the surface. Anisotropic thermal properties of carbon fibers induced by the anisotropic shape of CFs.	171
Figure 5.6. Thermal diffusivity with respect to the CF content. Blue points correspond to the thermal diffusivities perpendicular to the pressure axis (along the CF axis), and red points correspond to the diffusivities parallel to the pressure axis. Thermal diffusivities were measured on Cu/CF composites containing 4 vol% of Cu-Ti.	172
Figure 5.7. Thermal conductivity with respect to carbon fiber content. Comparison of analytical models and experimental values.	175
Figure 5.8. SEM micrographs of the cross-section of (a) a Cu/CF 40 vol% and (b) a Cu/CF 60 vol% composite.	176
Figure 5.9. Thermal conductivity values obtained for composites without (green) and with TiC interphases (red = 4 vol% of liquid phase, blue = 6 vol% of liquid phase).	178
Figure 5.10. Histogram showing the evolution of thermal conductivity for composites with and without different volume fractions of Cu-Zr.	180
Figure 5.11. Schematics of the FEM of randomly distributed diamond particles in a copper matrix.	183

Figure 5.12. Effective thermal conductivity of Cu/D composites with respect to the interfacial thermal resistance for different volume fractions of diamond particles of 60 μm in diameter. ...	184
Figure 5.13. Real diamond-Cu interface with voids, roughness, and, therefore, poor contact. ...	185
Figure 5.14. Effective thermal conductivity with respect to the diamond content for different interfacial thermal resistances. The experimental points corresponding to Cu(Cu-Zr)/D40 (blue) and Cu(Cu-Ti)/D40 (orange) are also reported.	188
Figure 5.15. Thermal conductivities of Cu/D composites without Cu-Ti (blue) and with Cu-Ti addition (red).	189
Figure 5.16. Histogram presenting the different thermal conductivities obtained for pure Cu, Cu/D with no interphase, Cu/D with TiC interphase, and Cu/D with ZrC interphase. Dashed line corresponds to the thermal conductivity of pure Cu.	190
Figure 5.17. Effective thermal conductivity with respect to diamond particle size for several volume fractions of reinforcements.	191
Figure 5.18. Theoretical and experimental thermal conductivities of composites with 40 vol% of diamond reinforcements of different sizes.	192
Figure 5.19. Comparison of thermal conductivities obtained for Cu/D composites with various interfaces [5].	196
Figure 6.1. Schematic set-up of MPTR.	202
Figure 6.2. Parallel (along the CF axis) and perpendicular thermal conductivities of a Cu/CF 40 % composite material used as substrate for diamond deposition.	203
Figure 6.3. Calculated and experimental phase of a diamond film deposited on Cu/CF 40 vol% composite.	204
Figure 6.4. Thermal cycle program imposed to Cu/CF, Cu(Cu-Ti)/CF and Cu(Cu-Zr)/CF composites with 40 vol% of carbon fibers.	205
Figure 6.5. AFM and SThM modes on the surface of a Cu-Ti/CF composite.	207

Figure 6.6. Phase and amplitude variations reported from the SThM probe while scanning a Carbon fiber/TiC/Cu zone.	208
Figure 6.7. Crystal structure of the 211 (n=1), 312 (n=2), and 413 (n =3) $M_{n+1}AX_n$ phases. Adapted from [124].	209
Figure 6.8. XRD pattern of powder obtained from Induction melting of Si, Ti, and C at the appropriate proportions for the synthesis of Ti_3SiC_2	210
Figure 6.9. SEM micrographs of the cross-section of a composite synthesized with Cu-Ti and Cu-Si liquid phases.	211
Figure 6.10. EDS line scans (a) across a carbon fiber, (b) across the residues in the matrix.	212
Figure 6.11. XRD pattern of a composite synthesized with Cu-Ti and Cu-Si liquid phases.	213

LIST OF TABLES

Table 2.1: Classification of the types of diamond.	29
Table 2.2. Classification of composite materials with respect to the matrix nature.	38
Table 2.3. Specifications required for new age heat-sink materials.	40
Table 3.1. Evolution of the electrical resistivity variation of Cu alloys at 20 °C with respect to the nature and content of carbide forming additives.	83
Table 3.2. List of carbide-forming elements which exhibit a eutectic transformation at a temperature which is inferior to Cu's melting point (1083 °C).	83
Table 3.3. Gibbs free enthalpy of formation of considered carbides at 25 °C.	84
Table 3.4. Specifications of alloyed copper powders.	84
Table 3.5. Specifications of K223HM carbon fibers used as reinforcements.	88
Table 3.6. Occupancy of ZrC sites given in atomic fractions per site.	99
Table 3.7. Theoretical, experimental and relative densities of Cu-C composites with CF content of 10-60 vol%.	104
Table 3.8: Atomic fractions and ratios of Cu, Cu-Ti, and C in the composite materials for each volume fraction of Cu-Ti.	106
Table 3.9. Theoretical and calculated Cu lattice parameters of Cu(Cu-Ti) ₈ /CF20.	109
Table 3.10. Atomic fractions and ratios of Cu, Cu-Zr, and C in the composite materials for each volume fraction of Cu-Zr.	113
Table 3.11: Theoretical and calculated Cu lattice parameters of Cu(Cu-Zr) ₁₄ /CF40.	117
Table 4.1. Diamond grain sizes and thicknesses with respect to deposition duration.	140
Table 4.2. Quality factors of diamond films with respect to deposition durations.	148
Table 4.3. Residual stresses of diamond films with respect to deposition duration.	149
Table 4.4. Quality factors and residual stresses of diamond films deposited on composites with various surfaces during 60 min with and without laser excitation.	163

Table 5.1. List of Debye's temperatures of Cu, D, TiC, and ZrC.	182
Table 5.2. Experimental and theoretical thermal conductivities with respect to diamond particle content. The theoretical conductivity was calculated using the modified Maxwell model and R_i calculated through the DMM.	185
Table 5.3. Phonon transfer probabilities and thermal boundary resistances calculated through the DMM for different interfaces.	186
Table 6.1. Quality factors and residual stresses of diamond films deposited on composites with various surfaces during 60 min with and without laser excitation.	201

1. Introduction

1.1. Motivations

The rapid development of the power electronics industry has led to important technological advances since the 1950s [1]. In fact, electrical energy has now become a technological tool used for faster and cheaper computing as well as for the development of new transportation (electric trains, cars, etc.). Power electronics typically consist of semiconductor devices which allow conversion of electrical current from alternative to direct or modification of the potential and the current intensity. Electronics and, therefore, microelectronics, deal with controlling electrical energy by generating, distributing, storing, and converting it to and from other energy forms. Electronics are widely used in information processing, telecommunications, and signal processing as well as in transportation systems (aeronautic, railway, and automotive) in the form of microelectronic components.

Although power electronics were set to develop rapidly, the physical means associated with the enhancement of either computing abilities or energy storage and transport have created limitations in their development and constitute a challenge in keeping the devices cool. The ability to keep a device at low temperature is critical when determining its lifespan, efficiency through time, and reliability. With miniaturization and the increase in operating power in components, new materials are needed to overcome pressing thermal management issues.

Electronic devices have been among the fastest advancing fields of the past half-century. Indeed, electronic devices have shrunk to the microscale and nanoscale, with next

generation technology aiming to use minimum sizes below 10 nm [2]. It is well known that the miniaturization and increasing density of transistors and other integrated circuits (ICs) over time has enhanced the performance of the components. Gordon E. Moore, co-founder of Intel[®], noticed that since 1958, when ICs were invented, the number of transistors per IC has doubled every two years [3]. He predicted that this trend would last for at least ten years. The semiconductor industry has used what is now called Moore's law as a basis to guide long-term research and development goals. This law has been the driving force for miniaturization and performance enhancement of IC-based devices. However, in 2015, Gordon E. Moore mentioned that he anticipated that the rate of IC progress, which has been exponential since the 1960s, would reach saturation in the next decade or so. Figure 1.1 shows the first published predictions of the increase in transistors per chip with respect to the time frame, as well as more recent evolutions.

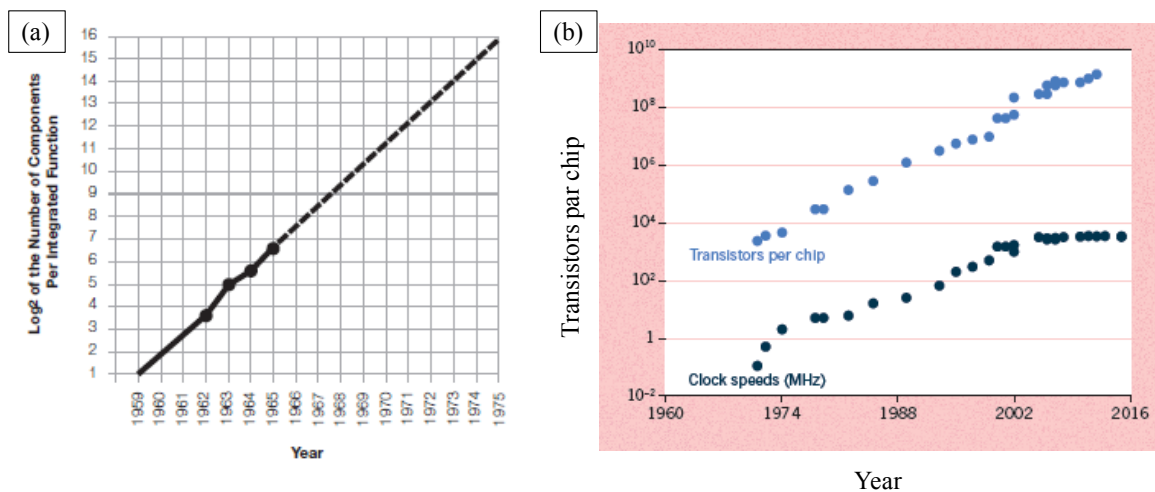


Figure 1.1. Moore's law. (a) Initial predictions published in 1965 [3] and (b) evolution up to 2016 [4].

In his 1965 article, Gordon E. Moore discussed what he called the “heat problem.” The one main question is, “Will it be possible to remove the heat generated by tens of

thousands of components in a single silicon chip?” The constant increase in active components in electronic devices increases the power required for good performance and, therefore, induces heat loads which need to be evacuated for the prolonged lifetime of the device. Poor heat dissipation can cause hot spots in a device, which dictates the overall reliability of the components. As a result, these hot spots dictate the thermal management solutions, including material selection, heat sink, and cold plate design, to name a few. Furthermore, if the required cooling cannot be attained, the performance of the component can be compromised, thereby reducing its power. This reduction of performance needs to be avoided, thus the great desire to enhance heat dissipation in such devices.

Figure 1.2 shows a three-dimensional (3D) view of a multichip power electronic module, where the chips are mounted together on an insulating ceramic substrate, a copper base plate, and a heat sink. The chips are bonded onto thin film copper (Cu) tracks through wire bonding. In a power electronic module, the active chips modulate the electrical energy. The insulating ceramic substrate is used to avoid electrical losses, while the Cu base plate and heat sink allow the heat produced by the chip to be dissipated.

The heat removal capacity of the package is limited by the intrinsic thermal conductivity of the different layers and the total thermal resistance, which is the sum of the thermal resistances of each layer constituting the component. In order to minimize the overall resistance, the cooling procedure must be well thought out by taking into account the physical properties of each material involved in the module. For a fully functional module, the operating temperature should be kept below the maximum operating temperature, which usually falls between 125 and 150 °C for a typical silicon (Si) chip. Furthermore, it is important to minimize thermomechanical stresses within the module

which, in the long term, cause the module to fail. In fact, thermomechanical stresses are generated by the thermal expansion coefficient (CTE) mismatch between the neighboring materials constituting the module's layers. Depending on each material, the CTE mismatch with its closest neighbor will cause either compressive or tensile stresses during thermal cycling that might affect the mechanical integrity of the module.

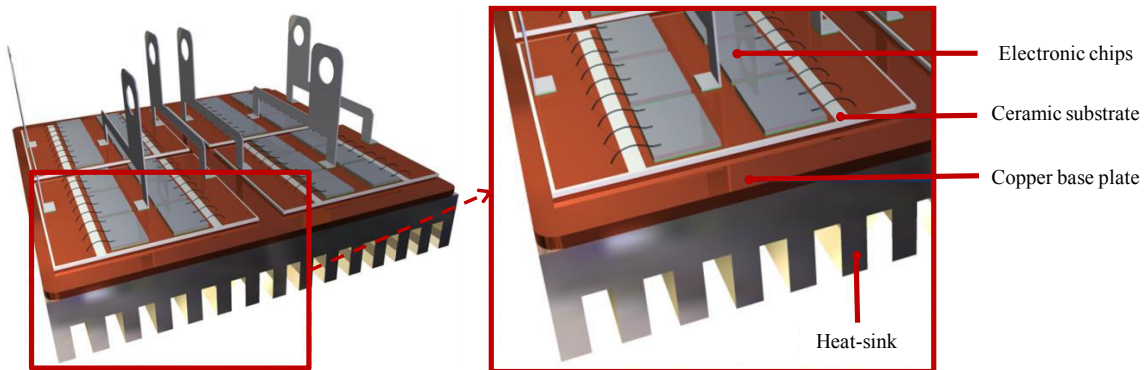


Figure 1.2. Three-dimensional view of a multichip power electronic module [5].

This work focused on the fabrication of heat-sink and heat-spreader materials that enable heat to be evacuated quickly from the layered assembly. The goal was to produce a heat spreader composed of multiple materials, which would allow even spreading of heat on a given surface, and a heat sink, which would evacuate the heat towards the cooling system. To this end, two objectives were identified:

1. Fabricate high purity diamond thin films with high in-plane thermal conductivity.
2. Fabricate a copper-carbon (Cu/C) metal matrix composite material with optimized interfaces synthesized with an innovative solid-liquid coexistent phase process.

The thin films and composite were assembled to form one heat spread/sink hybrid material with suitable CTEs, with respect to other materials in the module environment, high thermal conductivity, low weight, and high resistance to thermal cycling.

Diamond was at the heart of this research. It is a material of great interest for thermal applications, especially in the microelectronics industry. In fact, diamond combines, in a very unique way, exceptional thermal conductivity that can reach 2000 W/m·K with a high electrical resistivity that can reach 10^{13} Ω·cm. It is, therefore, the perfect candidate for applications needing a highly thermally conductive and highly electrically resistive material.

While diamond exhibits very high thermal conductivity, its heat capacity, on the other hand, is relatively low (6.19 J/mol·K at 300 K). In addition, diamond exhibits a fairly low CTE ($1-2 \times 10^{-6}$ K⁻¹), which makes it stable in terms of dimension under thermal cycling. Also, its CTE is close to that of traditional semiconducting materials, such as Si (2.6×10^{-6} K⁻¹); therefore, its thermomechanical stresses are limited by the very small CTE mismatch. Diamond allows the CTE to decrease, while the thermal conductivity of some materials increases when both are combined to form a composite.

Two types of materials were investigated for this work:

1. Polycrystalline diamond thin films through laser-assisted combustion chemical vapor deposition (CVD) synthesis.
2. Synthesis of Cu/C composites using the solid-liquid coexistent phase process.

In both cases, microstructure, chemical composition, and physical properties were investigated. Particular attention was paid to the interfaces, their structures, properties, and effect on thermal transfers within the composites and through the diamond films.

1.2. Overview of the Dual Ph.D. Program

This thesis work was carried out within the framework of an international collaborative dual Ph.D. program between two partners: the Laser-Assisted Nano-Engineering laboratory (LANE), part of the Department of Electrical and Computer Engineering of the University of Nebraska-Lincoln (UNL), in the United States, and the Metallurgy and Functional Materials group at the Institute of Condensed Matter Chemistry of Bordeaux (ICMCB-CNRS), at the University of Bordeaux (UB), in France. The Ph.D. program was evenly divided between the U.S. and France.

While my work in the U.S. revolved around the deposition of combustion CVD diamond films on different substrate materials, my time in France was dedicated to the synthesis of Cu/C composites. The supervisors of this work were Professor Yongfeng Lu, at UNL, and Director of Research, Dr. Jean-François Silvain, at ICMCB-CNRS. Thermal characterizations and evaluations were carried out in France at the Institute of Mechanics and Engineering (I2M), part of UB, under the supervision of Professors Jean-Luc Battaglia and Associate Professor Andrzej Kusiak. Thermodynamic simulations were carried out in collaboration with Associate Professor Jérôme Roger, from the Laboratory of Thermostructural Composites (LCTS), part of UB as well. Transmission electron microscopy (TEM) analyses and electron energy loss spectroscopy (EELS) measurements were carried out in collaboration with Professor Anne Joulain and Associate Professor Vincent Mauchamp, from the Institut Pprime in Poitiers, France.

This Ph.D. program has allowed training of undergraduate and graduate students both in France and the U.S. Mr. Loic Constantin was involved with the diamond deposition investigations carried out at UNL, while Miss Ana-Belen Moral-Balandín and Mr. Iñaki Cornu were involved with the synthesis of Cu/C composites at the ICMCB.

A brief dissertation outline is given in the next subsection.

The most significant contributions to this dissertation which were carried out at the LANE lab at UNL are:

1. Adopted laser-assisted combustion CVD processes (krypton fluoride (KrF), carbon dioxide (CO₂)), implemented in previous works [5–8], for the deposition of diamond films on composite substrates.
2. Used scanning electron microscopy to investigate the microstructure of the films as well as the interfacial contact between the substrate and the film.
3. Used Raman spectroscopy to quantify the phase purity and residual stresses in the diamond films.

The most significant contributions to this dissertation which were carried out at ICMCB-CNRS at UB are:

1. Established a database containing carbide-forming elements that are susceptible to forming carbide interphases, with respect to thermodynamic investigations.
2. Implemented the solid-liquid coexistent phase process for the in situ creation of interphases in the composites.

3. Synthesized fully dense Cu/C composites containing carbide interphases [9,10].
4. Used scanning and transmission electron microscopy to investigate the microstructure of the carbide interphases and their corresponding interfaces.
5. Evaluated the thermal performance of the synthesized composites using the laser flash method, thermal cycling, and scanning thermal microscopy.
6. Evaluated the impact of the interphase on the overall properties of the Cu-C composites.

1.3 Dissertation Outline

This dissertation is separated into six chapters. Chapter 1 details the motivations and outline of the work carried out. Chapter 2 includes fundamental and recent development related to this study. The synthesis of composite materials using the solid-liquid coexistent phase process, carried out at the ICMCB (UB), is described in Chapter 3. Chapter 4 is a description of the work carried out at the LANE lab (UNL) on diamond films obtained through laser-assisted combustion flame CVD on composite surfaces. Chapter 5 includes a discussion of the thermal properties of the composites. Finally, general conclusions on both diamond films and Cu-C composites are presented in Chapter 6, along with the future research directions that will be implemented.

2. Background and Reviews

2.1. Introduction

In attempting to miniaturize and enhance the performance of microelectronic components, one should focus on the evacuation of heat produced during the operation of the devices. With the increased powder densities in power electronic devices, and the increasing miniaturization of microelectronic devices, more heat related problems are caused and rely on poor heat dissipation. In fact, the limiting aspect of the evolution of microelectronic components is the poor thermal dissipation which is controlled by the heat-sink substrates. These substrates are well established and are usually composed of highly conductive metals, such as copper (Cu) and aluminum (Al). To enhance the thermal dissipation behavior of these materials, researchers all over the world have turned to composite materials, which combine two different materials to obtain one final composite with hybrid properties. The resulting properties of such materials are merely a combination or enhancement of the properties of the two constituents.

In this chapter, the materials chosen to create a composite material for the production of effective heat-sink devices are introduced. While the properties and synthesis methods of diamond, a key constituent of this work, are discussed, metal matrix composites are also discussed.

Also included is a review of the current state of the art of Cu/D composite materials which are considered to replace Cu and Al as heat-sink devices. The challenge of creating a chemical bond within a nonreactive system, such as Cu/C, is explained and current solutions are presented.

The thermal aspects to be taken into account for a deeper understanding of the heat transfer phenomena that take place within multimaterials are also discussed. The importance of being able to predict the thermal behavior of materials is highlighted, as such a prediction will allow tailoring of materials for specific applications.

2.2. Diamond: From Precious Gem to Common Applications

Hundreds of years ago, diamonds were known and treasured as gemstones. It was only later that light was shed on their exceptional properties. Diamond has many unequaled qualities and is very unique among minerals. It is the hardest known substance and the greatest conductor of heat. It has the highest melting point of any substance (4090° C) and the highest refractive index of any natural mineral. These exceptional properties have converted diamond from its primary use in expensive pieces of jewelry into an exquisite material with many applications, such as a coating for cutting and drilling tools and thermal dissipation for electronic devices, to name a few. The next subsections offer an overview of diamond's composition, crystal structure, and properties.

2.2.1. Composition and Crystal Structure

Diamond is an allotrope of carbon, such as carbon nanotubes or graphene, and is completely composed of carbon atoms. Each carbon atom is covalently bonded with four surrounding carbon atoms, forming four sp^3 -hybridized bonds, to produce a variation of a face-centered cubic structure called a diamond lattice. The diamond cubic structure belongs to the $Fd-3m$ space group. As seen in Figure 2.1(a), the lattice can be seen as the superposition of two identical face-centered cubic (FCC) lattices of carbon atoms. One of the lattices originates at the 000 point and the second at the $\frac{1}{4}\frac{1}{4}\frac{1}{4}$ point. Each carbon atom

is surrounded by four equidistant neighboring atoms situated at the corners of a tetrahedron. These four bonds indicate the tetravalent character of the carbon species. A unit cell has a count of 8 atoms, resulting in an atomic density of 1.77×10^{23} atoms/cm³, as the lattice parameter a is equal to 3.55676 Å. However, later studies have shown that different types of diamond, discussed in Section 2.2.2, present slight variations of the lattice parameter which are related to the impurity content present in the diamond phase [11].

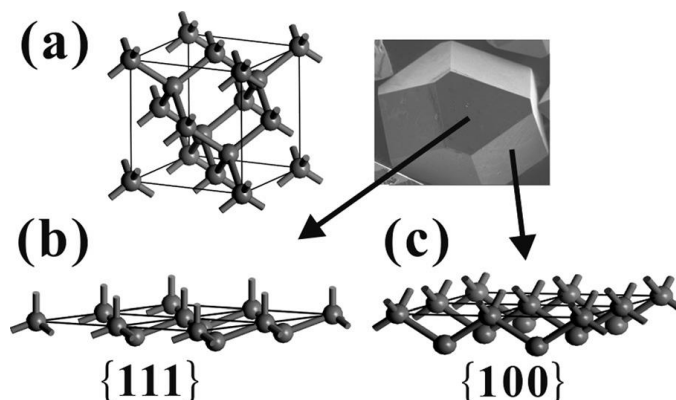


Figure 2.1. Schematic drawing of the diamond crystal structure: (a) the inner crystal, (b) the {111}, and (c) the {100} faces, respectively [12].

Owing to its crystal structure and bonding, diamond is the hardest known natural material, scoring 10 on the Mohs scale. This is due to the short covalent bonds between carbon atoms. In fact, the distance between two neighboring carbon atoms, in the case of diamond, is 154 pm [13]. Knowing that carbon's atomic radius is 77 pm, which is half of the distance between two atoms in the diamond structure, two bonded carbon atoms are tangent. The nature of the bonds is also responsible for diamond's high melting point.

Diamond crystallizes in all sorts of isometric forms, such as octahedral, dodecahedral, and hexoctahedral crystals. According to J. and E. Wilks, the octahedral form of diamond crystal is the most common and a typical example of natural diamond [14]. The plane on which the crystal grows is specified by Miller indices {111}. It also

forms in twinned crystals, where twinning is the tendency of some crystals to either repeat patterns or intergrow in a distinct way. Cubic diamonds have a perfect octahedral cleavage, meaning they only have four planes along which diamond can easily be separated. Those planes correspond to fewer and weaker bonds on which an impact can easily split the crystal and leave smooth surfaces. This diamond “cutting” relies on the directionality of the diamond’s hardness. This means that some directions are harder than others. For example, the hardest direction is the diagonal on the cube face $\{111\}$, while the softest is the dodecahedral plane. It is important to know that without the hardness being directional, diamond would be nearly impossible to fashion.

Diamond surfaces are highly shiny because of their hardness. They are also either hydrophobic or hydrophilic depending on how the surface’s carbon atoms terminate [15]. If they terminate with a hydrogen atom, the surface will be hydrophobic, while if they terminate with an oxygen atom or a hydroxyl radical, they will be hydrophilic. It is possible to modify the surface property completely by the use of different gas treatments.

2.2.2. Properties

2.2.2.1 Optical Properties

Natural diamond often contains structural defects and impurities, such as nitrogen and boron. Depending on the impurities and defects present in the crystal, its color is different. An extremely pure diamond crystal with no impurities is naturally transparent, while substitutional nitrogen atoms impart a pale-yellow color to the crystal. Diamonds are classified into the four types detailed in Table 2.1 based on the nature of the defects causing alterations in light absorption.

Table 2.1: Classification of the types of diamond.

Diamond Type	Ia	Ib	IIa	IIb
Impurities	Nitrogen Aggregates	Substitutional Nitrogen	No impurities	Boron
Appearance	Pale yellow	Gold yellow	Transparent	Blue

Being a product of nature, diamond's properties, size, and purity are variable and make every diamond crystal unique. All four types of diamonds can be found in nature, with Type I being the most prevalent (98%). Diamonds of Type I are those which contain the highest concentrations of nitrogen impurities (100-3000 ppm), either as aggregates (Type Ia) or substitutional atoms (Type Ib). Type II diamonds contain smaller amounts of nitrogen (inferior to 5 ppm). Type IIa, being the purest form of diamond, appears colorless, while Type IIb contains a higher concentration of boron than of nitrogen, which gives it a pale blue color. Figure 2.2 represents natural diamonds of each type and their respective shades.

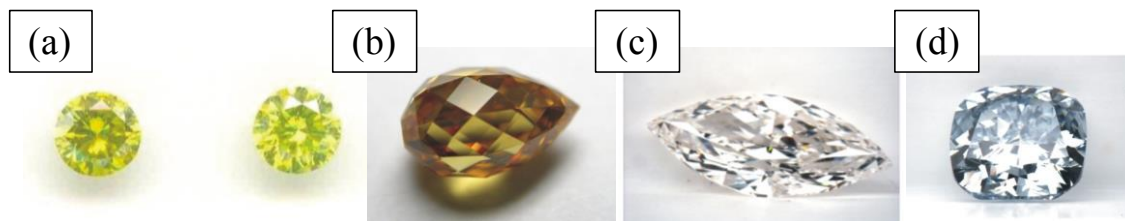


Figure 2.2. Four types of natural diamonds: a) Type Ia, b) Type Ib, c) Type IIa, and d) Type IIb.

While these are the natural colors of diamonds found in nature, it is possible to modify the color of a diamond by voluntarily inserting impurities. It is then possible to obtain green, pink, brown, and orange diamonds, to name a few.

Aside from natural diamonds, synthetic diamonds have emerged. High pressure high temperature (HPHT) synthesis produces colored crystals. Indeed, for the nucleation growth phenomenon to occur, one must add catalysts, which are usually transition metals. As a result, some of the catalyst's atoms remain inside the crystal inducing a colorful appearance. Chemical vapor deposition (CVD) on a synthetic diamond tends to have a dark grey shade, which is due to the presence of nondiamond carbon inside of the crystal. Synthetic diamonds are produced from engineered materials. It is possible to tailor their properties for the intended applications. The HPHT and CVD methods are assessed in Section 2.3.

One of the most important optical properties of diamond, from a jewelry perspective, is its refractive index, as it is particularly high (2.17) and varies with the incident wavelength. Even though diamond is isotropic because of its cubic structure, birefringence is observed because of the internal tensions that are present within the crystal. This is what induces a light dispersion and gives diamond its shiny aspect.

Another optical aspect of diamond is its reflexion capacity, which is also very high and depends on the refractive index. However, reflexion depends on the angle at which the incident light penetrates the crystal with respect to the normal surface of the diamond.

Diamonds also exhibit fluorescence when under ultraviolet (UV) light. Fluorescence is the capacity of a substance to absorb excitation light (photons) and to quickly release it under the form of emission light. The absorption of a photon will bring the molecule in an excited state and will return to the fundamental state either by fluorescence or phosphorescence. Typically, fluorescence is characterized by a very rapid photon emission, while phosphorescence, which requires a spin-orbit coupling, emits photons with a certain delay. Diamonds emit light of various colors and intensities depending on the type of impurities and defects that are included in the crystal.

2.2.2.2 Mechanical Properties

The density of a material is determined by the ratio of the material's weight to its volume. Diamond has an average density of 3.52 g/cm^3 , which means it's 3.52 times heavier than the same volume of water. As mentioned previously, diamond is the hardest known natural material; it is, hence, very resistant to scratching. A material's hardness is usually described by the Mohs scale, which ranks materials from the softest to the hardest by assigning a number from 1 to 10 (10 being the hardest). To determine a material's hardness, soft and hard tips are used to scrape the surface of that material (changing tips from the softest to the hardest) until the material is scratched. Diamond has a hardness of 10 according to the Mohs scale. However, hard materials are usually very fragile. In diamond, this fragility is due to the presence of a cleavage plane and to the directionality

of covalent carbon-carbon (C-C) bonds, which make diamond rigid. That is why diamond only has a fair to good tenacity, as do most ceramics.

2.2.2.3 Electrical Properties

For a covalent bond to be formed, electrons have to be shared between atoms, contrary to metallic bonds where electrons are considered to be a “gas” of electrons that are free to move. That is the main reason why most diamonds are very good insulators with an electrical resistivity of 10^{11} to 10^{18} $\Omega\cdot\text{m}$. However, Type IIb natural diamonds and synthetic diamonds doped with boron are p-type semiconductors, as the addition of boron in the lattice decreases the band gap. An N-type semiconductor can also be synthesized by doping synthetic diamond with phosphorus.

2.2.2.4 Thermal Properties

The very high thermal conductivity of diamond generated the sudden interest in introducing diamond in applications which require heat dissipation. Diamond’s conductivity at room temperature has been assessed at 2400–2500 W/m.K, which is five times more than that of Cu [16]. However, these values were obtained for crystals rather than synthetic films. High conductivity is a result of strong covalent bonding and low phonon scattering. Phonon behavior is important to understanding thermal transfers in materials; therefore, Section 2.5 is dedicated to the thermal phenomena.

Synthetic CVD diamond films usually exhibit thermal conductivities on the order of 300–700 W/m.K [17–19]. These conductivities are considerably lower than those measured for natural diamond. That is due to the polycrystallinity and phase purity of the diamond films which are obtained through CVD routes. Indeed, grain boundaries and impurities tend to scatter phonons in multiple directions [20].

Diamond exhibits a heat capacity of 6.19 J/mol.K at 300 K. Since an efficient heat-sink device should sustain as much heat as possible while maintaining its temperature, the heat capacity of the material should be as high as possible ($C_p^{Al} = 9.2$ J/g.K). However, diamond's heat capacity is quite low, in the temperature range of 0 to 800 K, which indicates that it would be more valuable as a heat spreader, rather than a heat sink.

Also, the coefficient of thermal expansion of diamond is fairly low, as it typically is for a ceramic. In a thermal conductivity range of 300–1200 K, the coefficient of thermal expansion (CTE) increases from 0.8×10^{-6} to $4.8 \times 10^{-6} \text{ K}^{-1}$. The CTE also makes diamond films attractive to electronic applications, as its CTE is close to that of the insulating layer and the silicon (Si) chip. However, diamond's CTE does induce problems when it is destined to be in contact with a metal, as it usually exhibits high CTE.

2.3. Diamond Synthesis

As natural diamond is only found in small quantities, it is vital to be able to synthesize diamond. Attempts to grow diamond were documented at the beginning of the nineteenth century, when diamond was proven to be an allotrope of carbon. However, the first successful and reproducible diamond synthesis was documented in 1955. The methods used to grow diamond were HPHT and CVD. These two methods still dominate the making of synthetic diamonds. A man-made diamond's properties are very dependent on the synthesis technique used. Some synthetic diamonds have shown greater hardness and thermal conductivity compared to natural diamond. The purpose of this subsection is to introduce the HPHT process and describe state-of-the-art diamond growth using various CVD routes.

2.3.1 High Pressure High Temperature Process

As mentioned above, it was only in the twentieth century that the importance of high pressure in converting graphite into diamond was taken into account. Thermodynamic calculations along with high pressure experimental setups allowed the General Electric (GE) team to produce the first synthetic diamond in 1955 [21]. For high pressure synthesis, techniques are split into: 1) methods of direct graphite-to-diamond conversion and 2) methods of catalytic diamond synthesis and growth. The pressure-temperature (P-T) phase diagram for carbon can be seen in Figure 2.3.

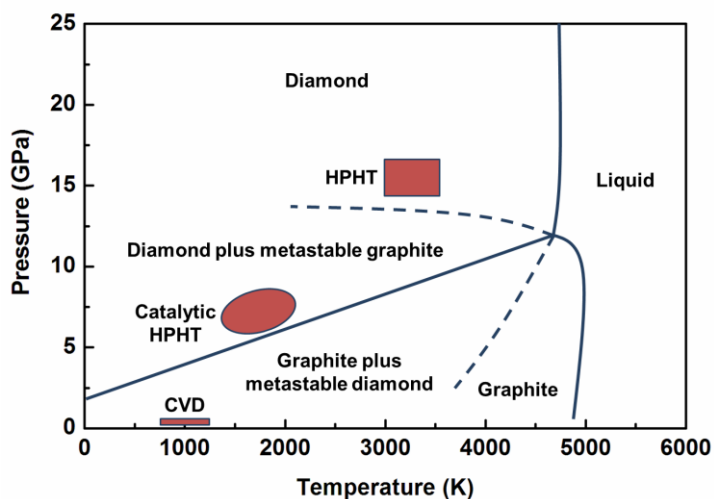


Figure 2.3. P-T phase diagram for carbon [22].

The most elaborate and well-studied process used for manufacturing single crystal diamonds consists of using metallic catalysts. Transition metals, such as iron (Fe), cobalt (Co) and nickel (Ni), among others, have proved to be efficient catalysts by GE. They are used either in elemental form or as alloy combinations and are currently the most commonly used catalysts for HPHT.

During the process, the metal is brought to a molten state and put in contact with graphite. The difference in the solubility of metastable graphite and stable diamond in the

melt, at high temperature, is the driving force for crystallization. Diamond crystallizes through the diffusion of carbon atoms and/or species across the surrounding film of metal melt. This process results in the synthesis of diamonds up to 1 mm in size.

2.3.2 Chemical Vapor Deposition

Chemical vapor deposition (CVD) diamond synthesis involves chemical reactions inside a gas phase and deposition on a substrate surface. Over time, the process, procedure, and parameters have been developed to attain high quality diamond synthesis. The typical CVD process involves a gas mixture of hydrogen [23] or oxygen and hydrocarbons (methane, ethylene, etc.). The primary function of hydrogen or oxygen is to terminate pending carbon bonds on the surface of the diamond layer. Hydrogen atoms in particular, tend to selectively etch nondiamond bonded material, thereby reducing the incorporation of nondiamond carbon in the film [24]. They can also crack neutral hydrocarbons and create reactive radicals, such as methylene (CH_2). These radicals can then bond and form trigonal sp^2 graphite or tetrahedral sp^3 bonds.

Bachman et al. were the first to demonstrate that diamond synthesis is possible in a small region of the carbon-hydrogen-oxygen (C-H-O) phase diagram [25]. A simplified version of the diagram is shown on Figure 2.4. As seen on the diagram, no diamond growth is achieved below the H-CO line. Diamond is deposited in a narrow zone close to the line, above which nondiamond carbon is synthesized.

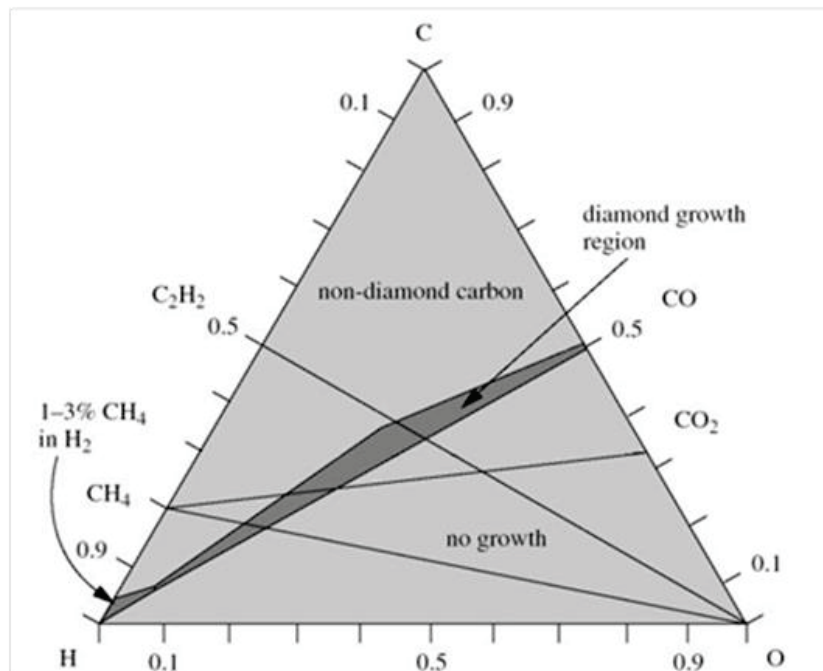


Figure 2.4. Simplified form of the atomic C–H–O diagram based on the diagram published by Bachman et al. [25].

2.3.3 Nucleation

Diamond nucleation is thought to start with the adsorption of sp^2 bonded gaseous polycyclic aromatic hydrocarbons onto the substrate [26]. These species are obtained through hydrogen abstraction and other chemical reactions that occur in the gas phase. Then the sp^2 bonded species can either desorb, be etched by atomic hydrogen, or form stable nuclei. It is important to note that a stabilized nucleus is obtained through the conversion of sp^2 to sp^3 , again by hydrogen abstraction. This occurs because the surface energy of the nucleus is drastically reduced by the sp^2 to sp^3 conversion, when compared to the initial sp^2 bonded species.

2.3.4 Growth

As mentioned previously, dangling carbon bonds are terminated with atomic hydrogen. Therefore, the top surface of the completed diamond surface can be represented by a layer of carbon atoms terminated by hydrogen. However, for growth to occur, it is necessary that hydrogen atoms be removed to create a chemically active site for carbon. The main difference between the nucleation and growth species is their size. Indeed, nucleation involves polycyclic species while growth species are small hydrocarbon molecules containing no more than two carbon atoms. Also, polycyclic aromatic hydrocarbons are not desired during growth as they are the cause of the presence of nondiamond carbon (sp^2 carbon) in the films.

The most common CVD techniques for diamond deposition include hot-filament (HF) CVD, direct current (DC) arc jet-assisted CVD, radio frequency (RF) plasma CVD, microwave (MW) plasma CVD, and combustion CVD.

Combustion flame CVD is one of the methods which is the most flexible and can be operated in open air. Another important advantage of this technique is the high growth rate of diamond films, which can reach 60 $\mu\text{m}/\text{h}$. However, the deposited material often contains significant amounts of nondiamond carbon. Also, because it is a flame method, the deposition area is small.

Hirose [27, 28] was the first to discover that an oxyacetylene flame could be used for diamond growth. This flame is the most popular system used in combustion CVD due to its high flame speed and temperature. The combustion flame process and setup used for this work is described in Section 4.2.

2.4. Metal Matrix Composites

In a broad sense, the word “composite” stands for “constituted of two or more parts.” However, the use of “composite material” or “composite” is used in a more restricted way. By definition, a composite material is an assembly of two materials of different natures, which complete each other and lead to a material whose performance is a combination of that of each constituent taken separately.

Typically, a composite material is composed of two or more discontinuous phases distributed in a continuous phase. Usually the discontinuous phase, which we define as the *reinforcement*, is harder and presents mechanical and physical properties superior to the continuous phase. The continuous phase is defined as the matrix.

Properties of composite materials mainly result from the properties of both the matrices and reinforcements, the geometric distribution of the reinforcements, and their interaction with the matrix (interface).

Composite materials can be classified into three categories, depending on the nature of the matrix material. Table 2.2 lists the three types of composites with respect to their matrices. Examples of reinforcements and applications are also mentioned.

Table 2.2. Classification of composite materials with respect to the matrix nature.

Type of Composite	Matrix	Reinforcements
Ceramic Matrix Composites (CMC)	Ceramics (SiC, Al ₂ O ₃ , TiC)	Ceramics (SiC, C, TiC, TiN)
Metal Matrix Composites (MMC)	Metals (Cu, Ti, Al)	Ceramics (SiC, C, TiC, TiN)

Type of Composite	Matrix	Reinforcements
Organic Matrix Composites (OMC)	Polymers (thermosetting and thermoplastic)	Glass, carbon, aramid

Composite materials can also be divided with respect to their interfacial bond. While CMCs are characterized by strong interfacial bonds, in the case of MMCs, the interfacial bonds can either be strong or weak. For example, a weak bond is achieved by the ductility of the metal which induces mechanical bonding by squeezing the reinforcement. Depending on the final properties of the composite, one should be careful about the interfaces. Indeed, a very strong interfacial bonding will make the entire composite fragile. The purpose of this research is to develop metal matrix composites. Therefore, the parts in these materials will be explained in the following subsections.

2.4.1. The Metal Matrix

Metal matrix composites were first developed in the 1960s. The American and French research group was focused on a monofilament of boron for potential industrialization, the cost of which was very high. Therefore, only the aeronautics and aerospace industries were interested in its development. However, many more reinforcements (fibers, filaments, and particles) were developed in the 1980s which broadened the possibilities for applications of MMCs. In this section, the role of the metal matrix and the material selection made with respect to thermal dissipation applications, will be discussed.

The matrix of a composite is defined as the continuous phase in which reinforcements are dispersed. In the case of metals, the matrix can either be a single phase (pure metal or solid solution) or a multiphase (precipitation-hardened alloy). For a long time, the main

role of the matrix was to hold the reinforcements in place. However, the importance of the matrix and its influence on the material's final properties need to be considered. It is, therefore, important to understand the interaction between the matrix and the reinforcements. The interfacial region, between the matrix and the reinforcement, plays a key role on the transfer of properties from the matrix to the reinforcement and vice versa. The interfacial zone will be discussed in Section 2.4.3.

One of the key aspects of composite materials is the ability to modify the properties of the matrix material. For instance, the aeronautics and aerospace industry require thermally efficient, lightweight materials. Up until now, Al and titanium (Ti) were used as pure metals or alloys; however, recent specifications deem these metals too heavy. However, their ductility as metals is still required. To this end, combining the ductility of the metal matrix and the lightweight nature of a ceramic reinforcement will allow the specifications imposed by the client (here the aeronautics industry) to be met.

In the microelectronics industry, specifications require thermally efficient materials, which are lightweight and resistant. Copper and aluminum have reached their limits and do not allow proper heat removal with new functioning frequencies. Their high CTE also induces complications because of their incompatibility with the insulating layer. To this end, the specifications for new heat-sink materials have changed and are given in Table 2.3.

Table 2.3. Specifications required for new age heat-sink materials.

Specifications for Heat Sink Materials				
High thermal conductivity	Low thermal expansion coefficient	Lightweight	Mechanical resistance	Low cost

Several matrices can then be considered for this type of application. Typical matrices are Cu [29–31], Al [32,33], and silver (Ag) [34] as they all present high thermal conductivities. Aluminum and Cu are more favorable than Ag mainly in terms of price. While Al is cheaper and lighter, its conductivity is lower than that of Cu and Ag. Copper, on the other hand, seems to be the best compromise between price, weight, and thermal properties. With a thermal conductivity of 385 W/K.m, Cu is chosen as the matrix material for a wide range of investigations.

Cu matrices were reinforced with a variety of reinforcements, such as carbon (carbon fibers, carbon nanotubes, graphene, graphite flakes, and diamond particles) and carbide reinforcements in fiber or particulate form (titanium carbide (TiC), silicon carbide (SiC), and molybdenum carbide (Mo₂C)).

2.4.2. The Reinforcements

Carbon reinforcements have been around for a while and have proven their efficiency in optimizing the properties of CMCs and MMCs. Carbon fibers, in particular, have been used in a plethora of applications. In this study, diamond particles exhibited very high thermal conductivities. Typically, diamond cuboctahedra are used as reinforcements in composites which require high strength and thermal conductivity.

The reinforcement phases can be either continuous, in the form of long fibers, or discontinuous, in the form of whiskers, particles, or short fibers. Figure 2.5 shows the types of continuous and discontinuous reinforcements possible.

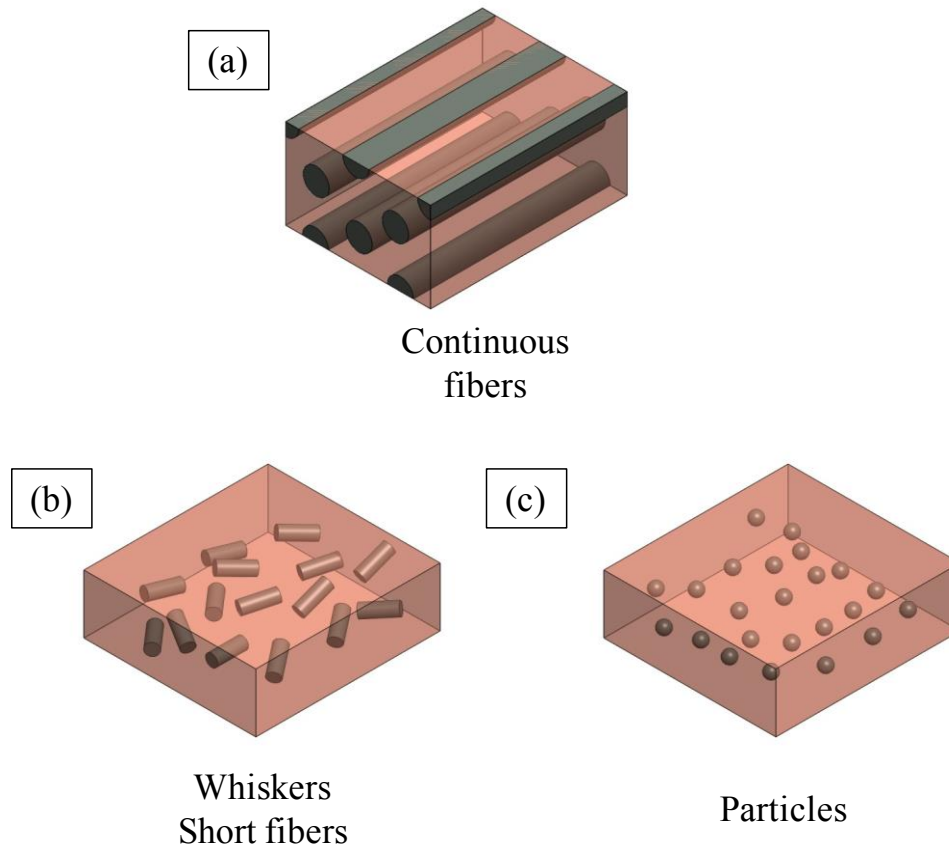


Figure 2.5. Types of metal matrix composites. (a) Continuous composite, (b) and (c) discontinuous composites.

2.4.3. The Interface

Even with its small size, the interface plays a very important role in the efficiency of a composite material. By definition, the interface in a composite material is the region separating the reinforcement from the matrix. It can be less than an atomic layer thick and consist of mechanical gripping or chemical bonding between the reinforcement and the matrix.

The rule of mixtures (ROM) can be used to describe the importance of the role of the interface in the composite's behavior. The following example describes the modulus and

tensile strength of an aligned, fiber-reinforced composite in the direction of the fiber alignment.

$$E_C = E_f V_f + E_M V_m \quad (2.1)$$

where E is the Young's Modulus and V is the volume fraction. The c, f, and M indices correspond to the composite, the fibers, and the matrix, respectively.

$$\sigma_C = \sigma_f V_f + \sigma_M^* V_M \quad (2.2)$$

where σ is the ultimate tensile strength, and σ_M^* is the stress sustained by the matrix at the composite failure strain.

Although a term describing the interface is not present in either Equation (2.1) or (2.2), the reinforcing mechanism implied by the ROM takes into account some of the interface properties. Should these properties not be assumed, the ROM would not be valid. In fact, the ROM assumes that when the composite is loaded in tension along the fiber alignment, the fibers and matrix strain together as a uniform material. This is only possible in the case of a strong interfacial bond, which allows the proper transfer of load from each phase to the other by shear at the interface.

While this is true in the case of mechanical behavior, it is also true in the case of thermal transfers. Poor interface bonds result in the presence of a thin layer of air between the reinforcements and the matrix. It is known that air is considered to be an insulating phase which acts as a barrier for thermal transfer. Therefore, particular emphasis should be brought to the interfacial zone so as to improve load or heat transfer between the phases constituting the composite material.

2.4.4. Reactive and Nonreactive Systems

While interfaces are always present in multimaterials, the assembly of two or more phases can induce the creation of a new phase, which will be referred to as the interphase. Interphases can also be obtained by coating the reinforcements with what will constitute the interphase. This is the case of well-known SiC fibers which are coated with a layer of pyrolytic carbon (PyC), as shown in Figure 2.6. However, in this study, the focus will be on the in situ synthesis of interphases.

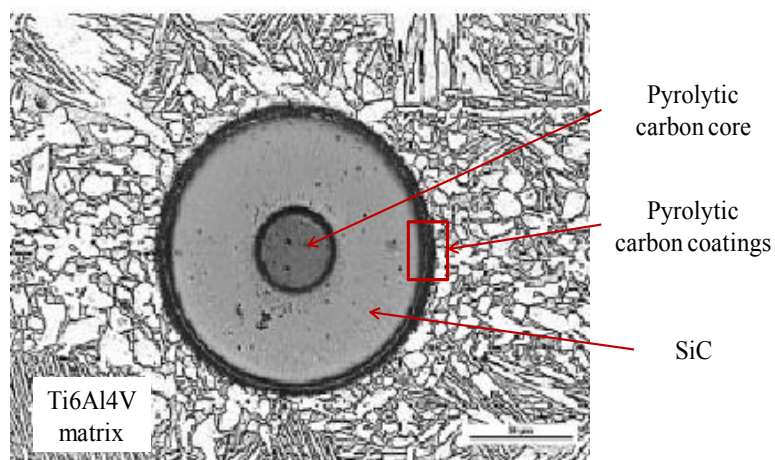


Figure 2.6. Cross-section of a SCS-6 SiC fiber coated with pyrolytic carbon within a Ti6Al4V matrix [35].

2.4.4.1 Reactive Systems

A reactive system is described as the assembly of two phases which are chemically active, which means that a chemical reaction can occur between them. The ability of two phases to react is determined by the chemical affinity that the two phases share. Typical examples are carbide forming elements (Ti, zirconium (Zr), Al, and Si, etc.) and carbon.

Chemical affinity can be detected by carrying out wetting tests to deduce the wettability of two phases. Wettability is the tendency for a liquid to spread on a substrate

and is generally measured in terms of angles. Indeed, there are different types of contact angles, which are shown in Figure 2.7. Wetting angles have to be combined with microstructural and chemical evaluations to determine the type of wetting between the two phases. Indeed, nonreactive systems can be described by two behaviors: (1) spreading of the liquid phase with no reaction or absorption of the liquid on the solid and (2) no spreading at all. In the case of a reactive system, though, the liquid phase reacts with the solid substrate to form a new phase between them (interphase).

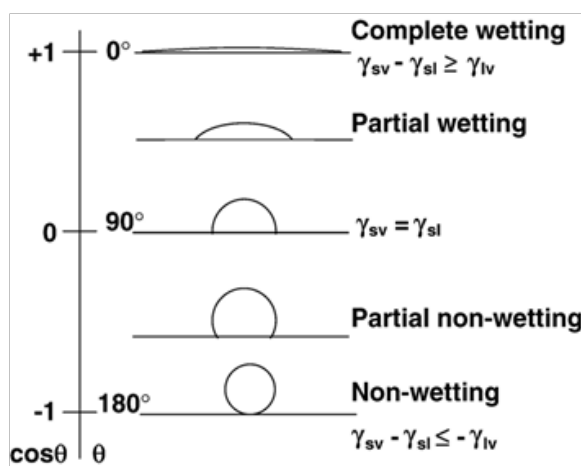


Figure 2.7. Liquid drop on a solid substrate with various contact angles [36], with γ_{sv} , γ_{sl} , γ_{lv} , the interfacial tensions between the solid-vapor, solid-liquid, and liquid-vapor phases, respectively.

K. Landry et al. have studied the wettability of Al and Al alloys on carbon [37]. Indeed, the Al-C system is a good candidate for metal matrix composites as Al forms a carbide when reacting with carbon. It is, therefore, important to acknowledge the wetting properties when describing the liquid processing of materials (infiltration by liquid metals). K. Landry et al. have shown that the wetting of carbon by aluminum is very sensitive to oxygen. The metals or alloys are usually coated with an aluminum oxide (Al_2O_3) layer due to the passivating behavior of Al. However, they showed that the final wetting angle, in the

case of the Al-C system at 1100 K, was around 69° , which indicates partial wetting of the carbon by the Al. Cross-section analyses have shown a continuous layer of reaction product covering the carbon substrate, as shown in Figure 2.8. Only aluminum and carbon are detected in the reaction layer, indicating that it is the aluminum carbide (Al_4C_3) which has been formed.

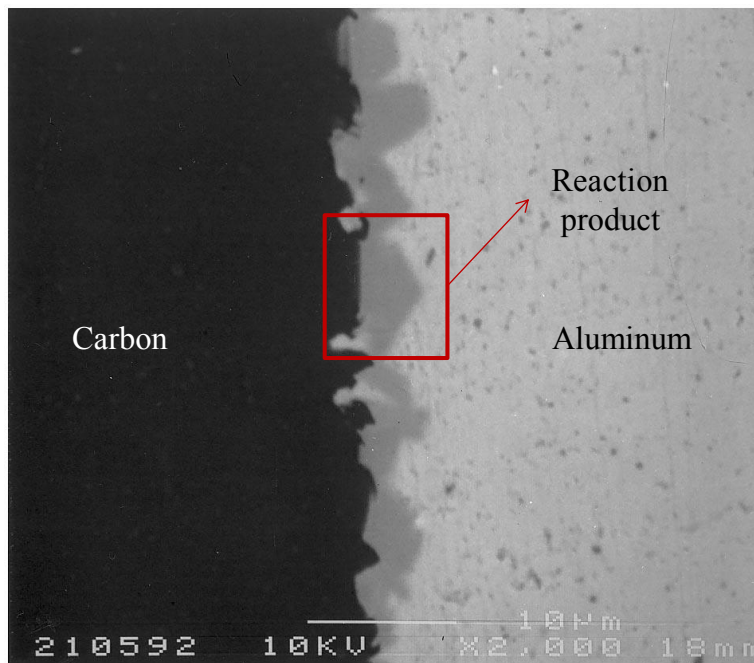


Figure 2.8. SEM micrograph of the cross-section of an Al-C specimen after 20400 s at 1100 K [37].

Another example of a reactive system was investigated by Ma et al. [38]. Here titanium-titanium boride (Ti-TiB) composites were prepared by reactive pressing. In this case, the reinforcement was created in situ. To this end, four reactive systems, namely Ti-B (titanium boride), titanium-titanium diboride (Ti-TiB_2), $\text{Ti-B}_4\text{C}$, and Ti-B-N were investigated. In all cases, the TiB reinforcement was obtained; however, in the cases of boron carbide (B_4C) and boron nitride (BN), the corresponding TiC and nitride were also detected. In summary, reactive systems allow the in situ creation of secondary phases.

2.4.4.2 Nonreactive Systems

Nonreactive systems are expressed by total nonwetting conditions, therefore, a wetting angle of 180° . There is zero adhesion between the liquid and the solid substrate which also indicates the absence of chemical affinity. The Cu-C and Ag-C systems are used as examples to illustrate nonreactive systems, as both systems exhibit a high degree of immiscibility. There is very little solubility of graphite, in each case, in both solid and liquid metals.

Since Cu has no chemical affinity with C, there is very little interaction between them. Therefore, to produce Cu/C composite materials, one should consider the insertion of alloying elements to promote their interaction. Mortimer et al. carried out several wetting tests using the sessile drop method to compare the wetting behavior of Cu and Cu alloys with C by measuring the contact angle between the C substrate and the fused metal [39, 40]. Alloying elements have been shown to improve the wetting of C by Cu. Metallographic examinations have also shown the occurrence of a reaction between the alloying elements (carbide-forming elements) and the carbon substrate, indicating the strong chemical affinity between these species. Figure 2.9 gathers the optical micrographs which illustrate the interfacial reaction that occurred between carbon and the various Cu alloys. One can distinguish four types of interphase morphology: (1) layers of near uniform thickness that extend all the way across the interface, (2) layers of near uniform thickness, present only at some parts of the interface, (3) flaky layers that are partially detached from the carbon substrate, and (4) interfacial zones containing small particles.

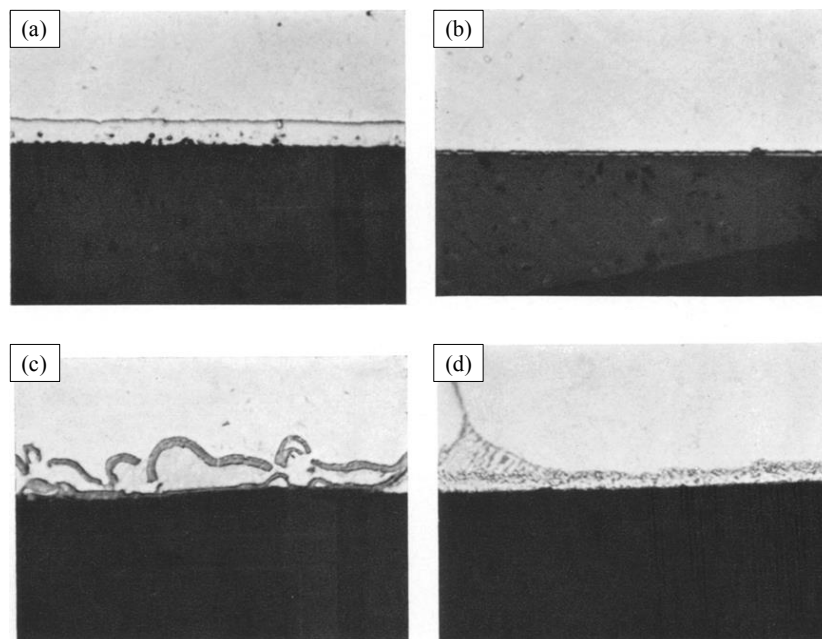


Figure 2.9. Optical micrographs showing the reactions that occurred at the interface between the C substrate and the Cu alloys containing (a) 1 at% chromium (Cr), (b) 1 at% Ti, (c) 1 at% tantalum (Ta), and (d) 1 at% Zr [40].

These reactions occurred while the alloys were under liquid form; therefore, the reactivity of the alloying elements was enhanced when compared to solid state reactions. However, A. Veillère et al. showed that in the case of Cu/C composites containing minor Cr additions, a Cr-C interphase is present after hot pressing at 950 °C under 40 MPa of pressure for 20 min and annealing at 1000 °C for 24 h [41]. In this case, the sintering temperature was not sufficiently elevated to produce a liquid phase, thus the reaction occurred in solid state and was governed by the solid diffusion of Cr. The micrograph shown in Figure 2.10 shows that the carbon fiber, although damaged by the sintering process, was coated by patches of Cr-based interphases.

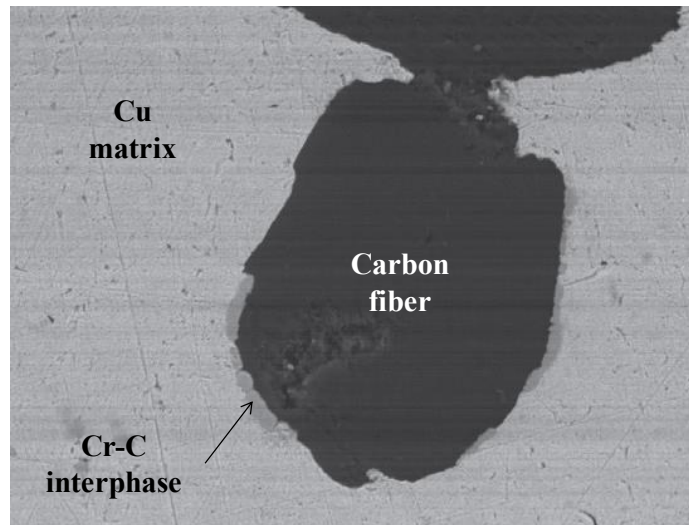


Figure 2.10. Scanning electron microscopy (SEM) micrograph of copper-chromium/carbon fiber composite after sintering and annealing treatment [41].

Chung et al. chose pressureless liquid phase sintering to produce Cu/D composites containing minor additions of Si, Co, Cr, tungsten (W), molybdenum (Mo), and Ti [42]. In this case the alloys were melted to allow better reaction between the additives and the diamond reinforcements. Titanium, Mo, and W were the only additives that resulted in integral shape composites. However, scanning electron microscopy (SEM) observations have shown interfacial pores in the case of the Mo- and W-containing composites. Only Ti has formed a continuous carbide interphase at the Cu-D interface.

While these examples show how the addition of alloying elements within the matrix allowed the creation of carbide interphases, other research groups opted for carbide-forming element coatings. Multiple investigations were carried out to determine the optimum coating thickness to deposit on the reinforcements. Thermal conductivities were also compared to deduce the optimum carbide-forming element coating. Although carbide-forming elements are very promising options for the creation of interfacial chemical bonding and, therefore, thermally efficient interphases, other options have also been

investigated and have shown promising results. Several studies have investigated the effect of functionalization of reinforcements, usually nanometric, prior to composite synthesis. For example, H. Pal et al. has used the molecular level mixing method to produce carbon nanotube (CNT)-reinforced silver matrix composites [43]. Both covalent and noncovalent functional groups were attached to the CNTs. They showed that noncovalent functionalization resulted in higher thermal conductivities, which is in agreement with theoretical predictions. In fact, noncovalent functionalization has shown an increase in the thermal conductivity of these composites with respect to pure Ag.

During his Ph.D., T. Guillemet showed that functionalizing diamond particles with submicronic copper particles increased the interfacial chemical bonding between diamond reinforcements and a Cu matrix, as shown in Figure 2.11 [5]. Microstructural and compositional characterizations showed the presence of a 7-nm-thick interphase between Cu particles and diamond reinforcements. This interphase was indexed to be a copper oxide, although the nature of the oxide has not been truly confirmed. Thermal diffusivity measurements have shown that higher values for coated diamond particles, when compared to pure Cu-D composites, indicate efficient interfacial heat transfer and efficient coupling of electronic and phonon conduction.

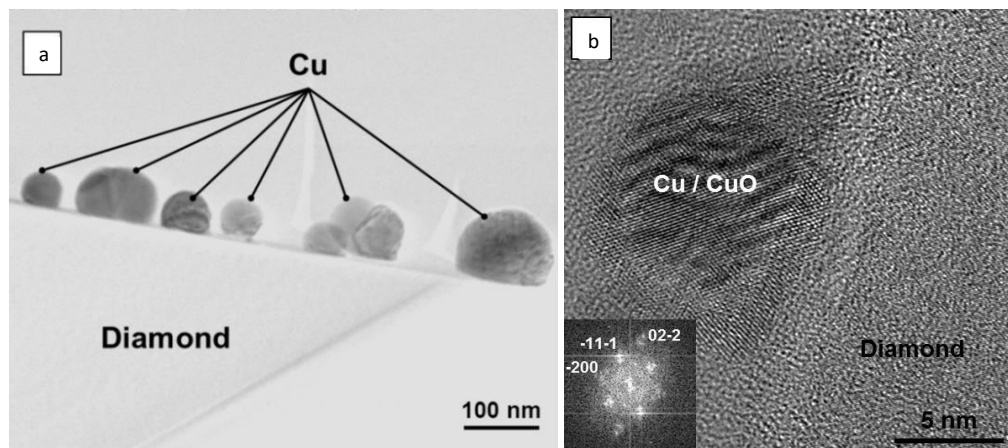


Figure 2.11. Transmission electron microscopy (TEM) micrographs of a Cu/Coated diamond particle obtained at the ICMCB during T. Guillemet's Ph.D. [5].

2.5. Heat Transfer Phenomena

Solids are considered to be an assembly of atoms and free electrons related to a periodic arrangement called a lattice. Thermal transport in a solid may be caused by two effects: either by the movement of free electrons or by the lattice vibrations (phonons).

Heat can be transferred by conduction through a solid or stationary fluid, convection from a surface to a moving fluid, or by radiation heat exchange between two surfaces. Heat conduction is the transfer of heat in the matter in the form of molecular vibration. It is especially relevant in solids but can also be applied to liquids and gas; however, in the latter phases, convection and radiation are more appropriate. Heat conduction can be described using Fourier's law, which relates the flux to the temperature gradient and is analogous to Fick's law in mass transfer [44]. Assuming that the conductivity is homogeneous in the material, Fourier's law is given by:

$$\varphi = -k\nabla T \quad (2.3)$$

where φ is the flux, k the thermal conductivity, and ∇T is the temperature gradient. Energy conservation is expressed locally by:

$$\rho C_p \frac{\partial T}{\partial t} = -\nabla \cdot \varphi \quad (2.4)$$

where ρ is the density, and C_p is the heat capacity related to the material. By inserting Fourier's law into Expression (2.4), one can obtain a diffusion equation for the temperature field:

$$\rho C_p \frac{\partial T}{\partial t} = k \nabla^2 T \quad (2.5)$$

the thermal diffusivity α is defined as:

$$\alpha = \frac{k}{\rho C_p} \quad (2.6)$$

By associating Equations (2.5) and (2.6), we obtain:

$$\nabla^2 T = \frac{1}{\alpha} \frac{\partial T}{\partial t} \quad (2.7)$$

The thermal diffusivity is introduced as it is the variable that is measured and allows the thermal conductivity to be deduced. As mentioned above, thermal energy is usually carried by both phonons and electrons. The thermal conductivity can, therefore, be written as:

$$k = k_e + k_{ph} \quad (2.8)$$

where k_e and k_{ph} are the contributions of free electrons and phonons, respectively. Each contribution can be directly linked to the ability of the material to conduct electrical current. Indeed, thermal and electrical conductivities of metals are directly related through the Wiedemann-Franz law [45]:

$$L = \frac{\kappa}{\sigma T} = \frac{\pi^2 k_B^2}{3e^2} = 2.44 \times 10^{-8} \text{ W} \cdot \Omega / \text{K}^2 \quad (2.9)$$

where L is the Lorenz constant, σ is the electrical conductivity, κ is the thermal conductivity, k_B is the Boltzmann's constant ($k_B = 1.3806 \times 10^{-23} \text{ J} \cdot \text{K}^{-1}$), e is the electron charge, and T is the temperature considered.

This law is only applicable in the case of free electrons which do not interact with either impurities or phonons. It is, therefore, verified at low temperatures, where collisions with impurities become negligible. Figure 2.12 shows schematic drawings of free electron collisions with impurities.

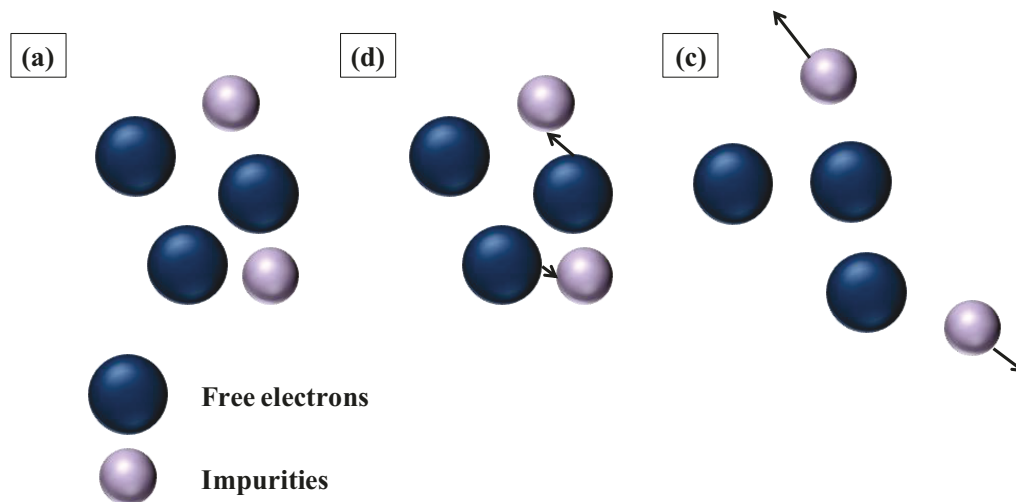


Figure 2.12. Schematic of the interactions between free electrons and impurities.

(a) Free electrons and impurities with no interaction, (b) collision between electrons and impurities, and (c) displaced impurities and electrons after collision.

As in diamond and most dielectric or ceramic materials, thermal energy is transferred through phonons. The vibrations of atoms in the lattice take the form of displacement waves and interfere with themselves, producing wave packets, which are termed phonons.

In fact, atoms are not fixed within the lattice but are connected by chemical bonds that can be considered as springs, in the harmonic approximation. Under the effect of temperature or an electromagnetic field, the atoms oscillate around their equilibrium position. This is due to the fact that phonons carry a certain amount of energy in the form of heat. According to the direction of the propagation of phonons, two waves are considered: longitudinal, when the movement is parallel to the propagation direction, and transversal when it is perpendicular (Figure 2.13).

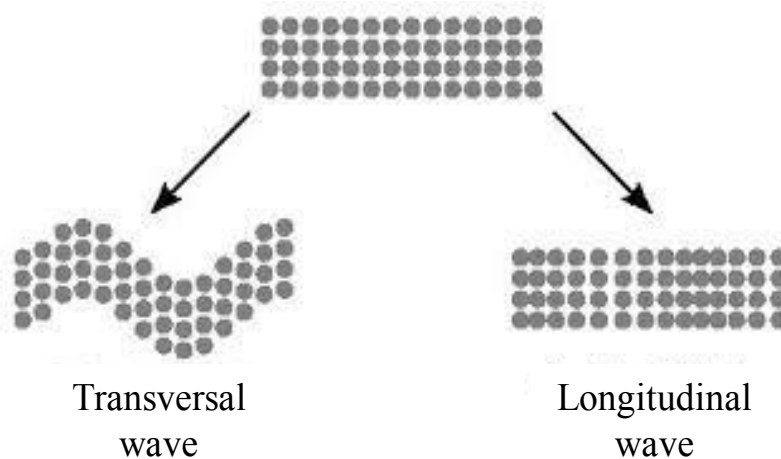


Figure 2.13. Example of a) longitudinal wave and b) transversal wave.

From a thermodynamic point of view at absolute zero (0 K), the lattice is in a “frozen” state, where atoms are no longer able to move. However, above 0 K, the lattice energy is no longer constant as atoms begin to vibrate. These random vibrations are seen as a gas of phonons and are directly linked to the temperature, hence the title “thermal phonons.” At high temperatures, atoms oscillate with large amplitudes and high frequencies, whereas at low temperatures, they do not vibrate as much. It is the atom’s oscillation that generates phonons. In conclusion, phonons are numerous for high temperatures, while they are fewer for lower temperatures. A schematic of the lattice vibrations when in contact with a heating source is given in Figure 2.14.

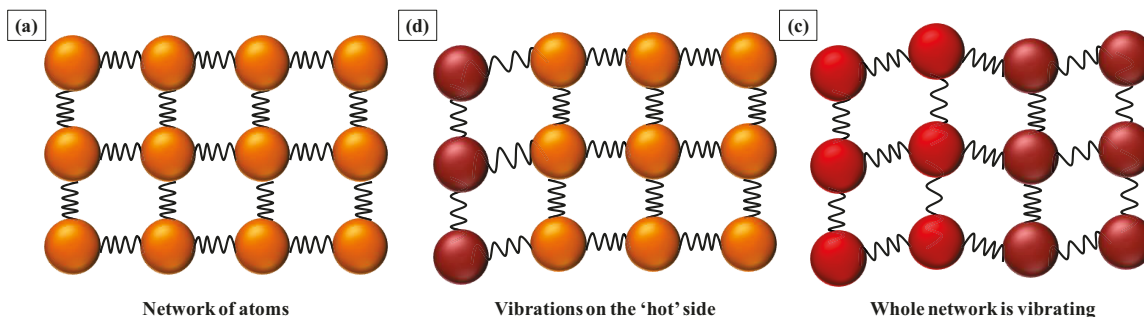


Figure 2.14. Schematic of lattice vibrations. (a) No vibration, (b) only one side is heated;

therefore, one side of the network starts vibrating, and

(c) the entire network vibrates.

Thermal conductivity can be assessed while taking phonon scattering into consideration along with the fact that the harmonic approximation is no longer relevant. In the case of a perfect spring, its length never changes with respect to the temperature, whereas in a solid, bonds can expand upon heating. Typically, the size of solids increases with temperature. This phenomenon is known as thermal expansion.

To further discuss the phonon effect on thermal conductivity, one has to determine the critical parameters on which thermal conductivity depend: phonon velocity and phonon mean free path. The equation relating these parameters to thermal conductivity is given below:

$$k = \frac{1}{3} C v l \quad (2.10)$$

where, C is the heat capacity, v is the phonon velocity, and l is the mean free path. The $1/3$ factor corresponds to the three directions in which the phonons can move.

The phonon mean free path is determined by the defects of the lattice. In a perfect crystal, there would be nothing to stop the phonons; therefore, the mean free path would be approximately the size of the crystal.

Defects, such as interstitial impurity atoms, dislocations, vacancies, and collisions between phonons, limit their mean free path through scattering.

Phonon scattering can take three forms:

1. *Boundary scattering*: a phonon hitting the boundary of a system.
2. *Mass defect scattering*: a phonon hitting an impurity within the system.
3. *Phonon-phonon scattering*: either a phonon breaking into two lower energy phonons or two phonons colliding and merging into one higher energy phonon.

All of these phenomena play a key role in heat transfer in solid materials. However, other phenomena are added to these, in the case of metals. Metals usually have less than four electrons in their valence band. Instead of creating shared electron pairs as in covalent bonds, atoms donate their electrons to a common electron “gas,” so that they are not associated with a particular atom. Therefore, the electrons are not localized and result in the metallic bond’s weakness when compared to a covalent bond. However, the electrons also result in high mobility of defects and, hence, their excellent formability. Also, electrons can carry heat and need to be considered in order to understand heat transfer within metals. Electrons are responsible for heat conduction in metals; however, in our case, electron heat carriers are not effective through a metal/ceramic interface. Actually, in such cases, the electrons transfer heat to the phonons of the metal which then interact with the phonons of the ceramic.

Knowing the limiting parameters for heat conduction in metals and covalent materials, it is important to discuss the heat transfer at the interface between these materials. The next subsection is dedicated to heat conduction across metal-diamond interfaces.

2.5.1. Heat Transfer Across a Metal-Diamond Interface

While heat conduction processes in metals and diamond are well understood, heat conduction processes across metal-diamond interfaces are still under investigation. As mentioned in Section 2.4.3, the interface is the fine line between two materials which constitutes an interruption in the regular crystalline lattice in which heat carriers propagate. It is thus expected that thermal resistance will be produced. This section, discusses heat transfer across a metal-diamond interface as well as the thermal boundary resistance which influences the thermal conductivity of an assembly.

As mentioned previously, phonons represent atomic lattice vibrations in a structured solid material. Phonons can be separated into two types: 1) optical and 2) acoustic phonons. Each of these phonons can either produce transversal or longitudinal waves. Optical phonons are also called incoherent because the lattice vibrations at different locations of the crystal exhibit different frequencies and different positions in the periodic motion of the lattice. These phonons correspond to the thermal lattice vibrations. The name “optical” phonon comes from the fact that they can be excited through optical excitation, such as visible and infrared light. After solicitation, however, phonons tend to get in phase with their neighbors. These are coherent atomic motions which are called “acoustic” phonons. These phonons can interfere with each other and are responsible for carrying thermal energy in solids, such as diamond [46].

Interfaces are localized defects which delimit two different phases. As defects, they are known to scatter the thermal energy carriers: electrons and phonons. This means that interfaces affect both the velocity and direction of the phonon motion, leading to a discontinuity in the temperature when heat flows from one material to the other.

Therefore, the interfacial thermal resistance (ITR) will be discussed. ITR results in a disturbance of the heat flow between the two constituents. Interfacial thermal resistance refers to the combined effect of two thermal resistances. Kapitza was the first to observe the thermal boundary resistance (TBR) by studying the heat conduction at the interfaces between copper and liquid helium [47]. Thermal boundary resistance occurs because of the difference in the physical properties of the two materials, particularly the differences in vibrational and electronic properties. The second interfacial effect is the thermal contact resistance (TCR), which is related to poor mechanical and chemical bonding between the constituents.

ITR (R_{int}) is defined as the ratio of temperature discontinuity (ΔT) occurring at the interface to the heat rate (\dot{Q}) per unit area (A), flowing across the interface between two phases in contact [48]:

$$R_{int} = \frac{\Delta T}{\dot{Q}/A} \quad (2.11)$$

In composite materials, ITR may be linked to the presence, at the interface, of thin layers of material with different properties than matrix and filler. Such layers may result from interdiffusion or corrosion of composite components, particle coating, and moisture absorption, as well as particle electrochemical treatment. Poor adhesion causes imperfect mechanical contact and also increases the value of ITR by increasing the TCR component. Thermal expansion mismatch may lead to the formation of gas-filled gaps in the interfacial region. Heat transfer by radiation and gas conduction only is permitted in such a gap; therefore, it acts as thermal resistance.

2.5.2. Heat Transfer at the Metal–Nonmetal Interface

While electrons dominate conduction in metals, phonons dominate in semiconductors and insulators, such as diamond. Therefore, for heat transport to occur across a metal–nonmetal interface, there needs to be an energy transfer between both heat carriers. There are two possible couplings, as shown in Figure 2.15: (1) coupling between the electrons of the metals and the phonons of the nonmetal through anharmonic interactions at the interface, and (2) coupling between electrons and phonons within the metal and then coupling between the phonons which belong to the metal and the phonons of the nonmetal material. While extensive research has been carried out on the first coupling, the second one has only been investigated at temperatures below 1 K [49]. Majumbar et al. conducted investigations to develop expressions to estimate the conductance at the metal–nonmetal interfaces at higher temperatures [50].

There are in both cases, therefore, thermal resistances that result from electron-phonon and phonon-phonon coupling. While electron-phonon coupling exists, it is expected to be negligible when compared to phonon-phonon coupling. That is why phonon-phonon coupling is important.

Two major models are considered when discussing phonon-phonon coupling: the acoustic mismatch model (AMM) and the diffuse mismatch model (DMM), which describe interfacial heat transfer at solid-solid interfaces and allow the thermal boundary resistance (TBR) to be determined.

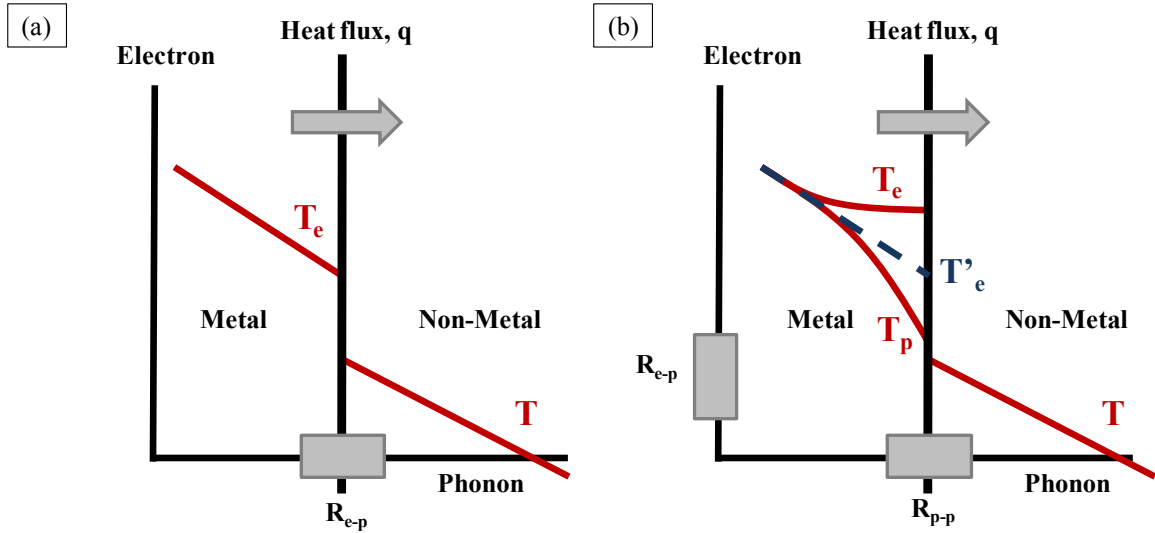


Figure 2.15: Schematic illustration of the two possible couplings for heat transport. (1)

Transfer from electrons from the metal and phonons from the nonmetal through anharmonic interactions, and (2) transfer of the electrons' energy to the phonons in the metal which has a resistance R_{e-p} and then transfer of the phonons' energy to the nonmetal across the interface with a resistance R_{p-p} [50]. The terms T , T_e , T_p , and T'_e stand for the temperature of the nonmetal, the electron and phonon temperatures of the metal, and the equivalent temperature of the metal, respectively.

In order to induce a heat flow across a boundary between two materials, there must be a temperature difference between the two sides of the interface. The thermal boundary conductance h_{Bd} is defined as the ratio of the heat flow (\dot{Q}) per unit area (A) across the interface, to the temperature discontinuity (ΔT) at the interface:

$$h_{Bd} = \frac{\dot{Q}}{A\Delta T} \quad (2.12)$$

The thermal boundary conductance is determined by the number of carriers (phonons) incident on the surface, the energy carried by each phonon, and the probability

that each phonon is transmitted across the interface. The thermal boundary resistance can now be defined as the inverse of the thermal boundary conductance.

While for thermal conductivity, one should focus on determining the mean free path of the carriers; in the case of thermal boundary conductivity, one should determine the transmission probability.

2.5.2.1 The Acoustic Mismatch Model

In the AMM, phonons are assumed to be governed by continuum acoustics and the interface is treated as a plane. Therefore, the phonons are treated as plane waves; and materials in which the phonons move are considered to be continuous media (i.e., as if there was no lattice). For phonons with wavelengths which exceed the typical interatomic spacing, the continuum approximation can be accurate. In this case, the transmission probability is the total fraction of the energy transmitted across the interface through the possible reflections and refractions of phonons incident to the interface, shown in Figure 2.16(a).

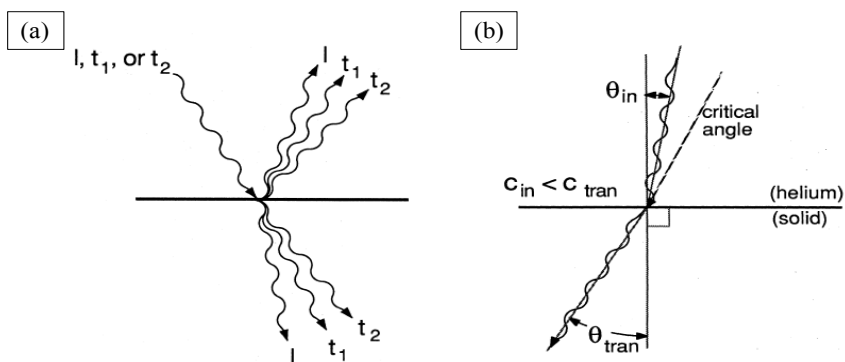


Figure 2.16. (a) Schematic of the possibilities within the framework of AMM for phonons incident on an interface, and (b) incident and transmitted phonon angles, related according to Snell's law [48].

The angles of reflection and refraction are determined using the acoustic analog of Snell's law for electromagnetic waves:

$$\sin \theta_{tran} = \frac{c_{in}}{c_{tran}} \sin \theta_{in} \quad (2.13)$$

where θ_{tran} and θ_{in} and c_{tran} and c_{in} are the transmitted and incident phonon angles and velocities, respectively.

In the AMM, each material is ascribed an acoustic impedance equal to the product $Z_i = \rho_i c_i$ of the mass density and the phonon velocity. Therefore, the formula of the transmission probability from Side $i = 1$ to Side 2 would be given by:

$$\tau_{1 \rightarrow 2} = \frac{4Z_2 Z_1}{(Z_1 + Z_2)^2} \quad (2.14)$$

Also, to simplify the calculations, all solids are assumed to be isotropic Debye solids, with the generalization that longitudinal and transverse speeds of sounds are different. Then, for frequencies below the Debye cutoff frequencies (ν_1^{Debye}), the thermal boundary conductance can be expressed as:

$$h_{Bd} = \frac{1}{2} \sum_j c_{1,j} \Gamma_{1,j} \int_0^{\nu_1^{\text{Debye}}} \hbar \nu \frac{dN_{1,j}(\nu, T)}{dT} d\nu \quad (2.15)$$

with

$$\Gamma_{1,j} = \int_0^{\pi/2} \alpha_{1 \rightarrow 2}(\theta, j) \cos \theta \sin \theta d\theta \quad (2.16)$$

At low temperatures, the upper limit of the integral can be set to infinity, and the equation can be solved:

$$R_{Bd} = \left[\frac{\pi^2 k_B^4}{15 \hbar^3} [\sum_j c_{1,j}^{-2} \Gamma_{1,j}] \right]^{-1} T^{-3} \quad (2.17)$$

The above analysis is only valid for phonons with frequencies which are less than the Debye cutoff of the material. Above the Debye cutoff, the probability of transmitted phonons is close to zero.

2.5.2.2 The Diffuse Mismatch Model

While the assumption that there was no phonon scattering at the interface was made for the AMM model, reflection measurements have shown that high frequency phonons are in fact scattered. The effect of scattering on the thermal boundary resistance has been explored and discussed in Swartz's Ph.D. thesis, published in 1987. Contrary to the AMM, in the DMM, all phonons are diffusely scattered at the interface, which makes the densities of phonon states the determinant of the probability of transmission. Also, the assumption that as soon as a phonon is scattered, it forgets where it came from and what mode it was, is made.

To summarize, the following assumptions must be made: (a) phonons are elastically scattered at the interface, (b) phonon transmission and reflection is completely diffuse, i.e., the phonon loses its memory of its initial mode and direction, and (c) materials on each side of the interface are isotropic, hence the acoustic velocities (longitudinal and transverse) are constant in all crystallographic directions.

For the DMM, the linear Debye approximation is used to calculate the phonon density of states. This approximation relies on the assumption that the phonon dispersion relationship in the lattice in the reciprocal crystallographic network (also called Brillouin zone) is linear.

The Debye temperature Θ_D is the temperature of a crystal's highest normal mode of vibration, which means the highest temperature that can be achieved due to a normal

vibration. This temperature is an important parameter as the Debye model is based on the DMM. Indeed, the Debye model originates from attempts to estimate the phonon contribution to the heat capacity of a solid and how it evolves with respect to temperature. Peter and Debye showed that the heat capacity varies with respect to a T^3 evolution law, at low temperatures. The Debye temperature is given by:

$$\theta_D = \frac{h\nu_m}{k_B} \quad (2.18)$$

where h is Planck's constant ($h = 6.62 \times 10^{-34}$ J.s), k_B is the Boltzmann constant, and ν_m is the Debye frequency. Debye's frequency is a function of the number of atoms in the solid and the speed of sound in the material.

As mentioned previously, the DMM assumes diffuse reflection and transmission; therefore, the probability of transmission from Side 1 to 2 is the same as the probability of reflection from Side 2 to 1. The phonon transmission probability is, therefore:

$$\tau_{1 \rightarrow 2}(\omega) = \frac{\sum_{s=l,t} \nu_{s,2}^{-2}}{\sum_{s=l,t} \nu_{s,1}^{-2} + \sum_{s=l,t} \nu_{s,2}^{-2}} \quad (2.19)$$

where ν_s can either denote ν_l or ν_t , which correspond to the longitudinal and transverse phonon velocities, respectively. Therefore, the interfacial thermal resistance can now be written as:

$$R_{Bd} = \frac{4}{\tau_{1 \rightarrow 2} C_{p,1}(T) \nu_1} \quad (2.20)$$

knowing that Side 1 corresponds to the material with the lowest Debye temperature ($\theta_D(1) < \theta_D(2)$).

While the AMM and DMM allow conclusions to be reached on phonon transfer across interfaces, both models have limits and remain approximations. The DDM will be discussed further in Chapter 5.

2.5.3. Metal Matrix Composites for Thermal Management

In a constant effort to find highly conductive materials, composites have been investigated as they allow the physical properties of two or more materials to be combined. The Cu-C and Al-C systems have been widely studied, and numerous enhanced thermal conductivities have been reported. While it is not necessarily true for the Al-C system, the absence of chemical bonding in Cu-C composites requires interface engineering to increase the thermal conductance at the Cu/C interface. Indeed, low thermal conductance (h_c) tends to decrease the equivalent thermal conductivity of the overall material. Several values of composite thermal conductivities (k_c) have been reported in the literature for the Cu-diamond and Cu-graphite systems. These conductivities vary with reinforcement content and dimensions, the production process, and the interface engineering.

As mentioned in the previous sections, the interface is an important factor that influences the thermal conductivity of the final material. Schubert et al. reported a thermal conductivity of 215 W/m.K for a volume fraction of 42% in diamond reinforcements of 120 μm in diameter [29]. Also, Tao et al. reported a variation in k_c from 150 to 42 W/m.K with volume fractions of 220-245- μm -sized diamond particles of 50 to 70% [51]. Yoshida and Morigami reported the highest thermal conductivity for a pure Cu/D composite obtained through high pressure sintering [30]. The thermal conductivity reached a maximum value of 742 W/m.K for 70 vol% of 90-100- μm -sized diamond particles. The thermal conductance at the interface was calculated to be about $h_c \approx 3 \times 10^7$ W/m².K. These remarkable values were mainly the result of the fabrication process which involved high temperatures ($T_{\text{sintering}} = 1180$ °C) and pressures ($P_{\text{sintering}} = 4.5$ GPa). Despite the weak interfacial bonding between Cu and diamond, the thermal conductivity increased because

of the close packing between diamond particles, which was induced by the sintering process. Moreover, Yoshida and Morigami discussed the effect of diamond particle size on the effective thermal conductivity and reported an increase in thermal conductivity with increasing sizes. Particulate composites have shown that adding conductive particles to the metal matrix enhances the effective thermal conductivity of the material only in the case of relatively large particle size [52]. With decreasing average particle radius, the effective thermal conductivity decreases; and the area of interfacial contact per unit volume increases. In such cases, the ITR begins to play a significant role in the overall heat transfer.

2.5.3.1 Analytical and Numerical Models

Typical experimental investigations on thermal conductivities of composites are often accompanied by theoretical predictions. While various models exist, the effective thermal conductivity derived by Hasselman and Johnson has proven to be very efficient [53]. This model accounts for the shape and size of the reinforcements and for the interfacial thermal resistance h_c . However, it also considers that the reinforcements are organized within the matrix. The effective thermal conductivity, for spherical reinforcements, is given by:

$$k_{eff} = k_m \frac{\left[2 \left(\frac{k_r}{k_m} - \frac{k_r}{ah_c} - 1 \right) \varphi + \frac{k_r}{k_m} + \frac{2k_r}{ah_c} + 2 \right]}{\left[\left(1 - \frac{k_r}{k_m} + \frac{k_r}{ah_c} \right) \varphi + \frac{k_r}{k_m} + \frac{2k_r}{ah_c} + 1 \right]} \quad (2.21)$$

where k_{eff} , k_m , and k_r are the thermal conductivities of the composite, the matrix, and the reinforcement, respectively, h_c is the interfacial thermal resistance, φ is the volume fractions of reinforcement, and a is the reinforcement's diameter.

While most analytical models are able to predict thermal conductivities for low volume fractions of reinforcements, the theoretical thermal conductivities are usually

underestimated at higher fractions. Every and Tzou used Bruggeman's approach to introduce infinitesimal changes to an already existing material, allowing the modified Bruggeman model to be more accurate for higher reinforcement content [52]:

$$(1 - \varphi^3) = \left(\frac{k_m}{k_{eff}} \right)^{(1+2\alpha)/(1-\alpha)} \left(\frac{k_{eff} - k_r(1-\alpha)}{k_m - k_r(1-\alpha)} \right)^{3/(1-\alpha)} \quad (2.22)$$

where α is a dimensionless parameter which depends on the interfacial thermal resistance between the matrix and the reinforcement. Indeed, α is defined as $\alpha = a_k + a$, where a is the particle radius and a_k is the Kapitza radius calculated through $a_k = R_{int}k_m$, with R_{int} being the Kapitza resistance.

While Every and Tzou's proposed model was a big step forward in understanding the influence of the microstructure on the physical properties of particulate composites, there is still much effort to be put into understanding what happens at high reinforcement content [52]. When increasing the amount of reinforcement per unit volume, one eventually reaches a point of unavoidable contact between reinforcements. In the case of highly thermally conductive reinforcements, the transfer between two particles is easier than between the particle and the matrix. These paths of particles tend to increase the effective thermal conductivity of the composite and usually appear after a certain volume fraction, which is known as the percolation threshold [54].

Experimental and theoretical investigations have been carried out to account for the formation of segregated networks in different composite materials. Relationships linking volume fractions of reinforcements and particle size ratios have allowed the percolation threshold in different types of composite materials to be predicted. For instance, in the case of spherical particle composites, the distribution can be either random or segregated [55].

In the random distribution, reinforcement and grains that constitute the matrix have similar sizes and shapes and can occupy any site in the arrangement. In the case of the segregated distribution, the reinforcements are usually smaller in effective size and tend to segregate on grain boundaries between the matrix grains.

Kim et al. focused on the silicon nitride/silicon carbide ($\text{Si}_3\text{N}_4/\text{SiC}$) particulate composite [56]. They proposed a theoretical model which takes into account the volume fractions of SiC particles that are required to form a percolating network, with respect to the size ratio of SiC particles and Si_3N_4 grains. They showed that, compared to a homogeneous random distribution of particles, composites with segregated distribution require smaller amounts of particles to reach higher conductivities (here electrical) by forming a percolating network.

Bhattacharyya et al. took into account the shape of the reinforcements to offer a model able to estimate the threshold volume fraction (percolation threshold – f^*) [57]. In their case, a conducting path is required within insulating matrices (polymers). For their model, they assumed that the polymer particles are deformed during the hot compaction process and produce cubic shapes. The metal particles do not undergo any deformation but are arranged along the polymer grain boundaries. Finally, a fully dense material was assumed to be obtained after hot compaction processing. The metal particles were considered to be rectangular parallelepipeds. The theoretical model presented in their work takes into account the shape as well as the size ratios of polymer grains to metal particles. Calculations are in agreement with the experimental data found in the literature.

Devpura et al. developed a numerical model for the prediction of the effective thermal conductivity of composite materials close or past the percolation threshold [54,58].

Numerical simulations, including percolation and interfacial thermal resistance, were performed and are in good agreement with experimental data, as shown in Figure 2.17.

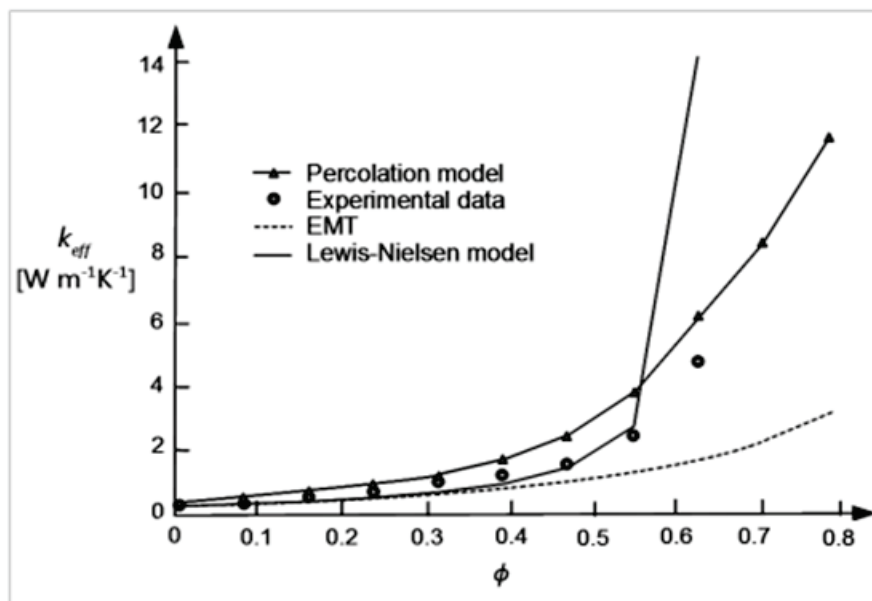


Figure 2.17. Comparison of effective thermal conductivity of bimodal distribution of Al_2O_3 filler in a polyethylene matrix (with a filler-to-grain ratio of 65:9 μm) as predicted by various models and experimental points taken from [58].

2.5.3.2 Experimental Data

As mentioned previously, Cu/D composite materials are widely investigated for thermal management applications. Owing to the lack of chemical affinity between Cu and C, carbide forming elements are either deposited on the reinforcements or used to alloy the Cu matrix.

Most studies have been using vacuum microdeposition and sputtering technologies to coat the diamond particles with either carbides or carbide-forming additives. Liu et al. produced copper matrix composites reinforced with carbon fibers which were coated with Mo_2C or TiC prior to the sintering process (spark plasma sintering (SPS)) [59]. The molten salt method was used to synthesize the carbide coatings. Scanning electron microscopy

characterizations have shown that the coatings were homogeneous and present on all fibers, while x-ray diffraction (XRD) analyses have shown that there were only the carbides on the fibers. Thermal conductivities of 290 and 297 W/m.K were measured for the Mo₂C- and TiC-containing composites, respectively. These values were obtained for composites containing 40 vol% of coated fibers. The thermal conductivity of a pure Cu/C composite at 40 vol% was 206 W/m.K, showing the enhancement of the conductivity with the presence of the carbides.

On the other hand, Yang et al. opted for a W coating on graphite particles using magnetron sputtering [60]. However, instead of coating the graphite and then mixing it with copper powders, they used electroless plating to deposit copper particles on the surface of the W pre-coated graphite. The composite powder was then washed and deoxidized prior to hot pressing. The graphite particles were shown to be homogeneously distributed within the final composite, which was accounted for by the electroless plating step. The presence of the W coating allowed wetting of copper onto the graphite particles. It also enhanced the interfacial adhesion between the graphite and copper by forming a thin tungsten carbide (WC) interlayer during the sintering step. The thermal conductivity of composites with 70 vol% of graphite varied from 110 W/m.K, for a pure Cu/C composite, to 158 W/m.K for the W-containing one.

Other examples include the work of Li et al. on Ti-coated diamonds as reinforcements of composites obtained through gas pressure infiltration, which exhibited a thermal conductivity of 716 W/m.K with 65 vol% of diamond particles of 62–75 μm sizes [61]. Kang et al.'s work on chromium carbide (Cr₇C₃) coatings [62] resulted in 562 W/m.K for 65 vol% of diamond particles of 70 μm.

Bai et al. chose to functionalize the reinforcements in a particular way. The diamond particles were mixed with Cu and W powders and brought to high temperature inside a vacuum induction furnace under hydrogen atmosphere. The residual Cu-W melt was removed, and the particles were mixed with Cu powder and sintered using SPS to form the composite. X-ray diffraction patterns showed the presence of WC and a pseudo Cu-W alloy that were supposed to envelop the diamond particles. Using this method, thermal conductivity reached a maximum value of 672 W/m.K for 46 vol% of diamond particles 200 μm in size [63].

Dewar et al. reported that alloying of copper promotes wetting and bonding of the matrix to the diamond reinforcements [64]. Adhesion was enhanced with minor Ti, Cr, Zr, and boron (B) additions to the Cu powders prior to the synthesis process, usually pressure-assisted sintering (hot isostatic pressing (HIP), high pressure (HP), SPS).

Thermal conductivity has also been evaluated with respect to the content of carbide-forming elements, such as B and Cr [65] or Ti [42,66]. In these cases, the carbide-forming additives were directly alloyed to the copper matrix. The composites were obtained by gas pressure-assisted liquid infiltration and SPS, respectively. The Cu-Cr/D composites had a fixed volume fraction of 60% in diamonds 200 μm in diameter. The thermal conductivity reached a maximum value of 600 W/m.K for an intermediate Cr content. Copper-boron/diamond (Cu-B/D) composites reached a maximum conductivity of over 700 W/m.K at an intermediate concentration in B as well.

These studies confirm the interest that exists in creating a chemical bond between the Cu matrix and the diamond reinforcement to improve thermal properties of composite materials. However, one must be careful with the alloyed Cu as it can be sensitive to

impurities. Also, while alloying the Cu matrix has been shown to be efficient, the amount of alloying element is usually a few atomic percentages, which in some cases can be too much. Che et al. showed that there was an optimum conductivity with respect to the Ti coating thickness (Figure 2.18) and, therefore, Ti content [66].

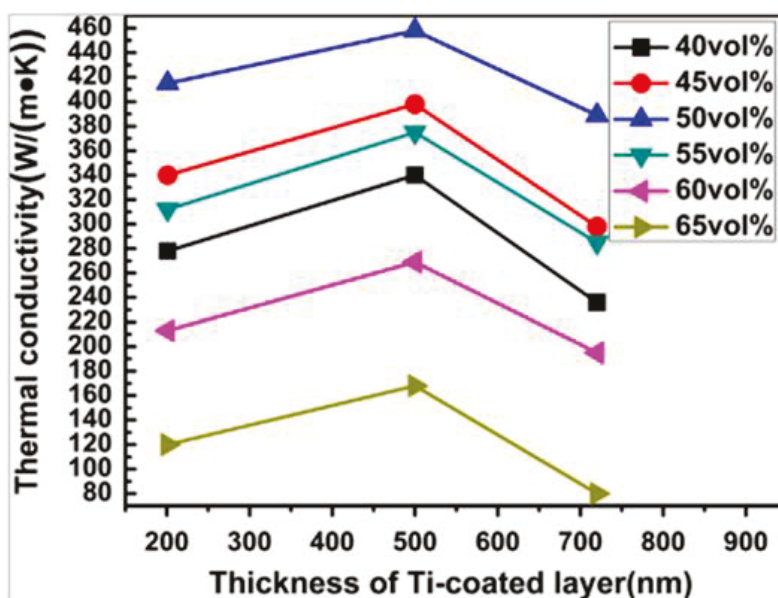


Figure 2.18. Thermal conductivity with respect to the thickness of the Ti coating deposited on diamond particles, from [66].

2.6. Conclusion

To conclude, the major properties of diamond as a thin film and as a reinforcement in metal matrix composites were reviewed. Indeed, diamond was chosen for this study because of its high thermal conductivity and low thermal expansion coefficient, which not only allows the thermal and thermomechanical properties of composites to be tailored but also matches the requirements for implementation in microelectronic components.

The objective of this study was to fabricate diamond-based multimaterials that could sustain heat fluxes while being implemented in microelectronic components. To that

end, optimization of these multimaterials, in terms of chemistry and physical properties, was carried out and is presented in this chapter.

The major issue for the creation of Cu-D multimaterials is the absence of chemical affinity between Cu and C which results in weak interfacial bonds (mechanical) and, therefore, poor property transfer. Reactive and nonreactive systems were reviewed and show the importance of having a strong interfacial bond for proper property transfers in composite materials. The interface between the matrix and the reinforcements has a nonnegligible effect on the lifespan and performance of these composites. The major part played by the interfaces in the heat conduction process through metal-diamond interfaces was emphasized. While the intrinsic properties of the materials selected to form the multimaterials, are crucial for the enhancement of heat conduction, the thermal resistance at the interface between materials had a nonnegligible effect on the overall thermal properties of the final material. Therefore, it is necessary to find chemical bonding solutions which allow a decrease of the interfacial thermal resistance and facilitate electron-phonon and phonon-phonon coupling across the interfaces. Different methods of creating chemical bonds within composite materials were discussed, for example, inserting carbide-forming elements into the composite materials.

Finally, analytical and numerical models and experimental data allowed prediction and confirmation of the “composite effect” resulting from the combination of two or more materials in an attempt to obtain thermally efficient multimaterials. The models presented in this chapter show the many parameters that can influence heat conduction in isotropic and anisotropic materials.

3 Copper/Carbon Composite Materials

3.1 Introduction

Heat sink materials are currently under investigation by several research groups, as they could allow increasing power densities in microelectronic components as well as promote the miniaturization of such devices. Copper (Cu) is widely used in the microelectronics industry because of its high thermal conductivity ($k = 400 \text{ W}\cdot\text{m}^{-1}\cdot\text{K}^{-1}$), high electrical conductivity ($\sigma = 6.48 \times 10^7 \text{ S}\cdot\text{m}^{-1}$), and ductility. However, the elevated coefficient of thermal expansion (CTE) of Cu ($17 \times 10^{-6} \text{ K}^{-1}$) induces thermomechanical strains at the interface with the alumina ($7.2 \times 10^{-6} \text{ K}^{-1}$) insulating layer making up the microelectronic component.

By definition, thermal expansion is the tendency of matter to change its volume upon heating. Copper has a greater tendency to expand compared to diamond. Figure 3.1 shows how, after heating and cooling, the CTE mismatch of copper and the insulating layer induced residual stresses in the material. The flexion of the assembly was due to the need of Cu to expand while being attached to the direct bonding copper (DBC) or the aluminum oxide (Al_2O_3) coating. This induced microcracks in the brittle ceramic. In addition, since no chemical affinity was observed between the two layers, the coating will eventually peel off.

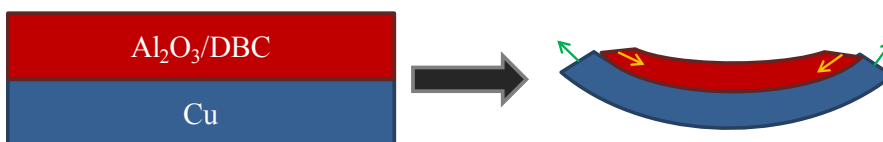


Figure 3.1. Schematic view of how CTE mismatches lead to compressive stresses (yellow arrows) and tensile stresses (green arrows) for $\alpha_{\text{Al}_2\text{O}_3} < \alpha_{\text{Cu}}$.

To overcome this issue, Cu and aluminum (Al) heat sinks were replaced by metal matrix composites, particularly Cu matrix composites reinforced with carbon. Diamond has attracted a lot of interest as its CTE is situated between $1\text{--}2 \times 10^{-6} \text{ K}^{-1}$ and its thermal conductivity between $1000\text{--}2000 \text{ W.m.}^{-1}\text{K}^{-1}$. Therefore, by combining the high thermal conductivities of both entities and their drastically different CTEs, one can expect to obtain a thermally effective material with adaptive properties.

However, a permanent issue when considering the copper-carbon (Cu-C) system is the absence of chemical affinity between the two constituents. In fact, the solubility of carbon (C) in Cu is minuscule and only takes place at very high temperatures. G.A. Lopez et al. determined that the equilibrium values vary from 4.8 ± 0.5 at. ppm at 1143 K to 7.4 ± 0.5 at. ppm at 1293 K of C in solid Cu [67]. The binary phase diagram, shown in Figure 3.2(a), shows the nonmiscible character of Cu and C. The experimental values of the solubility limit of C in solid Cu presented in the work of G.A. Lopez et al. are given in Figure 3.2(b).

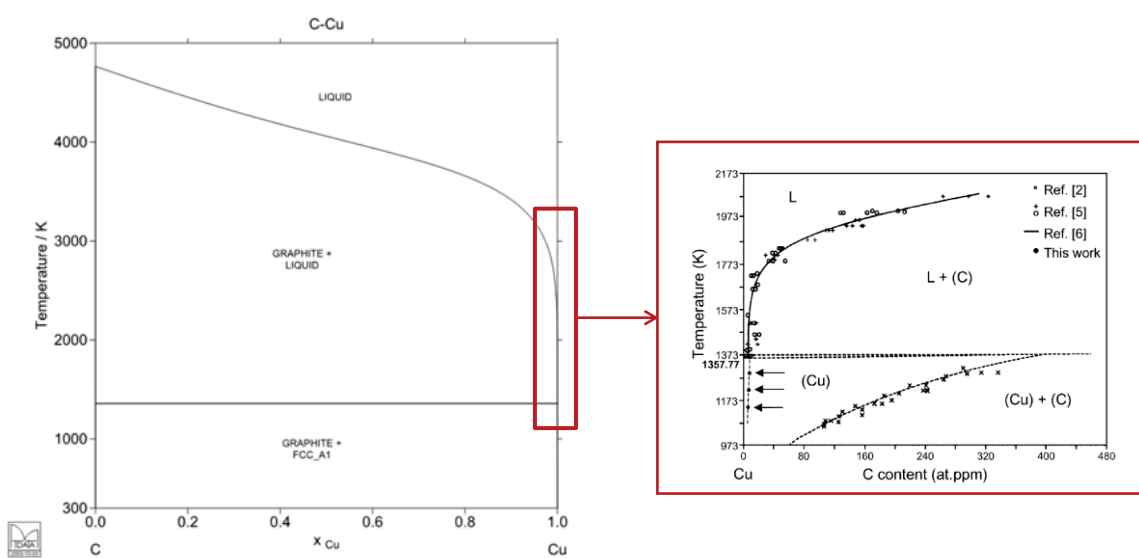


Figure 3.2. Binary phase diagram of the Cu-C system. Closer view of the solubility limit of C in solid Cu at high temperatures.

The absence of wettability of carbon by molten copper is a major obstacle in the fabrication of Cu/C composites. The nonreactivity prevents the creation of a solid solution which could lead to a chemical interphase between the Cu matrix and the reinforcement. The absence of chemical affinity and, therefore, of wettability indicates that any Cu-C bonding will be purely mechanical. However, for thermally efficient assemblies, the interfacial bonding between matrix and reinforcement is of the utmost importance. Indeed, mechanical bonding deteriorates with time, especially in materials used for thermal cycling, as the expansion and retraction of the materials induces stresses and results in the creation of voids at the interface. Also, thermal conduction requires intimate bonding between the two constituents and is only possible in the presence of a strong chemical bond.

In order to create a strong chemical bond between the Cu matrix and the C reinforcements (either carbon fibers or diamond particles), several options were investigated. The functionalization of the reinforcements by submicronic Cu particles through the creation of oxygen (O) bonds was carried out during the Ph.D. of T. Guillemet [5]. Another well-known process is the insertion of alloying elements to create an interphase between the matrix and the reinforcement. For this process, carbide forming elements (X) are preferred as they possess a strong affinity with C and tend to create strong covalent C-X bonds through carbide interphases. The carbide-forming element can either be used as a coating deposited directly on the reinforcements or as an additive in the matrix. At high temperature, the additives will tend to diffuse towards the C reinforcement and react with it.

Carbide-forming elements in Cu/C composites have been extensively studied in past years. They lead to strong interphases and improved thermal properties while bringing an additional mechanical resistance to the composite. They also allow the CTE of the composite to decrease, as their CTE values are lower than those of metals.

However, in terms of processing, carbide-forming elements require high temperatures to form their corresponding carbide. Also, the diffusion of the elements is not always complete at the end of the sintering process and often requires a post-sintering heat treatment to purify the matrix.

This chapter deals with the synthesis of Cu/C composite materials using a “continuous solid-liquid coexistent state” during hot pressing. The solid-liquid coexistent state was achieved by the use of X-alloyed Cu powder with specific characteristics. Fabrication and characterization of Cu/C composite materials was carried out at the Institute of Condensed Matter Chemistry of Bordeaux, under the direction of Research Director Jean-François Silvain. Associate Professor Jérôme Roger from the Laboratory of Thermo-Structural Composites of the University of Bordeaux has conducted and assisted with thermodynamic simulations.

3.2 The Solid-Liquid Coexistent Phase Process

Since only mechanical bonding can occur between Cu and C, their assembly is not optimum. In fact, in terms of thermal properties, the lack of chemical bonding between the two constituents facilitates the insertion of air in the assembly. Air acts as an insulator, which reduces the thermal conductivity of the final material. Therefore, the objective was to produce Cu/C composites that were bonded chemically. To this end, carbide interphases

are being considered. These interphases will be found at the interface between the Cu matrix and the C reinforcements, as shown in Figure 3.3.

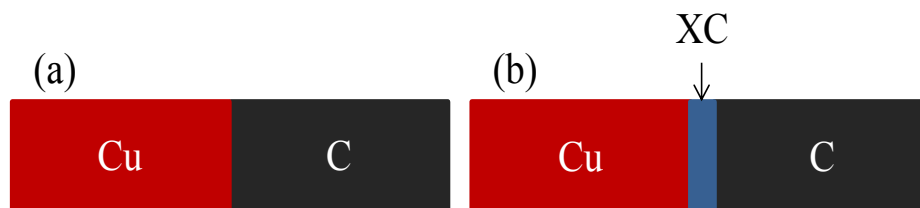


Figure 3.3. Schematic view of (a) a Cu-C nonreactive interface and the (b) presence of an XC carbide interphase.

Several processes lead to the formation of carbide interphases; in this case, the solid-liquid coexistent phase process was chosen. This process is well known for use with Al-based composites [32]. To our knowledge, however, the process has never been used for Cu-based metal matrix composites (MMCs). In the case of Al-based composites, the liquid phase enhances the reactivity of Al with the reinforcement. In the case of Cu-based composites, the liquid phase is expected to enhance the reactivity of the additive with the C reinforcements.

As mentioned previously, this process involves the coexistence of both a solid and a liquid phase. The presence of the liquid phase induces several advantages. First, it is well known that the diffusion of atoms in a liquid is much faster than in a solid and will facilitate the diffusion of the alloying element species towards carbon. Furthermore, the liquid phase will enhance the reactivity of carbon and carbide forming species. Finally, this liquid phase will allow a larger amount of reinforcements to be inserted into the composite. Indeed, a high content of reinforcements creates networks into which it is difficult for powders to penetrate, resulting in porous materials (a downside of regular net-shaped processes with

high reinforcement content). This is why a composite is limited to a certain amount of reinforcements.

For the solid-liquid coexistent phase process, three starting constituents were required: the Cu powder which will constitute the majority of the matrix and which will remain solid during the sintering process, the Cu-X powder, which needs to have a lower melting point than Cu, and the carbon reinforcement. Contrary to most matrix alloying techniques, the Cu-X powder will be added in small quantities. Indeed, most studies use the alloyed Cu powder as the matrix; they, therefore, use Cu-X alloys of up to 3 at. % in the X element [68–72]. A schematic view of the solid-liquid coexistent phase process steps is given in Figure 3.4. First, the powders are mixed together; then a temperature situated between the melting point of Cu and that of the Cu-X alloy is reached, and a uniaxial load is applied for a certain amount of time. Ideally, at the end of the sintering process, the reinforcements are coated with a XC interphase; and the matrix is completely purified.

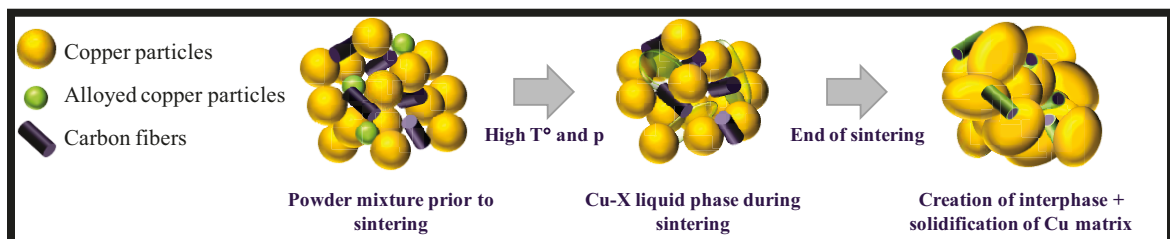


Figure 3.4. Schematic of the solid-liquid coexistent phase process. The initial powder mixture (Cu + Cu-X+ CF) is sintered under load at high temperature. During the sintering plateau, the Cu-X liquid phase is generated. Finally, at the end of the sintering process, the carbon fibers are coated with a XC interphase.

3.2.1 Starting Materials

3.2.1.1 The Copper Matrix

Copper has been chosen as the matrix material as it gives a good compromise between thermal properties and price. Its characteristics are presented in Section 2.4.1. Copper powders exist in several forms, the most common of which are spherical copper powders, obtained through atomization, and dendritic copper powders obtained through an electrolytic route. Atomization consists of melting a bulk metal and breaking the liquid into droplets that will then solidify into powders. Several breakup methods exist, such as pressure, spray, electrostatic, and ultrasonic. The most popular is pressure atomization and is the process mainly used in industry. Here, the liquid metal breaks up by the impact of a fluid (gas) under high pressure. The electrolytic route consists of reducing Cu ions (Cu^{2+}) to metallic Cu. The Cu ions are provided by various precursors, such as oxides, carbonyls, and sulfates, and are reduced in an aqueous solution by means of an electric current. Often, dendritic powders are also called electrolytic since the morphology is obtained through this process. The dendritic powders used as matrix materials were provided by Eckart Granulate Verden GmbH.

Figure 3.5 provides scanning electron microscopy (SEM) micrographs of the dendritic Cu powder used as the matrix. The micrographs confirm the presence of dendrites and show that their length averaged up to 35 μm . The Cu powders were crystallized and did not contain any impurities nor significant oxide quantities, as shown on the X-ray diffraction (XRD) pattern in Figure 3.6. The three major peaks at 43°, 51°, and 74° were typical signs of the face centered cubic (FCC) structure of Cu.

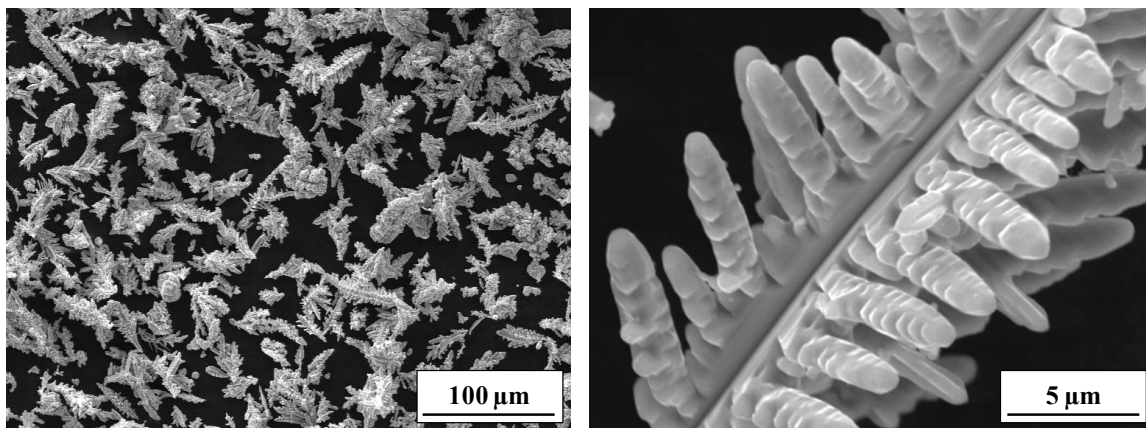


Figure 3.5. SEM micrographs of dendritic copper powders used for the composite matrix.

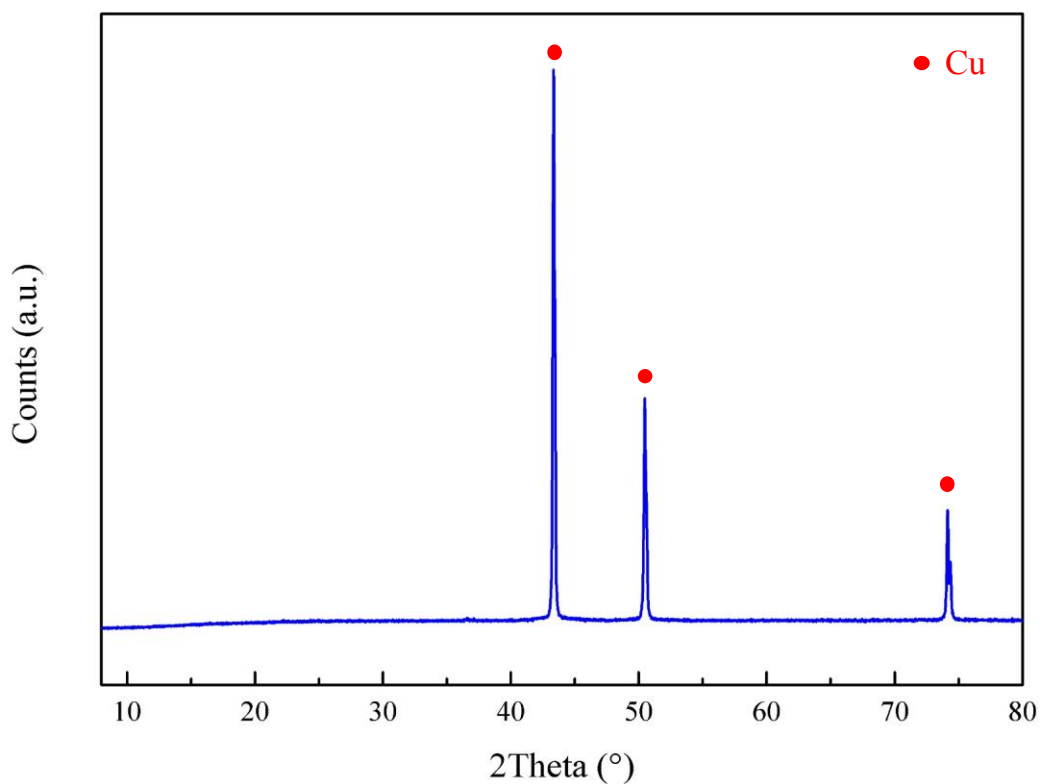


Figure 3.6. XRD pattern of the dendritic Cu powder.

Dendritic powders were chosen instead of spherical Cu powders because of their high aspect ratio (surface/volume). High aspect ratio powders require less energy to deform and, therefore, require a lower sintering temperature than spherical powders to be densified. The composite materials used in this study were obtained through a powder metallurgy

process. Therefore, pressure and temperature were applied on the powder mixture to densify the material. Lower sintering temperatures and/or pressures reduce the cost of manufacturing.

3.2.1.2 The Alloyed Copper

The solid-liquid coexistent phase process that was considered for this work requires the presence of a liquid phase during sintering. For that, a Cu-based alloy with a melting point inferior to the melting point of pure Cu was required. Therefore, the choice of the alloy moved toward carbide-forming additives, as these species tend to react with carbon to create a chemical interface between the matrix and the reinforcement.

The specifications for the carbide forming additives (X) were: (1) a processing temperature lower than that of pure Cu, and (2) an alloy constituted mainly of Cu. Such alloys allow the insertion of a very small amount of additive species. In fact, it is important in this case to limit the amount of element X, as what does not react with the reinforcement will remain in the Cu matrix as impurities. It has been shown that Cu's thermal and electrical properties are very sensitive to the nature and content of impurities. In fact, one study has shown that the properties of several elements in Cu can be drastically affected by a few atomic percent of additive element [73]. Table 3.1 provides the variation of electrical resistivity for 1 at. % and 1 wt. % of several carbide forming elements. As electrical and thermal properties are closely linked together, it is safe to say that thermal conductivity also suffers from the presence of additives. One can see that each element considered here has a different effect on the electrical resistivity of Cu. Therefore, it is important that the additive content in the composite material be as low as possible so that the properties of the Cu matrix can be salvaged.

Table 3.1. Evolution of the electrical resistivity variation of Cu alloys at 20 °C with respect to the nature and content of carbide forming additives.

Properties		Carbide forming additives					
		Al	Cr	Fe	Si	Ti	Zr
Electrical resistivity variation ($\Delta\rho$ in $\mu\Omega\cdot\text{cm}$)	1 at. % added	0.95	4	9.3	3.1	16	11.5
Electrical resistivity variation ($\Delta\rho$ in $\mu\Omega\cdot\text{cm}$)	1 wt. % added	2.22	4.9	10.6	7	21.6	8
Maximum solubility (1 at. %)		9.4	0.03	0.14	2	0.4	<0.1

The selection of the carbide-forming elements was based on their ability to form solid solutions with Cu and carbides with C. Therefore, comparable atomic radii and electronegativities between Cu and the additive, as well as crystal structures, were investigated. Profound analyses of the Cu-X phase diagrams and Gibbs free energy of formation of the carbides were conducted. The Cu-X couples should present a eutectic transformation at a temperature which is inferior to the melting temperature of pure Cu. Several carbide-forming additives presenting eutectic points with Cu are given in Table 3.2.

Table 3.2. List of carbide-forming elements which exhibit a eutectic transformation at a temperature which is inferior to Cu's melting point (1083 °C).

Carbide forming elements	Eutectic transformation temperature (°C)	Composition in Cu (wt. %)
Y	830	58
Ti	875	87
Hf	950	85
B	1013	97.46
Zr	966	91.61

Carbide forming elements	Eutectic transformation temperature (°C)	Composition in Cu (wt. %)
Si	802	84

To refine the carbide-forming element choices, it is important to look at the energies of formation of the carbides. Table 3.3 includes the Gibbs free energy formation of various carbides, from highest (left) to lowest (right). One can notice that boron carbide (B_4C) has the highest energy of formation, which indicates that the carbide will have more difficulties in forming compared to the other carbides given here. Yttrium carbide (Y_2C) and hafnium carbide (HfC) have also been discarded because of low Cu composition in the alloy and price, respectively. Therefore, the final choice was set to titanium (Ti), silicon (Si), and zirconium (Zr). Due to oxidation phenomena and because of the incomplete study of the Cu-Si-C system, silicon carbide (SiC) interphases will not be discussed here.

Table 3.3. Gibbs free enthalpy of formation of considered carbides at 25 °C.

Carbide	B_4C	SiC	TiC	ZrC	Y_2C	HfC
$\Delta_f G^\circ$ (kJ·mol ⁻¹)	-14.2	-68	-90.4	-96.5	-108	-209.6

The alloys considered for this work were produced by atomization with a composition of 27 at.% of Ti and 6 at.% of Zr, as specified in Table 3.4. The powders were provided by NANOVAL GmbH & Co. KG. Differential thermal analysis of the alloy powder showed that the melting temperature of the Cu-Ti powder is 888.5 °C, while that of Cu-Zr is 980.8 °C.

Table 3.4. Specifications of alloyed copper powders.

X	Theoretical	Experimental			
composition	melting point	melting point	Powder	d₅₀	
Alloy	(at.%)	(°C)	(°C)	shape	(µm)

Cu-Ti	27	875	888.5	Spherical	16.7
Cu-Zr	6	966	980.8	Spherical	19.5

Scanning electron microscopy analyses have shown the spherical shape of both powders obtained due to the atomization process used for their production. Figure 3.7 consists of SEM micrographs of the two alloyed Cu powders. While the data provided by NANOVAL GmbH & Co. KG gave a mean particle size (d_{50}) of 16.7 and 19.5 μm for Cu-Ti and Cu-Zr, respectively, the SEM analyses showed the polydispersity of the powders. Indeed, particles as small as 2 μm were observed. However, knowing that both alloys would melt during the sintering process, the polydispersity of the powder was not studied.

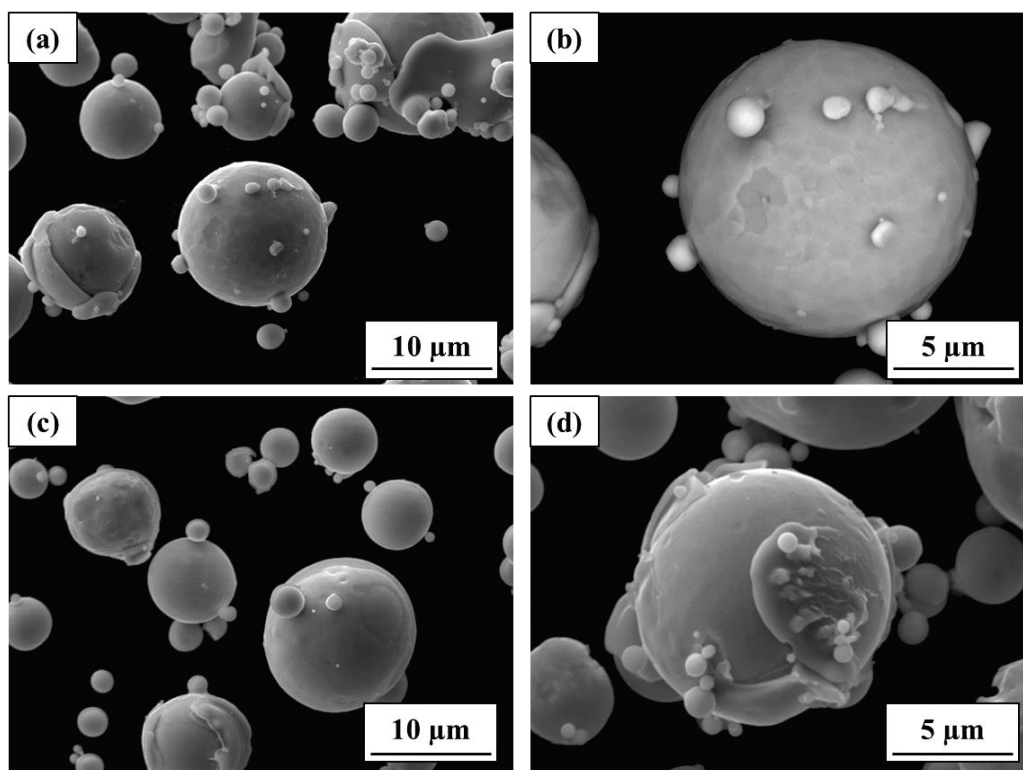


Figure 3.7: SEM micrographs of (a), (b) Cu-Ti alloy and (c), (d) Cu-Zr alloy powders.

The phases constituting the powders were determined using XRD analyses. High quality XRD patterns of both Cu-Ti and Cu-Zr powders are given in Figure 3.8. The Cu-Ti alloy was composed of two defined compounds, Cu_2Ti and Cu_4Ti , while the Cu-Zr alloy

was composed of a solid solution of Zr in Cu and Cu_5Zr . These phases were verified on the binary phase diagram of each system and confirmed the composition in Ti and Zr.

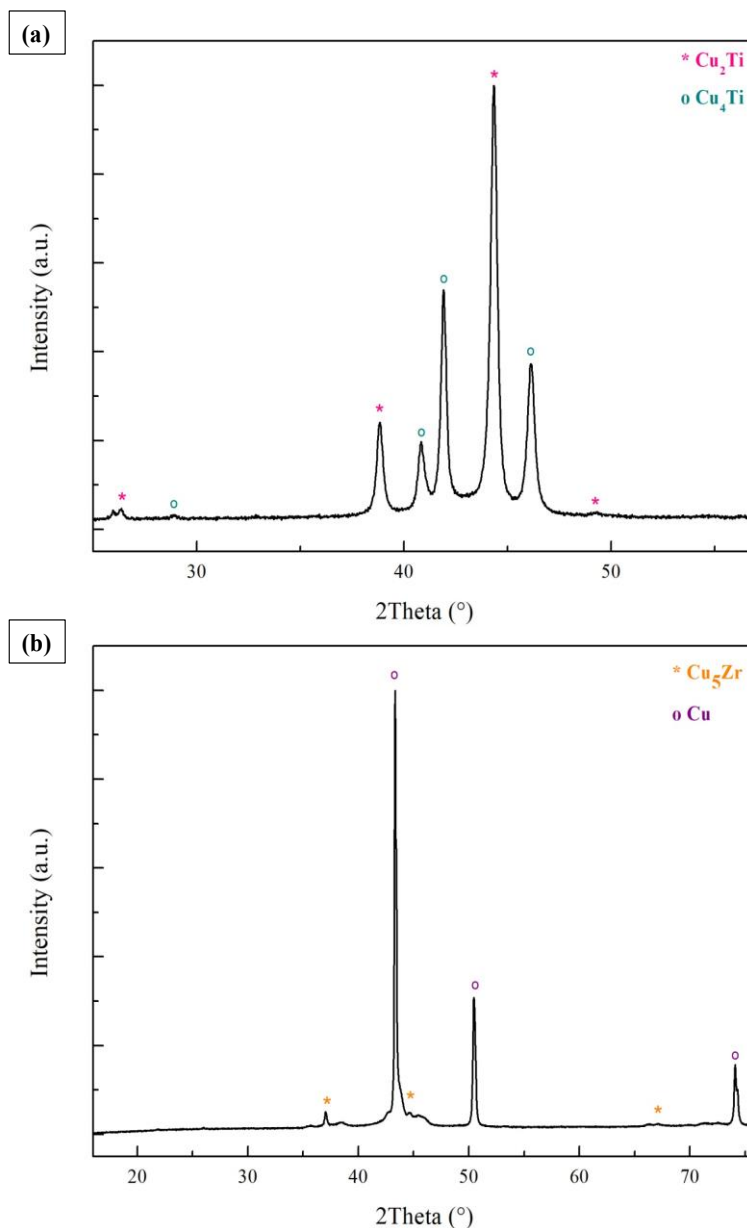


Figure 3.8: High quality XRD patterns of (a) Cu-Ti and (b) Cu-Zr alloyed powders.

3.2.1.3 The Carbon Reinforcements

Two types of carbon reinforcements were used for the synthesis of the composite materials: carbon fibers (CFs) and diamond particles (D). Diamond particles are more promising for optimum heat dissipation; and because of their high thermal conductivity,

their hardness does not allow for easy machining of diamond-based composites. Therefore, preliminary studies and investigations on the reactivity of the alloying elements with carbon was assessed on carbon fiber-based composites.

Carbon Fibers. The atomic structure of CFs is similar to that of graphite. Both consist of graphene sheets, i.e., carbon atoms arranged in a hexagonal pattern. The difference, however, lies in the arrangement of the graphene sheets. While graphite is a crystalline material in which the sheets are stacked parallel to one another, CFs can exhibit two types of arrangements. Depending on the synthesis route, the CFs can be either turbostratic or graphitic. In turbostratic CFs, the graphene sheets are randomly folded together; however, in graphitic CFs, the structure is identical to that of single crystal graphite.

As stated previously, the structure of the CFs depends on the synthesis route and, more particularly, on the precursors. Indeed, CFs can be obtained by different types of precursors which can be categorized as follows [74]:

1. *Acrylic precursors:* Used by most industrial manufacturers. The most current one is polyacrylonitrile (PAN).
2. *Cellulosic precursors:* In theory, the carbon content of these precursors is less than 50%. However, due to the synthesis process, the final carbon content reaches only 25–30%.
3. *Pitch-based precursors:* These precursors are used for the synthesis of high modulus carbon fibers, which results from their graphitic structure.
4. *Other precursors:* Phenolic resins and vinylidene chloride were investigated but are not commercially viable.

The selection of the precursor is made based on the application. In the case of a heat sink and thermally efficient materials, pitch-based precursors are preferred.

Pitches are mixtures of polyaromatic molecules and heterocyclic compounds rich in carbon (> 80%). Pitch sources can be obtained from several sources, such as petroleum refining and destructive distillation of coal, which are natural, and pyrolysis of polyvinyl chloride (PVC), a synthetic source. Pitch precursors have the advantage of a higher degree of orientation, which is what enhances the graphitic structure of the fibers. The production of CFs from pitch-based precursors involves several stages: production of precursor fibers, stabilization of the precursor fibers, carbonization, and finally graphitization. The carbon fibers used in this investigation were the K223HM, CTN DIALEAD™/BOBBINS provided by the Sumitomo Corporation Europe Limited. These are pitch-based CFs. They have a structure in which graphite plates are highly oriented in the vertical direction of the CF. In our work, milled fibers were preferred because of their dimensions. Their specifications are given in Table 3.5.

Table 3.5. Specifications of K223HM carbon fibers used as reinforcements.

Grade	Tensile Modulus	Tensile Strength	Density	Thermal Conductivity	Average Length	Diameter
Units	GPa	MPa	g/cm ³	W/m·K	μm	μm
K223HM	900	3800	2.2	550 // to the CF axis [5-10] ⊥ to the CF axis	250	10

This grade of CFs was selected as these CFs exhibit interesting thermal properties. However, as mentioned previously, the CF structure contains highly oriented graphite

plates which induce anisotropy, not only in terms of shape but also in terms of properties. More particularly, the anisotropy in properties relies on the different types of bonds present in CFs. While, the carbon atoms are covalently bonded in the plate, the stacks are held together by van der Waals forces. Therefore, the property transfer along each direction differs.

Figure 3.9 shows a SEM micrograph of a CF and a schematic of how the anisotropy of shape influences the thermal conductivity of the fiber. The micrograph allows observation of the alignment of carbon filaments along the primary axis. Therefore, it is along that direction that the properties are optimum.

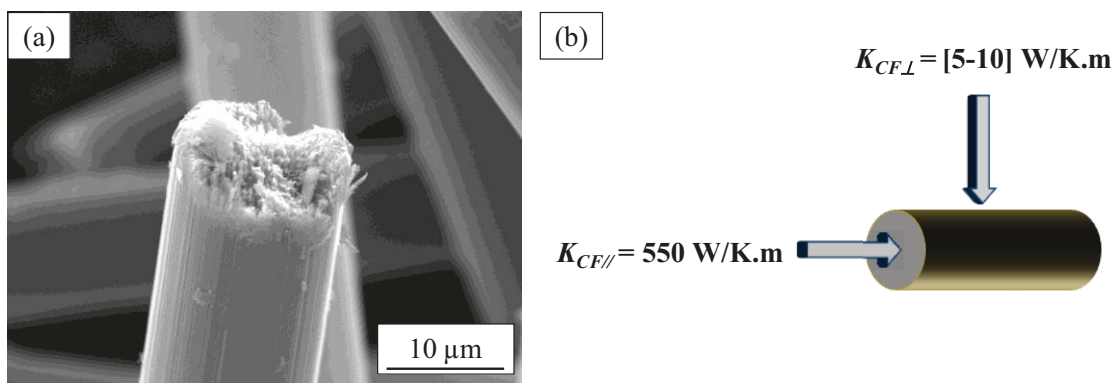


Figure 3.9. (a) SEM micrograph of a CF and (b) anisotropic thermal conductivity caused by the anisotropy of shape of the CF.

Diamond Particles. Diamond particles were used for the synthesis of thermally efficient composite materials. Diamond particles have not only a higher thermal conductivity than carbon fibers but also an isotropic shape and, therefore, properties. However, due to its crystal structure, as discussed in Section 2.2.1, diamond is the hardest material found in nature. It is, therefore, very hard to machine diamond-based materials.

The diamond particles used in this investigation were provided by two companies: Henan Zhongxing Corporation (China) and Tomei Diamond Co., Ltd (Japan). The

diamond powders from Henan Zhongxing Corporation were MBD6 quality grade diamonds and are shown in Figure 3.10.

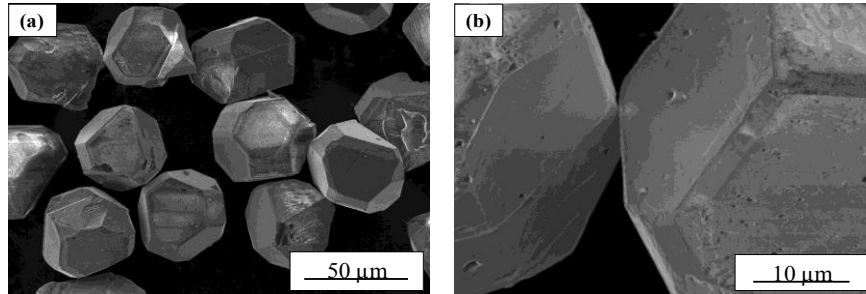


Figure 3.10: MBD6 grade diamond particles used as reinforcements in the Cu-D composites.

3.2.2 Sintering

Metal matrix composites can be produced using several methods that can be grouped into two routes, liquid and solid, depending on the state of the matrix during the fabrication process. While the liquid route has been getting more attention in the past few years, some drawbacks have been noticed, such as agglomeration and segregation, which causes nonuniform distribution of the reinforcements and a higher tendency for chemical reaction at the matrix-reinforcement interface. Powder metallurgy (PM) or net shape processing, which is a solid route process, could help minimize these drawbacks while maintaining low manufacturing costs. The viability of PM comes mainly from the ease of control of the microstructure and the uniformity of the material. Properties, such as thermal conductivity and ductility, can easily be varied by controlling the density and reinforcement content. The PM process relies on traditional blending/mixing of the initial powders (matrix and reinforcements), cold pressing, and sintering. Post-sintering treatments, such as plastic working (extrusion) and heat treatments, can be considered.

3.2.2.1 Mixing

For the purpose of this study, mechanical alloying by the means of ball milling was not necessary. Conventional 3-directional (3D) mixing of the powders was preferred. Therefore, the powders were mixed in a Siemens 3D mixing device (Figure 3.11) for 90 min at 20 RPM.

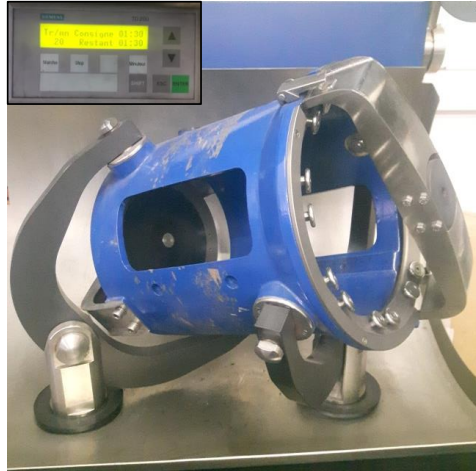


Figure 3.11. 3D mixing device used for powder homogenization.

3.2.2.2 Cold Compaction

This very simple process is widely used for better packing. Several techniques exist depending on the direction of the force applied, such as uniaxial single action pressing or cold isostatic pressing. It is an important step in PM as the initial compaction will affect the densification level of the compacts during the sintering step.

3.2.2.3 Sintering Mechanism

Sintering consists of bonding powder particles at high temperature. Typically, sintering takes place at a temperature below the melting point of the powders, indicating that the consolidation is ensured by solid state atomic diffusion. Indeed, atomic movements reduce the high surface energy of the particles, thus deforming them to create “necks” between the particles. Neck growth induces shrinkage and densification of the powders, thus ensuring the consolidation of the material.

Three stages can be distinguished in the sintering process and are given in Figure 3.12 [75]. Stage 1 starts with the loose powders. Then, after compaction in Stage 2, the powder particles are sufficiently close so as to be in contact with each other. During Stage

3, at sintering temperature, diffusion processes cause “necks” to form and grow at the cold weld contact points. The relative density (experimental density/theoretical density) is close to 75%. Individual particles can no longer be distinguished, and pores are situated at the trijunctions of adjacent grains. This stage is characterized by rapid shrinkage and slow grain growth. When the relative density reaches 91–95 %, the interconnected pore channels become unstable and form individual isolated pores at the grain boundaries. This phenomenon takes place during Stage 4, where open porosity becomes closed. At the end of the sintering process, slow densification and fast coarsening take place.

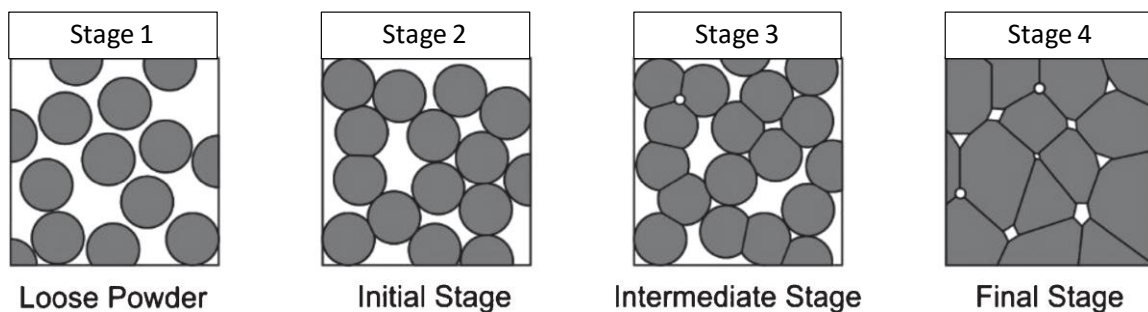


Figure 3.12. The stages of sintering: Stage 1, loose powder; Stage 2, initial stage with contact points between particles; Stage 3, intermediate stage including the creation of "necks" between particles and an increase in the relative density and localization of pores at the trijunctions of adjacent grains; and Stage 4, final stage with a relative density between 91 and 95%, and the pores are now closed [75].

During the sintering process, the stages are strongly affected by both the intrinsic properties of the starting powders and external factors, such as temperature, time, pressure, and surrounding atmosphere in the chamber. In the case of metal/ceramic composite materials, densification depends on the composition and the initial particle size of both constituents. Compaction pressure during sintering (hot pressing), heating rate, and sintering time affect the kinetics of compaction. Usually, higher pressures increase the final density of the material.

3.2.2.4 Experimental Setup

The synthesis of the composite materials of this study was carried out using an induction heating, uniaxial, hot-pressing process. Hot-pressing techniques depend on three parameters: temperature, time, and pressure. Tuning these parameters allows the final microstructure of the material to be adjusted. Hot pressing is a pressure-assisted sintering process which can be described by the stages identified in Section 3.2.2.3. The main difference between hot pressing and free sintering is that the pressure helps the sintering process by increasing the contact surface between the grains, thereby decreasing the time required for full densification.

The sintering of the composites was carried out using a Termolab press. It relies on the combination of an induction heating system and a hydraulic pressing jack. Induction heating consists of heating an electrically conductive material (graphite) through electromagnetic induction, where high frequency alternative currents are generated by a high-power, radio-frequency generator and passed through a copper coil. The high frequency alternative currents trigger the creation of eddy current when passing through the copper coil, which induces free electron motion inside the structure of the graphite mold. The resistance to electron motion in the graphite leads to the heating of the mold which, by contact, heats up the material inside the mold. The induction heating technique is widely used in PM as it has the advantage of heating the material without direct contact with the heat source. The hot-pressing apparatus used for this study is shown in Figure 3.13.

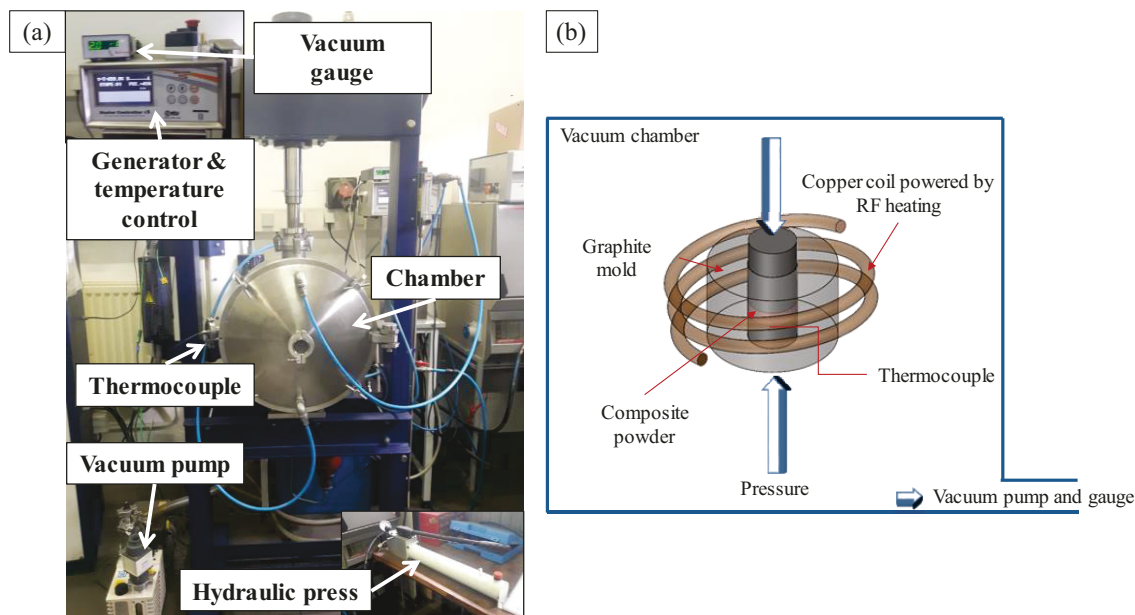


Figure 3.13. (a) Photograph and (b) schematic of the uniaxial hot-press apparatus.

3.2.3 Thermodynamic Assessments

Prior to experimental investigation, preliminary thermodynamic analyses of the equilibrium in the Cu-Ti-C and Cu-Zr-C systems were performed with Thermo-Calc Software [76]. The thermodynamic equilibria calculated using this software were based on the CALculation of PHase Diagrams (CALPHAD) methodology [77, 78]. In constructing the necessary databases, it was important to gather the free enthalpies and the excess free enthalpies of the different components and phases that can occur in the system being considered. The relevant thermodynamic descriptions of the Cu-Ti and Ti-C systems reported by J. Wang et al. and L.F.S. Dumitrescu et al., respectively, were used for the equilibrium calculations of the Cu-Ti-C system [79–81]. The thermodynamic assessment of the CU-Zr and Zr-C systems were reported by R. Arroyave et al. [82].

3.2.3.1 The Cu-Ti-C System

Figure 3.14 shows the calculated Cu-rich side of the Cu-Ti phase diagram and the isothermal section of the Cu-Ti-C ternary phase diagram at 950 °C. For a composite

composition of 56 vol % in Cu, 4 vol% in Cu-Ti, and 40 vol% of C, one can predict the mole and volume fractions of Cu, titanium carbide (TiC), and C that will be formed after reaching 950 °C, which is the sintering temperature for this system. The reaction that takes place during the sintering is the following:



However, TiC is not a defined compound but an intermediate solid solution, as can be seen on the phase diagram in Figure 3.15. Therefore, the composition in C can vary. The calculation of the isothermal section of the Cu-Ti-C diagram at 950 °C, shown in Figure 3.14(b), indicates that a reaction occurred between the liquid alloy and C to form titanium carbide (TiC_x) with $x = 0.97$ for an excess of C.

If the reaction is total, the final volume percentage of TiC_{0.97} is expected to be, at most, equal to 4% in the final composite and about 40% in the CF. Therefore, five compositions were identified. The expected volume percentage of TiC_{0.97} was then comprised of between 0.8 and 4.0% in the composite. The corresponding compositions are indicated in the isothermal section by hourglass marks corresponding to the reaction between the liquid alloy and carbon and to the final composite.

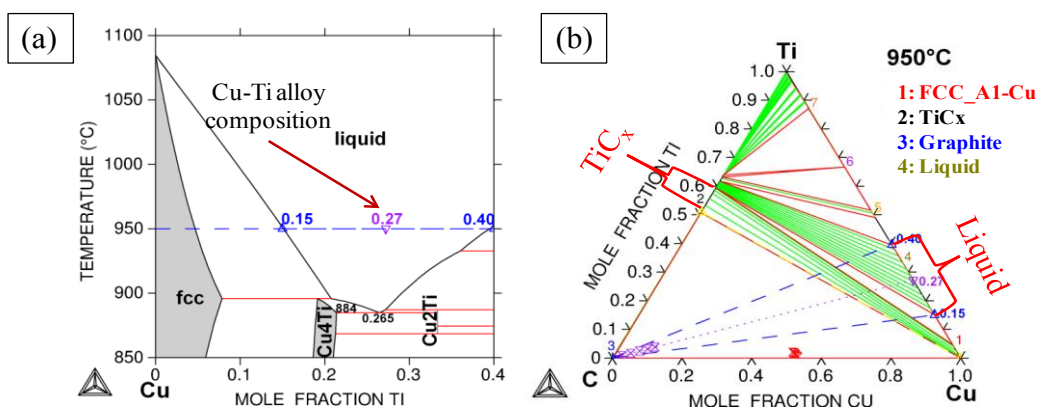


Figure 3.14. Cu-Ti-C system: (a) Cu-rich side of the Cu-Ti phase diagram and (b) isothermal section at 950 °C [79–81].

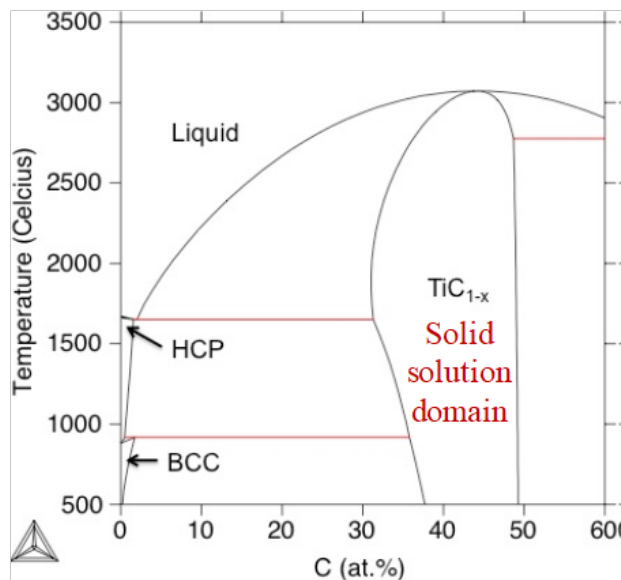


Figure 3.15. Calculated Ti-C binary phase diagram according to the assessment of Dumitrescu et al [81].

The mole and volume fractions of pure Cu (FCC_A1), TiC_{0.97}, and CF within the final composite are given in Figure 3.16(a) and (b), respectively. At 25 °C, as shown in Figure 3.17(a) and (b), the calculations indicate that the phases are pure Cu (FCC_A1), TiC_{0.99}, and CF. The mole and volume fractions are then practically similar at this temperature. These equilibrium calculations confirmed the reaction at the interfaces between the CFs and Ti-containing alloy to form TiC_x. The as-formed composite was mainly composed of pure Cu, CFs, and a low quantity of TiC_x phase, representing less than 4 vol%. The only variation identified by a temperature change was an increase in the C content within TiC_x when the temperature decreased.

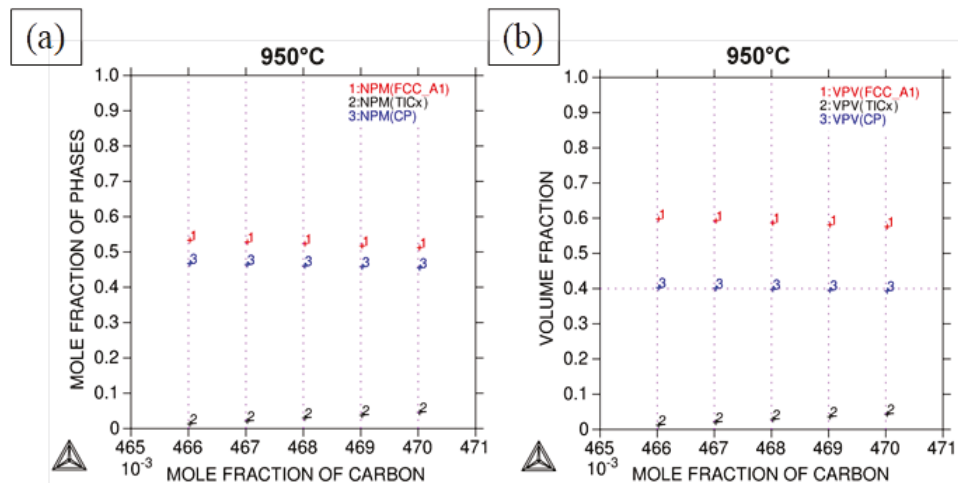


Figure 3.16. Equilibrium composition calculations of the five samples at 950 °C: (a) mole and (b) volume fractions of phases.

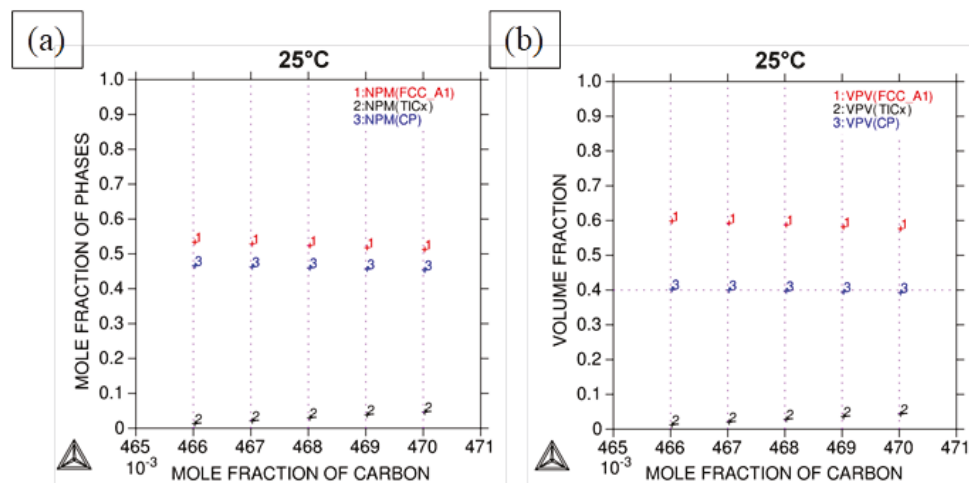


Figure 3.17. Equilibrium composition calculations of the five samples at 25 °C: (a) mole and (b) volume fractions of phases.

3.2.3.2 The Cu-Zr-C system

Figure 3.18 shows the calculated Cu-rich side of the Cu-Zr phase diagram and the isothermal section of the Cu-Zr-C ternary phase diagram at 1050 °C, which is the sintering temperature for this system. In the same ways as for the Cu-Ti-C system, for a composite of a given composition, one can predict the mole and volume fractions of Cu, ZrC, and C

that will be formed after reaching the sintering temperature. The reaction that takes place during the sintering is the following:



Just as mentioned earlier for TiC, ZrC is also an intermediate solid solution. The calculation of the isothermal section of the Cu-Zr-C diagram at 1050 °C, shown in Figure 3.18, indicates that a reaction occurred between the liquid alloy and C to form zirconium carbide (ZrC_x) with metal and nonmetal sites being occupied, as shown in Table 3.6.

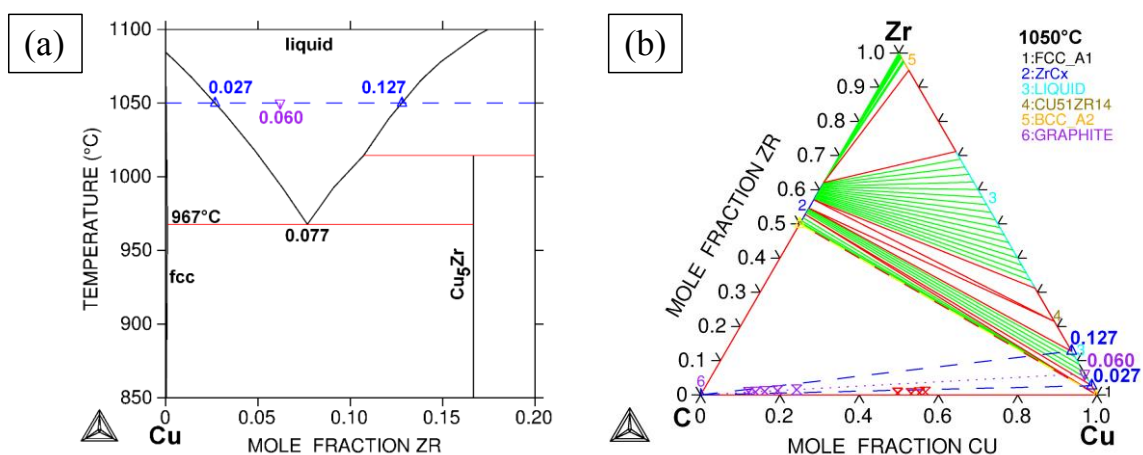


Figure 3.18. Cu-Zr-C system: (a) Cu-rich side of the Cu-Zr phase diagram and (b) isothermal section at 1050 °C.

Table 3.6. Occupancy of ZrC sites given in atomic fractions per site.

Temperature	Zr site	Cu site	C site
1050 °C	0.9997	0.0003	0.9997
25 °C	0.9908	0.0092	1

The mole and volume fractions of pure Cu (FCC_A1), ZrC, and CF within the final composite are given in

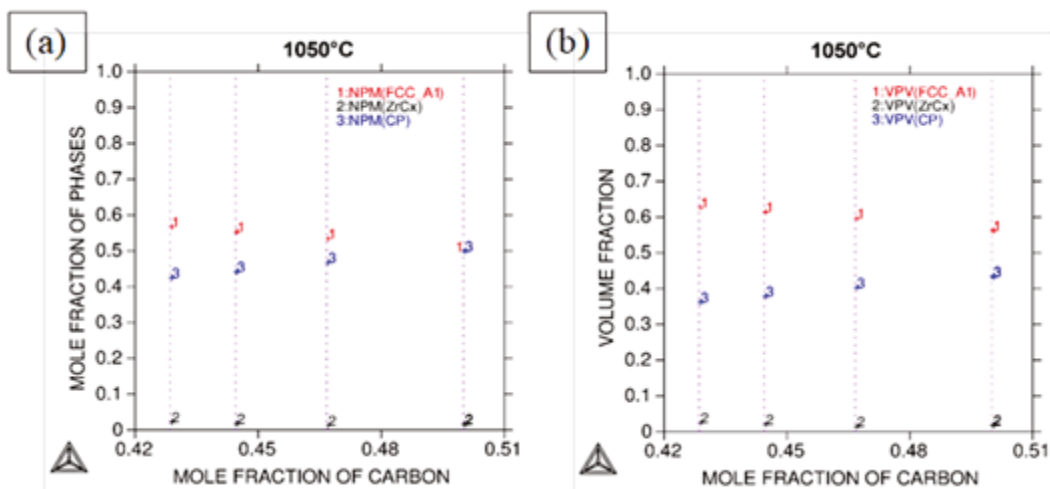


Figure 3.19 (a) and (b), respectively. At 25 °C, as shown in Figure 3.20 (a) and (b), the calculations indicate that the phases are pure Cu (FCC_A1), stoichiometric ZrC, and CF. These equilibrium calculations confirm the reaction at the interfaces between the CFs and Zr-containing alloy to form ZrC_x. The as-formed composite is mainly composed of pure Cu, CFs, and a low quantity of ZrC_x phase. Finally, one can note that the ZrC is richer in Cu at 25 °C rather than at 1050 °C, which is counterintuitive; however, the proportions are too small, and unexpected variations can occur.

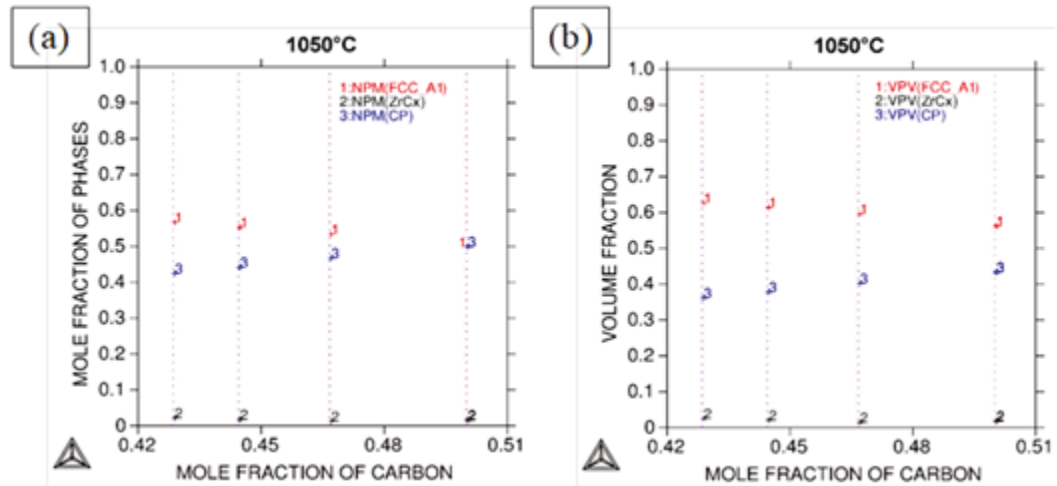


Figure 3.19. Equilibrium composition calculations of the four samples at 1050 °C: (a) mole and (b) volume fractions of phases.

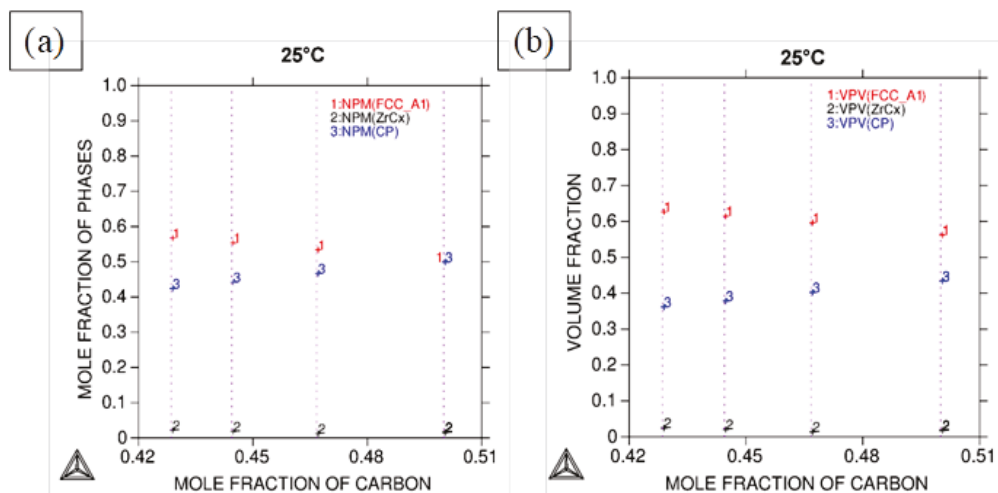


Figure 3.20: Equilibrium composition calculations of the four samples at 25 °C: (a) mole and (b) volume fractions of phases.

3.3 In Situ Creation of the XC Interphases

Cu(Cu-X)/C composites using different volume fractions of Cu-X powders and carbon reinforcements were synthesized using the solid-liquid coexistent phase process. The first part of this section includes information on the synthesis of the materials and the

impact of the solid-liquid coexistent process on the densities of the composites and on their microstructure. The second part of this section describes the growth of the interphases.

As mentioned previously, the solid-liquid coexistent process was chosen for the synthesis of the composite materials. Contrary to regular powder metallurgy processes, this process allows both a solid and a liquid phase to coexist. The liquid phase consisted of the alloyed Cu-X powder, while the solid phase consisted of the copper dendritic powders and carbon reinforcements. The process used is well known in Al-based composites [32]; to our knowledge, however, the process has never been used for Cu-based MMCs. The presence of the liquid phase has been shown to enhance the reactivity between the carbide-forming elements and the carbon reinforcement as well as the density of the materials. In the case of Al-based composites, the liquid phase enhances the reactivity of Al with the reinforcement. In the case of Cu-based composites, the liquid phase is expected to enhance the reactivity of the additive element with the C reinforcements, which should allow the temperature of the carbide formation to decrease.

3.3.1 Cu/C Composite Materials

Before including the Cu-X alloys and, therefore, the liquid phase in the powder mixture, basic Cu/CF composites were synthesized using the hot-pressing apparatus described in Section **Erreur ! Source du renvoi introuvable.**. These composites serve as references to put the impact of the interphase in evidence. For that, Cu/CF composites with CF contents ranging between 10 and 60 vol% were synthesized in the hot pressing chamber at 650 °C, for 30 min under 50 MPa of uniaxial pressure. The synthesis of the Cu(Cu-Ti)/CF and Cu(Cu-Zr)/CF composites was done at 950 °C and 1050 °C, respectively, for 30 min under 50 MPa of uniaxial pressure.

As mentioned in Section 0.3, carbon fibers are anisotropic in terms of shape and proportions. This anisotropy causes the anisotropy of the composite material. During the sintering process, the pressure applied will tend to randomly orient the carbon fibers in the plane, which is perpendicular to the pressure axis. This will cause two different microstructures depending on the observation plane. Figure 3.21 shows the different microstructures. Figure 3.21(a) corresponds to the cross-section microstructure while Figure 3.21(b) corresponds to the surface's microstructure. Therefore, the composite material will exhibit anisotropic properties with respect to the solicitation plan.

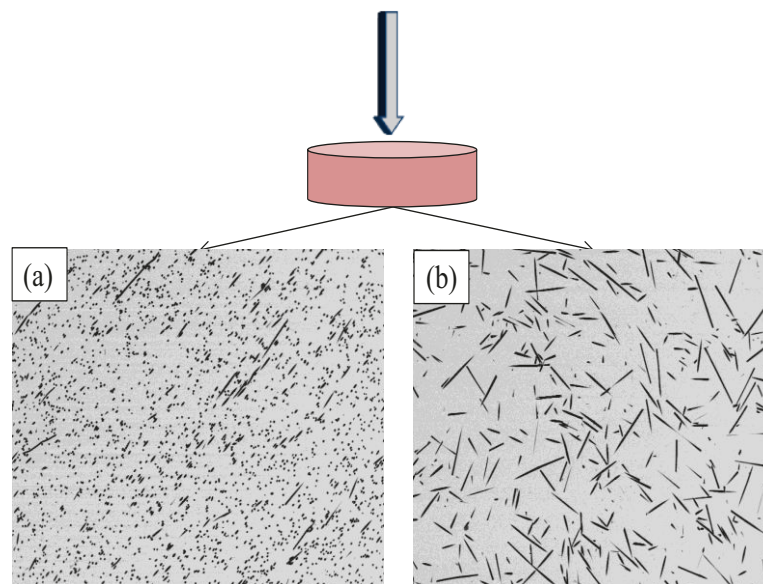


Figure 3.21. Orientation of carbon fibers in the composite (a) cross-section, observation perpendicular to the pressure axis, and (b) surface, observation parallel to the pressure axis.

The experimental densities were measured using Archimedes' principle. This principle states that the upward force exerted on a body immersed in a fluid (water, alcohol, etc.) is equal to the weight of the fluid that the body displaces. The densities were measured using the following formula:

$$\rho_C = \frac{m_{air}}{m_{air} - m_{water}} \times \rho_{water} \quad (3.3)$$

where ρ_C and ρ_{water} are the density of the composite and of the water ($\rho_{water} = 1 \text{ g}\cdot\text{cm}^{-3}$) and m_{air} and m_{water} are the masses of the sample measured in the air and in the water, respectively.

The measured densities were compared to the theoretical densities calculated though the rule of mixture (ROM) given below:

$$\rho_{theory} = \rho_m V_m + \rho_r V_r \quad (3.4)$$

where ρ_m , ρ_r , and ρ_{theory} are the theoretical densities of the copper matrix, the carbon reinforcements, and of the composite, respectively; and V_m and V_r are the volume fractions of the copper matrix and the carbon reinforcements, respectively.

The theoretical densities were related to the experimental ones using the relative density of the composites corresponds to the level of compaction reached by the material. The relative density is calculated using the following equation:

$$D_{relative} = \frac{\rho_C}{\rho_{theory}} \times 100 \quad (3.5)$$

where $D_{relative}$ is the relative density of the material. Due to the small amount of liquid phase inserted in the composites, the theoretical densities do not take the carbide into account. The compositions and relative densities of the composite materials are given in Table 3.7. It is important to be able to quantify the density of the material, since porosity is a major obstacle for thermally efficient materials. In fact, air is a very good thermal insulator ($k_{air} = 0.0262 \text{ W}\cdot\text{K}^{-1}\cdot\text{m}^{-1}$) and will play an important role in decreasing the thermal conductivity of the composite.

Table 3.7. Theoretical, experimental and relative densities of Cu-C composites with CF content of 10-60 vol%.

Compositions in CF (vol%)	10	20	30	40	50	60
Theoretical density (g/cm ³)	8.3	7.6	6.9	6.3	5.6	4.9

Experimental density (g/cm³)	8.2	7.5	6.6	6	5.3	4.6
Relative density	98.6	98.9	96.3	95.8	95.4	93.8

One can notice that relative densities range from 93.8–98.9% when no liquid phase is present. The decrease of the relative density with increasing carbon fiber content is noticeable and is explained by the intertwining of the CFs. Indeed, increasing reinforcement content drastically affects the creeping process of the matrix. Also, the reinforcement geometry causes contact points between CFs which can block copper particles from inserting the created pores.

Figure 3.22 shows SEM micrographs of two composites, one with 40 vol% of CFs and one with 60 vol%. One can notice the increased contact points between carbon fibers in the composite containing 60 vol% of CFs and the resulting porosity, circled in red.

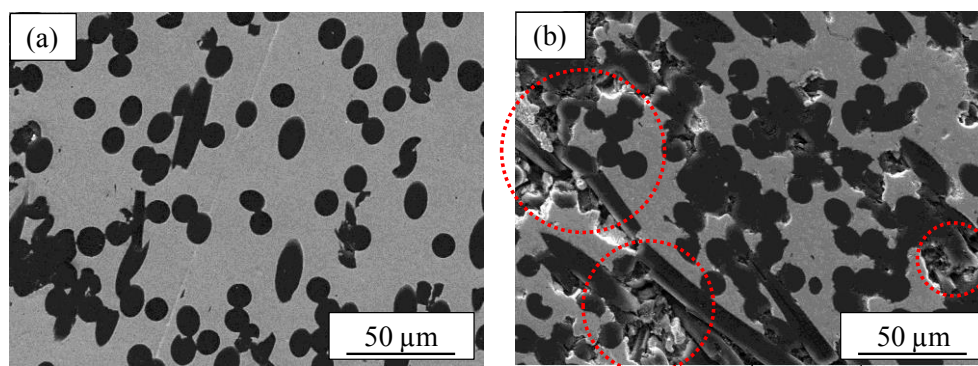


Figure 3.22. SEM micrographs of Cu-CF composites (a) with 40 vol % and (b) with 60 vol % of CFs.

It is, therefore, important to fill in the residual porosity in these composite materials and bring a chemical bonding at the interface between Cu and C. Wan et al. have shown the delamination that occurs in Cu-C composites when the interface is not chemical [83]. Figure 3.23 shows the delamination that occurs in a Cu-C composite with no chemical interfaces.

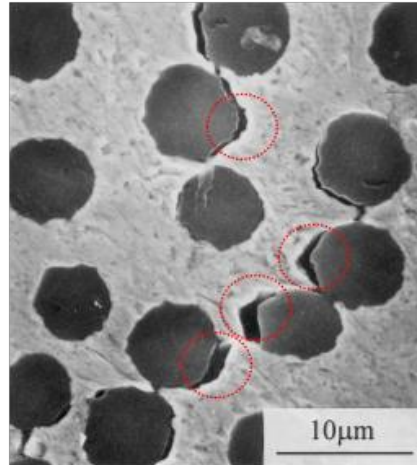


Figure 3.23. SEM micrograph of a Cu/C composite showing debonded interfaces [83].

As mentioned previously, the presence of air under the form of pores will cause a drastic decrease in heat conduction within the material. It is, therefore, vital to not only decrease the porosity level at high volume fractions of reinforcements but to also create a chemical bond between the matrix and the reinforcements to fully exploit the properties of the composite's constituents.

3.3.2 Cu(Cu-Ti)_x/C Composite Materials

Cu(Cu-Ti)_x/CF composites were fabricated with varying Cu-Ti volume fraction content (2–10 vol%). The atomic percentages of each constituent with respect to the Cu-Ti volume fraction and the final Cu:Cu-Ti:C ratios are given in Table 3.8.

Table 3.8: Atomic fractions and ratios of Cu, Cu-Ti, and C in the composite materials for each volume fraction of Cu-Ti.

Vol% of Cu-Ti	Cu	At. % Cu-Ti	CF	Ratios Cu : Cu-Ti : C
2	0.518	0.016	0.466	32 : 1 : 29
4	0.502	0.031	0.467	16 : 1 : 15
6	0.485	0.047	0.468	10 : 1 : 10

8	0.469	0.063	0.468	7 : 1 : 7
10	0.452	0.078	0.470	6 : 1 : 6

The microstructure of the composites was characterized using SEM, VEGA II SBH, TESCAN). The samples were coated with resin and then polished (TegraPol 21, Struers) using silicon carbide (SiC) sandpapers and diamond pastes prior to SEM analyses. Figure 3.24 shows the SEM micrographs of Cu/CF20 with 4, 8, and 10 vol% of Cu-Ti powders. The chemical contrast provided by the backscattered mode of the SEM allowed the interfacial zone surrounding the CFs to be distinguished. The interphase created appeared to be homogeneous and was present on most of the CFs.

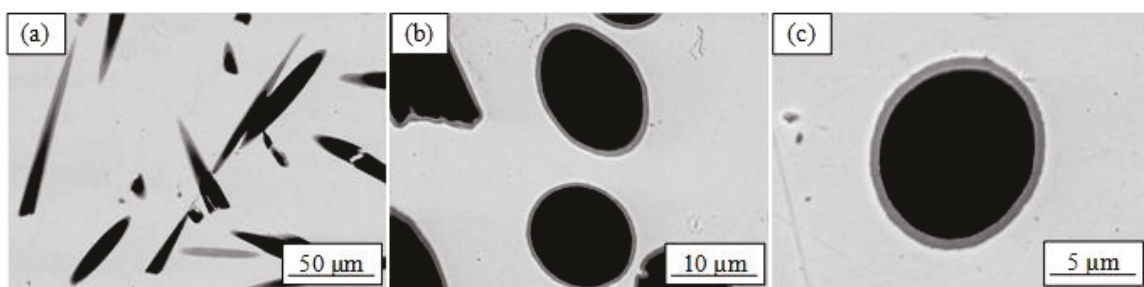


Figure 3.24. SEM micrographs in backscattered electron (BSE) mode of $\text{Cu}(\text{Cu-Ti})_x/\text{CF}_{20}$ composites with (a) 4, (b) 8, and (c) 10 vol% of Cu-Ti alloyed powders.

Energy dispersive X-ray spectroscopy (EDS) was used to identify the chemical nature of the interphase. Figure 3.25 shows an EDS scan line obtained through the cross-section of a CF. One can observe that the interfacial zone is rich in Ti. Also, little or no Ti signal was observed in the matrix region which suggests that all of the Ti diffused to the CFs.

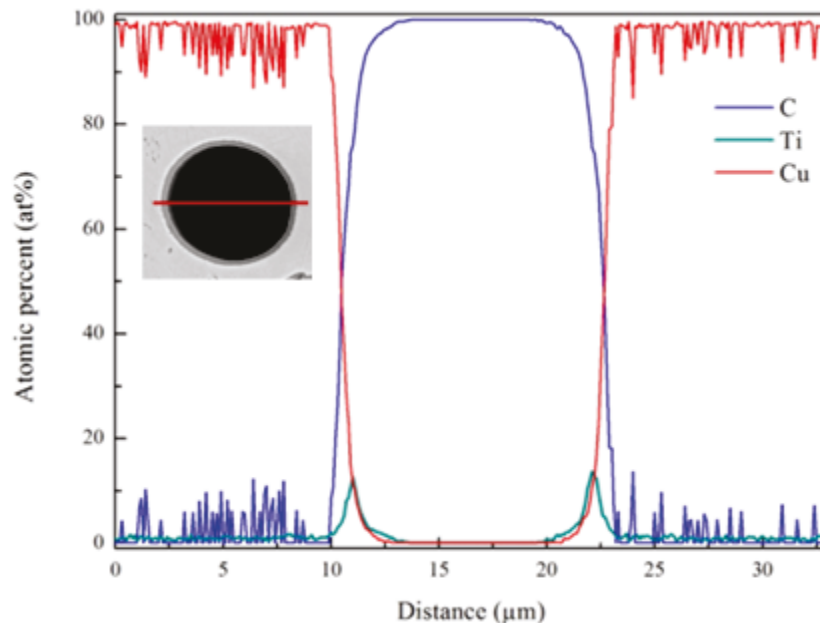


Figure 3.25: EDS line scan obtained through the cross-section of a CF coated with a Ti-based interphase inside the Cu matrix.

To confirm this hypothesis, high resolution XRD data were collected for a 2-theta range between 30 and 65° on a bulk Cu(Cu-Ti)₈/CF20 composite. Le-Bail-type structural refinements were carried out to determine the lattice parameters of the Cu matrix. The XRD pattern is shown in Figure 3.26.

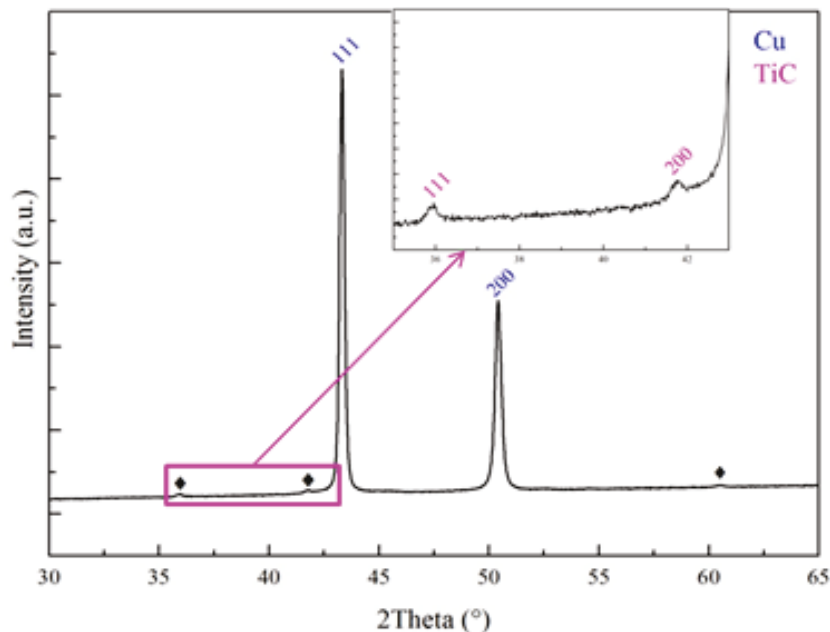


Figure 3.26. High quality XRD pattern obtained from a Cu(Cu-Ti)₈/CF20 composite in a 2-Theta range of 30 to 65°.

The theoretical and measured FCC Cu lattice parameters (Bragg R-factor of 2.22) are listed in Table 3.9. There was no significant difference between the theoretical and the experimental lattice parameters which, therefore, confirms the absence of a solid solution of Ti in Cu for this composite.

Table 3.9. Theoretical and calculated Cu lattice parameters of Cu(Cu-Ti)₈/CF20.

	a	b	c
Theoretical lattice parameters (Å)	3.615	3.615	3.615
Calculated lattice parameters (Å)	3.6189(9)	3.6189(9)	3.6189(9)

Figure 3.27(a) is a representative transmission electron microscopy (TEM) micrograph of a Cu(Cu-Ti)₄/CF10 composite which shows the CF, the interfacial zone, and the Cu matrix. The interfacial zone is around 200 nm thick and is made up of facet-shaped nanograins (Figure 3.27(b)) of about 50 nm in size. No decohesion occurred at either interface (CF-interfacial zone or interfacial zone-Cu). Figure 3.27(c) shows the electron

diffraction pattern obtained in the interfacial zone. Rings were observed that were made up of discrete spots, which are characteristic of nanocrystalline structures.

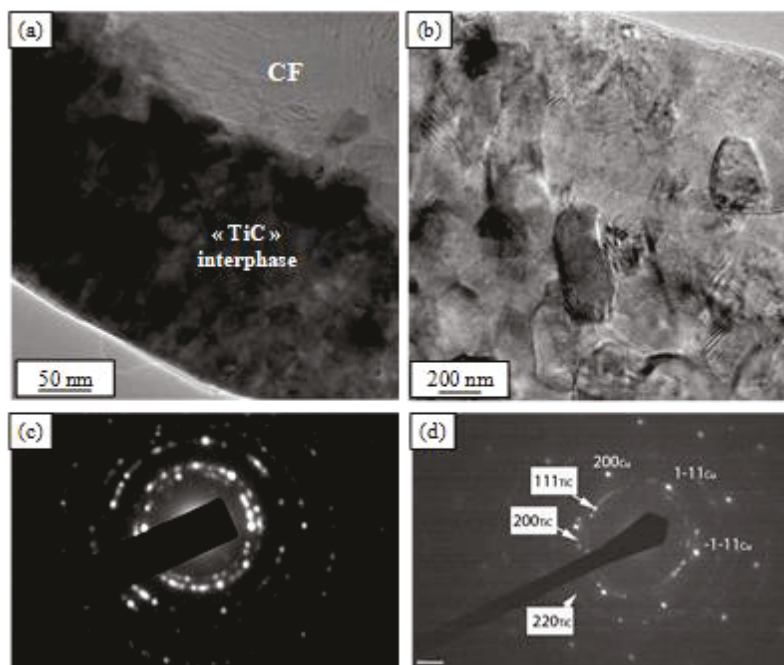


Figure 3.27. TEM images of $\text{Cu}(\text{Cu-Ti})_4/\text{CF10}$ composite material. (a) Overall view of a CF, the interfacial zone, and the Cu matrix, (b) enlarged interfacial zone of micrograph (a), where a polycrystalline structure is observed. (c) Electron diffraction patterns of interfacial zone and (d) an area where both the interfacial zone and the Cu matrix are present.

The ring diameters corresponded to the TiC structure, while extra spots came from the Cu matrix. The diffraction pattern shown in Figure 3.27(d) was obtained from a selected area containing both the interfacial zone and a Cu grain oriented along the $\langle 011 \rangle$ direction. Titanium carbide nanocrystalline spots are superimposed, with the spots corresponding to the well-oriented microscopic Cu grains.

Figure 3.28 shows the electron energy loss spectroscopy (EELS) and energy-dispersive X-ray (EDX) spectra collected on the interphase in the $\text{Cu}(\text{Cu-Ti})_4/\text{CF10}$ sample. For the EELS data, two different areas ($\sim 0.2\text{--}0.5\ \mu\text{m}$ in diameter) of the interphase were investigated; presenting very similar spectral features. As evidenced in Figure

3.28(a), the interphase contained both Ti and C. The quantification of the [Ti-C] atomic ratio was deduced from the spectra using the following formula:

$$[Ti/C] = \frac{I_{Ti}(\Delta) \cdot \sigma_C(\beta, \Delta)}{I_C(\Delta) \cdot \sigma_{Ti}(\beta, \Delta)} \quad (3.6)$$

where $I_{Ti}(\Delta)$ and $I_C(\Delta)$ are the characteristic loss signal in the spectra for Ti and C, respectively, usually given by the area integrated over an energy edge Δ beyond the corresponding edge after background removal. The partial cross-section of $\sigma_{Ti}(\beta, \Delta)$ and $\sigma_C(\beta, \Delta)$ is within an acceptance angle β and an energy window Δ .

The calculations give a composition ranging between $TiC_{0.95}$ and stoichiometric TiC. The fact that the measured TiC composition was almost stoichiometric is very consistent with the electron energy loss near edge structures (ELNES) at the C-K edge given in Figure 3.28(b). These fine structures were very similar to those reported by Calmels et al. [84] given the sensitivity of the C-K edge ELNES to alloying effects or vacancies [84–86], as they confirmed that the local order around the C atoms was very close to that of pure TiC. Given that Cu was evidenced in the interphase region from EDX maps (Figure 3.28(c)), the energy range corresponding to the Cu $L_{2,3}$ edges was also investigated by EELS. One can also notice that all of the Ti was situated in the interfacial region, which confirmed the EDS-SEM analyses. It is, therefore, possible to confirm that all of the Ti diffused and reacted.

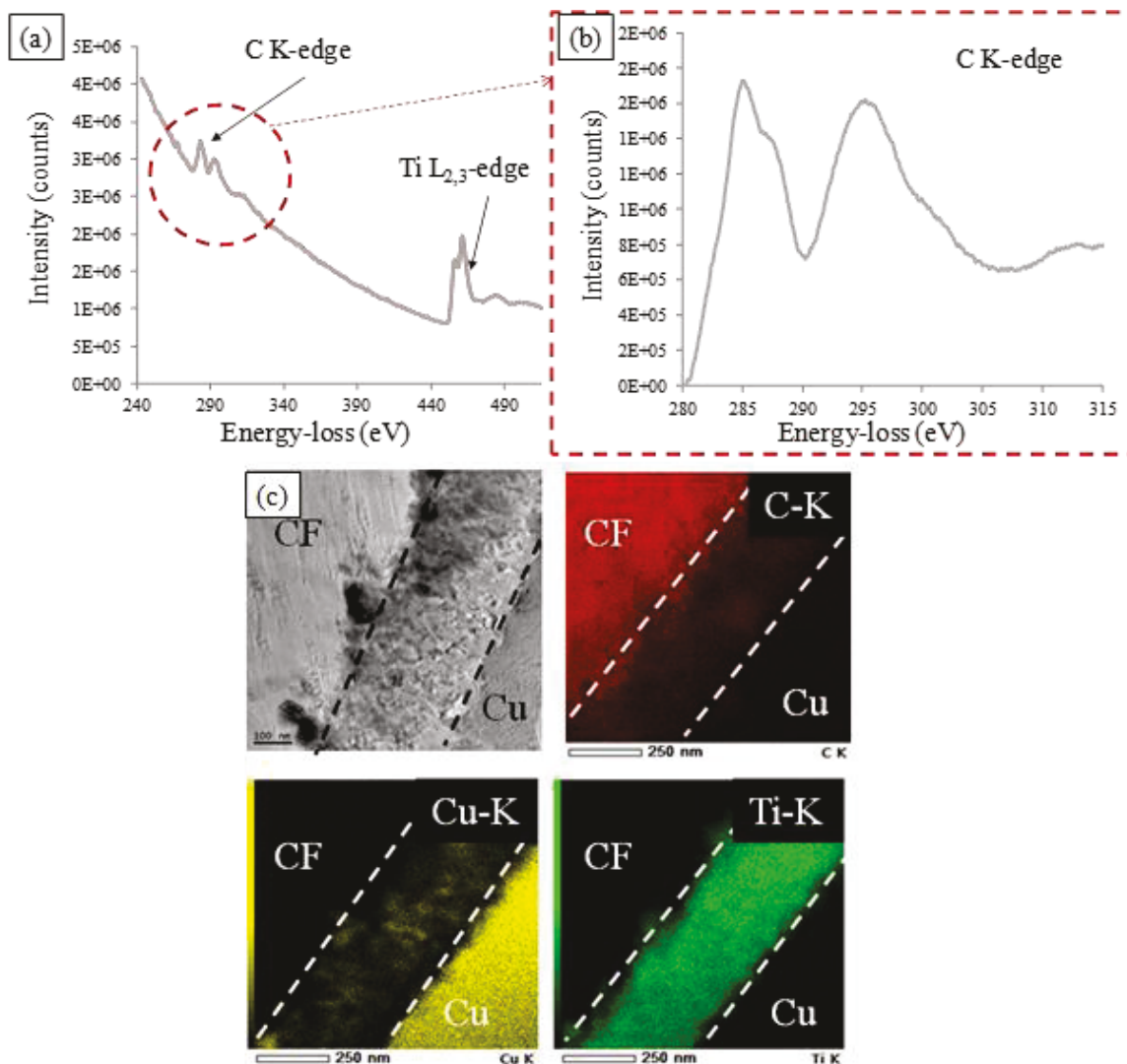


Figure 3.28. (a) EELS spectrum collected between 240 and 515 eV in the interphase area of the Cu(CuTi)4/CF10 sample, (b) ELNES at the C K-edge, (c) TEM bright field micrograph (left) and corresponding EDX map at the C-K edge (red), Cu-K edge (yellow), and Ti-K edge (green).

As shown in Figure 3.29, Cu (black line) was indeed present in the interfacial region but in a very small concentration, which explains the poor signal-to-noise ratio (SNR). Given that the transition metal (TM) $L_{2,3}$ edge reflects the TM d -band filling, it was very sensitive to the valence of the considered element. The Cu edge recorded in the interphase region was compared to reference spectra recorded in Cu, Cu_2O , and CuO samples [73]. In

addition to confirming the presence of Cu, the comparisons provided in Figure 3.29 indicate that the Cu in the interphase region was in a rather metallic state.

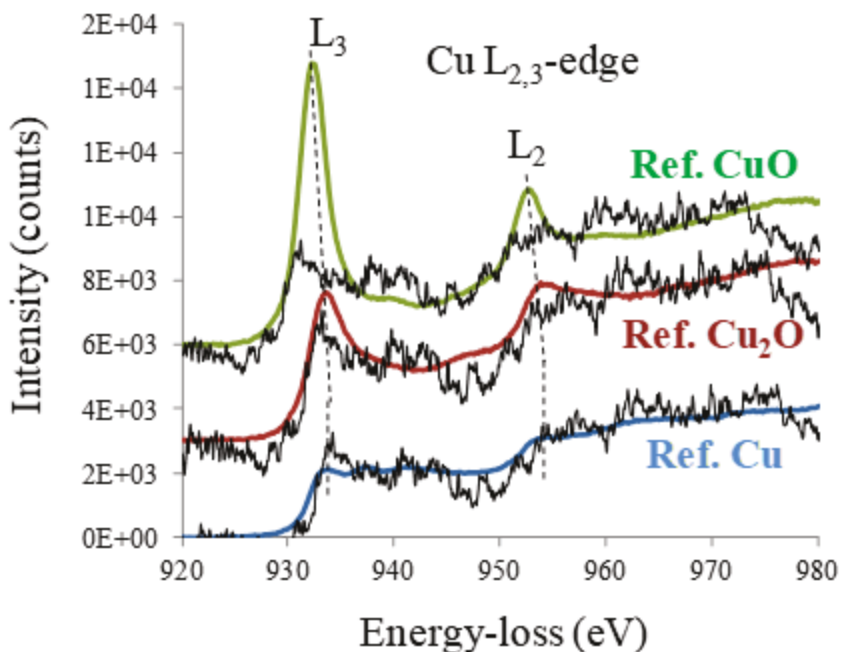


Figure 3.29: ELNES at the Cu L_{2,3} edge. The Cu edge recorded in the sample (black line) is compared to reference spectra obtained on Cu (blue line), Cu₂O (red line), and CuO (green line), which were taken from [27]. For the sake of clarity, the reference spectra were vertically shifted; and the energy of the Cu edge onset was adjusted to that of the reference spectra.

3.3.3 Cu(Cu-Zr)/C Composite Materials

The Cu-Zr volume fractions, atomic fractions, and the Cu:Cu-Zr:C ratios are given in Table 3.10. The volume fractions of the Zr-based alloy were varied between 8 and 16 vol%.

Table 3.10. Atomic fractions and ratios of Cu, Cu-Zr, and C in the composite materials for each volume fraction of Cu-Zr.

Vol % of Cu-Zr	At. %	Cu : Cu-Zr : C ratios
----------------	-------	-----------------------

	Cu	Cu-Zr	C	
8	0.466	0.067	0.467	7:1:7
10	0.449	0.084	0.467	5:1:6
12	0.431	0.101	0.468	4:1:5
14	0.414	0.118	0.468	4:1:4
16	0.396	0.135	0.469	3:1:3

The microstructure of the composites was characterized using SEM. The samples were coated in resin and polished using SiC sandpapers and diamond pastes prior to SEM observations. Figure 3.30 gathers the SEM micrographs of $\text{Cu}(\text{Cu-Zr})_x/\text{CF40}$ composites with (a), (b) 14, and (c) 20 vol% of Cu-Zr powders. Contrary to what was observed on the $\text{Cu}(\text{Cu-Ti})_x/\text{CF}$ composites, no chemical contrast, other than that corresponding to carbon and copper, has been identified. This would indicate the absence of a ZrC interphase or a thickness of interphase which is too small to be observed using SEM.

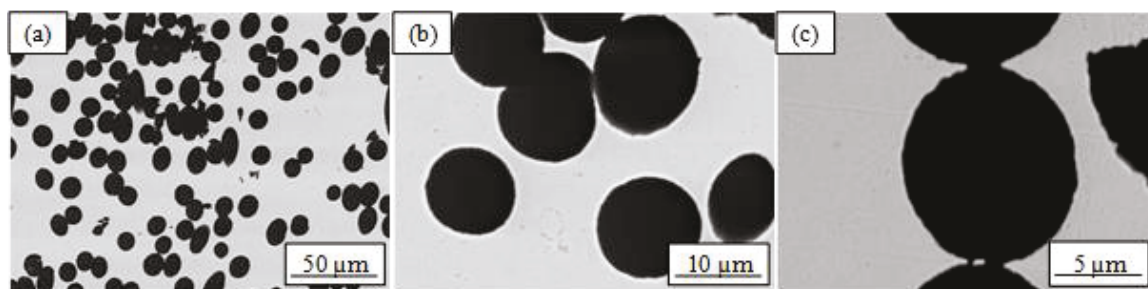


Figure 3.30. SEM micrographs in BSE mode of

$\text{Cu}(\text{Cu-Zr})_x/\text{CF40}$, with (a), (b) 14, and (c) 20 vol% of Cu-Zr alloyed powders.

EDS line-scans have been carried out to verify the presence of Zr close to the Cu-C interface. As can be seen in Figure 3.31, Zr has been detected on either side of the CF, while very little signal has been observed inside the Cu matrix.

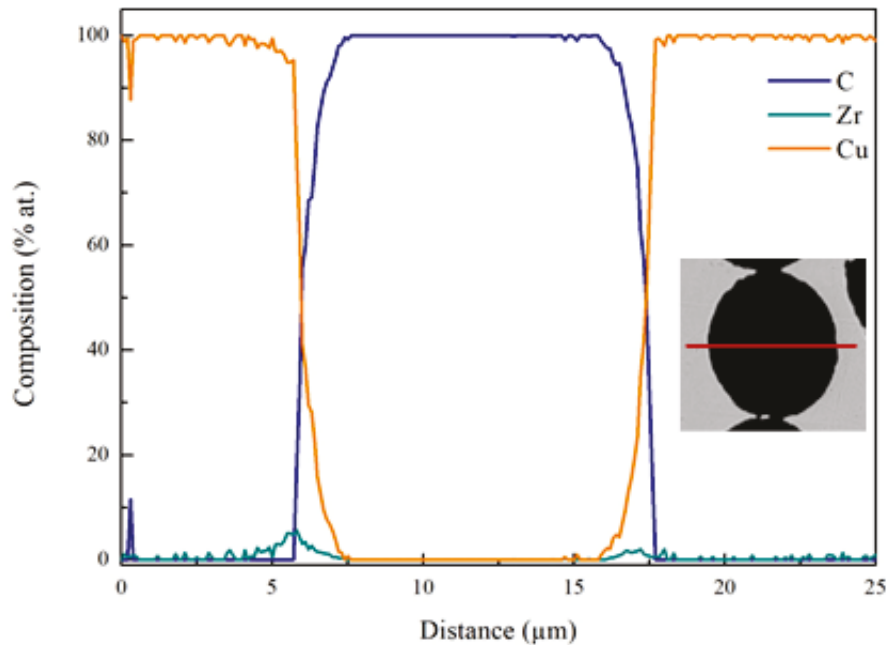


Figure 3.31. EDS line scan obtained through the cross-section of a CF coated with a Zr-based interphase inside the Cu matrix.

Chemical etching of the composite was carried out using a diluted nitric acid (HNO_3) solution. The aim of the chemical etching was to dissolve the Cu matrix on the surface and allow the observation of the ZrC interphase which was detected through the EDS line scan. Figure 3.32 shows a micrograph of a $\text{Cu}(\text{Cu-Zr})_{20}/\text{CF}_{40}$ composite after chemical etching for 2 min. One can observe the interphase surrounding the carbon fibers which appear to be slightly textured.

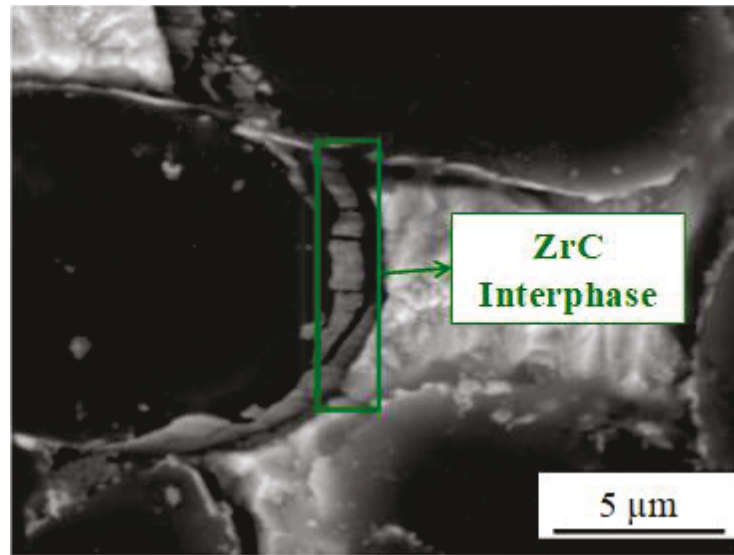


Figure 3.32: SEM micrograph in BSE mode of a $\text{Cu}(\text{Cu-Zr})_{20}/\text{CF40}$ composite after chemical etching of 2 min in diluted HNO_3 .

The identification of the interphase was confirmed through high quality XRD analyses, shown in Figure 3.33. The characteristic peaks of FCC ZrC appear between 33° and 39° as well as between 55° and 70° . Structural refinements have allowed the experimental lattice parameter of the Cu matrix to be determined and conclude in the presence of a solid solution of Zr in Cu.

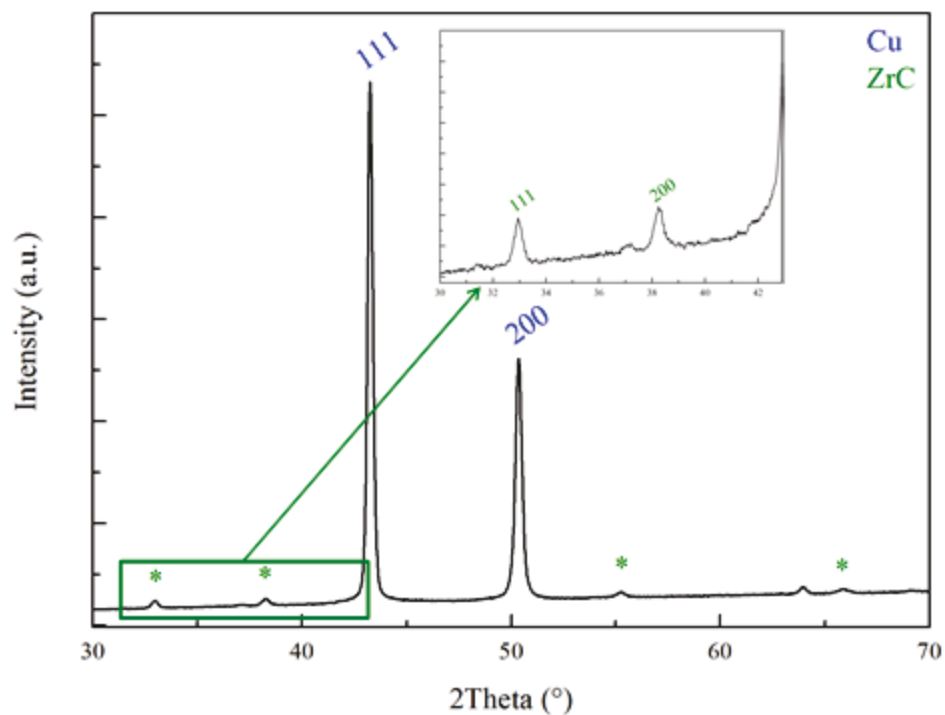


Figure 3.33: High quality XRD pattern obtained from a Cu(Cu-Zr)₁₂/CF₄₀ composite in a 2Theta range of 30 to 70°.

The theoretical [87] and measured Cu lattice parameters (Bragg R-factor of 0.778) are listed in **Table 3.11**. The increase of the Cu lattice parameter confirms the presence of a solid solution of Zr in Cu. This was expected since the Zr atoms are larger than the Cu atoms, which can increase the difficulty of the Zr diffusion within the Cu lattice.

Table 3.11: Theoretical and calculated Cu lattice parameters of Cu(Cu-Zr)₁₄/CF₄₀.

	a	b	c
Theoretical lattice parameters (Å)	3.615	3.615	3.615
Calculated lattice parameters (Å)	3.6362(3)	3.6362(3)	3.6362(3)

Transmission electron microscopy analyses allowed the interphase to be observed and indexed as ZrC. Figure 3.34(a) and (b) show representative TEM micrographs of a

Cu(Cu-Zr)₁₄/CF40 composite. The thickness of the interphase was measured and ranged between 100 and 125 nm. The microstructure of the interphase appears to be columnar, with approximately 40 nm large monocrystalline grains. As with the Cu(Cu-Ti)_x/CF composites, no debonding was observed between either the interphase and the matrix or the interphase and the CF, which indicates the presence of a strong bond between the constituents. Figure 3.34(c) shows the diffraction patterns observed in the interfacial zone. One can observe a lack of rings, which indicates that the polycrystallinity of the ZrC was not as strong as for Ti. Figure 3.34(d) shows the diffraction pattern of an area where both the interphase and the Cu matrix are present. The ZrC spots obtained in the previous pattern were confirmed and differentiated from those of Cu.

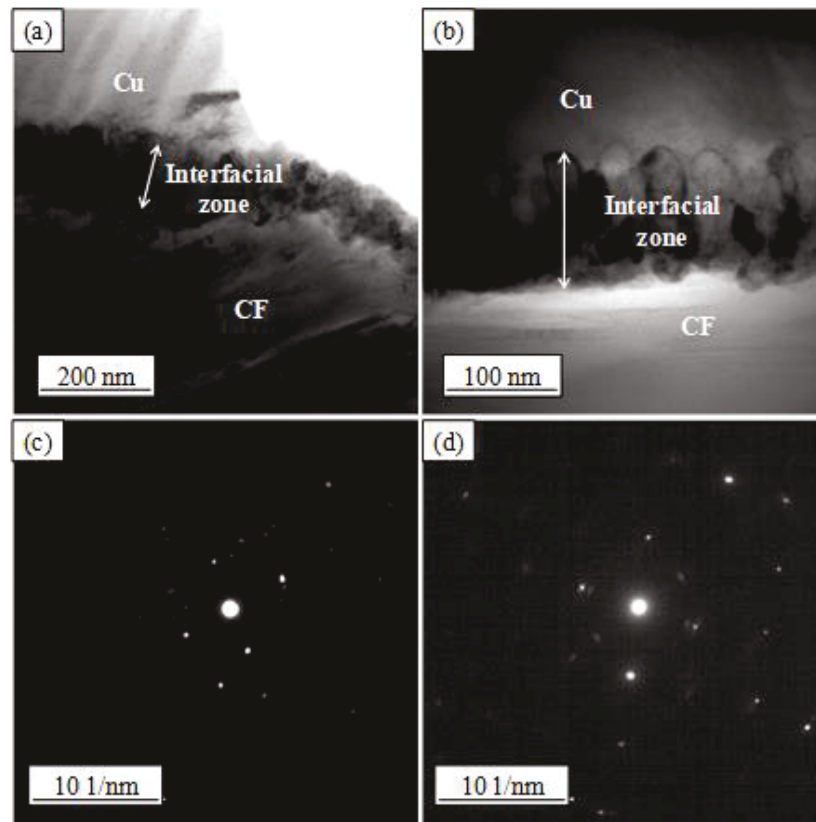


Figure 3.34: Transmission electron micrographs of Cu(Cu-Zr)₁₄/CF₄₀ composite material. (a) Overall view of a CF, the interfacial zone, and the Cu matrix and (b) higher magnification of a similar zone. Electron diffraction patterns of (c) the interfacial zone and (d) an area where both the interfacial zone and the Cu matrix are present.

3.3.4 Diamond-Based Composite Materials

While CF reinforcements have allowed composite materials to be characterized, the main objective of this investigation was to form thermally efficient composite materials. Although CFs showed high thermal conductivities along their axes, the optimum carbon form for high thermal conductivity is diamond. Therefore, diamond composites were synthesized using Cu-Ti and Cu-Zr alloyed powders. The volume fractions of the alloyed powders were set to 4 vol% of Cu-Ti and 14 vol% of Cu-Zr, while the diamond content was fixed at 40 vol%. To be able to observe the microstructure of the composites,

cryofractures were carried out in liquid nitrogen. For the sake of comparison, a Cu/D40 composite material was also synthesized and observed using SEM.

Figure 3.35 gathers the SEM micrographs obtained after cryofracture of the Cu/D40 ((a)-(c)), Cu(Cu-Ti)4/D40 ((d)-(f)), and Cu(Cu-Zr)14/D40 ((g)-(i)) composites. The first observation made for the Cu/D40 composite was the lack of cohesion between the Cu matrix and the diamond reinforcements. This was due to the lack of chemical affinity between the constituents. One can clearly see that the shock induced by the cryofracture caused a certain amount of diamond particles to detach from the matrix, leaving traces of their positions. The few diamond particles which remained attached were surrounded by air (voids), which can clearly be seen in Figure 3.35(c). However, the composite materials synthesized with either Cu-Ti or Cu-Zr exhibited a completely different behavior when under harsh mechanical solicitation, such as cryofracture. One can observe that instead of detaching, the diamond particles broke and remained in the matrix. Higher magnifications show that the diamonds were split along a certain plan which indicates that the rupture was fragile.

Since a material is never perfect, defects and weak points are always present. Under mechanical solicitation, these defects will cause the creation of cracks in the material which will be able to propagate [88]. In the case of composite materials, and depending on the type of matrix-reinforcement bond present, the cracks will either be able to go around the reinforcement or go through it. In a composite material, which has weak matrix-reinforcement bonds, the cracks or the stress created by the solicitation of the material will not affect the reinforcement. This was observed with the Cu/D40 composite, where only mechanical gripping was involved. In the case of strong matrix-reinforcement bonds,

however, the cracks and/or stress will propagate through the composite as if it was a homogeneous material. This is the case of the Cu(Cu-Ti)/D40 and Cu(Cu-Zr)/D40 composite materials. Finally, while the interphase is still not visible in the composite containing Zr, the TiC interphase is visible and can be seen in Figure 3.35(f).

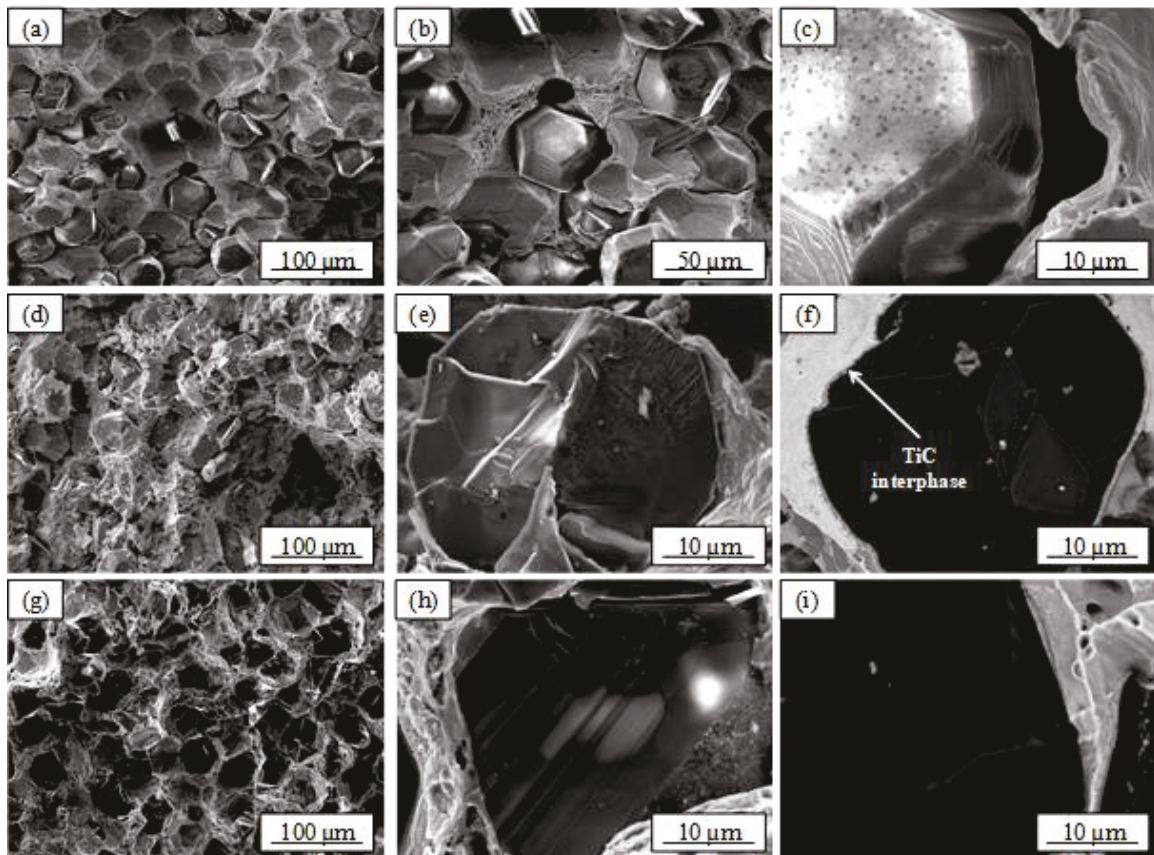


Figure 3.35: Scanning electron micrographs of fracture surfaces of (a)-(c) Cu/D, (d)-(f) Cu(Cu-Ti)/D, and (g)-(i) Cu(Cu-Zr)/D composite materials.

3.4 Conclusion

To conclude this chapter, a new process was used to synthesize Cu/C composites by introducing a liquid phase during the sintering process. Thermodynamic investigations showed the viability of the Cu-Ti-C and Cu-Zr-C systems that were selected for this work. The thermodynamic simulations predicted a total reaction of the carbide forming element

and the creation of nearly stoichiometric TiC_x and ZrC_x . These predictions were confirmed for TiC using EELS.

Carbon fiber reinforcements were used to allow machining of the composites for easier characterization. The in situ creation of homogeneous TiC and ZrC interphases was observed and confirmed through different microstructural, structural, and chemical analyses. These carbide interphases were obtained at lower temperatures than those at which they are usually formed. Transmission electron microscopy analyses showed carbide microstructures in the form of nanograins for TiC and columns for ZrC.

The liquid phase was shown to help the purification of the Cu matrix, at high volume fractions of carbon, as it enhanced the diffusion of the carbide forming elements toward the carbon reinforcements. At low volume fractions (10 vol%), the driving force for Ti diffusion was smaller; therefore, some Ti remained in solid solution within the Cu matrix.

The presence of the liquid phase also allowed the relative densities of the composites to be increased for higher volume fractions of reinforcements, when compared to a simple Cu/C composite material. The thickness of the interphase depended on the Cu-X amount inserted in the composite. Indeed, increased amounts of Cu-X resulted in thicker interphases.

Finally, the creation of the carbides in diamond-reinforced composites was also confirmed. The presence of the interphases led to fragile diamond rupture, during cryo-fracture, which indicates that the bonds between the matrix, interphases, and reinforcements was strong. It is, therefore, expected that these interphases will enhance the thermal conductivity of the composite materials.

4. Combustion CVD of Diamond Films

4.1. Introduction

The objective of combustion chemical vapor deposition (CVD) in this research was to coat nondiamond substrates (copper/carbon (Cu/C) composites) with uniform and adherent diamond films. While several CVD processes exist, the combustion flame process was selected for this study because of its open-air operation, low cost, and fast deposition rate.

The research team at the Laser-Assisted Nano-Engineering laboratory (LANE) has successfully used laser-assisted vibrational excitation of precursor molecules to promote diamond growth quality and enhance the growth rate. The laser-assisted diamond growth discussed in T. Guillemet's Ph.D. thesis [5] was used for this research project. While previous studies have been carried out on tungsten carbide (WC) and silicon (Si) substrates, the innovation brought to the laser-assisted CVD process used at LANE is the effect of the surface of a nondiamond substrate and more precisely on copper/carbon (Cu/C) composites.

The benefit of having a diamond film on the surface of the improved composite heat-sink material has been proved through simulations carried out by Dr. Pierre-Marie Geffroy at Science des Procédés Céramiques et de Traitements de Surface (SPCTS) at the University of Limoges in France.

The impact of diamond films on heat dissipation allows the behavior of a diamond film on Cu/C composite surfaces to be predicted and is proof of their significance [89]. The temperature profiles of copper/carbon fiber (Cu/CF) 40 vol% substrates with and without

a diamond coating are reported in Figure 4.1(a) and (b), respectively. Several heat sources are integrated on the same heat sink. One can observe that the isovalue lines of the temperature are clearly shifted due to the planar heat spreading induced by the diamond coating, in the case of the diamond film/composite assembly. This planar heat spreading at the surface of the heat sink leads to an increase in the heat dissipation by conduction through the substrate but also by convection on the substrate surface close to the heat sources, in particular. The latter mode can have a large impact, especially when the heat source sizes are small and the substrate is thick.

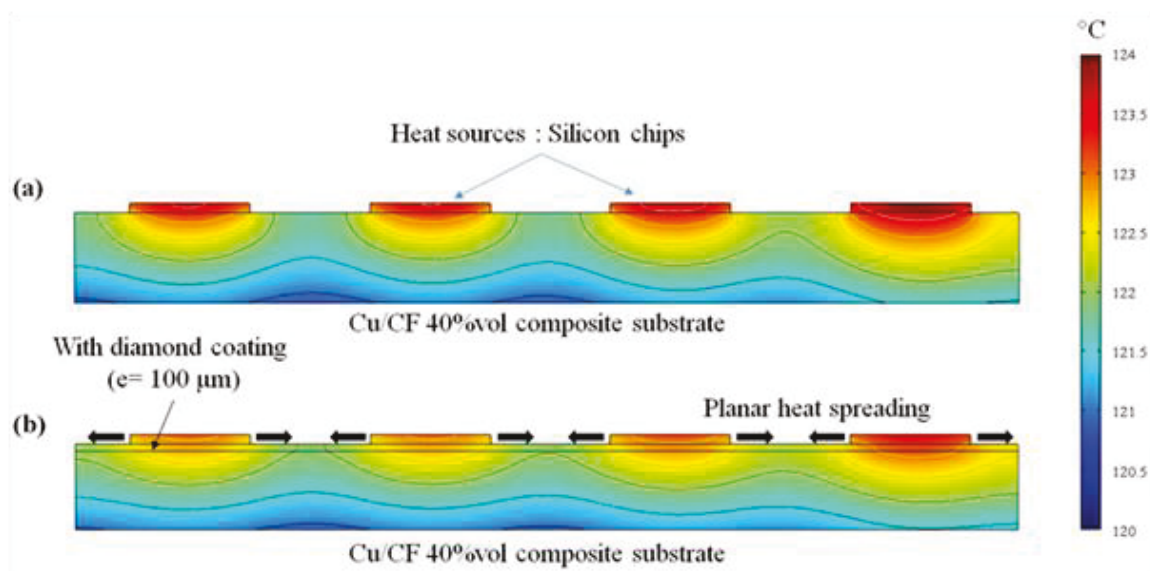


Figure 4.1. Simulation of heat dissipation in a Cu/CF 40 vol% substrate and a diamond film-Cu/CF 40 vol% substrate [89].

Therefore, the relevance of having a diamond film deposited on the surface of a heat sink device, is shown. In the previous chapter, the effect of reinforcement content on the thermal expansion coefficient (CTE) of composite materials, was discussed. In this chapter, the effect of the CTE and the surface morphology and/or chemistry on diamond

film adhesion will be demonstrated. Part of this research aimed to modify the surfaces by varying the geometries of the reinforcements to promote mechanical gripping.

This work was supervised by Pr. Yongfeng Lu of the Electrical and Computer Engineering Department at the University of Nebraska-Lincoln.

4.2. Combustion Synthesis of Diamond Films

4.2.1 Principle

Chemical vapor deposition diamond synthesis was developed and is used to deposit uniform polycrystalline diamond films on various substrates. While several types of CVD exist, the combustion flame process allows high growth rates and phase purity to be reached while maintaining flexibility in terms of setup and low cost. However, this process presents some disadvantages, such as thermal damages on the substrate material due to direct irradiation by the flame. Also, the deposition area is limited to the size/diameter of the flame. In fact, the flame geometry is an important factor in the combustion flame process. The flame used is typically a mixture of acetylene (C_2H_2) and oxygen (O_2) [90]; however, ethylene (C_2H_4) was also present in the gaseous precursor mixture in this study.

The oxyacetylene flame geometry is shown in Figure 4.2. One can observe three distinct zones: the inner flame, the acetylene feather, where the diamond deposition takes place, and the outer diffusion flame. The geometry of the flame is mainly influenced by the oxygen-to-hydrocarbons ratio ($O_2: C_xH_y$). This ratio also affects the growth rate and the quality of the diamond film deposited. For example, a ratio of 1 corresponds to a neutral flame where the acetylene feather disappears as all of the acetylene is consumed in the inner flame. The highest purity diamond has been obtained from hydrocarbon-rich flames which correspond to a ratio between 0.5 and 1.

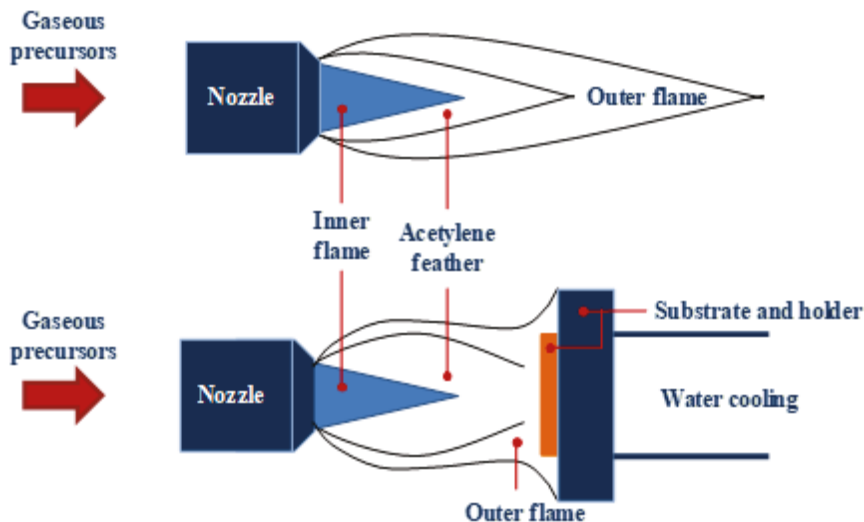


Figure 4.2. Schematic view of the oxyacetylene combustion flame geometry.

The combustion of the oxyacetylene flame takes place in two steps:

Step n°1: Oxygen and acetylene burn in the inner flame. The oxygen combines with carbon to produce carbon monoxide while the remaining hydrogen is liberated.



Step n°2: Due to the exothermic nature of the reaction Eq. (4.1), the flame temperature can rise up to 3000 K. High temperatures can affect the liberated hydrogen (H_2) by dissociating it into atomic hydrogen.



The dissociation of H_2 enhances the amount of H available in the feather region where diamond deposition is expected. A small part of the acetylene is also transformed into radicals, $\text{CH}_3\cdot$ for example. These hydrocarbon radicals lead to the incorporation of carbon species onto the growth surface. Other species, such as C_2 and $\text{CH}\cdot$ are assumed to take part in the reaction by selectively etching the hydrogen bonded to the surface and stabilizing sp^3 carbon bonds.

Another critical parameter of combustion flame CVD is the substrate temperature. The optimum temperature for diamond formation not only depends on the torch design but also on the nature of the substrate. Earlier studies carried out by Guillemet et al. showed that the substrate temperature for diamond formation on Si [91,92] and WC [93–96] substrates ranges between 760 and 780 °C, while preliminary tests during this research reported that the optimum temperature for diamond formation on Cu-based materials ranges between 700 and 740 °C [89].

Monitoring the temperature becomes challenging as extreme heat fluxes are constantly present. Therefore, the temperature is measured through either optical pyrometry or by thermocouples. In the case of optical pyrometry, a good approximation of the overall temperature is given; however, the local temperature cannot be determined. Also, in the case of a thin substrate, the measure becomes even more difficult as the pyrometer averages the temperature of the substrate and that of the water-cooled stage. The thermocouples are usually placed on the backside of the substrate. While the measurement is precise locally, it does not correspond to the real temperature. In fact, the substrate undergoes heat gradients, where the hottest place is the top surface and the coolest the backside. Therefore, thermocouples often underestimate substrate temperature.

While substrate temperature has an effect on diamond growth rate, it also drastically affects the diamond film morphology. Increasing growth rates are obtained for higher temperatures. However, the optimization of the growth rate reaches a maximum at a given temperature, after which the growth rate and the diamond film quality decrease. Quality is supposed to be impacted by oxidation and/or graphitization of the diamond surface at high temperatures in the presence of O₂. Depending on the substrate temperature, the film

morphology is usually dominated by $\{111\}$ and $\{100\}$ facets due to the lower growth rate relative to $\{110\}$ facets. The increase of substrate temperatures tends to promote growth along the $\langle 111 \rangle$ direction, thereby exposing $\{100\}$ square-shaped facets. The temperature at which $\{100\}$ facets are observed corresponds to a temperature where maximum growth rate is attained. The triangular-shaped $\{111\}$ facets are usually observed at intermediate temperatures. Therefore, as temperature increases, the diamond crystals' morphology changes from octahedron to cubic. The morphology can be determined using the $\{100\}$ to $\{111\}$ facet normal velocity ratio, which is given by Eq. (4.3) [97]. The facet growth velocity ratio is given by:

$$\alpha = \sqrt{3} \frac{V_{001}}{V_{111}} \quad (4.3)$$

where α is the facet growth velocity ratio, and V_{001} and V_{111} are the normal facet velocity of (100) and (111) facets. The evolution of diamond crystal morphology, or kinetic Wulff shapes, with respect to increasing the facet growth velocity ratio, is given in Figure 4.3 [98].

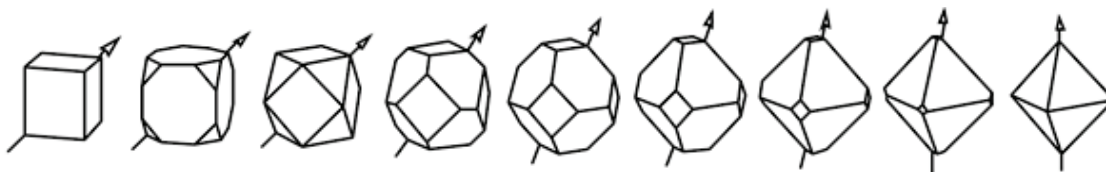


Figure 4.3. Evolution of diamond crystal morphology as a function of the facet growth velocity ratio. From left to right, α increases from 1 (cubic) to 3 (octahedron) with a step of 0.25. The arrows indicate the fastest growth direction [98].

4.2.1.1 Experimental Setup

The diamond deposition schematic setup is shown in Figure 4.4. The combustion torch, with a diameter of 1.5 mm, delivers a gas mixture of acetylene (C_2H_2 , 99.999%),

ethylene (C_2H_4 , 99.6%), and oxygen (O_2 , 99.996%) with a volume ratio of 1:1:2 respectively (620:620:1200 standard cube centimeters (sccm)). The distance between the inner flame cone and the top of the substrate was maintained at 1.5 mm. The substrates were positioned using an X-Y-Z moving stage. A cooling system, below the stage, was used to regulate the deposition temperature, kept between 700 and 740 °C. The substrate temperature was monitored using an infrared pyrometer (OS3752, Omega Engineering, Inc.).

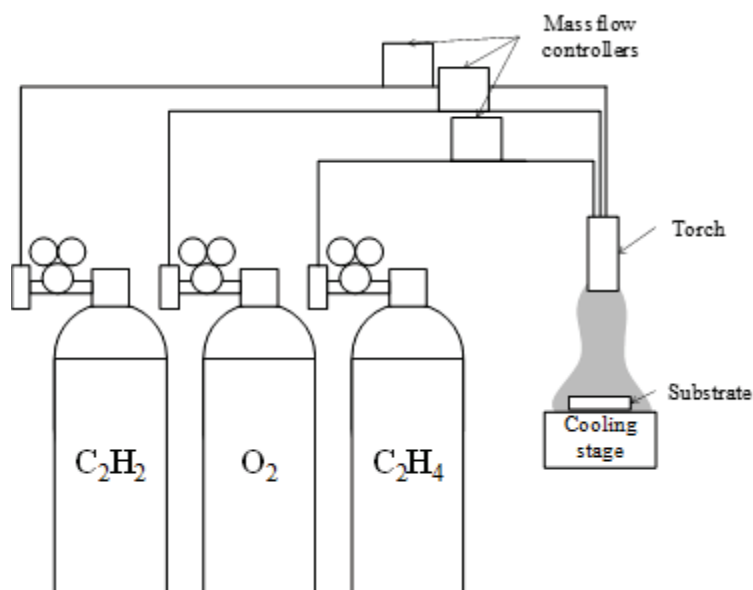


Figure 4.4. Schematic diagram of the diamond deposition setup.

Diamond films were deposited on Cu/CF composite materials which were synthesized at Institute of Condensed Matter Chemistry of Bordeaux (ICMCB). The composite materials consisted of a copper matrix and short carbon fiber (CF) reinforcements. The CFs (K223HM, CTN DIALEAD/BOBBINS, Sumitomo Corporation Europe) are preground to an average length of 200 μm . Dendritic copper powders (Ecka Granulate Velden GmbH) (d_{50} close to 35 μm) were used as the matrix material. The

sintering of the composite materials was carried out using a Termolab press. The powders were mixed and compacted in a steel mold heated by an induction system. The powders were pressed at 650 °C under 40 MPa for 30 min. The temperature was controlled with the use of a thermocouple which was inserted into the steel mold. The chamber was put under vacuum (10^{-2} mbar range) to prevent the oxidation of the copper matrix during heating and/or cooling. Composites with 10%, 20%, 30%, 40%, and 50% volume fractions of CFs were densified. The final porosities observed were inferior to 4% for 10 to 40% CF and 7% for 50%. Furthermore, the CFs showed no specific degradation. The final outcome was pellets 40 mm in diameter and 2 mm in thickness. The pellets of the composites, up to 40% volume fraction of CFs, were then cut into $6 \times 6 \times 2$ mm³ pieces using an ISOMET™ 1000 precision saw. The substrates were then manually polished using silicon carbide (SiC) sandpaper.

4.3. Diamond Growth on Cu/C Composite Materials

4.3.1. First Instance of Diamond Deposition

In order to visualize and predict the nucleation and growth processes of the diamond films on Cu/CF composite substrates, diamond depositions of 2, 5, and 15 min were carried out on Cu/CF 40 vol% composites. Figure 4.5 shows the evolution of a Cu/CF40 vol% composite surface before and after 2, 5, and 15 min of diamond deposition. The initial surface shows the preferential orientation of the fibers, which is perpendicular to the compression axis leading to a random distribution of CFs in that plane (Figure 4.5, (a)). Naturally engineered surfaces occur because combustion CVD is operated in open air and at high temperature, which results in the consumption of the exposed CFs. In fact, operating in open air and at a high concentration of O₂ causes the CFs to burn and leave fiber-shaped

voids on the surface. It is important to note that CFs are consumed in the exposure of the combustion flame. The consumption of the CFs started after 2 min (Figure 4.5, (b)) of diamond deposition. By 5 min (Figure 4.5, (c)), the fibers were completely consumed, leaving fiber-shaped voids. By the end of the 15 min diamond deposition (Figure 4.5, (d)), a mixture of sp^2 and sp^3 carbon was observed on the surface with a predominance of sp^2 carbon. The predominance of sp^2 carbon was confirmed through Raman analyses carried out on the cross-sections of the diamond films, close to the Cu/CF-diamond interface.

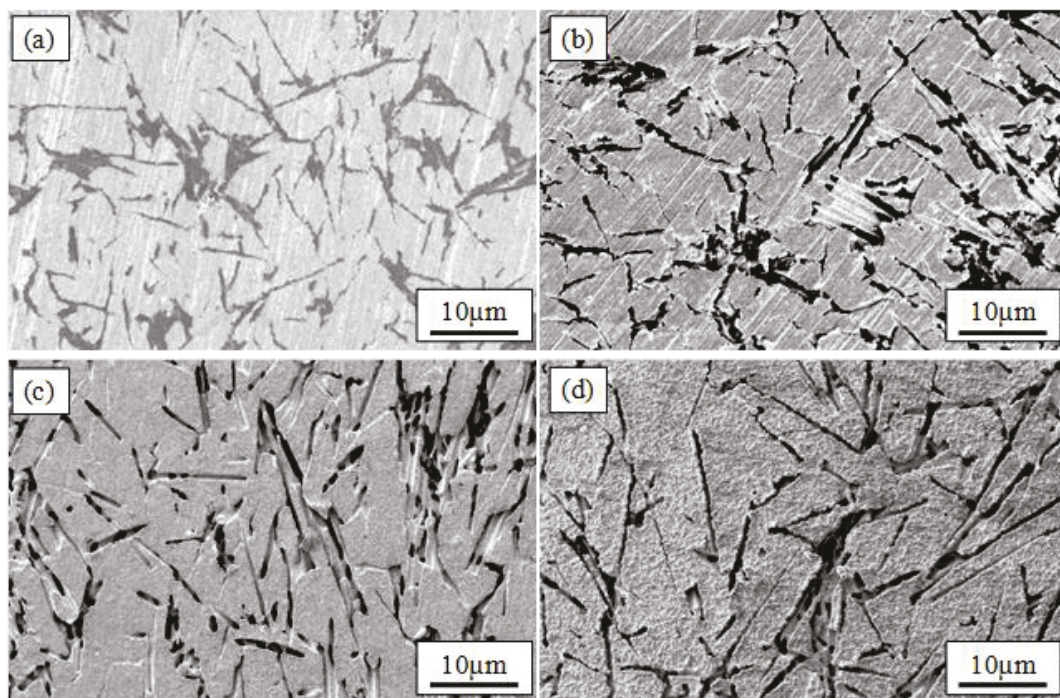


Figure 4.5. Cu/CF 40 vol% surface (a) before diamond deposition, (b) after 2 min, (c) after 5 min, and (d) after 15 min of diamond deposition.

Depending on the depth at which the CFs are situated, with respect to the surface (maximum 10 μm), the voids will be either open or closed, as seen in Figure 4.6. Such voids can act as mechanical gripping sites of the diamond film on the composite substrates [96,99].

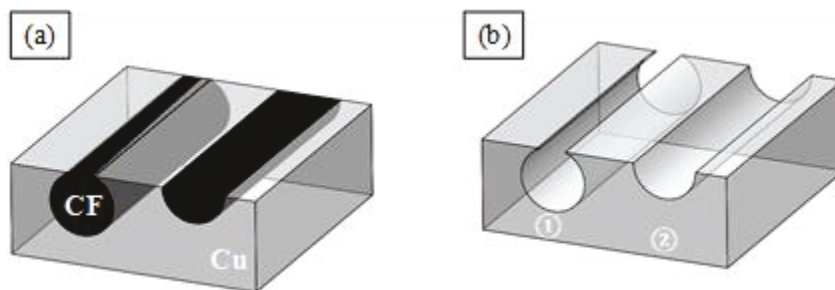


Figure 4.6. Schematic views of the initial surface and the voids left on the surface after the CF consumption. (a) Before diamond deposition, (b) ① closed void (the gap of the void is sufficiently small to trap deposited carbon), and (b) ② open void (the gap of the void is large enough that it cannot trap carbon), after diamond deposition.

Longer diamond depositions were carried out on 10 %, 20 %, 30% and 40%vol Cu/CF composites until a detachment of the diamond film was observed. The diamond films easily peeled off from the low CF content composites and remained attached on the surface of the high content in CF composites (Cu/CF 40 vol%). Scanning electron micrographs of the surface of a Cu/CF 20 vol% composite and the bottom face of a peeled-off diamond film are shown in Figure 4.7 (a) and (b), respectively. The micrographs confirm the initial growth of a diamond-like carbon film, as shown in one of our earlier studies [100], and show protrusions of ball-like carbon that extend from the surface. The presence of ball-like carbon inside the voids on the upper surface of the composites confirms the initial growth of carbon within the voids and, therefore, the enhancement of mechanical gripping.

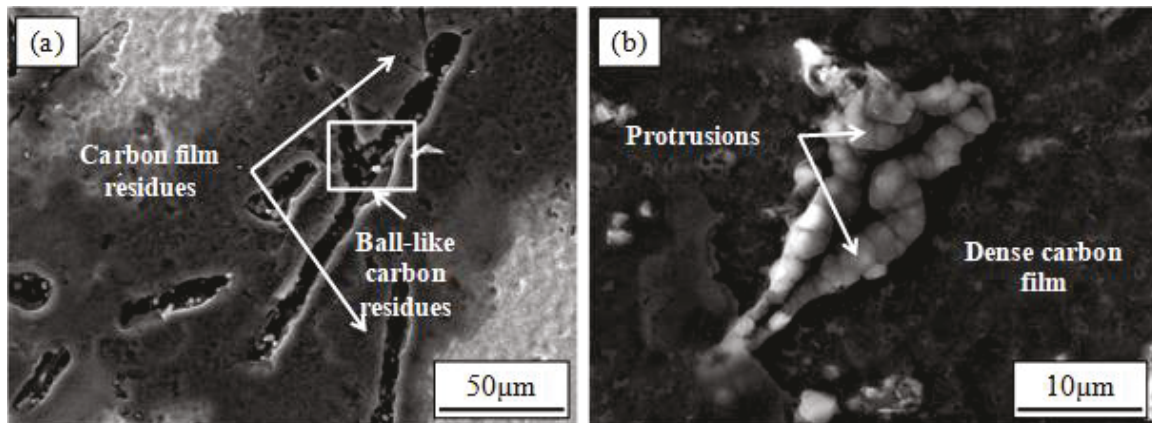


Figure 4.7. SEM micrographs of (a) the surface of a Cu/CF 20 vol% composite after diamond film peel-off and (b) the bottom face of diamond film with ball-like carbon protrusions.

The SEM micrographs in Figure 4.8 demonstrate that the nucleation and growth process of the diamond films grown using the CVD combustion process follow the Volmer-Weber mode [101]. After an incubation period, the nucleation of germs starts in the voids created by the consumption of the CFs and then moves onto the top surface (Cu matrix). These germs grow in three dimensions and finally coalesce to form a dense film. Variations in substrate temperatures during the first stages of deposition can affect the crystallinity of the carbon being deposited and would explain the presence of ball-like carbon within some voids.

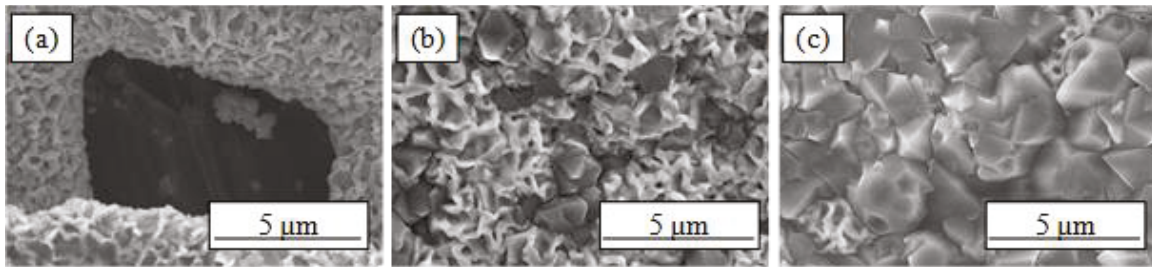


Figure 4.8. SEM micrographs showing the early stages of diamond deposition in the matrix region. (a) Creation of diamond nuclei in the voids (after 5 min deposition), (b) creation of diamond nuclei on the top surface (after 10 min deposition), and (c) diamond crystal coalescence (after 15 min deposition).

It has been noted that the substrate temperature critically affects the crystallinity of the deposited film. Previous studies have shown that the optimum substrate temperature ranges for diamond deposition on silicon and tungsten carbide substrates is between 760 and 780 °C [102]. However, this range does not allow diamond film deposition on copper-based substrates. The SEM micrographs in Figure 4.9 show the effect of temperature on diamond film deposition. The optimum temperature range is between 720 and 755 °C, as higher and lower temperatures result in nondiamond films. The SEM micrograph corresponding to the diamond deposition at 720°C shows randomly oriented diamond crystals with a predominance of {111} triangular faces. This indicates that growth along the <100> direction was faster. In the next section, one can notice that {100} textures are obtained for depositions at temperatures situated at 740 °C, which indicates how narrow the temperature window is for controlled textures of diamond films.

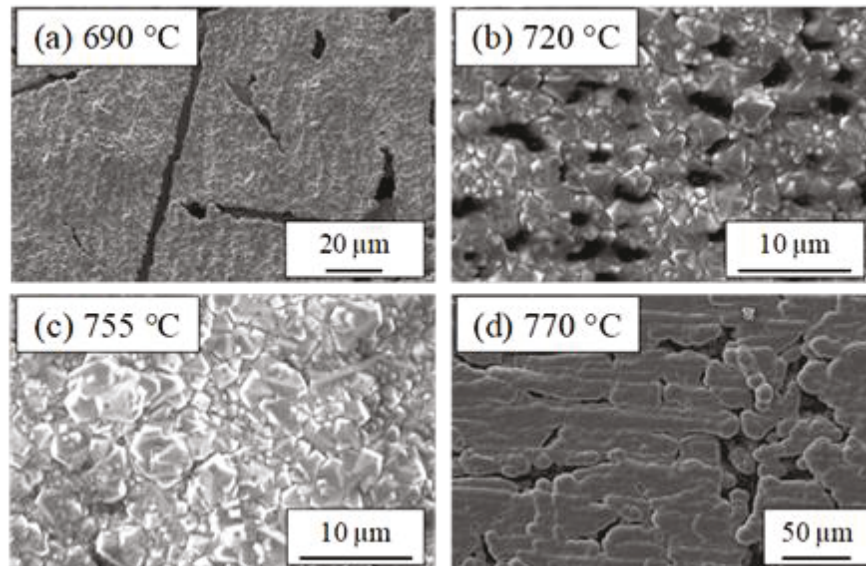


Figure 4.9. SEM micrographs of films deposited on Cu/CF composites after 30 min of deposition at various temperatures. (a) 690 °C, no diamond presence, (b) 720°C, randomly oriented diamond crystals, (c) 755 °C, randomly oriented diamond crystals, and (d) 770 °C, amorphous carbon.

4.3.2. Diamond Film Microstructure

Diamond films were deposited on Cu and composite surfaces as circular spots of 5–10 mm. The combustion flame deposition enabled the deposition of resisting diamond films depending on the different volume fractions of CFs. Attempts to maintain the substrate temperatures at 740 °C were made difficult by the heat fluxes and thermal inertia of the water-cooled stage and hot spots on the surface of the composite substrates caused by the CF consumption. Diamond depositions were carried out ranging between 710 and 750 °C.

Diamond depositions of 30 min were carried out on substrates of pure Cu and Cu/CF composites of 10, 20, 30, and 40 vol% in CFs. Figure 4.10 shows how the diamond films behaved after they were removed from under the combustion flame. The diamond

film deposited on the pure Cu substrate (Figure 4.10(a)) peeled off completely and instantly. The SEM micrograph corresponds to a part of the free-standing diamond film obtained. The diamond films deposited on the Cu/CF composites with CF contents of 10 to 30 vol% have all cracked and parts have peeled off as soon as the substrate was taken from under the flame. In contrast, the diamond films deposited on Cu/CF 40 vol% composites remain attached and uncracked. The adhesion of the films is explained by both the decreased CTE of the Cu/CF 40% composite and the large amounts of fiber-shaped voids on the surface. In fact, the composites, with 40 vol% of CFs, indicate the presence of a larger amount of fibers exposed on the surface when compared to composites with lower CF contents.

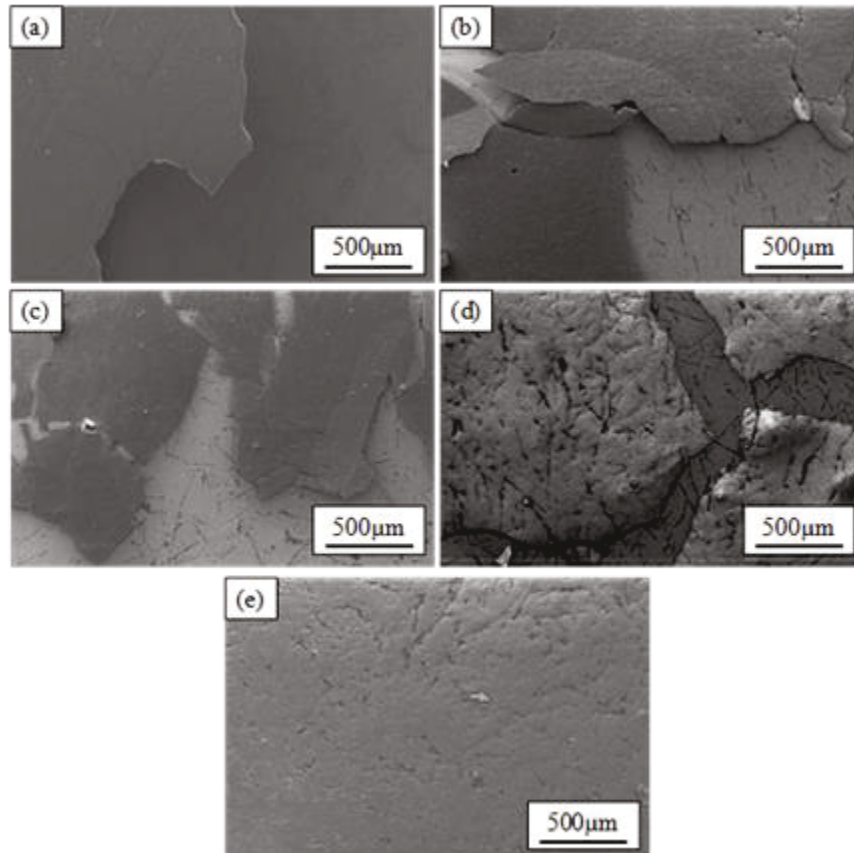


Figure 4.10. SEM micrographs of diamond films after diamond depositions of 30 min.

(a) Cu, (b) Cu/CF 10 vol%, (c) Cu/CF 20 vol%, (d) Cu/CF 30 vol%, and
(e) Cu/CF 40 vol% substrate.

From this section on, the diamond depositions presented were carried out on Cu/CF 40 vol% composites.

4.3.2.1 Top Surface Microstructure

Diamond depositions of several durations were carried out. The films obtained were dense and polycrystalline and mainly consisted of randomly oriented diamond crystals (Figure 4.11). As mentioned previously, the exposed facets have a strong dependence on the substrate temperature. It has been shown that temperatures of 730–740 °C promote the growth of the crystals along the $\langle 111 \rangle$ direction, exposing $\{100\}$ faces. That is the case

for the diamond films obtained after 30, 60, 180, and 240 min depositions, for which the deposition temperatures varied between 730 and 750 °C. The remaining diamond films were deposited at an average substrate temperature of 710 °C. All depositions were successful in terms of adhesion and homogeneity.

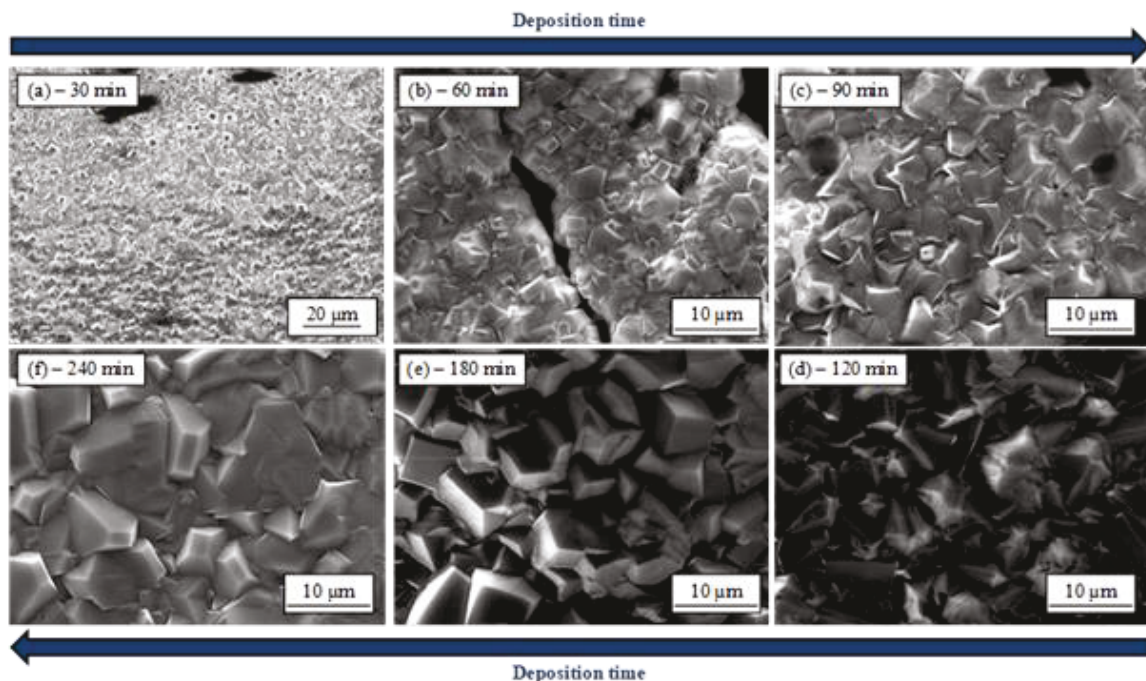


Figure 4.11. SEM micrographs of diamond films deposited on Cu/CF 40 vol% composite substrates for (a) 30, (b) 60, (c) 90, (d) 120, (e) 180, and (f) 240 min.

4.3.2.2 Cross-Section Microstructure

The cross-sections of the diamond films were obtained using ion polishing. Since the diamond deposited was polycrystalline and brittle, it did not respond well to traditional polishing treatments. In fact, it either damaged the polishing disks or peeled off. To avoid these problems, ion polishing was considered and carried out. The cross-section polisher apparatus from Gatan (cross-section polisher Ilion+ II System) for SEM cross-section observations, allowed polishing a section of the substrate by the means of ion

bombardment. Argon (Ar^+) ions were sent with a certain velocity on the copper/carbon fiber-diamond (Cu/CF-D) surface and ejected carbon and copper atoms. The final surface was polished to the atomic scale and allowed very clear observations of the polished sections.

According to the cross-sectional SEM micrographs of the deposited diamond films shown in Figure 4.12, the growth was columnar. This indicates that the majority of diamond crystals grew along the $\langle 111 \rangle$ direction, hence exposing $\{100\}$ faces on the surface, and that the facet velocity growth ratio was close to 1 [98]. The growth rates were calculated from the thicknesses given in Table 4.1 and are equivalent for all diamond films (approximately $0.12 \mu\text{m}/\text{min}$).

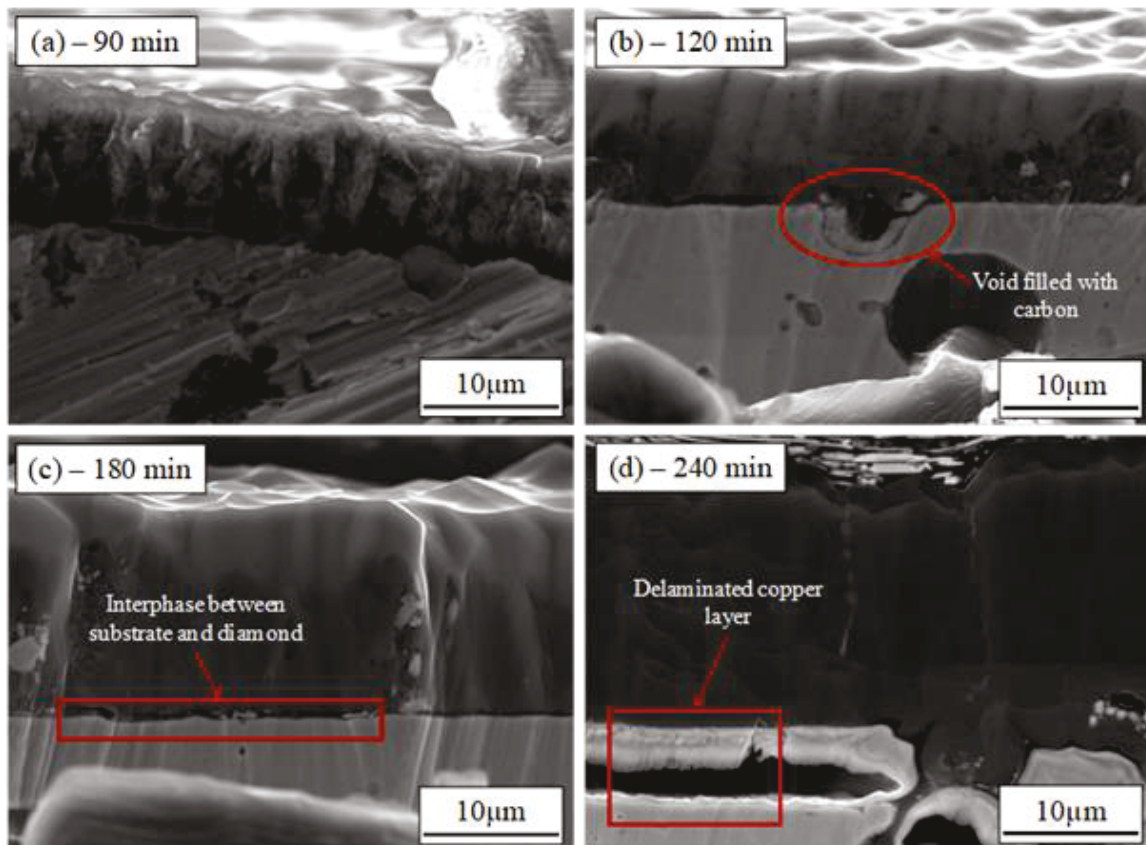


Figure 4.12. SEM micrographs of the cross-sections of diamond films deposited for (a) 90, (b) 120, (c) 180, and (d) 240 min.

Table 4.1. Diamond grain sizes and thicknesses with respect to deposition duration.

Deposition Time (min)	90	120	180	240
Film Thickness (μm)	9.39	16.74	22.38	25.41

From what was observed, the thickness increased with deposition time, which was expected. What is interesting to note is the lack of chemical affinity between copper and diamond when observing the polished cross-section, as shown on micrographs (a) and (b) in Figure 4.12. Depositions of 180 min show the presence of an interphase between the

composite and the diamond films, whereas 240 min depositions show the presence of a delaminated copper phase which appears to be chemically bonded to the diamond.

4.3.3. Diamond Film Phase Purity and Residual Stresses

Raman spectroscopy was used to quantify the phase purity and stress levels in the diamond films deposited. These are important parameters that need to be understood and optimized to integrate the CVD diamond films in functioning devices.

4.3.3.1 Raman Principle and Setup

Raman spectroscopy is a nondestructive characterization technique relying on inelastic photon scattering caused by the interaction of a monochromatic laser beam and matter. The frequency difference between the exciter and the scattered photons gives information on the chemical nature of the sample.

The Raman spectrum obtained can be analyzed in several ways in order to get the desired information:

- The position of the peaks is linked to the chemical species present in the sample.
- The full width half maximum (FWHM) is related to the structure of the sample.
- The intensity of the peaks can be linked to the concentration of the species.
- The shifting of peaks with respect to the theoretical position is linked to the stress levels.

Raman Principle. Spontaneous Raman spectroscopy was used to characterize the diamond films. A monochromatic beam produced by a continuous laser is focalized on the

sample to stimulate its vibrational modes. The majority of incident photons are either transmitted, reflected, or absorbed, while a lower fraction is scattered. The solid lattice is excited from the ground state to a virtual energy state by an incident photon. After relaxing from the virtual energy state, it will either emit a photon of the same energy as the incident one (Rayleigh scattering or elastic scattering) or emit a photon with a different energy (Raman scattering or inelastic scattering). The difference in energy of the emitted photons with respect to the incident ones causes the Raman shift. If the vibrational state of the lattice is higher in terms of energy than the initial state, the emitted photon will be shifted to a longer wavelength. This is known as Stokes Raman scattering. However, when the final vibrational state is lower in energy than the initial state, then the emitted photon will be shifted to shorter wavelengths. This is known as anti-Stokes Raman scattering (Figure 4.13, (a)).

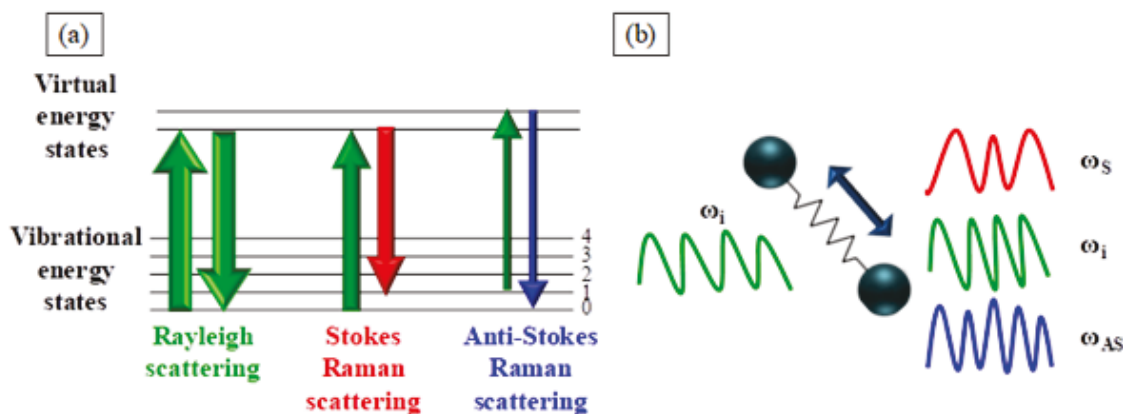


Figure 4.13. (a) Energy level diagram showing the states involved in Raman spectroscopy. The line thickness is representative of the signal strength. (b) Light-matter interaction processes in Raman spectroscopy.

Carbon materials are often characterized through the use of Raman spectroscopy as it is highly sensitive to symmetric covalent bonds with little or no natural dipole moment,

which constitute the carbon materials. Knowing that every peak and band in a Raman spectrum corresponds to a particular vibrational frequency of a bond within the material, it is possible to distinguish the type of C-C bonds that are characterized. The Raman spectrum of diamond is very simple and consists of a single peak (single vibrational frequency) situated at 1332 cm^{-1} (Figure 4.14). The presence of that one band is related to the C-C bonds in the tetrahedral crystal structure of diamond, which all have the same orientation and strength.

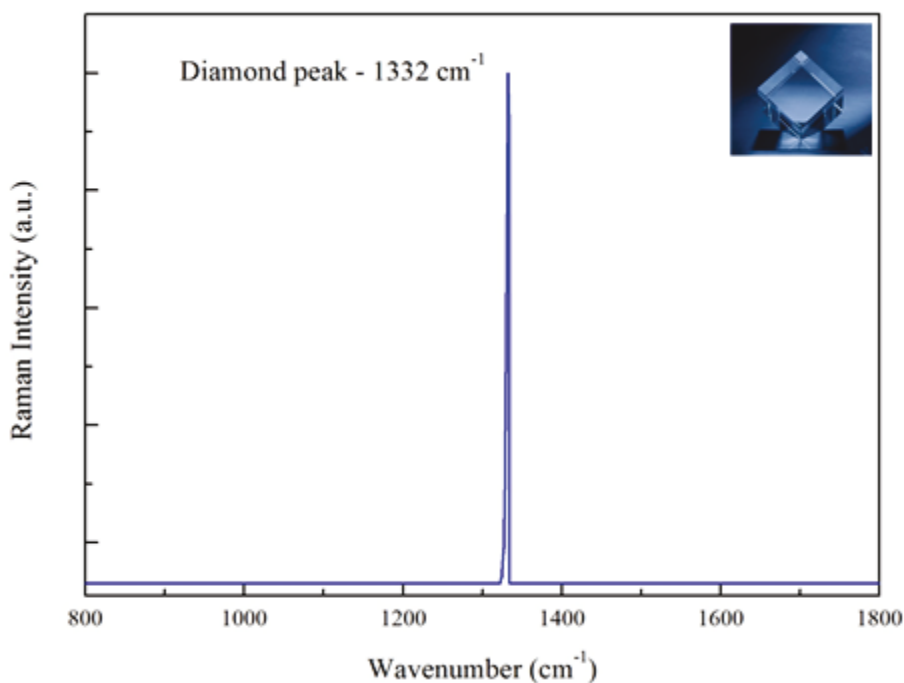


Figure 4.14. Typical Raman spectrum of diamond. Sharp peak at 1332 cm^{-1} .

In the case of diamond films deposited with combustion flame CVD, the Raman spectrum exhibits more bands that indicate the presence of nondiamond carbon in the films. A representative Raman spectrum of the diamond film deposited on a Cu/CF composite at $740\text{ }^{\circ}\text{C}$ is shown in Figure 4.15. Peaks appear at ~ 1332 , ~ 1375 , and $\sim 1500\text{ cm}^{-1}$ and correspond to the different peaks of carbon. As mentioned earlier, the intense peak at 1332 cm^{-1} corresponds to diamond (sp^3 carbon). The D-band at $\sim 1375\text{ cm}^{-1}$ indicates the

presence of disordered graphite, and the G-band corresponding to ordered graphite is situated at $\sim 1500\text{-}1580\text{ cm}^{-1}$, which are both representative of sp^2 -hybridized carbon features. The contribution of impurities is usually quantified using the peak intensity of each contributing peak or band. On the other hand, mechanical stresses are deduced by the Raman shift of the diamond peak. In fact, a compressive or tensile stress induces a shift to higher or lower wavenumbers, respectively [103, 104].

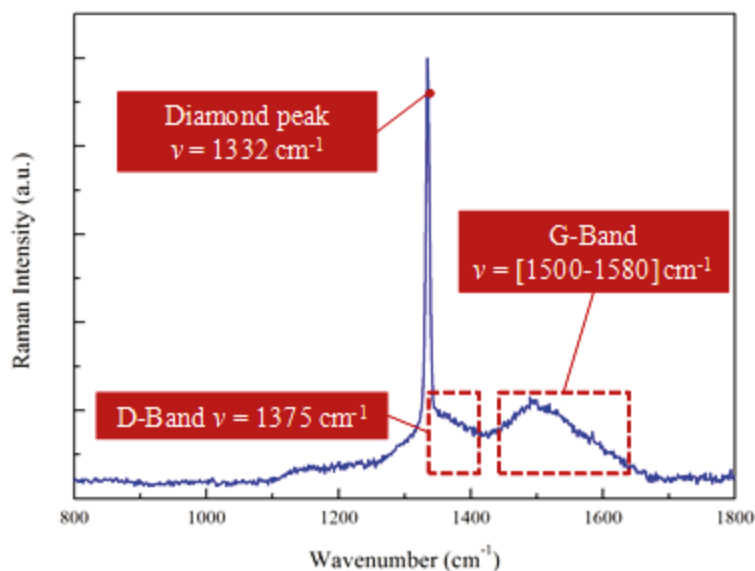


Figure 4.15. Typical Raman spectrum of a diamond film deposited through the use of combustion flame CVD.

Typically, continuous wave laser light is focused by an objective lens onto the sample. The scattered light is collected with the same lens and sent through a monochromator. Finally, the remaining scattered light is detected with a charge coupled device camera. The light with wavelengths close to the laser light wavelength (elastic Rayleigh scattering) is filtered out using a notch filter. A simplified schematic is given in Figure 4.16.

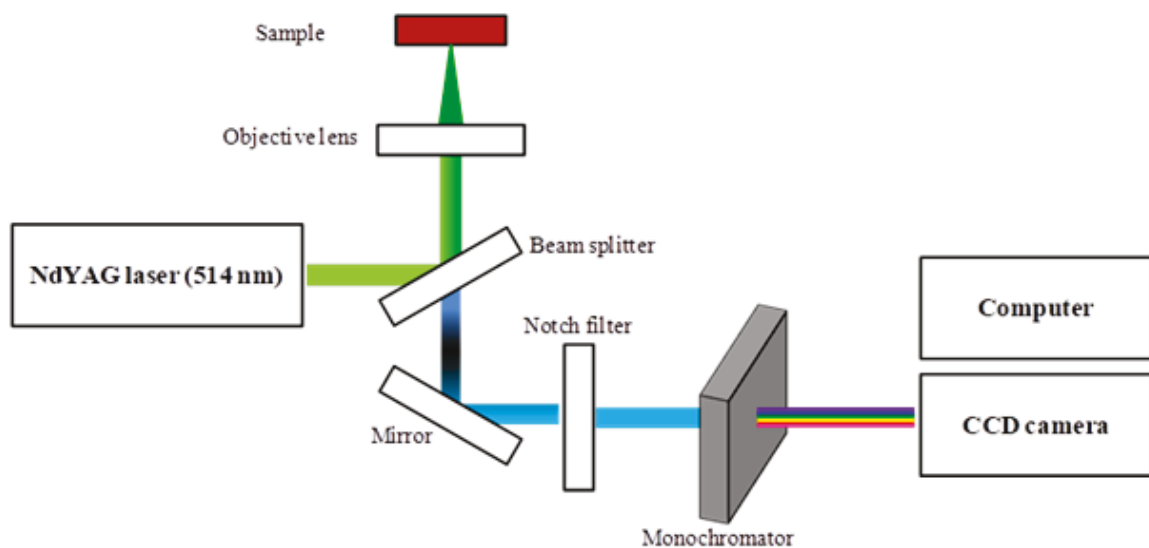


Figure 4.16. Simplified Raman setup schematic.

The Raman investigations were carried out using a micro-Raman spectrometer (inVia™ H 18415, Renishaw) with a 514 nm argon ion laser as the excitation source. The laser power was fixed to 50 mW. The spot diameter was about 1 μm , while the probed volume of a point measurement was about 1 μm^3 . The grating used was 3000 lines/mm in order to achieve the highest resolution. The collected information was measured only from the laser spot-covered regions; therefore, several points were collected, and average values are presented in this work.

4.3.3.2 Phase Purity

Thermal conductivity of diamond films is directly related to defects, impurities such as nitrogen (N), oxygen (O), and nondiamond carbon presence [105]. The diamond phase purity of the diamond films was revealed through Raman spectroscopy by the ratio between the intensities of the sp^3 -hybridized carbon (peak at 1332 cm^{-1}) and that of the sp^2 -hybridized carbon (D-band and G-Band).

Figure 4.17 shows the Raman spectra obtained from diamond films grown on Cu/CF 40 vol% composites without laser resonant excitation of ethylene molecules, with

respect to various durations. As mentioned previously, stress-free diamond peaks are usually situated at 1332 cm^{-1} ; however, in the case of our copper-based substrates, compressive thermomechanical stresses at the substrate/film interface caused the peaks to shift to higher wavenumbers.

All films exhibited a sharp peak located from 1331 to 1334 cm^{-1} . The nondiamond carbon features contributed to the spectra as well, revealing a nonnegligible amount of impurities in the diamond films. The D-band (1375 cm^{-1}) and the graphitic carbon broad band ($[1500-1580]\text{ cm}^{-1}$) showed decreasing intensities with increasing deposition times. This indicated a decrease of sp^2/sp^3 carbon ratio in the film and, therefore, phase purity enhancement with increasing film thickness.

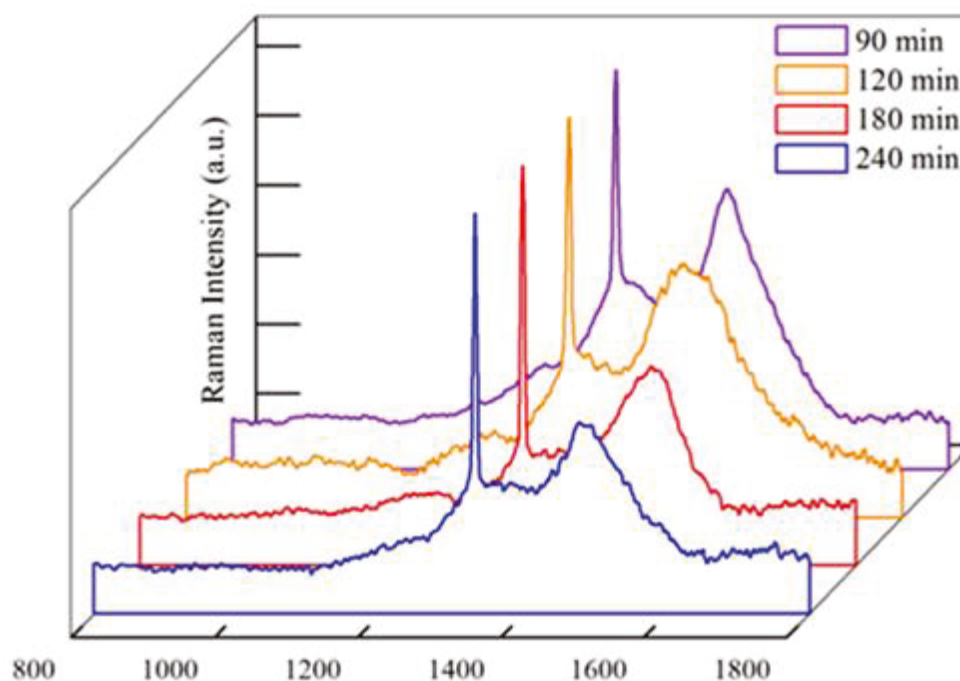


Figure 4.17. Raman spectra of diamond films deposited on Cu/CF 40 vol% composites after 90, 120, 180, and 240 min.

The diamond phase purity was quantified through the calculation of the diamond quality factor [106], using Equation (4.4).

$$Q_{514nm} = \frac{I_{Diamond}}{\left(I_{Diamond} + \frac{I_{a-carbon}}{233}\right)} 100(\%) \quad (4.4)$$

where $I_{Diamond}$ is the intensity of the diamond peak and $I_{a-carbon}$ is the sum of the intensities observed for nondiamond carbon. The coefficient 233 corresponded to the Raman intensity ratio between amorphous carbon and diamond at an excitation wavelength of 514 nm.

The values of the quality factor were superior to 85% and reached 95 % in the case of 240-min-long diamond depositions. This is attributed to the fact that with increasing deposition durations and, therefore, thicknesses, the films tended to grow with less

nondiamond carbon trapped. Indeed, as the thickness increased, the diamond grain size increased as well; and there were, therefore, fewer grain boundaries. Since amorphous carbon and impurities tended to locate at the grain boundaries, the overall quality of the diamond film improved when the amount of grain boundaries decreased. The calculated quality factors are given in **Table 4.2**.

Table 4.2. Quality factors of diamond films with respect to deposition durations.

Deposition Time (min)	90	120	180	240
Film Thickness (μm)	9.39	16.74	22.38	25.41
Quality Factor (%)	83.4	91.7	92.1	95.1

4.3.3.3 Residual Stresses

Residual stresses are divided into two contributions: thermal stress which is provoked by the CTE mismatch between the diamond film and the substrate, and intrinsic stress, which is related to the grain boundary formation and impurity content during diamond growth. As diamond is characterized by a very low CTE ($[1-2] \times 10^{-6} \text{ K}^{-1}$), it is often incompatible with conventional nondiamond substrates, such as metals. The thermal stresses in these cases are often compressive and result in the diamond film cracking and eventually peeling off [94, 107–109]. The stresses were quantified as follows [109]:

$$\sigma = 0.567(\nu_m - \nu_0) \quad (4.5)$$

where ν_m and ν_0 are the observed Raman peak positions of stressed and unstressed (1332 cm^{-1}) diamond, respectively. Diamond films of different thicknesses showed peak shifts to higher wavenumbers compared to stress-free diamond films. These peak shifts confirm the

presence of compressive stresses in the film. The peak shift, however, was less important as the diamond film thickness increased. While for 90 and 120 min of diamond depositions the diamond peak was situated close to 1334.6 cm^{-1} , longer deposition times showed a decrease in the shift to 1333 cm^{-1} . Therefore, the overall residual stresses decreased to less than 1 GPa in the diamond film obtained after 240 min of deposition. The decrease of the compressive residual stresses was related to the increase of the tensile stresses (intrinsic stress). Compressive stresses resulted from the CTE mismatch between the diamond films and the substrate material, whereas, tensile stresses resulted from the constraints created during diamond growth. Therefore, the effect of the CTE was compensated by the diamond growth effect. Then, one can conclude that the growth mode of the diamond film is more influent on the residual stresses than thermal mismatch, after a certain thickness. Therefore, the CTE is sufficiently decreased. Quality factors and residual stresses are given in Table 4.3.

Table 4.3. Residual stresses of diamond films with respect to deposition duration.

Deposition Time (min)	90	120	180	240
Film Thickness (μm)	9.39	16.74	22.38	25.41
Peak Position (cm^{-1})	1334.61	1334.20	1334.13	1333.09
Residual Stresses (GPa)	-1.48	-1.25	-1.21	-0.62

High content CF materials were successfully coated with resisting diamond films in open air using combustion flame CVD. Raman spectroscopy revealed a decrease of total residual stresses with increasing thickness, indicating an increase of intrinsic tensile stresses during diamond growth. The insertion of CFs resulted in improvements of the

copper-based substrates. They allowed the substrate's CTE to be tailored which resulted in a decrease in thermally induced stresses at the diamond/substrate interface. The CFs also brought additional roughness to the surface, due to their consumption, which increased the possibility of mechanical gripping and the number of reactive sites.

4.4. Laser-Assisted Combustion Flame CVD of Diamond Films

Multienergy diamond deposition involves the combination of multiple energy sources to achieve chemical reactions in the flame environment. Typically, laser chemical processing involves two processes: photothermal and photochemical. For this investigation, laser-assisted combustion flame CVD was used to attain multienergy deposition of diamond films on composite surfaces. Two lasers of different wavelength ranges were used to assess the effect of photothermal and photochemical processes on the quality of deposited diamond films.

4.4.1 Vibrational excitation of precursor molecules

4.4.1.1 Principle

Particles and molecules present in the combustion flame environment store energy under various forms, as shown in Figure 4.18. The chemical reactions which take place in CVD diamond growth are directly linked to the vibrational energy which causes bonds to break and rearrange within a molecule. While most CVD routes involve translational energy, which is provided through heating, vibrational energy appears to play a very important role for chemical reactions. In fact, translational energy can quickly be converted to vibrational energy through the collisions that occur in the flame environment. However, the number of collisions and, therefore, the energy required for this conversion is immense

when compared to the conversion of translational to rotational energy, which only takes a few collisions.

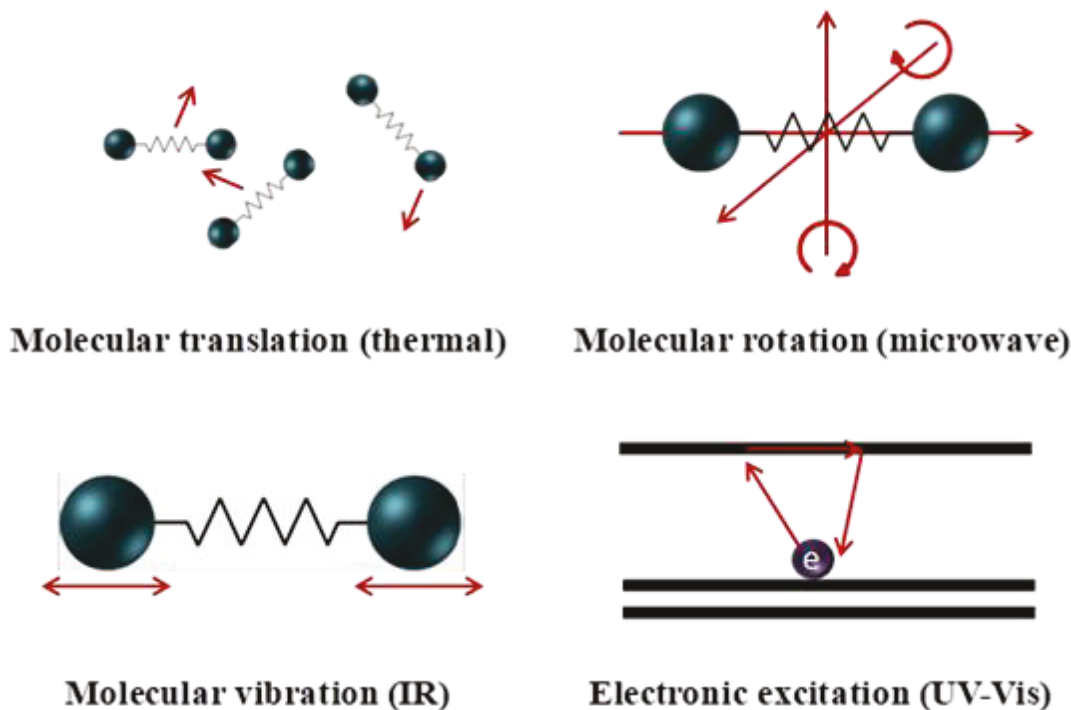


Figure 4.18. Schematic of energy storage for a diatomic molecule.

In this work, the combustion flame provided the species with translational energy, which was translated by heat. The laser source provides the species with vibrational energy. Most molecular vibration frequencies are in the infrared (IR) range; therefore, the ideal lasers for resonant excitation of molecular vibrations are IR lasers. The use of a laser source in the IR range should, therefore, excite the vibrational modes, thus provoking an amplification of the vibration and an increase in the probability that a bond will break.

The use of the ethylene as a gaseous precursor for diamond deposition (discussed in Section 4.2) becomes significant for multienergy deposition. Indeed, the vibrational modes of C_2H_2 molecules show very low IR activity, while C_2H_4 shows several active vibrational modes. More precisely, the CH_2 -wagging mode of C_2H_4 falls in the range of

the wavelength tunable CO₂ laser used in this study. The addition of C₂H₄ molecules to the initial oxyacetylene flame combined to the CO₂ laser excitation allows the multienergy deposition process to be achieved during combustion flame CVD.

The CO₂ laser was selected for this work because of its high efficiency and high output power. While most CO₂ lasers produce a fixed wavelength of 10.591 μm, CO₂ wavelength tunable lasers allow targeting of a range of 9.2–10.9 μm. A wavelength of 10.591 μm does not match the frequency of any vibrational mode of either precursor molecule. However, optical absorption spectra have shown the absorption of CO₂ laser energy by a O₂/C₂H₂/C₂H₄ combustion flame at different wavelengths. The spectra were obtained through optical emission spectroscopy (OES) analyses during T. Guillemet's [5] time at UNL, such as the OES spectrum in Figure 4.19. Two absorption peaks were clearly detected: one at a wavelength of 10.22 μm and one at a wavelength of 10.532 μm. Both wavelengths were investigated in a previous study and showed that a wavelength of 10.532 μm was more suitable than one at 10.22 μm [110]. The corresponding absorption peak was associated to the Q branch ($\Delta J=0$) of the CH₂-wagging mode of C₂H₄ molecules, which is located at 10.534 μm.

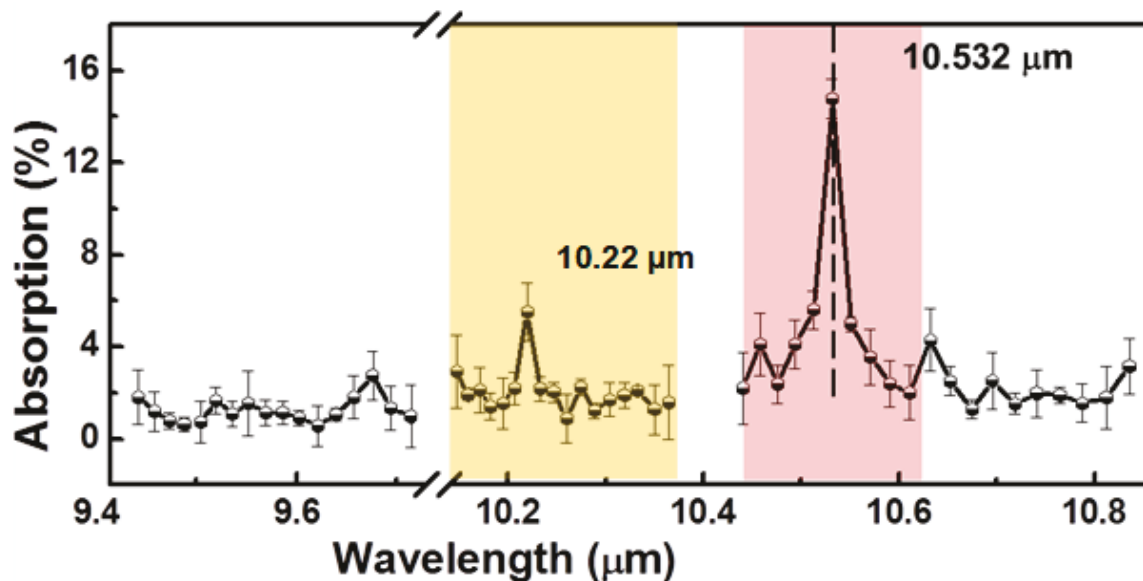


Figure 4.19. OES spectrum, showing the optical absorption of the CO₂ laser excitation by the combustion flame.

Thus, a laser wavelength of 10.532 μm, was used to achieve multienergy conditions for diamond deposition by combining the electromagnetic energy of the laser source to the thermal energy of the combustion flame, leading to maximum optical absorption by the flame. The absorption of the laser energy by the combustion flame was also observed visually through the change in the flame shape and size (Figure 4.20). The irradiation shows an increase in the flame velocity and shrinkage of the flame size, which revealed enhanced chemical reactions in the flame environment.

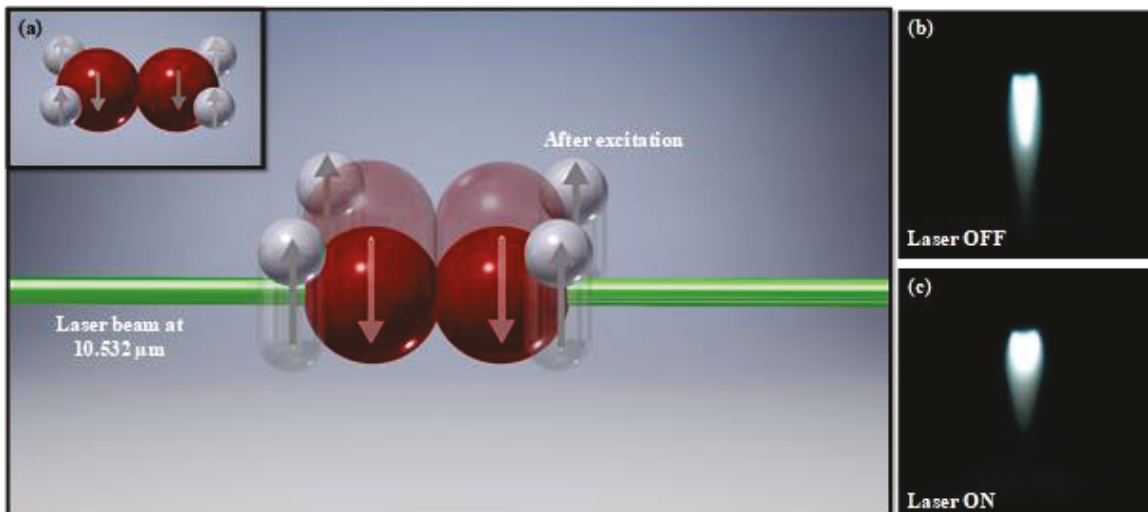


Figure 4.20. (a) Scheme of how the laser excitation at $10.532 \mu\text{m}$ affects the wagging mode of a C_2H_4 molecule. Photographs of the combustion flame (b) without and (c) with $10.532 \mu\text{m}$ laser irradiation.

4.4.1.2 Experimental Setup

The diamond deposition setup used is shown in Figure 4.21. It consisted of a wavelength tunable CO_2 laser (XL1000, PRC Laser Corporation) with a $9.2\text{--}10.9 \mu\text{m}$ wavelength range associated to a combustion system. The combustion system was the same as presented in Section **Erreur ! Source du renvoi introuvable.**4.2. The combustion flame was generated through a welding torch with a 1.5 mm nozzle size. The wavelength of the CO_2 laser was tuned to $10.532 \mu\text{m}$. The laser beam was guided through the combustion flame using a zinc selenide (ZnSe) convex lens with a focal distance of 25.6 cm. The distance between the lens and the nozzle was 30 cm. The laser beam was focused to be 2 mm in diameter to cover the inner combustion flame. The laser power was set to 780 W during diamond growth, and the distance between the inner flame and the top of the substrate was maintained at 1-2 mm.

The laser was operated in continuous wave mode (CW). The substrate temperature was monitored using an IR pyrometer (OS3752, Omega Engineering, Inc.) and regulated using the water-cooled stage. The substrate temperature was kept between 700 and 750 °C.

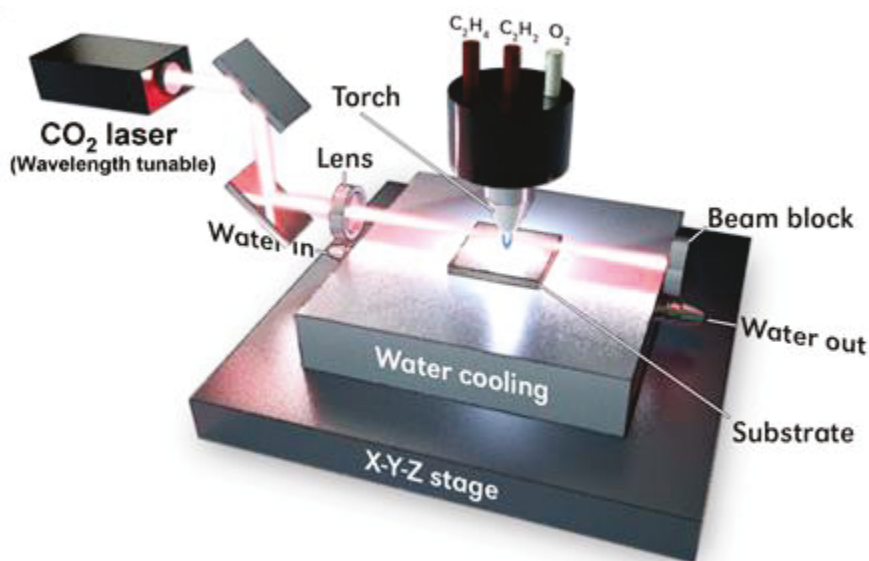


Figure 4.21. Experimental setup for CO₂-laser-assisted combustion flame CVD of diamond films.

4.4.2 Electronic Excitation of Precursor Molecules

While CO₂ laser irradiation has been proved efficient for enhancing the vibrational modes of ethylene molecules, ultraviolet (UV) lasers have also been studied for use in laser-assisted CVD. In the case of the photothermal process, multiple photons in the visible infrared (Vis-IR) range are absorbed to elevate molecules to higher vibrational levels until an atom is ionized or a molecule is dissociated [111]. This phenomenon occurs in CO₂-assisted diamond deposition. In a photochemical process, molecules can be electronically dissociated in a single step by absorbing visible ultraviolet (UV-vis) photons.

4.4.2.1 Principle

In previous studies carried out at LANE, a krypton fluoride (KrF) excimer laser was used to increase the diamond film quality and deposition rate. A complete study on the optimization of the KrF-assisted process was carried out and used as reference for the work described in this section.

The KrF excimer laser used is a nanosecond pulsed laser with a wavelength of 248 nm which is close to the wavelength used to excite carbon atoms (247.9 nm). The excitation and relaxation of carbon atoms by 247.9 nm light is shown schematically in Figure 4.22.

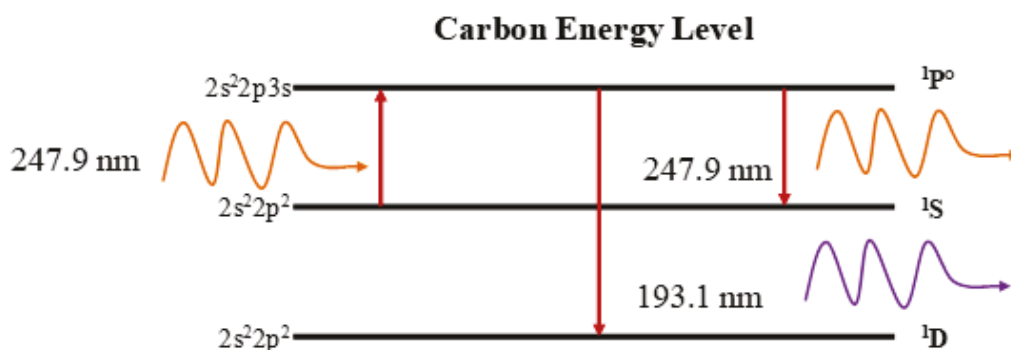


Figure 4.22. Schematic diagram showing electron excitation of carbon atoms.

4.4.2.2 Experimental Setup

The KrF-assisted diamond deposition setup is shown in Figure 4.23. It consists of a KrF excimer laser (Lambda Physik COMPex 205, Coherent) with a UV wavelength 248 nm and a pulse width of 23 ns, associated to the combustion system described previously in Section 4.2. The laser beam was directed normally through the combustion flame and parallel to the substrate. A UV convex lens with a focal length of 25 mm was used to focus the laser beam from its original size of $\sim 20 \text{ mm} \times 10 \text{ mm}$ to $\sim 2 \text{ mm} \times 1 \text{ mm}$, which is of the same order of magnitude of the inner flame size. Diamond depositions were

carried with a laser frequency of 40 Hz and voltage of 25 kV. The substrate temperature was monitored using the IR pyrometer (OS3752, Omega Engineering, Inc.) and regulated using the water-cooled stage. The substrate temperature was kept between 700 and 750 °C. All deposition durations were fixed to 60 min.

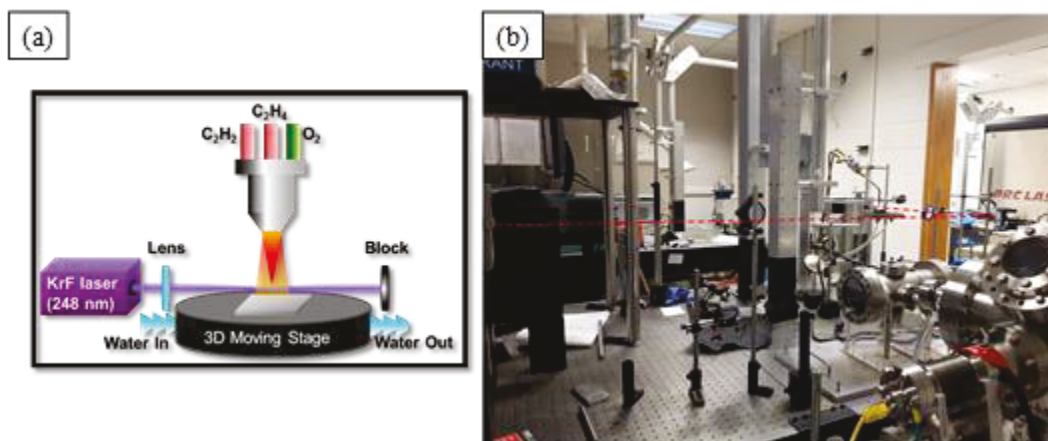


Figure 4.23. KrF-assisted diamond deposition setup. (a) Schematic and (b) set-up and laser path.

4.5. Laser-Assisted Diamond Growth on Cu/C Composite Materials

4.5.1. Exposed Surfaces

In Section 4.3.1, the presence of CFs on the surface of a substrate was shown to induce the in situ creation of gripping sites during diamond deposition. These gripping sites are caused by the consumption of the CFs and are shaped equivalently (fiber-shaped voids).

For the next part of the research, composites reinforced with 40 vol% CFs were synthesized; however, the top surface of each composite was modified using carbon reinforcements of different shapes, shown in Figure 4.24.

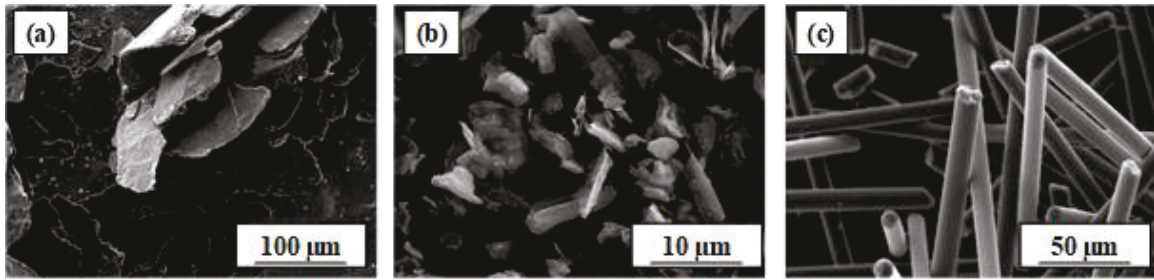


Figure 4.24. SEM micrographs of the carbon reinforcements used.

(a) Graphite flakes, (b) carbon powder, and (c) carbon fibers.

The consumption of the carbon reinforcements was verified by carrying out 2-10 min diamond depositions and analyzing the resulting surfaces using SEM. Also, the roughness and shapes of the voids were mapped using an optical profiler which is discussed in the next section. Sections 0 and 0 discuss longer diamond depositions (30, 60, and 120 min) and the complete analysis of the diamond films, in terms of microstructure and film quality.

4.5.2 Surface Roughness

The surfaces of the composites were observed after 2, 5, and 10 min of diamond deposition. Figure 4.25 shows the SEM micrographs collected from surfaces containing graphite flakes (GFs), carbon fibers, and carbon powder (CP). One can notice the roughness induced by the diamond deposition and the creation of voids of various geometries. While, the GFs consumed left large complex-shaped voids, the CP left larger patches of small voids on the surface.

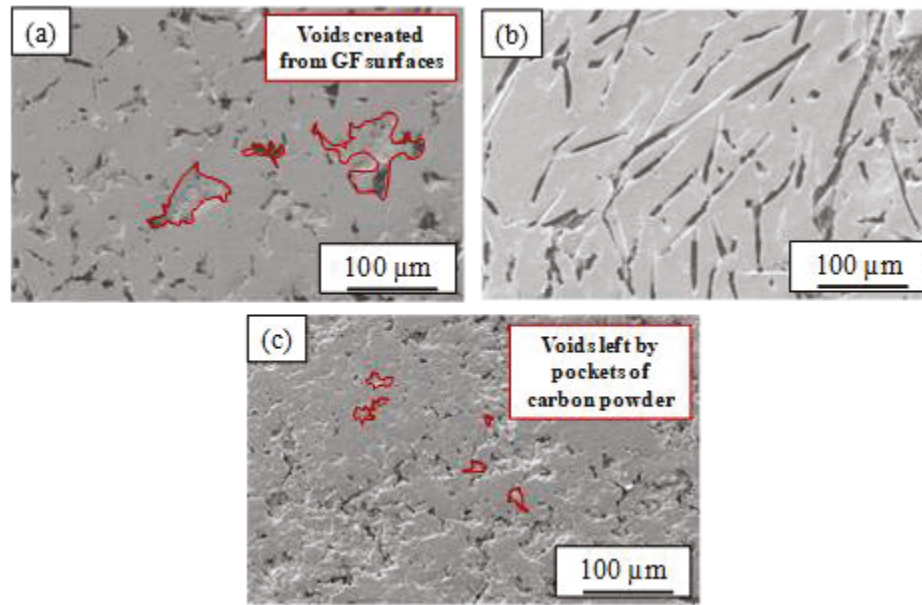


Figure 4.25. SEM micrographs of top surface after 5 min of diamond deposition on surfaces containing (a) GFs, (b) CFs, and (c) CPs.

The induced roughness of each surface was assessed using an optical profiler. The 3D maps obtained for the surfaces containing GFs, CFs, and CP are given in Figure 4.26. While the surface containing GFs (Figure 4.26(c)) seems to have been the most damaged, the overall roughness of the area was similar to that of the surface containing CP. In fact, the overall roughness for both substrates was situated at around $8\ \mu\text{m}$. While CFs are larger in diameter, the CP tended to aggregate and caused the creation of large patches of voids after consumption of the C by the combustion flame, as shown in Figure 4.26(b).

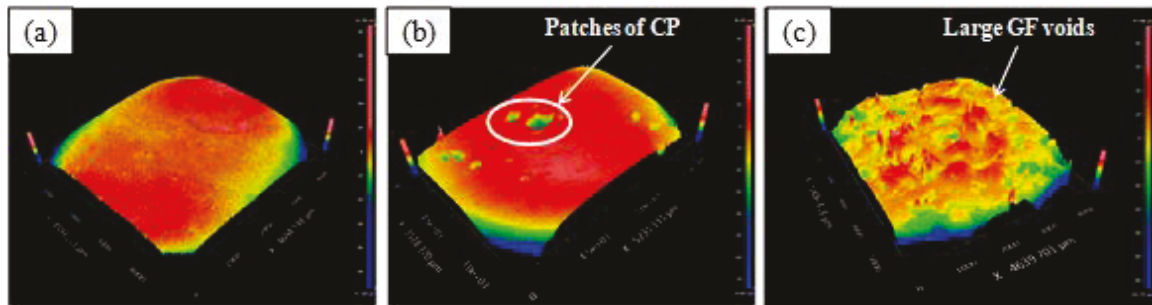


Figure 4.26. Optical profiler 3D maps of the composite substrates after 5 min of diamond deposition with (a) CFs, (b) carbon powder, and (c) GFs on surfaces.

4.5.3 Diamond Film Microstructure

Shown in Figure 4.27 are the SEM micrographs of the top surface of diamond films obtained after 60 min of diamond deposition with no laser excitation on surfaces containing (a) CFs, (b) GFs, and (c) CP. While continuous films were observed on composites with GFs, the size of the diamond crystals were much smaller than those observed on the other two surfaces. However, CF and CP surfaces resulted in discontinuous diamond films and dispersed diamond particles. The morphologies of the diamond films obtained for these 60 min diamond depositions are not comparable to the morphologies discussed in Section 4.3.2 as they were not carried out on the same flame setup.

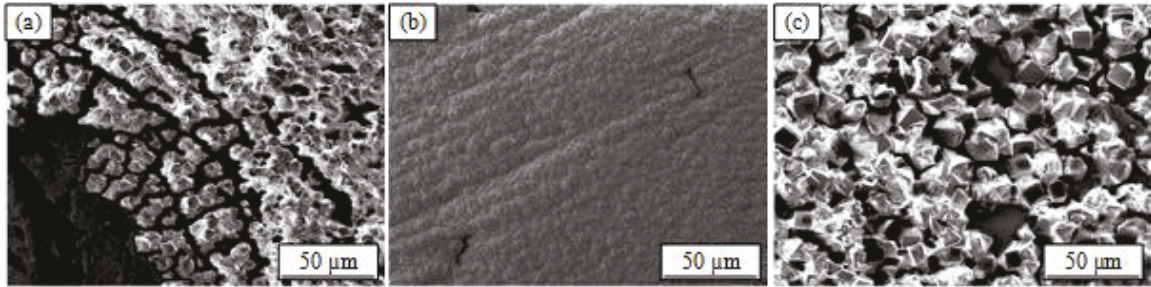


Figure 4.27. SEM micrographs of the top surface of diamond films deposited with no laser excitation on surfaces with (a) CFs, (b) GFs, and (c) CP.

Figure 4.28 consists of the SEM micrographs of diamond films obtained after 60 min of diamond deposition with CO₂ laser excitation on surfaces containing (a) CFs, (b) GFs, and (c) CP. One can observe that continuous films were obtained for each surface. While the crystal size for the CF and CP surfaces did not change drastically with CO₂ irradiation, the crystal size obtained on the GF surface increased by a factor of 7.

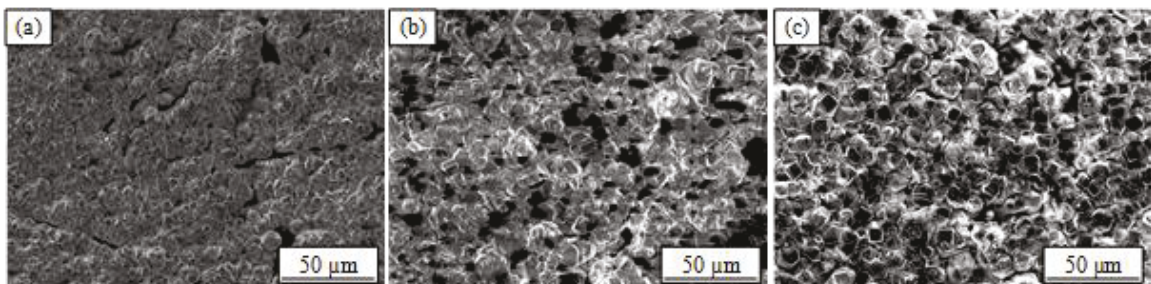


Figure 4.28. SEM micrographs of the top surface of diamond films deposited with CO₂ laser excitation on surfaces with (a) CFs, (b) GFs, and (c) CP.

Figure 4.29 consists of SEM micrographs of the diamond film surface obtained after 60 min of diamond deposition with KrF laser excitation on surfaces containing (a) CFs, (b) GFs and (c) CP. These depositions also resulted in continuous films with grain sizes that were the same order of magnitude as those obtained through CO₂-assisted diamond depositions.

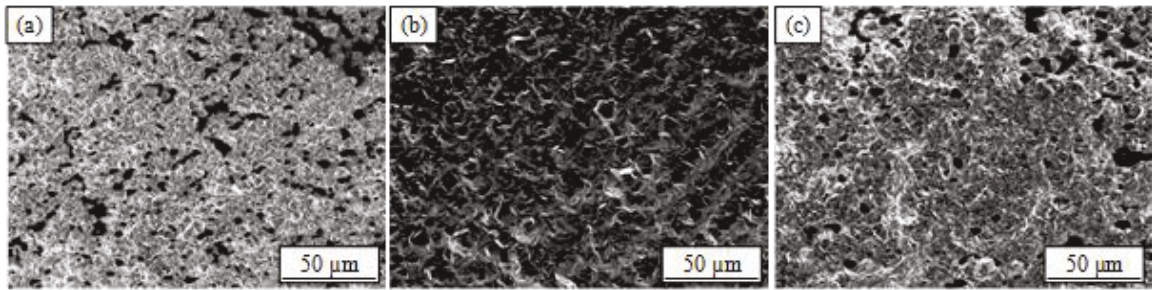


Figure 4.29. SEM micrographs of the top surface of diamond films deposited with KrF laser excitation on surfaces with (a) CFs, (b) GFs, and (c) CP.

It is important to note that the laser had no particular effect on the surface morphology of the diamond films except a slight increase in the crystal sizes. The initial small crystal sizes obtained were due to the rough surfaces, which increased the amount of nucleation sites. Therefore, a larger number of grains were deposited resulting in a large amount of small crystals. The process should be situated in a nucleation-favorable mode rather than in a growth-favorable one. Cross-section analyses, that need to be carried out, will allow conclusions to be drawn on this hypothesis.

4.5.4 Diamond Phase Purity and Residual Stresses

Diamond film phase purity and residual stresses for the diamond films deposited on the different composite surfaces were investigated, and the results are listed in Table 4.4). One can note that the phase purity of the diamond films obtained through CO₂-assisted diamond depositions were the highest obtained, followed closely by the KrF-assisted depositions. There was, therefore, a noticeable enhancement of phase purity when laser excitation was combined with the combustion CVD process. However, the surface morphology had no effect on diamond phase purity. On the other hand, one can observe that residual stresses did not vary significantly with laser excitation but rather with surface morphology. The highest residual stresses were obtained for the CP surfaces. Although CP

was distributed on the overall surface, the depth of the voids created was smaller than those obtained from GF and CF consumption. Also, due to aggregation, CP tends to create large voids, as seen on the 3D map in Figure 4.26(b). These observations may explain the increase in the residual stresses for these surfaces. However, the investigations carried out were insufficient to be able to determine what effect the surface morphology has on residual stresses. Future works to complete this study are discussed in the last chapter of this dissertation.

Table 4.4. Quality factors and residual stresses of diamond films deposited on composites with various surfaces during 60 min with and without laser excitation.

Surface	Laser Conditions	Quality Factor (%)	Residual Stresses (GPa)
Carbon fibers	No laser	87.7	-0.01
Carbon fibers	CO ₂ – 800 W	94.7	-0.05
Carbon fibers	KrF – 40 Hz, 25 kV	94.1	-0.09
Graphite flakes	No laser	95.3	-0.08
Graphite flakes	CO ₂ – 800 W	99,0	-0.07
Graphite flakes	KrF – 40 Hz, 25 kV	97.8	-0.08
Carbon Powder	No laser	95.3	-0.10
Carbon powders	CO ₂ – 800 W	98.8	-0.12
Carbon Powder	KrF – 40 Hz, 25 kV	96.4	-0.13

4.6. Conclusion

This chapter demonstrates that fast deposition of high-quality diamond films on Cu/C composite substrates is possible using laser-assisted combustion CVD. The synthesis process shows advantages compared to traditional CVD routes, such as flexibility, low cost, and high growth rates. The multienergy diamond deposition process established in previous studies was shown to be as effective on Cu/C substrates and resulted in high phase purity.

The optimum substrate temperature for diamond deposition was determined to be in the range of [700-740] °C. Temperatures close to 740 °C resulted in {100} faceted crystals while lower temperatures promoted randomly oriented crystals.

Raman spectroscopy shed light on the increase in the phase purity with increasing diamond film thickness which is related to larger diamond grains. Also, it revealed the decrease of total residual stresses with increasing thickness, indicating the increase of intrinsic tensile stresses during diamond growth. The insertion of CFs improved copper-based substrates. Carbon fibers allowed the substrate's CTE to be tailored and brought about a decrease in thermally induced stresses at the diamond/substrate interface.

The various reinforcement geometries used allowed different mechanical gripping sites to be created, which promoted nucleation and insured good adhesion of the diamond films onto the composite substrates. However, further analyses are required to draw conclusions on the effect of the void morphologies on diamond film phase purity and residual stresses.

Also, thermal characterization of the films needs to be carried out to assess the feasibility of using these CVD diamond films as heat spreaders in microelectronic

components. Finally, their performance will provide confirmation of the behavior predicted by simulations.

5. Physical Properties

5.1. Introduction

In Chapter 3, the synthesis of copper/carbon (Cu/C) composites through the use of the solid-liquid co-existent phase process is discussed. Carbon reinforcements under the form of either carbon fibers (CFs) or diamond particles were used as they exhibited high thermal conductivities. In the case of CFs, however, especially because of their anisotropic shape, the thermal properties were anisotropic. It is, therefore, important to investigate the direction in which the thermal properties are measured so that realistic input on the performance of the material can be provided.

Copper (Cu) is widely used in the electronics industry because of its high thermal conductivity ($k = 400 \text{ W/m.K}$) and electrical conductivity ($\sigma = 6.48 \times 10^7 \text{ S/m}$), as well as for its ductile behavior. Copper/carbon composites, and more particularly copper/diamond (Cu/D) composites, allow tailoring of both the thermal expansion coefficient (CTE) and thermal conductivity of the materials by varying the volume fraction of reinforcement. As mentioned in Chapter 2, Cu/D composites have attracted a lot of attention during past years, as their characteristics make them excellent candidates for heat sink devices [29, 31, 62, 68, 112]. The lack of chemical affinity between copper and carbon is a permanent issue to which the insertion of carbide forming elements (titanium (Ti) [66, 68, 70], zirconium (Zr) [69, 71], tungsten (W) [60, 113], chromium (Cr) [41, 65], and boron (B) [65]) has been proven to be beneficial.

While physical vapor deposition (PVD) and molten-salt methods have been used to coat reinforcements prior to mixing and sintering, alloying the matrix was the option chosen for this work. One can observe that the minor insertion of Ti and Zr alloyed copper

powders in the initial composite powder mixture allowed the formation of titanium carbide (TiC) and zirconium carbide (ZrC) interphases. The use of the solid-liquid co-existent process allowed a diffusion and reactivity enhancement of the carbide-forming elements and, therefore, the obtainment of homogeneous and well-distributed carbide interphases (Figure 5.1).

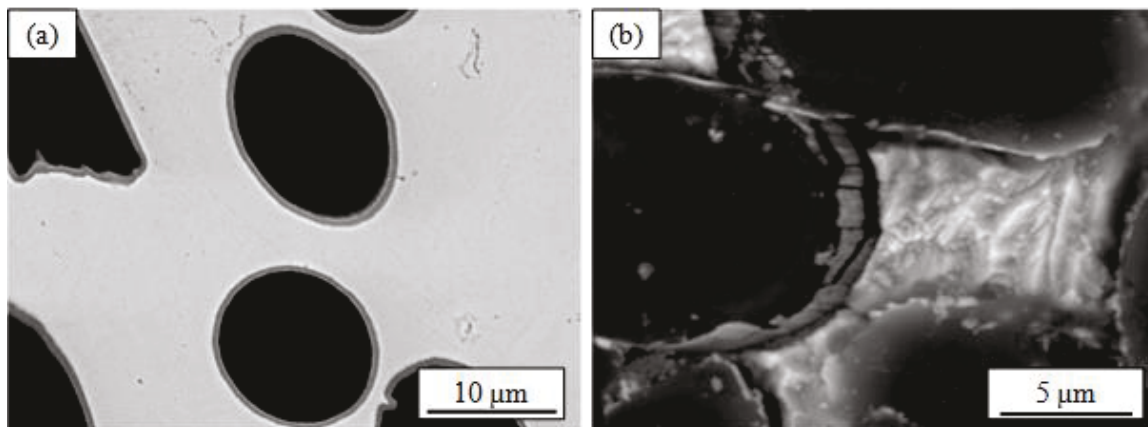


Figure 5.1. Scanning electron micrographs of Cu/CF composites with (a) TiC interphases, and (b) ZrC interphases (after chemical etching).

This chapter deals with the thermal characterization and performance of Cu/C composites (C = carbon fibers and diamond particles) with and without carbide interphases. The analytical and numerical models conducted to predict the behavior of the composites are presented in the first part of the chapter. Conclusions are then drawn on their viability with respect to the experimental data obtained. Also, conclusions are drawn based on the effect of the interphases on the thermal transfer in the composites, obtained using the solid-liquid co-existent phase process, and compared with interphases obtained through other processes.

Thermal diffusivity measurements on Cu/CF composites were carried out at the Institute of Condensed Matter Chemistry of Bordeaux (ICMCB), while those on Cu/D

composites were carried out at the Institute of Mechanics and Engineering (I2M) of the University of Bordeaux. Pr. Jean-Luc Battaglia and Dr. Andrzej Kusiak from I2M provided help, technical support, and expertise to thermally characterize the composite materials.

5.2. Experimental Setups

Thermal conductivity is a major property for heat dissipation materials since high thermal conductivities indicate the speed at which the heat will be spread. Thermal conductivity cannot be directly measured; therefore, thermal diffusivity measurements were carried out. The conductivities were deduced using:

$$k_c = C_p \times \rho \times \alpha \quad (5.1)$$

where k_c is the thermal conductivity ($W/m.K$), C_p is the specific heat capacity ($J/kg.K$), ρ is the density (kg/m^3), and α is the thermal diffusivity (m^2/s) of the material. The specific heat was calculated using the rule of mixtures:

$$C_{p_c} = w_m C_{p,m} + w_r C_{p,r} \quad (5.2)$$

where $C_{p,m}$, and $C_{p,r}$ are the specific heats of the copper matrix ($C_{p,Cu} = 392 J/kg.K$), and the reinforcements ($C_{p,CF} = 720 J/kg.K$, $C_{p,D} = 681 J/kg.K$), respectively; and w_m and w_r are the weight fractions of the matrix and the reinforcements, respectively. For the sake of simplifying the system and because of the very small concentration of carbide in the composite, the carbides' specific heats were not taken into account.

Thermal diffusivity of the CF composites was measured using the flash laser method in the axial direction of small cylinders of 6 mm in diameter and a height between 3 and 6 mm, using a Netzsch LFA 457 apparatus, as shown in Figure 5.2.

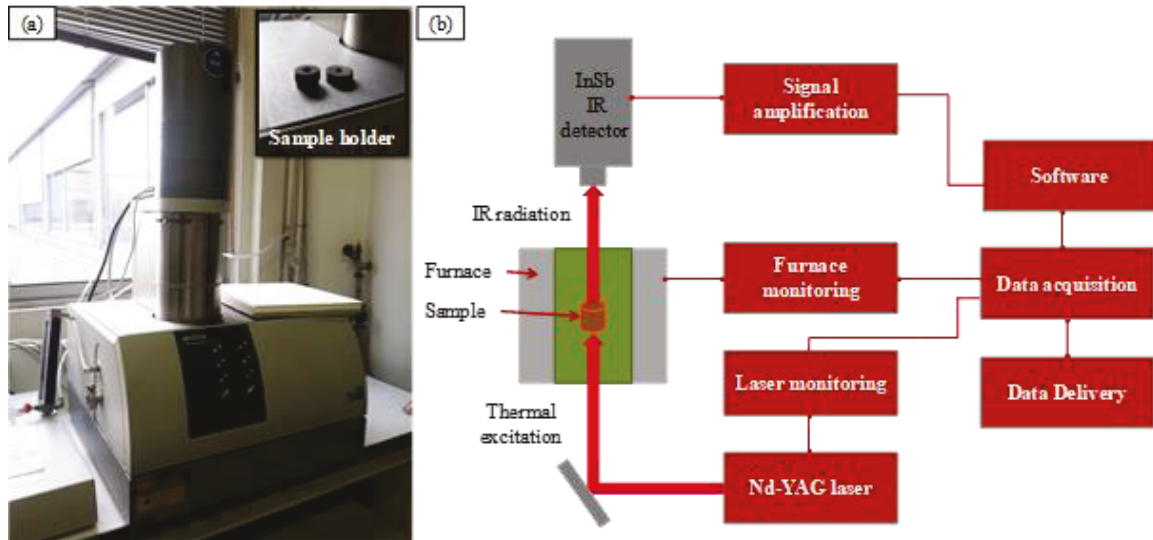


Figure 5.2. Flash laser apparatus: (a) photograph and (b) schematic of the setup.

The thermal diffusivity of the diamond (D) composites was measured with a homemade flash laser apparatus at I2M (Figure 5.3) on cylinders of 20 mm in diameter and between 4 and 6 mm in height.

Thermal diffusivity measurements rely on the thermophysical property that defines the speed of heat propagation by conduction. Therefore, the higher the thermal diffusivity, the faster the heat propagates in that material. It involves uniform radiation of a sample over its bottom face with a short laser pulse up to a given temperature, as shown in Figure 5.4(a). The time-temperature of the top face of the sample is collected from a temperature detector with fast thermal response. Then, based on the thermogram obtained (Figure 5.4(b)), the sample's thermal diffusivity is determined by the thickness (e) of the sample and the time it takes the sample to reach half of the maximum temperature ($t_{1/2}$).

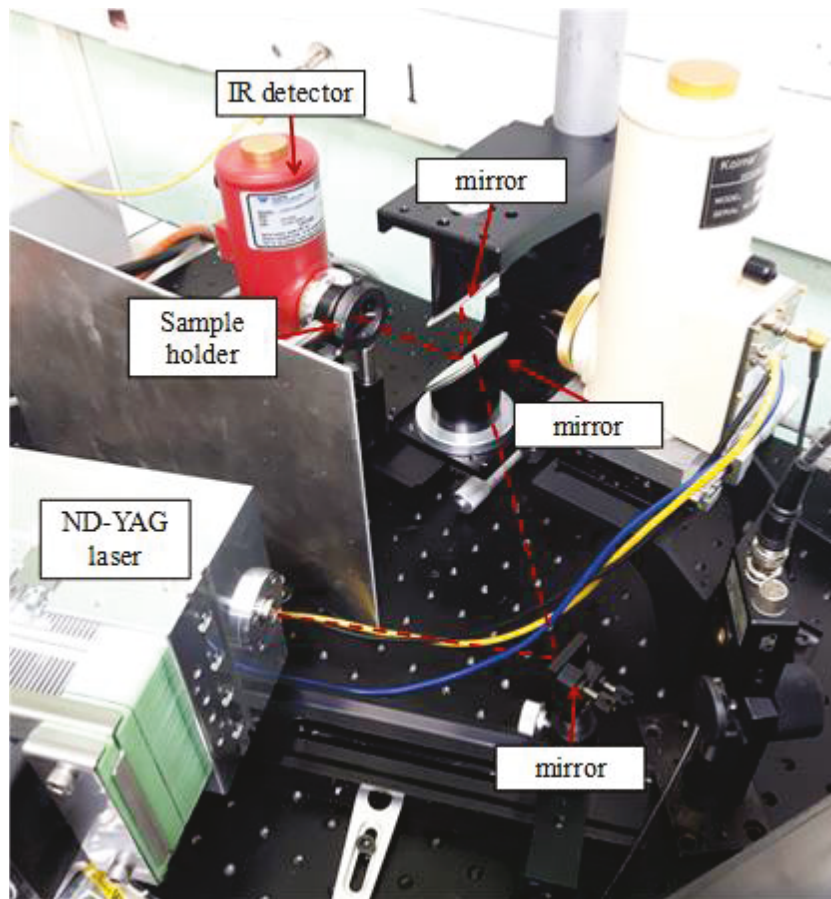


Figure 5.3. Experimental setup implemented at the I2M.

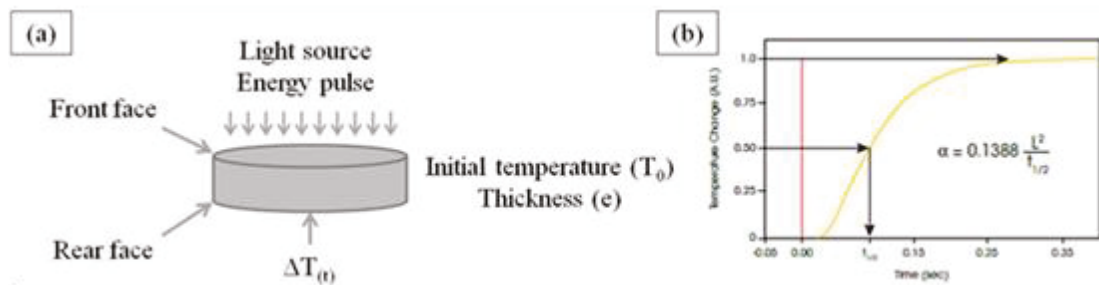


Figure 5.4. (a) Schematic of the thermal diffusivity measurement and
(b) thermogram example.

5.3. Thermal Characterization of Cu/C Composites

5.3.1. Cu/CF Composites

5.3.1.1 Cu/CF Composites With No Interphase

As mentioned previously, the Cu/CF composites were thermally characterized at the ICMCB using a commercial Netzsch apparatus. The thermal conductivities of the Cu matrix and the CF reinforcements were set to be 385 and 278 W/K.m, respectively. Due to the random distribution of the CFs in the plane of measurement (perpendicular to the pressure direction), the conductivity value of the CFs was taken to be the average of the conductivity along (550 W/K.m) and perpendicular to the CF axis (5 W/K.m), as shown in Figure 5.5.

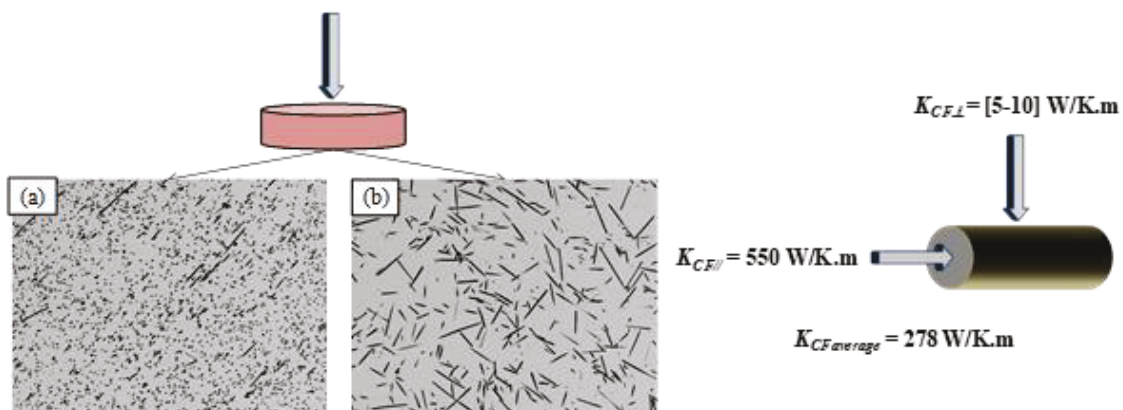


Figure 5.5. Micrographs of a Cu/CF composite taken (a) on the cross-section and (b) on the surface. Anisotropic thermal properties of carbon fibers induced by the anisotropic shape of CFs.

Therefore, a decrease in the thermal conductivity with increasing CF content was expected. Instead of reinforcing the matrix with a phase which is more conducting, it was reinforced with a material which has a lower average thermal conductivity.

One can observe the different response of the thermal diffusivity for the same composite, analyzed in the two different directions: parallel and perpendicular to the CF

axis, as shown in Figure 5.6. The thermal diffusivities were measured on Cu/CF composites containing 4 vol% of Cu-Ti. The behavior of the points at 10 vol% are discussed later in this chapter.

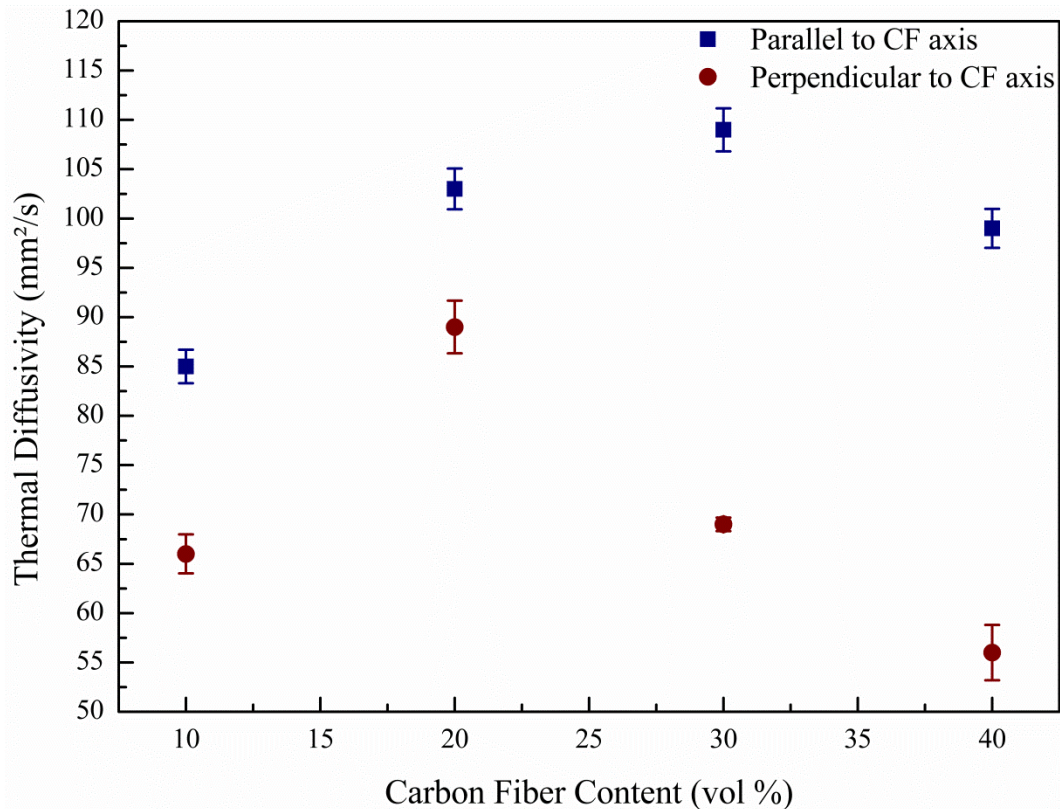


Figure 5.6. Thermal diffusivity with respect to the CF content. Blue points correspond to the thermal diffusivities perpendicular to the pressure axis (along the CF axis), and red points correspond to the diffusivities parallel to the pressure axis. Thermal diffusivities were measured on Cu/CF composites containing 4 vol% of Cu-Ti.

As mentioned in Chapter 2, several analytical models were developed in order to predict the thermal conductivity of multimaterials. The difficulty lies in the determination of a model which takes into account the shape, orientation, interfacial resistance, and distribution of the CFs in the Cu matrix. The model must also be applicable for a fiber-

reinforced composite considered to be thermally anisotropic. Therefore, three models were used for comparison and to draw conclusions on the viability of such analytical models.

The first model used was Fricke's model, given below [114]:

$$k_C = k_m \left[\frac{k_r + (n-1)k_m - (n-1)V_r(k_m - k_r)}{k_r + (n-1)k_m + V_r(k_m - k_r)} \right] \quad (5.3)$$

This model only takes in account the thermal conductivities of the matrix and the reinforcement (k_m and k_r , respectively), the reinforcement volume fraction (V_r), and a shape factor (n), which was taken to be equal to 25 as it corresponds to the aspect ratio of the CFs (length/diameter of 250/10).

The second model taken is Hasselman & Johnson's (Section 2.5.3) which takes into account the interfacial conductance ($h_c = 1/R_i$). However, it remains approximate on the distribution of the reinforcements and their shape and orientation, in the case of anisotropic reinforcements [53].

$$k_C = k_m \frac{\left(\frac{(k_\theta k_r)^{1/2}}{k_m} - \frac{(k_\theta k_r)^{1/2}}{ah_c} - 1 \right) V_r + \left(1 + \frac{(k_\theta k_r)^{1/2}}{k_m} + \frac{(k_\theta k_r)^{1/2}}{ah_c} \right)}{\left(1 - \frac{(k_\theta k_r)^{1/2}}{k_m} + \frac{(k_\theta k_r)^{1/2}}{ah_c} \right) V_r + \left(1 + \frac{(k_\theta k_r)^{1/2}}{k_m} + \frac{(k_\theta k_r)^{1/2}}{ah_c} \right)} \quad (5.4)$$

where k_c , k_m , and k_r , are the thermal conductivities of the composite, the matrix, and the reinforcement, respectively. The tangential thermal conductivity of the reinforcement is k_θ , V_r is the volume fraction, and a the radius of the reinforcement. The interfacial conductance is h_c , which is the inverse of the interfacial resistance.

The third model is that of Lewis & Nielsen. In this case, the distribution, orientation, and shape of the reinforcements are taken into account; however, the interfacial resistance is not. It is given by the following equation [115]:

$$k_c = k_m \left(\frac{1 + \left(A \times \frac{\frac{k_r}{k_m} - 1}{\frac{k_r}{k_m} + A} \times V_r \right)}{1 - \frac{\frac{k_r}{k_m} - 1}{\frac{k_r}{k_m} + A} \times V_r \times \left(1 + \left(\frac{1 - \Phi_m}{\Phi_m^2} \right) \right)} \right) \quad (5.5)$$

where k_c , k_m , and k_r are the thermal conductivities of the composite, the matrix, and the reinforcements, respectively. The volume fraction of reinforcements is V_r , A is the shape factor of the reinforcements, and Φ_m is the maximum volume fraction of reinforcement with respect to their distribution in the matrix. A comparison of the models and the experimental data is given in Figure 5.7.

The most unrealistic model is Fricke's model, which does not coincide with any experimental points. This is due to the fact that Fricke's model does not take in account the interfacial thermal resistance and the distribution and the orientation of the reinforcements.

A strong deviation of the experimental results compared to the Lewis & Nielsen model appeared to start at 30% vol. This model, which takes into account the geometrical aspect of the reinforcement, assumes, like the Hasselman & Johnson model, an infinite volume of composite material. It was, therefore, a phenomenon of contact which induces this deviation.

In order to match the experimental data to the theoretical values, the Hasselman & Johnson model must take into account a variation of the interfacial conductance h_c (inverse of the resistance R_i). For a volume fraction of reinforcement of less than 30 vol% the thermal conductance was equal to 10^6 W/m².K, and 10^7 W/m².K for a volume fraction of more than 30%. Somewhere between 30 and 40 vol%, the percolation threshold was met. This variation was therefore, attributed to the presence of a contact phenomenon between

the CFs. Indeed, a fiber-fiber contact can generate residual porosities, which cannot be annihilated by the “squeezing” effect, since the Cu matrix cannot reach the zone of contact between the fibers.

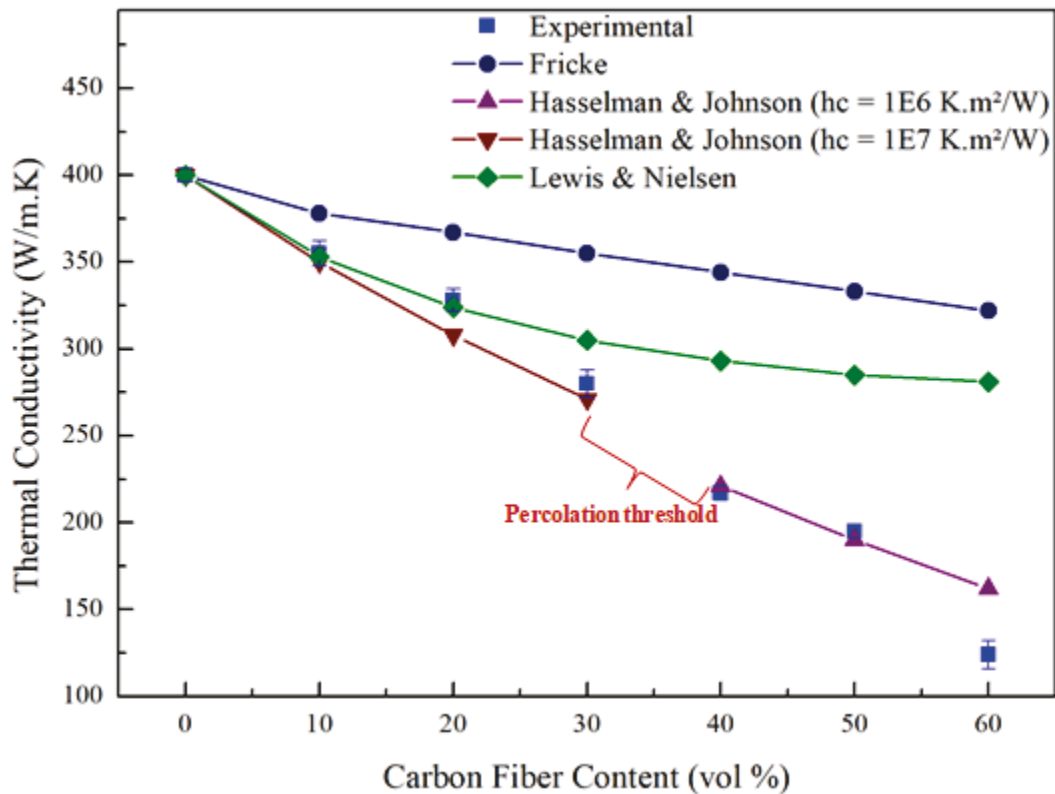


Figure 5.7. Thermal conductivity with respect to carbon fiber content.

Comparison of analytical models and experimental values.

In a Cu/CF composite, the interface is purely mechanical and results from the compression of the Cu around the CFs during the cooling step. The porosities created at the fiber-fiber contacts then increase the interfacial resistance within the composite material, which leads to a drastic drop in the thermal conductivity. Finally, a slight deviation for 60% of reinforcement can be observed. This variation can be explained by a change in the orientation of the CFs, with respect to the plane perpendicular to the pressure axis, caused by an obstruction effect that has become critical.

To illustrate this disorientation, Figure 5.8 consists of two SEM micrographs of a composite containing 40 vol% of CF and one containing 60 vol%. Both micrographs are from the cross-sections of composites where the majority of carbon fibers should appear as dark circles. However, in both cases one can see that there are contact points between fibers. While the fibers are approximately well oriented, in the case of the 40 vol% composite, that is not the case for the 60 vol% of CFs.

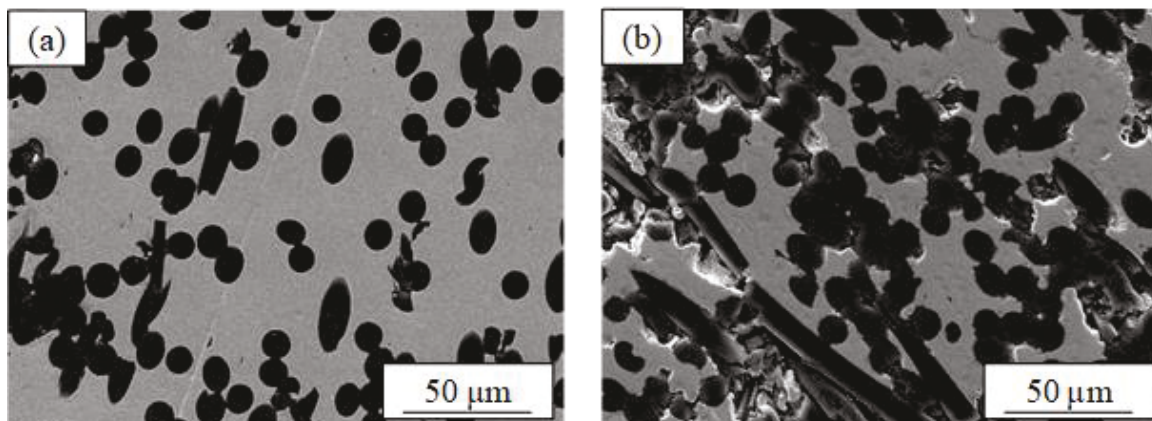


Figure 5.8. SEM micrographs of the cross-section of (a) a Cu/CF 40 vol% and (b) a Cu/CF 60 vol% composite.

5.3.1.2 Cu-Ti Additions

The thermal conductivities of Cu/CF composites from 10 to 60 vol% without and with TiC interphases are reported in Figure 5.9. As expected, the thermal conductivity decreased as the CF content increased since the CF conductivity was lower than that of the Cu matrix. The first observation is the drastic decrease in thermal conductivity for 10 vol% CF when 4 and 6 vol% of Cu-Ti liquid phase was present in the material. The same behavior was observed for 10 vol% in Figure 5.6.

The poor thermal conductivity can be explained by the fact that the carbon within the composite was not sufficient to attract Ti towards it. Therefore, Ti has a tendency to

remain in the Cu matrix as a solid solution. This tendency was verified by structural refinement of a high quality X-ray diffraction (XRD) pattern of the Cu(CuTi)₄/CF10 composite. Only Cu peaks were observed, and the calculated lattice parameter was equal to 3.62427(5) (Bragg R-factor of 0.184). It was concluded that the expansion of the lattice was caused by the presence of Ti in solid solution and explained the poor thermal conductivity observed for 10 vol% of CF.

It is known that the transport properties (thermal and electrical conductivities) of Cu-Ti solid solutions were lower than those of pure Cu. For example, for a solid solution of Ti in Cu that reached 0.04 wt%, the electrical conductivity was much lower than that of pure Cu [116]. To confirm the effect of Ti impurities on copper's thermal conductivity, a solid solution of Ti in Cu (Cu_{Ti}) was prepared; and its thermal diffusivity was measured. The resulting thermal conductivity obtained for the Cu_{Ti} sample was 210.6 W/m.K, which was almost half of that of pure Cu. For the sake of comparison, a CuZr solid solution was also synthesized. The thermal conductivity of this alloy was 342.9 W/m.K. Therefore, Ti has a detrimental effect on Cu's properties, while Zr impurities cause a decrease of less than 10%.

However, for higher volume fractions of CFs, the effect of the interphase became more important as the diffusivities obtained were higher than the ones for the composites with no Cu-Ti. This indicated that the majority of the Ti reacted with carbon and allowed the creation of an interphase, which enabled the proper transfer of heat from the matrix to the fiber and vice versa.

For CF content that exceeded 20 vol%, the thermal conductivities of composites containing 4 and 6 vol% of Cu-Ti were higher than those without Cu-Ti. This deviation

can be explained by the presence of a strong chemical bonding between the matrix and the reinforcement, caused by the presence of the interphase. The creation of such chemical interphases, in comparison with the mechanical bonding induced during cooling by the difference in CTEs between the CF and the Cu matrix in Cu/CF materials, improved the heat transfer from the matrix to the reinforcement and vice-versa, thereby increasing the final thermal conductivity of the composite materials. Also, the high thermal conductivities indicated that the majority of the Ti reacted and was no longer in solid solution in Cu. This means that the reaction that occurred during the solid-liquid co-existent phase process was complete and all Ti formed TiC.

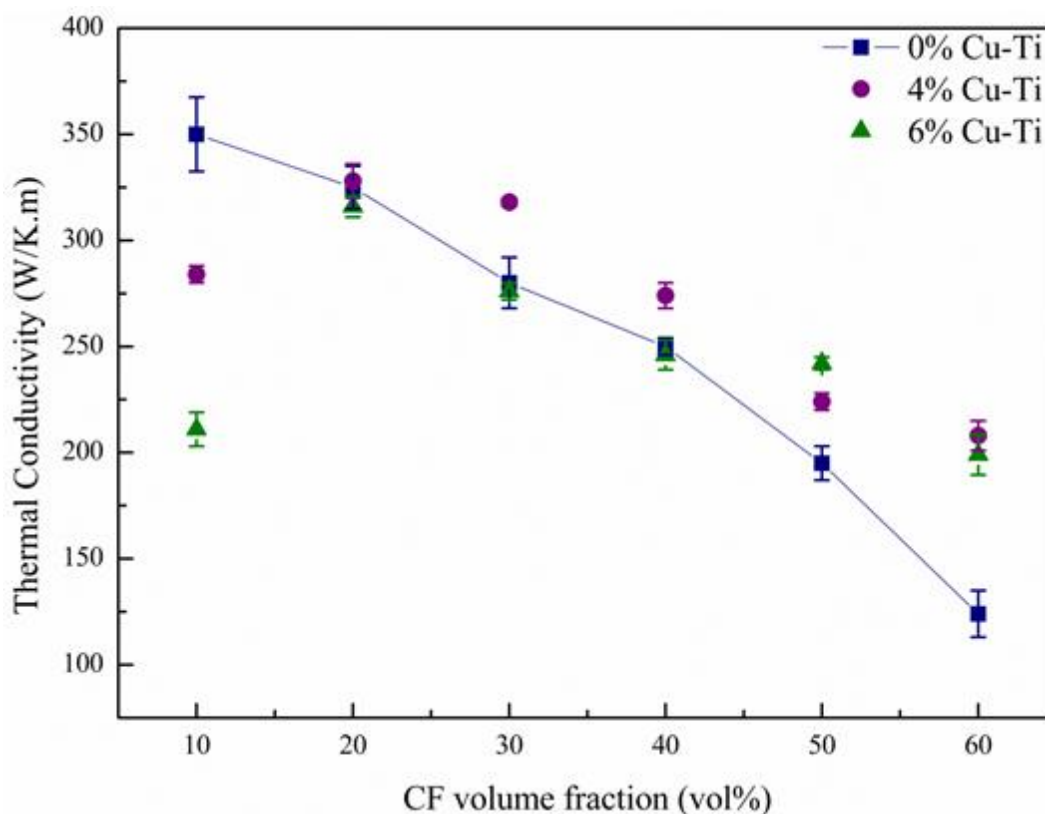


Figure 5.9. Thermal conductivity values obtained for composites without (blue) and with TiC interphases (purple = 4 vol% of liquid phase, green = 6 vol% of liquid phase).

5.3.1.3 Cu-Zr Additions

Previously, the amount of the Cu-Zr liquid phase was not mentioned. Indeed, the first characterizations were based solely on the presence or absence of the ZrC interphase. It appeared, therefore, that the increase in the quantity of liquid phase was trivial and would lead to an increase of the interphase. However, for optimum thermal conductivity, it has been shown, several times [69, 117], that an optimization of the thickness of the ZrC interphase was necessary in order to access a better transfer of properties between the matrix and the reinforcement. In the course of this research, several composite materials containing different volume fractions of Cu-Zr liquid phase have been prepared for 40 vol% of CF. For clarity, only three samples will be discussed here (Figure 5.10). One can notice that the amounts of Cu-Zr are higher than those of Cu-Ti (12-16 vol % of Cu-Zr vs 4-6 vol% of Cu-Ti). That is due to the fact that alloys have different compositions. Indeed, while the Cu-Ti alloy contains 27 at. % of Ti, the Cu-Zr only contains 6 at.% of Zr.

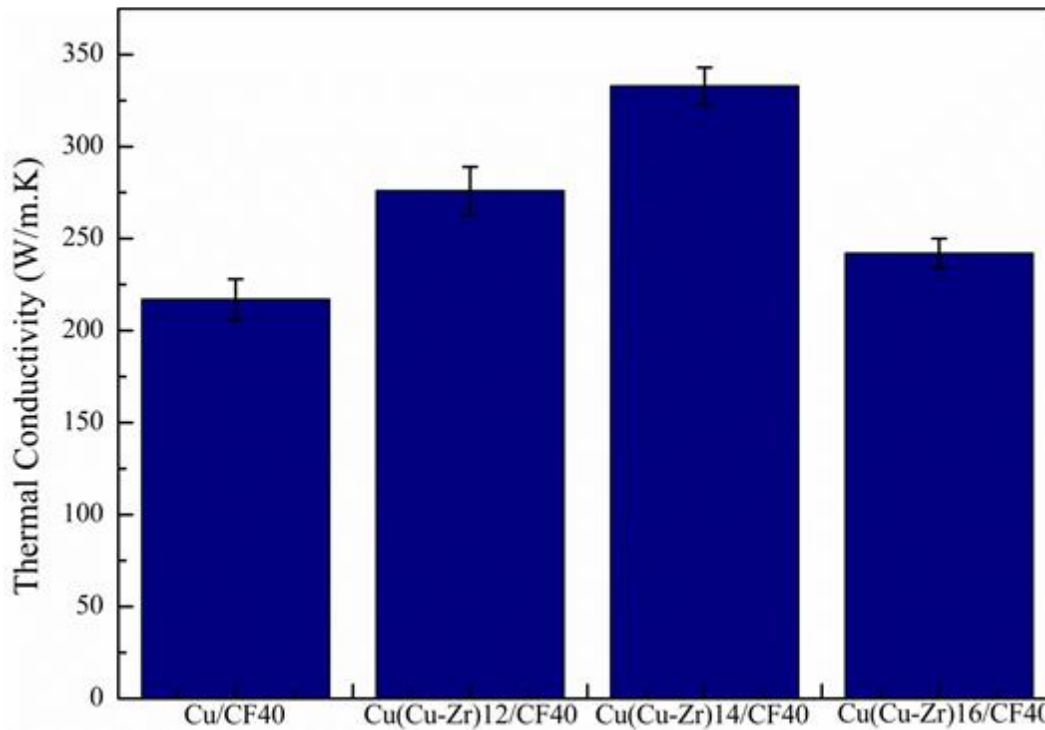


Figure 5.10. Histogram showing the evolution of thermal conductivity for composites with and without different volume fractions of Cu-Zr.

Depending on the different liquid phase fractions, the thermal conductivity increased to a maximum before decreasing. For 40% vol reinforcement, the maximum thermal conductivity was obtained for 14 vol % of liquid phase. This percentage is, therefore, adequate in the optimization of the conductivity of the composite material Cu(Cu-Zr)/C. Indeed, the maximum thermal conductivity obtained was 333 W/m.K for a composite material with 14 vol% of Cu-Zr. Initially, without the presence of Zr, this composite exhibited a thermal conductivity of 217 W/m.K. Therefore, the presence of ZrC at the interface allowed the increase in the conductivity of the composite material. The possible existence of a solid solution $(\text{Cu})_{\text{Zr}}$ within the matrix had little impact on the thermal conductivity, as discussed previously for Ti impurities.

While composites reinforced with carbon fibers resulted in low thermal conductivities, it is now important to turn to highly conductive reinforcements, such as diamond particles.

5.3.2. Cu/D composites

Before presenting the experimental data obtained for both CF and D composites, the effect of the thermal boundary resistance and the predictions made using the diffuse mismatch model (DMM) are discussed.

As mentioned in Section 2.5.2, the DMM takes into account the fact that all phonons are scattered at the interface. The density of states measurements from neutron scattering experiments were reported for Cu [118, 119], diamond [120], TiC [121], and ZrC [122] and were used for this work. The prominent peaks for Cu and D were located at 7 and 37 THz, respectively, which are close to the cutoff frequencies (7.3 and 40 THz, respectively). Thus, it is clear that the high difference between cutoff frequency for Cu and D caused the poor heat transfer through phonon elastic scattering. Therefore, the heat transfer needed to be done through inelastic scattering to enhance the thermal conductivity of a Cu/D composite.

To have a better idea on how to increase the heat transfer at the interface between Cu and D, the Debye's temperatures (Table 5.1) found in the literature are reported: $\theta_{D,Cu} = 310 \text{ K}$ and $\theta_{D,dia} = 1860 \text{ K}$. The TiC and ZrC Debye's temperatures were 614 and 491 K, respectively. As both temperatures were comprised between the ones of Cu and D, both carbides were interesting candidates for the role of the interphase.

Liang and Tsai used molecular dynamics to prove that the insertion of a layer between two materials with dissimilar phonon spectra was an effective way to reduce the

thermal boundary resistance. They used a system with an interlayer of a few nm, whose Debye temperature was close to the square root of the product of the Debye temperature of the two separated solids. In fact, they predicted a reduction of over 60 % of the thermal boundary resistance [123]. In the case of Cu/D composites, the Debye temperature of the intermediate layer should be close to $\theta_{D,i} = \sqrt{310 \times 1860} \sim 760 \text{ K}$, with ($\theta_{D,Cu} = 310 \text{ K}$, and $\theta_{D,dia} = 1860 \text{ K}$) to allow such reduction.

Table 5.1. List of Debye's temperatures of Cu, D, TiC, and ZrC.

Compound	Cu	D	TiC	ZrC
Debye's temperature (K)	310	1860	614	491

Equations (2.19) and (2.20) were used to calculate the transmitted phonon probability and thermal boundary resistance (phonon-phonon transfer), respectively, in the case of a Cu/D composite. The transmitted phonon probability was $\tau = 0.035$, which is extremely low and, therefore, representative of the poor heat transfer between Cu and D. The resulting thermal boundary resistance (R_i), estimated to be $1.29 \times 10^{-8} \text{ K.m}^2/\text{W}$, was used in the modified Maxwell analytical model presented in Section 2.5.3 to calculate the effective thermal conductivity of Cu/D composites.

The dispersion of diamond particles within the matrix was modeled using finite element modeling (FEM). Figure 5.11 shows the diamond particles modeled, as well as some random distributions for 10%, 30%, and 60% of diamond. The process involved filling a given volume of matrix material with diamond particles until reaching a maximum fill ($\Phi_{max} = 74.5\%$). Then diamond particles were randomly removed from the volume until reaching the volume fractions required for the calculations.

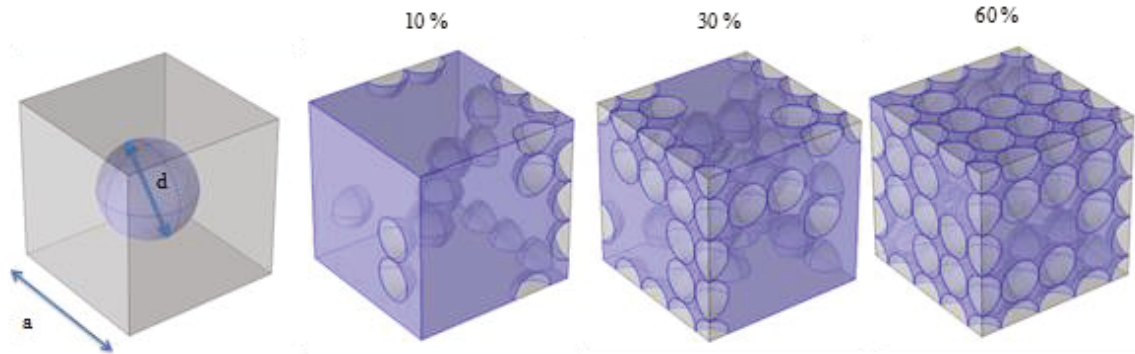


Figure 5.11. Schematics of the FEM of randomly distributed diamond particles in a copper matrix.

5.3.2.1 Interfacial Thermal Resistance Dependence

Figure 5.12 shows the evolution of the effective thermal conductivity of Cu/D composites of different volume fractions of diamond particles of $60\ \mu\text{m}$ in diameter. The calculated value of R_i is also reported in Figure 5.12 (discontinuous red line). The evolution of k_{eff} with respect to the interfacial thermal resistance (R_i) shows how detrimental a high R_i is to the thermal conductivity of the composites. One can notice the inversion point at which, for all volume fractions, the effective conductivity was the same for a given interfacial thermal resistance ($R_i \approx 5 \times 10^{-8}\ \text{K}\cdot\text{m}^2/\text{W}$). It is shown that, although higher volume fractions of reinforcements tended to increase the thermal conductivity, this was no longer true after the inversion point, where higher thermal conductivities were obtained for low volume fractions. Also, one can notice that the inversion point was situated at approximately $400\ \text{W}/\text{m}\cdot\text{K}$ which is the thermal conductivity of the matrix material (Cu). This indicates that for $R_i \approx 5 \times 10^{-8}\ \text{K}\cdot\text{m}^2/\text{W}$, the effect of the diamond reinforcements was completely compensated by R_i .

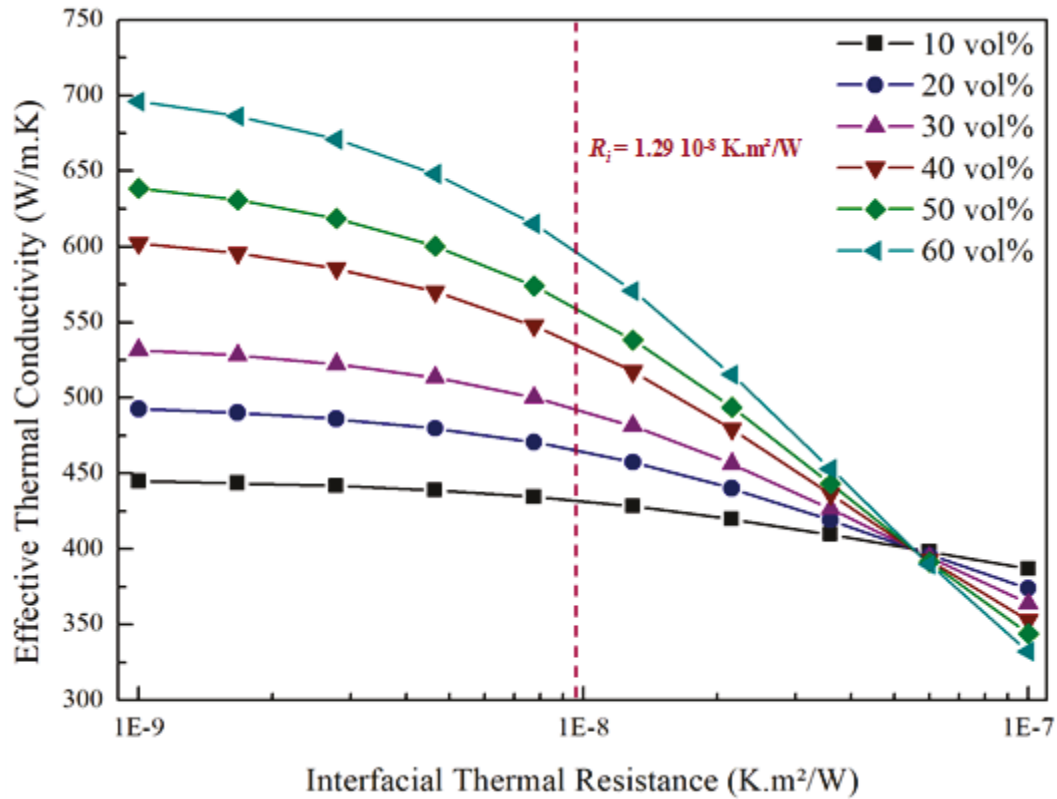


Figure 5.12. Effective thermal conductivity of Cu/D composites with respect to the interfacial thermal resistance for different volume fractions of diamond particles of 60 μm in diameter.

In Chapter 2, the effect of particle size on thermal conductivity, taken from Every and Tzou's work [52] was mentioned. It showed that thermal conductivity tends to increase with increasing particle sizes. Therefore, the effective thermal conductivity with respect to the interfacial thermal resistance for particle sizes of 150 μm was recalculated. The inversion point moved to higher interfacial thermal resistances, but occurred around 400 W/m.K, as in the case of 60 μm diamonds.

The experimental thermal conductivity values are included in Table 5.2. The theoretical thermal conductivity was calculated using the modified Maxwell model, with R_i being calculated using the DMM. One can notice that all theoretical conductivities are

overestimated. That is due to the interfacial thermal resistance, which is too low to be realistic. Indeed, the DMM assumes that the interface is perfect between diamond and Cu. However, in the case where no interphase is present, the adhesion between the matrix and the reinforcement in a nonreactive system was purely mechanical. Therefore, the interface can be rough, containing voids or other defects, as shown in Figure 5.13.

Table 5.2. Experimental and theoretical thermal conductivities with respect to diamond particle content. The theoretical conductivity was calculated using the modified Maxwell model and R_i calculated through the DMM.

Diamond Particle Content (vol %)	10	20	40
Theoretical thermal conductivity (W/m.K) for $R_i = 1.29 \times 10^{-8} \text{ K.m}^2/\text{W}$	428	458	517
Experimental thermal conductivity (W/m.K)	384 ± 23	360 ± 34	312 ± 22

In summary, the interfacial thermal resistance calculated through the DMM is underestimated, which makes the DMM incomplete for the prediction of thermal resistance.

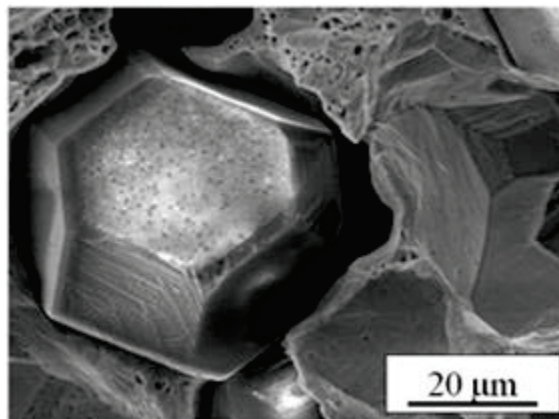


Figure 5.13. Real diamond-Cu interface with voids, roughness, and, therefore, poor contact.

5.3.2.2 Interphase Dependence

In order to predict the interfacial thermal resistance in Cu/D composites with TiC or ZrC interphases, one should calculate the phonon-phonon coupling from the Cu to the carbide and from the carbide to the diamond, as well as the contribution of the carbide interphase. For the phonon-phonon couplings, the DMM Equation (2.20) was used. The phonon transfer probabilities and thermal boundary resistances resulting from the calculations are reported in Table 5.3. One can note the difference in phonon transmission and interfacial resistance between the interfaces involving a carbide and a Cu/D one.

Table 5.3. Phonon transfer probabilities and thermal boundary resistances calculated through the DMM for different interfaces.

Interface	Phonon Transfer Probability ($\tau_{1 \rightarrow 2}$)	Thermal	Thermal Conductance ($h_c = 1/R_{Bd}$)
		Boundary Resistance (R_{Bd})	
Cu/D	0.035	1.29×10^{-8}	7.76×10^7
Cu/TiC	0.124	3.67×10^{-9}	2.73×10^8
Cu/ZrC	0.171	2.65×10^{-9}	3.77×10^8
TiC/D	0.205	3.03×10^{-9}	3.30×10^8
ZrC/D	0.150	3.45×10^{-9}	2.90×10^8

To fully calculate the interfacial thermal resistance with the interphase contribution, one should take in account the carbide's intrinsic physical properties. The interphases synthesized were over 100 nm thick. Therefore, their thermal conductivity needs to be taken into account. In order to do that, a term of thickness over the conductivity of the carbide in question was inserted into the sum of R_{ph-ph} as follows:

$$R_i = R_{Cu/(TiC \text{ or } ZrC)} + \frac{e_{(TiC \text{ or } ZrC)}}{k_{(TiC \text{ or } ZrC)}} + R_{(TiC \text{ or } ZrC)/D} \quad (5.6)$$

where $R_{Cu/(TiC \text{ or } ZrC)}$ and $R_{(TiC \text{ or } ZrC)/D}$ are the thermal boundary resistances at the Cu/carbide and carbide/D interfaces, respectively. The interphase's thickness is given by $e_{(TiC \text{ or } ZrC)}$ and $k_{(TiC \text{ or } ZrC)}$ is the carbide's thermal conductivity. The resulting interfacial thermal resistances, R_i , obtained are $R_{Cu/TiC/D} = 3.05 \times 10^{-8} \text{ K.m}^2/\text{W}$ and $R_{Cu/ZrC/D} = 1.59 \times 10^{-8} \text{ K.m}^2/\text{W}$. The dependence of the thermal conductivity on the interfacial thermal resistance, of a composite with carbide interphase, with respect to the diamond content is presented in Figure 5.14. The thermal conductivity decreased as thermal resistance increased, which was expected. However, the quality of the interphase is as important as for poorly adherent and even discontinuous interphases; R_i tends to increase, thus decreasing the overall thermal conductivity. Two experimental points are reported in Figure 5.14: composites with ZrC and TiC interphases. As can be seen, the experimental points fit nicely with the theoretical predictions which indicated that the Cu/carbide and carbide/D interfaces were adhered well and were continuous enough to have a positive effect on the conductivity of the composite.

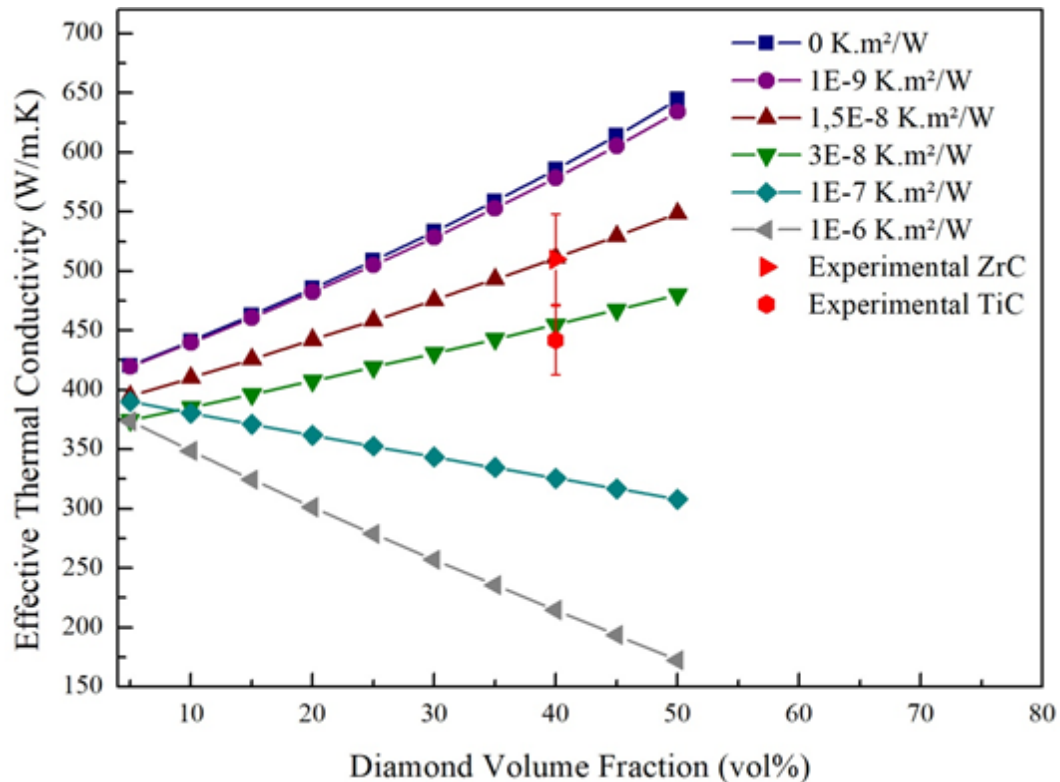


Figure 5.14. Effective thermal conductivity with respect to the diamond content for different interfacial thermal resistances. The experimental points corresponding to Cu(Cu-Zr)/D40 (blue) and Cu(Cu-Ti)/D40 (orange) are also reported.

The thermal conductivities of composites reinforced with diamond particles of 60 μm were synthesized with and without Cu-Ti additions. The conductivities obtained are reported in Figure 5.15. One can notice that Ti addition is not beneficial to the thermal conductivity of the composites with up to 30 vol% of diamond particles. That is due to the Ti impurities that remain in the Cu matrix for low volume fractions. Although the same behavior was observed for CF-reinforced composites but only at 10 vol% of CF, in the case of diamond particles, the surface at which the reaction occurs is different and might require longer sintering times or even higher temperatures. However, after 30 vol%, the presence of Ti improves the transfer at the interface causing the conductivities of composites with Cu-Ti to be higher than the ones without. Then the thermal conductivities tend to drop at

higher D contents, which can be due to the insufficient amount of Ti in the composite. Indeed, increased D contents result in larger surfaces to coat, therefore, more Ti should be added.

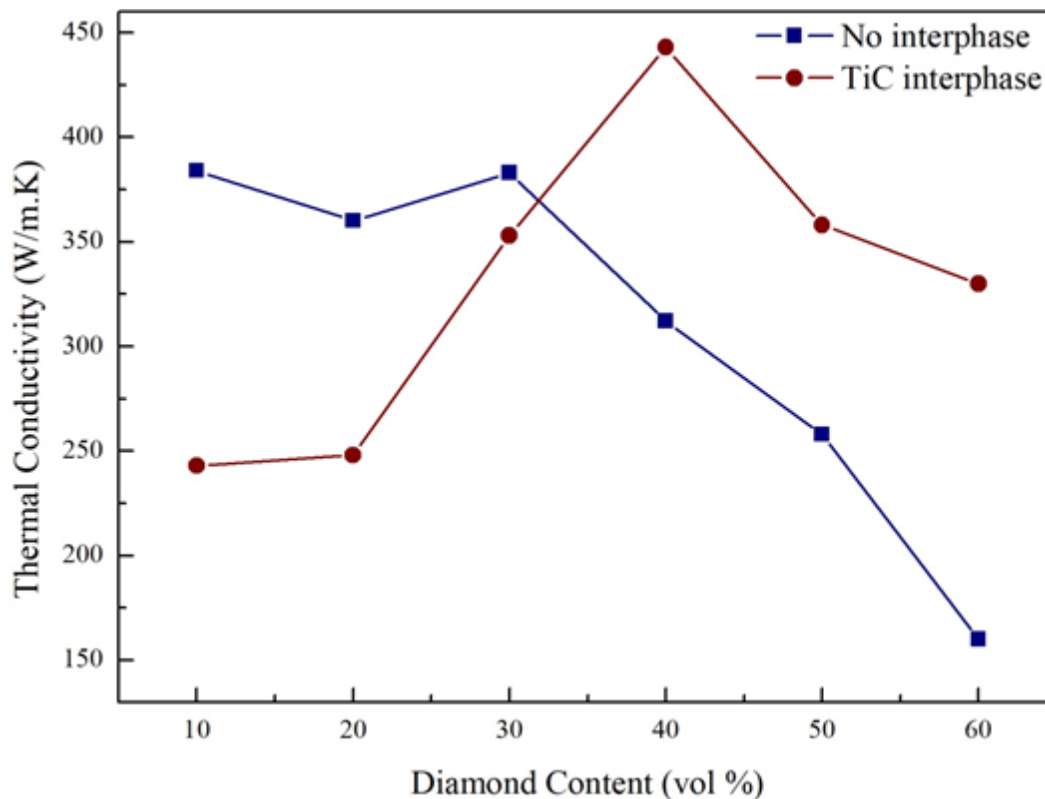


Figure 5.15. Thermal conductivities of Cu/D composites without Cu-Ti (blue) and with Cu-Ti addition (red).

To be able to compare the evolution of the thermal conductivity with respect to the interphase, composites with 40 vol% of diamond particles were synthesized without any additives, with Cu-Ti and with Cu-Zr. The histogram comparing the thermal conductivities is given in Figure 5.16. One can see how the presence of the interphase has a positive effect on the thermal conductivity. Indeed, the conductivity of the Cu/D composite with no interphase is situated below that of pure Cu, which is due to the poor interfacial bond between the matrix and the reinforcements, which cause the interfacial thermal resistance

to be very high. However, in the case of TiC and ZrC interphase-containing composites, the conductivities exceed that of pure Cu, proving that a composite effect takes place by combining the physical properties of both diamond and Cu. Therefore, the carbide interphases created during the solid-liquid co-existent phase process allow a better transfer of properties within the composite. This is due to the nature of the bonds that exist between the matrix, the interphase and the reinforcements (covalent).

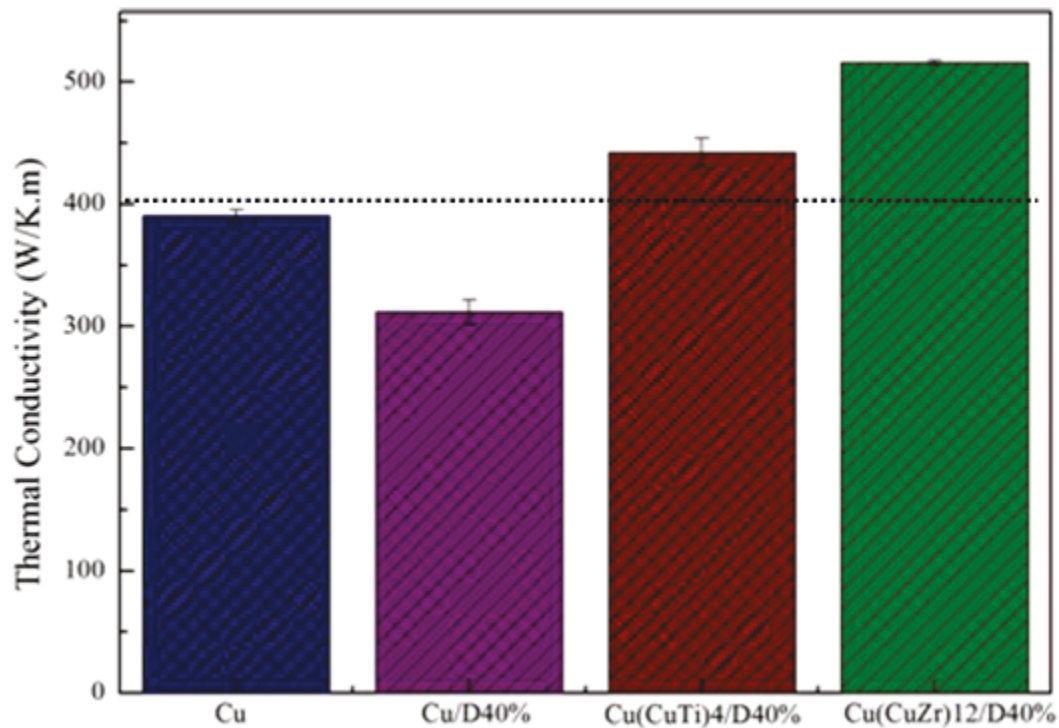


Figure 5.16. Histogram presenting the different thermal conductivities obtained for pure Cu, Cu/D with no interphase, Cu/D with TiC interphase, and Cu/D with ZrC interphase.

Dashed line corresponds to the thermal conductivity of pure Cu.

5.3.2.3 Particle size dependence

Since it was shown and confirmed that the diamond particle size has a non-negligible effect on the thermal conductivity of composite materials, calculations of the variation of thermal conductivity with respect to the particle size for various volume fractions were carried out. Figure 5.17 shows that the thermal conductivity is indeed impacted by the volume fraction of reinforcement as well as by the particle size.

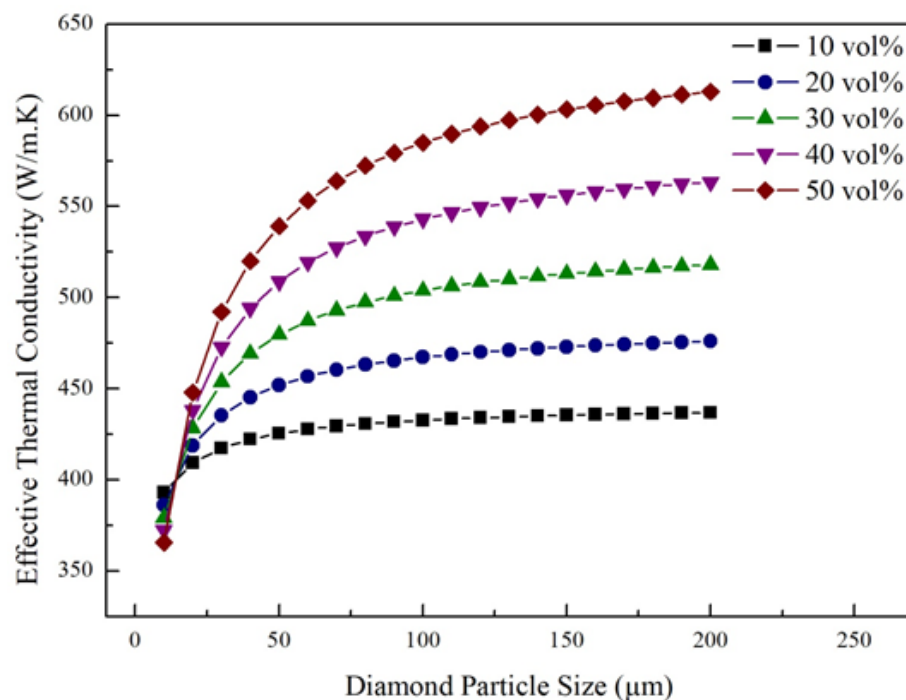


Figure 5.17. Effective thermal conductivity with respect to diamond particle size for several volume fractions of reinforcements.

Indeed, the increase of thermal conductivity of a composite is very drastic between 10 and 150 μm . It then reaches a maximum value and stabilizes with increasing particle size, assuming that the thermal conductivity is the same whatever the size of the diamond.

In order to show that effect, composite materials composed of 40 vol% of diamond reinforcements with different sizes, were synthesized. The experimental values were reported on the theoretical curves determined for 40 vol% of diamond reinforcements, in

Figure 5.18. The modified Maxwell model was used to calculate the ideal curve, while the FE model using a random distribution of diamond particles within the matrix was used to calculate the realistic curve. One can notice that the experimental thermal conductivities are in the same order of magnitude as the theoretical ones, as well as a slight increase of the conductivity with increasing diamond particle size. Also, a very good fit of the experimental points with the realistic model can be observed which indicates that the developed FE model describes quite nicely the synthesized composites. Finally, since the theoretical values are close to the experimental ones, one can say with some confidence, that the intrinsic thermal conductivity of the diamond particles used is close to 1000 W/m.K.

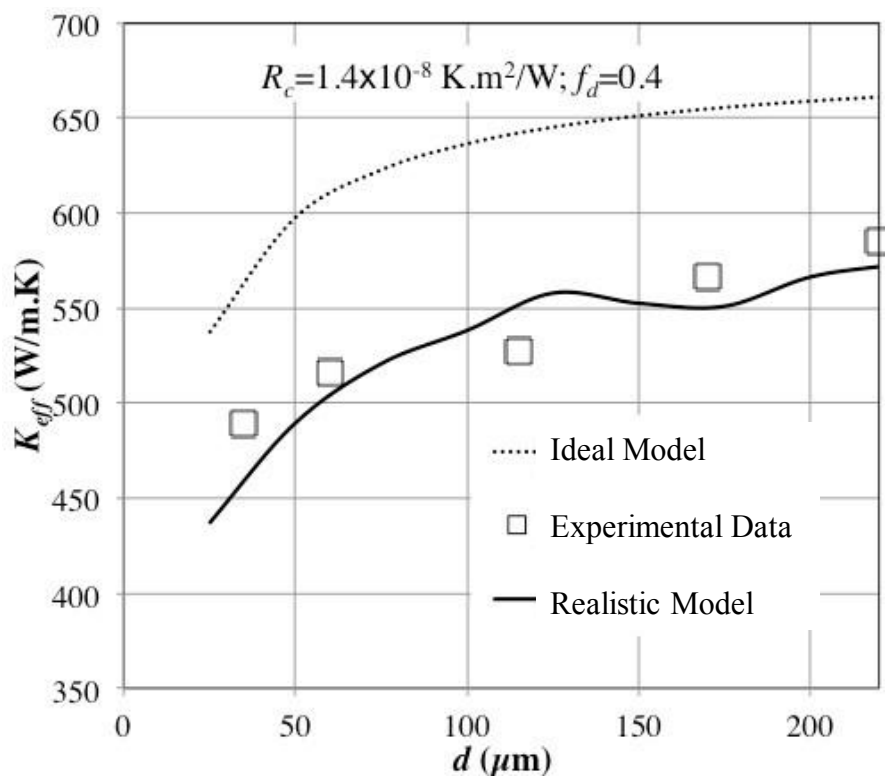


Figure 5.18. Theoretical (Ideal and Realistic Models) and experimental thermal conductivities of composites with 40 vol% of diamond reinforcements of different sizes.

5.4. Conclusion

The Cu/C composites that were discussed in Chapter 3 were used for thermal characterization. The thermal conductivity is in the center of this chapter as it is an important factor in the good performance of these composite materials as heat sink devices.

The composites presented here were synthesized using a powder metallurgy process relying on hot-pressing. However, some of these composites were fabricated through the use of the solid-liquid co-existent phase process. In fact, Ti and Zr have been able to form hundreds of nanometers-thick carbide interphases at the Cu/C interface. These interphases are expected to improve the thermal transfer within the composites.

Two systems were presented here, CF-reinforced composites, and D-reinforced composites. For CF reinforcements, one needs to take in account the distribution and the orientation of the CFs as their anisotropic shape, and hence thermal properties, cause the material to be anisotropic as well. Indeed, depending on the analysis direction, the CFs are either aligned along their primary axis or perpendicular to it. Knowing that the thermal conductivity of the CF is higher along its primary axis, the analysis along that direction often results in higher thermal conductivities. However, both directions (parallel to the axis of the CF or perpendicular) result in thermal conductivities which are inferior to the thermal conductivity of Cu. To simplify the anisotropy, supposing that the reinforcement has an average conductivity of 278 W/m.K, which is inferior to that of Cu and therefore, reduces the overall conductivity of the composite.

Also, it is not trivial to predict the thermal behavior of anisotropic materials with analytical models. Indeed, most problems arise from the absence of distribution, orientation, shape factor, and interfacial thermal resistance contributions.

The thermal conductivities of the composites synthesized using the solid-liquid co-existent phase process, with Ti and Zr, exhibit higher thermal conductivities than pure Cu/CF composites, although the overall thermal conductivity is still lower than pure Cu's. However, the presence of a carbide interphase is beneficial for the transfer of properties within the composite.

The impact of the liquid phase quantity inserted in the composite, and therefore Ti or Zr amounts, is also shown. In fact, there is a Zr content which presents the highest thermal conductivity.

The thermal characterizations that were carried out on the D-reinforced composites allowed achieving a thermal conductivity which is higher for the composite than for pure Cu. Along with the experimental analyses analytical calculations were carried out to predict the interfacial thermal resistances and effective thermal conductivities for Cu/D, Cu-Ti/D and Cu-Zr/D composites. It was shown that the DMM model used to predict the interfacial thermal resistance in a Cu/D composite is not realistic enough as it does not take in account any morphological aspects of the interface, such as roughness, voids, and other defects.

Also, the interfacial thermal resistance in a Cu-X/D composite (with X = Ti, Zr) includes the contribution of the carbide ($e^{TiC \text{ or } ZrC} / k_{TiC \text{ or } ZrC}$ term). The solid-liquid co-existent phase process is shown to allow reaching interfacial thermal resistances ranging between $1.5 - 3.05 \times 10^{-8}$ K.m²/W, which is fairly low. Indeed, a thin film obtained through sputtering on clean and smooth surfaces, usually exhibits thermal resistances in the order of 10^{-9} K.m²/W. Therefore, nearly thin film-quality interphases can be obtained through a process which can easily be industrialized.

The impact of diamond particle size on thermal conductivity, which had been mentioned in the literature, was confirmed. The highest thermal conductivities achieved for one given volume fraction of diamond particles were for diameters of 170 to 200 μm .

On another note, the predictions of thermal conductivities for the composites that contain Ti and Zr are quite accurate, although further investigations should be carried out to confirm and establish a methodology.

Finally, the thermal conductivities of the composites obtained through the solid-liquid co-existent phase process are well situated when compared to the literature and past investigations at the ICMCB. For the sake of comparison, Figure 5.19 gathers the thermal conductivities obtained for Cu/D composites with B_4C , Cr_3C_2 and submicronic Cu interphases obtained during T. Guillemet's PhD [5], as well as the ones presented in this work for TiC and ZrC interphases.

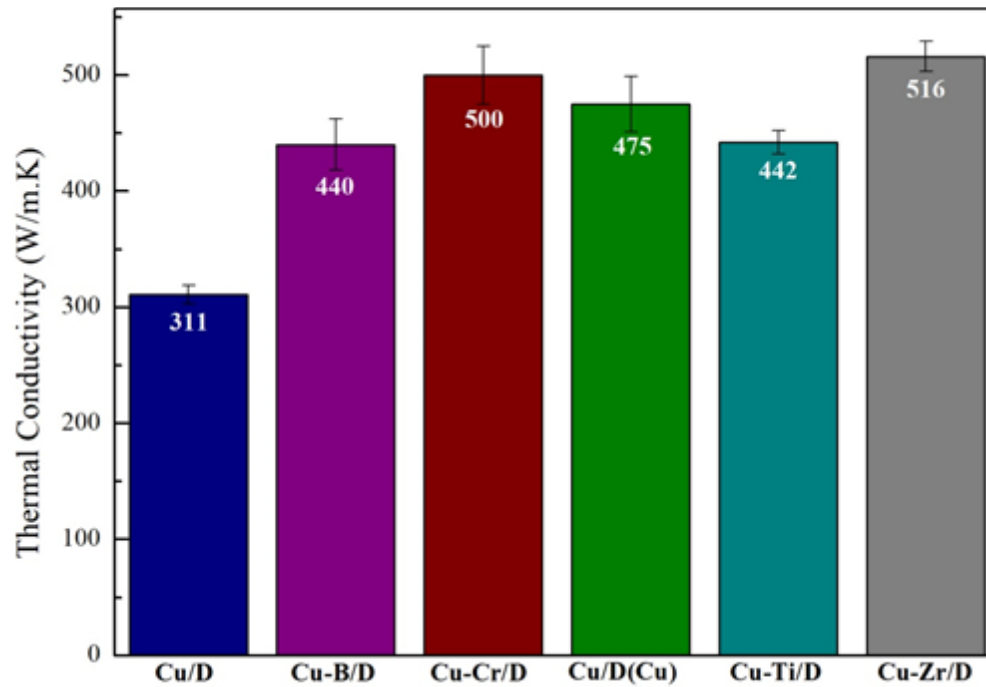


Figure 5.19. Comparison of thermal conductivities obtained for Cu/D composites with various interfaces [5].

The efficiency of these composites materials in terms of conductivity has been determined however, their holding under thermal cycling will allow determining where our composites are situated in the path of commercialization.

6. General Conclusions and Outlooks

6.1 General conclusion

Diamond was situated in the center of this work. It is a very promising candidate for thermal dissipation applications due to its exceptional thermal properties. The objective was to use diamond-based multi-materials to replace heat-spreads and heat-sinks in microelectronic components. Indeed, to enhance the miniaturization and power density of components, one should focus on the dissipation of the heat created during the component's operation.

The diamond-based multi-material solution was investigated in the framework of a dual French-American PhD program between the College of Engineering of the University of Nebraska-Lincoln, in the U.S., and the Institute of Condensed Matter Chemistry, at the University of Bordeaux, in France. The joint team offered to replace metallic heat-sink materials by thermally efficient composite materials coated with thin diamond films.

In France, carbon reinforced copper matrix composites using an innovative solid-liquid co-existent phase process during hot-pressing, were fabricated. This process takes in account the insertion of an alloyed powder which has a lower melting point when compared with the matrix and reinforcement powders. Therefore, this powder will be in liquid state during the sintering at high temperature, while the remaining powders will stay in solid state. The alloyed powders used contained a carbide forming additive (Ti or Zr) whose diffusion and reactivity were enhanced by the liquid phase. The final composites were fully dense, even at high reinforcement volume fractions, and consisted of carbon reinforcements, coated with a carbide interphase, homogeneously dispersed in a Cu matrix.

The purity of the Cu matrix strongly depends on the amount of carbon present in the composites. In fact, low volume fractions of carbon decrease the driving force initiating the diffusion of the carbide forming element which then tends to remain in solid solution in Cu. It was shown that, depending on the element, the final properties of the composite can be compromised. Indeed, the negative impact of Ti in Cu solid solution on the thermal conductivity of Cu, while the effect of Zr in Cu solid solution is almost negligible.

Further analyses on the TiC interphases have confirmed the composition of the carbide predicted by thermodynamic simulations. Indeed, the solid-liquid co-existent phase process allowed the creation of a near-stoichiometric TiC. Electron energy-loss spectroscopy also showed that metallic Cu can be found in the interfacial zone, which indicates the solidification of Cu during the sintering process.

Work was also carried out on the optimization of the synthesis process to obtain controlled thickness interphases. Indeed, with increasing liquid contents the thickness of the interphases increases as well.

TEM analyzes have allowed determining the microstructure of the interphases. The FCC structure of both carbides, and observed microstructures constituted of nanograins, in the case of TiC, and nano-columns, in the case of ZrC, were confirmed. Also, no detachment either at the Cu-interphase, or at the interphase-C interfaces were noticed.

Thermal characterizations have allowed determining the thermal performance of the composites and showed that the presence of an interphase is crucial for a proper transfer of heat load within the composite. Analytical models were compared with experimental data and were shown to be effective in the case of isotropic reinforcements; however, they are not representative of composites with anisotropic reinforcements. The phonon-phonon

transfer from Cu to diamond has been enhanced through the addition of the carbide interphases.

The interfacial thermal resistances that are unavoidable in multi-materials, were investigated and showed that the solid-liquid co-existent phase process helps with the creation of less resistive interfaces. In fact, it is evidenced that the control of the interfacial thermal resistance has a non-negligible effect on the overall thermal conductivity of the composite materials.

Finally, the overall thermal conductivity of Cu/D and Cu/CF composites were improved with the presence of the ZrC and TiC interphases.

In the U.S., laser-assisted combustion flame CVD was used to deposit polycrystalline diamond films on Cu/CF composites. The presence of carbon fibers on the surface allowed the creation of voids during deposition which increased the number of mechanical gripping and nucleation sites. The diamond films deposited have shown to have a good adherence with the composite substrate. The diamond film quality increased with deposition duration which shows that the quality of the diamond film depends on the immediate surface on which it is being deposited. Indeed, deposition on diamond induces easier formation of sp^3 bonded carbon, while direct deposition on Cu induces the deposition of a mixture of sp^2 and sp^3 .

CO_2 -assisted combustion flame CVD allowed the increase of the phase purity of the deposited diamond film. Indeed, the enhanced vibrations caused by the CO_2 laser with the ethylene molecules results in higher energy levels which initiate sp^3 C deposition rather than sp^2 . Investigations on KrF-assisted combustion flame CVD on composite substrates was also initiated with promising results which are presented in the next section.

6.2 Future directions

6.2.1 Diamond deposition

As mentioned in *Chapter 4*, the final investigation carried out at LANE-UNL consisted of determining what effect a given surface has on the quality and residual stresses of diamond films deposited through laser-assisted combustion flame CVD. A reminder of the quality factors and residual stresses given in Chapter 4, below in Table 6.1.

The increase of the quality factors, for laser-assisted diamond films, indicates the increase of the phase purity of the film. CO₂-assisted depositions resulted in the highest phase purities which can indicate that vibrational excitation is more suitable for quality increase than electronic excitation. Evaluations of diamond films deposited on various substrates should be carried out so as to prove that the surface is not responsible for this difference.

While it is mentioned that no effect of the surface morphology has been noticed on diamond phase purity, a variation of the residual stresses with respect to the surface morphology was observed. In fact, the highest residual stresses are obtained for the carbon powder surfaces. Although carbon powders are distributed on the overall surface, the depth of the voids created is smaller than the ones obtained from graphite flake and carbon fiber consumption. Such considerations should be confirmed by carrying out cross-section analyzes on the diamond films and composite substrates. Being able to visualize the depth of the voids created as well as the mechanical gripping mechanism for each surface will allow confirming our hypotheses.

Table 6.1. Quality factors and residual stresses of diamond films deposited on composites with various surfaces during 60 min with and without laser excitation.

Surface	Laser conditions	Quality factor (%)	Residual stresses (GPa)
Carbon fibers	No laser	87.72	-0,01
Carbon fibers	CO ₂ – 800 W	94,73	-0,05
Carbon fibers	KrF – 40 Hz, 25 kV	94.05	-0,09
Graphite flakes	No laser	95.26	-0,08
Graphite flakes	CO ₂ – 800 W	99,00	-0,07
Graphite flakes	KrF – 40 Hz, 25 kV	97.84	-0,08
Carbon Powder	No laser	95.28	-0,10
Carbon powders	CO ₂ – 800 W	98,80	-0,12
Carbon Powder	KrF – 40 Hz, 25 kV	96.43	-0,13

6.2.2 Thermal evaluation of diamond films

While bulk diamond can reach thermal conductivities up to 2000 W/m.K, CVD diamond is often limited to 1100 W/m.K. That is due to the imperfections of the diamond film, such as impurities, grain boundaries and grain sizes. Thermal evaluation of our diamond films would allow determining its efficiency as a heat-spread for potential commercialization. It is, however, important to note that for diamond films of several micrometers, the interfacial thermal resistance needs to be taken in account, as it can be significant to the overall thermal behavior of the diamond film. The following measurements were carried out by Associate Professor Andrzej Kusiak at the I2M, in Bordeaux.

Modulated Photothermal Radiometry (MPTR) was carried out on the diamond films deposited on Cu/CF 40 vol% composite substrates. MPTR is a thermal metrology technique which relies on the measurement of infrared radiations emitted by a surface in response to a transient photothermal excitation. The set-up is shown in Figure 6.1.

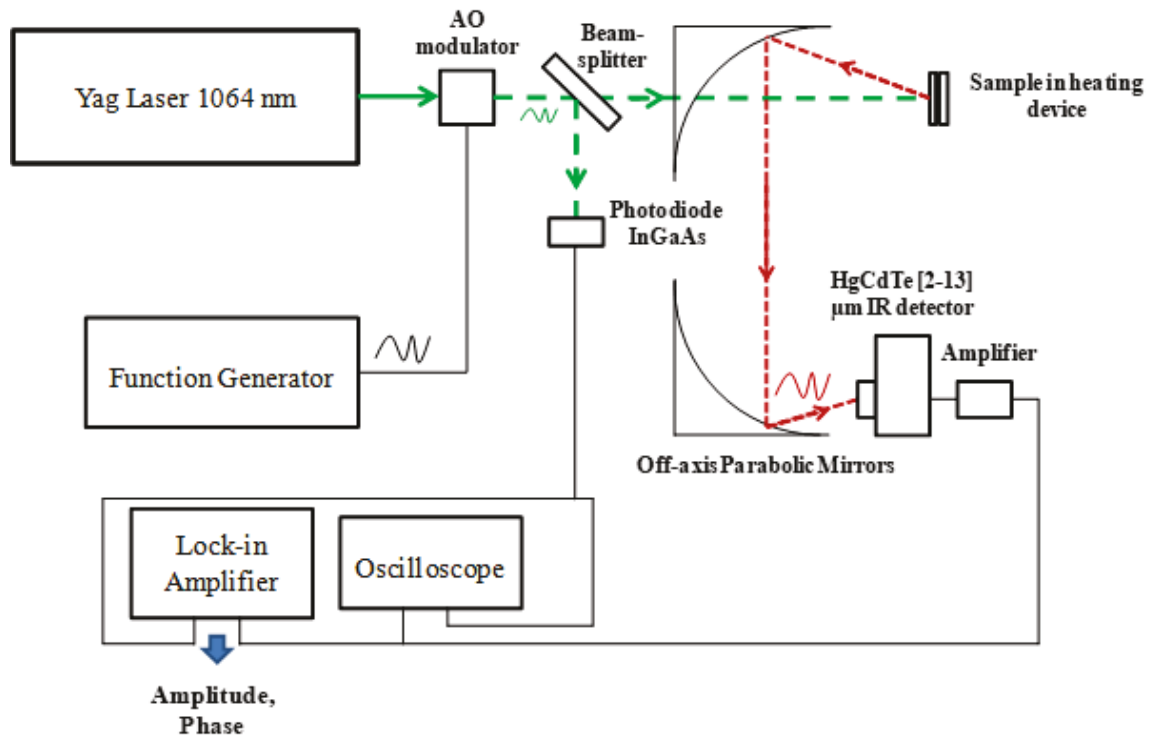


Figure 6.1. Schematic set-up of MPTR.

To get the most accurate evaluation, the conductivity of the substrate needs to be taken into account. Knowing that the composites are anisotropic, two thermal conductivities are considered, the thermal conductivity along the carbon fiber axis, and the conductivity perpendicular the carbon fiber axis, as shown in Figure 6.2.

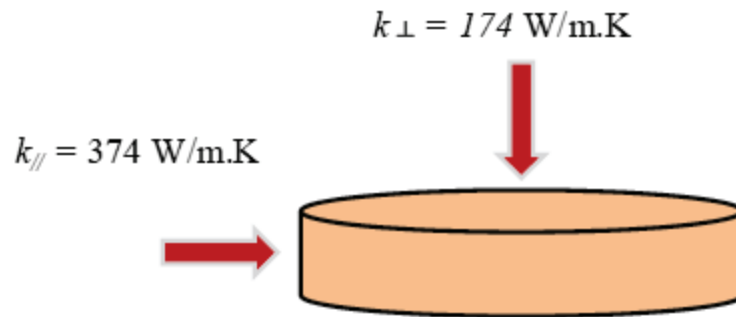


Figure 6.2. Parallel (along the CF axis) and perpendicular thermal conductivities of a Cu/CF 40 % composite material used as substrate for diamond deposition.

The diamond films were coated with 100 nm of Pt thin film which acts as an optical transducer; so that the diamond film can absorb the laser excitation (convert photons into a heat flux). Indeed, diamond is optically transparent, and its absorptivity is close to zero.

The first results obtained are given in Figure 6.3. The experimental points are followed by the modeled phase change which take in account the experimental conductivities of the substrate (in green), the conductivity which is parallel to the fiber axis (in red), and the one which is perpendicular to the fiber axis (in blue). One can see that at low frequencies the anisotropy of the composite substrate influences the phase change. The identified thermal resistance for this diamond film was found to be $2.5 \times 10^{-8} \text{ K.m}^2/\text{W}$.

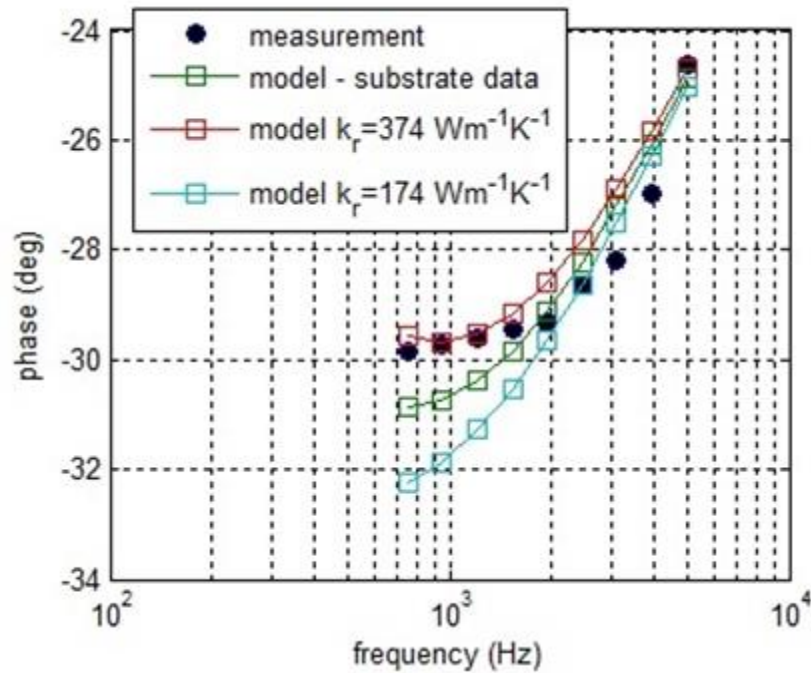


Figure 6.3. Calculated and experimental phase of a diamond film deposited on Cu/CF 40 vol% composite.

The results reported here are only preliminary. Difficulties have been encountered because of the roughness of the diamond films. Indeed, the diamond films deposited are polycrystalline and therefore exhibit a very rough surface. Also, knowing that voids are created during the diamond deposition process, additional roughness is present because of the uneven deposition in the voids and on the remaining Cu. Additional characterization of the thickness and roughness should allow retrieving sufficient information on the film morphology to adapt the models to the experimental data.

6.2.3 Thermal evaluation of composites

While thermal conductivities of the composite materials were determined, information is lacking on the behavior of the composites after thermal cycling. At the time

at which this dissertation is written, thermal cycles are in progress following the program given in Figure 6.4.

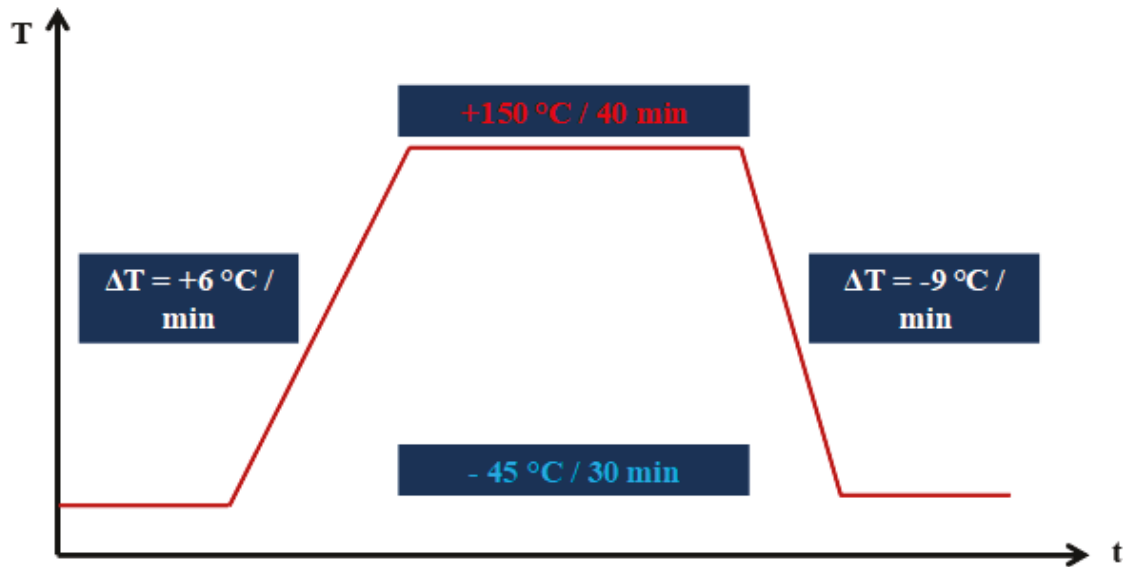


Figure 6.4. Thermal cycle program imposed to Cu/CF, Cu(Cu-Ti)/CF and Cu(Cu-Zr)/CF composites with 40 vol% of carbon fibers.

The cycle starts at $-45 \text{ }^\circ\text{C}$, then the temperature is increased up to $+150 \text{ }^\circ\text{C}$, with a heating rate of $6 \text{ }^\circ\text{C}/\text{min}$. After a plateau of 40 min at $150 \text{ }^\circ\text{C}$, the temperature is cooled to $-45 \text{ }^\circ\text{C}$, with a cooling rate of $-9 \text{ }^\circ\text{C}/\text{min}$, and maintained for 30 min . The cycle is repeated 50, 100, 200, and 500 times. At each series, thermal diffusivity measurements are carried out to determine whether the thermal conductivity of the composite remains the same as before thermal cycling or if it deteriorates. Indeed, the composites containing TiC and ZrC interphases should have increased life times, therefore, their conductivity should not decrease after just a few cycles. On the other hand, Cu/CF composites with no interphases are expected to deteriorate in terms of thermal properties because the purely mechanical bonding between matrix and reinforcement will suffer from expansion and compression after thermal cycling. Therefore, a delamination at the Cu-CF interface is expected.

6.2.4 Thermal evaluation of interphases

While analytical models have allowed predicting the interfacial thermal resistance, experimental data would confirm our hypotheses. Also, TiC and ZrC are not defined compounds; therefore, their stoichiometry can vary in $1-x$ (TiC_{1-x} and ZrC_{1-x}). Therefore, their actual thermal conductivities are not known. To this end, thermal scanning microscopy (SThM), which is a thermal metrology technique inspired by atomic force microscopy (AFM), will be used. In this case the AFM tip is replaced by a SThM probe which will act as the heat source and the detector. This SThM probe has a size of a few tens of nanometers, which makes it suitable for nano and micro-scale analyzes. The probe scans the surface while applying a temperature gradient and allows mapping the surface which is analyzed. These measurements were carried out by Professor Jean-Luc Battaglia and Research Engineer, Alain Sommier, at I2M, in Bordeaux.

Figure 6.5 shows the topographies in AFM and SThM mode obtained on a Cu/CF composite with 4 vol% of Cu-Ti, therefore with a TiC interphase.

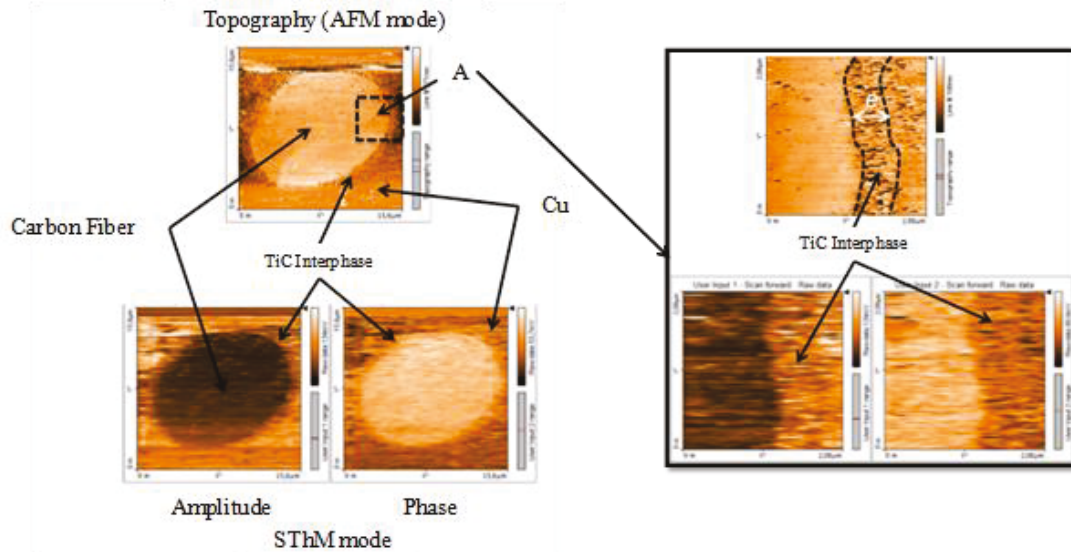


Figure 6.5. AFM and SThM modes on the surface of a Cu-Ti/CF composite.

Figure 6.6 gather the amplitude and phase variations collected from the probe while scanning a CF/TiC/Cu zone. One can observe the smooth decrease of both amplitude and phase when the probe passes from the CF to the TiC and from the TiC to the Cu. This indicates that the CF-TiC and TiC-Cu interfaces have low thermal resistance.

Although these results seem promising, this technique is very sensitive to the state of the surface. Indeed, contact mode analyzes require very smooth surfaces in order to get interpretable results. Therefore, several polishing techniques are planned to be tested until determining the most suitable one for the smoothest surface possible. Some options include ion polishing and electro-polishing.

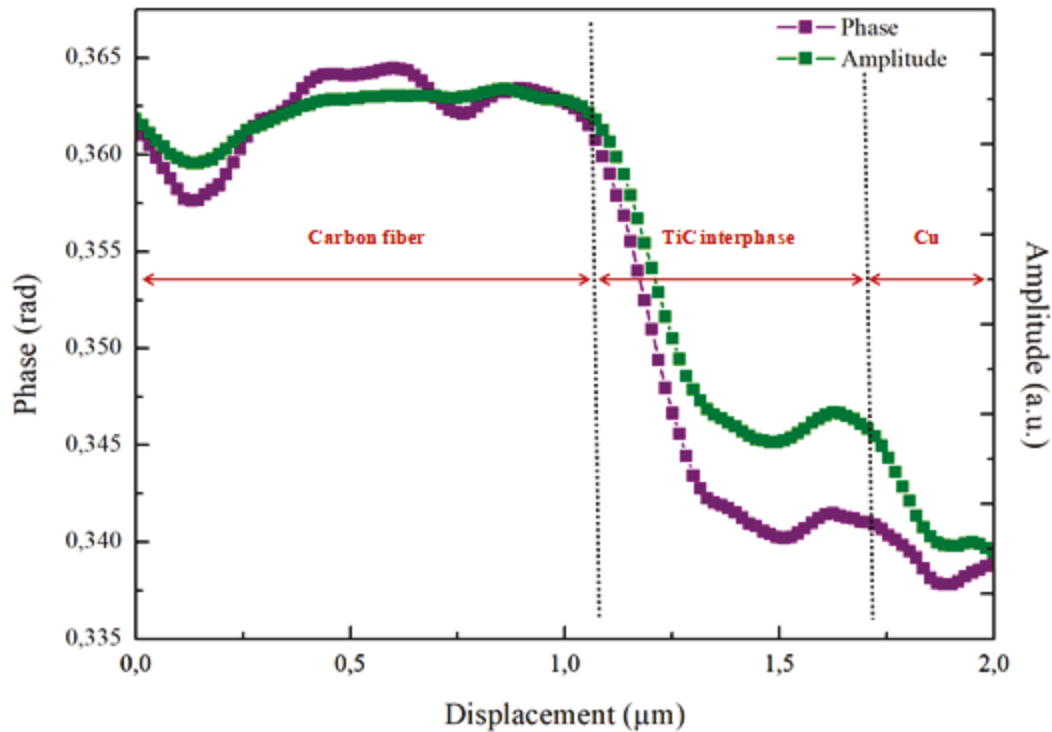


Figure 6.6. Phase and amplitude variations reported from the SThM probe while scanning a Carbon fiber/TiC/Cu zone.

6.2.5 Alternative interphases

TiC and ZrC interphases have been successfully synthesized in Cu/CF and Cu/D composites. However, these interphases do not present the highest thermal conductivities (both k_{TiC} and k_{ZrC} are [30-45] W/m.K). One can imagine using the solid-liquid co-existent phase process to synthesize interphases with higher thermal conductivities, such as MAX phases.

MAX phases are a new class of nanolaminated carbide and nitride materials with a common formula $M_{n+1}AX_n$ with $n = 1 - 3$. Due to their laminated structure (Figure 6.7), these phases exhibit a unique combination of ceramic and metallic properties, as first reviewed by Barsoum et al. [124].

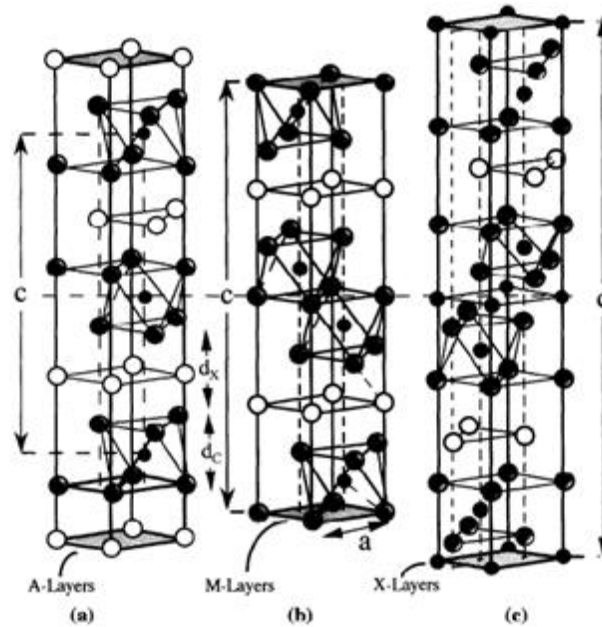


Figure 6.7. Crystal structure of the 211 ($n=1$), 312 ($n=2$), and 413 ($n=3$) $M_{n+1}AX_n$ phases.

Adapted from [124].

MAX phases usually present higher thermal conductivities than regular carbide materials. Also, used as interphases, their nanolaminated structure would also increase mechanical resistance. Indeed, laminated interphases allow the deviation of cracks. For the sake of curiosity and since powders were available at the ICMBC, Ti_3SiC_2 was selected as a potential candidate. This sub-project was carried out in collaboration with Mr. Tadhg Mahon, at the ICMCB-CNRS.

The first step was to synthesize the MAX phase as bulk using induction melting by mixing in the appropriate proportions Ti, Si and C powders. The resulting pellet was ground, and the powder was analyzed through routine XRD from 8 to 80 °. The XRD pattern is given in Figure 6.8.

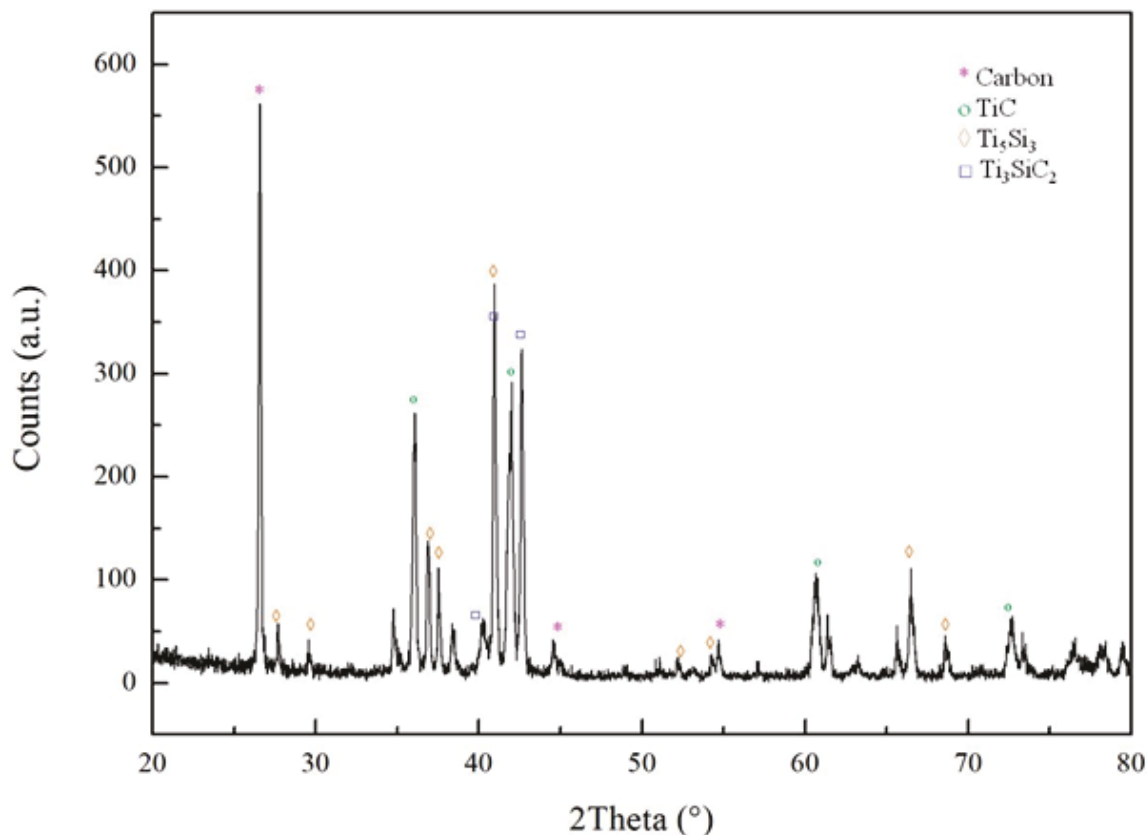


Figure 6.8. XRD pattern of powder obtained from Induction melting of Si, Ti, and C at the appropriate proportions for the synthesis of Ti_3SiC_2 .

One can observe that the powder obtained is not pure, in fact Ti_5Si_3 , TiC and C were indexed. Therefore, multiple steps of homogenization and induction melting are necessary to obtain the desired Ti_3SiC_2 phase.

The solid-liquid co-existent phase process was used by combining pure Cu powder, Ti-alloyed Cu powder, Si-alloyed Cu powder and carbon fibers. After mixing, the powders were densified at $950\text{ }^\circ\text{C}$, during 30 min, under a pressure of 50 MPa which was applied during the plateau. Indeed, both Cu-Ti and Cu-Si powders melt at 888.5 and $854.8\text{ }^\circ\text{C}$, respectively.

The resulting pellets were 99 % dense. The SEM micrographs given in Figure 6.9 represent the cross-section of the composite. One can see that interphases are present; however, they do not look as homogeneous as they were when only Cu-Ti was added.

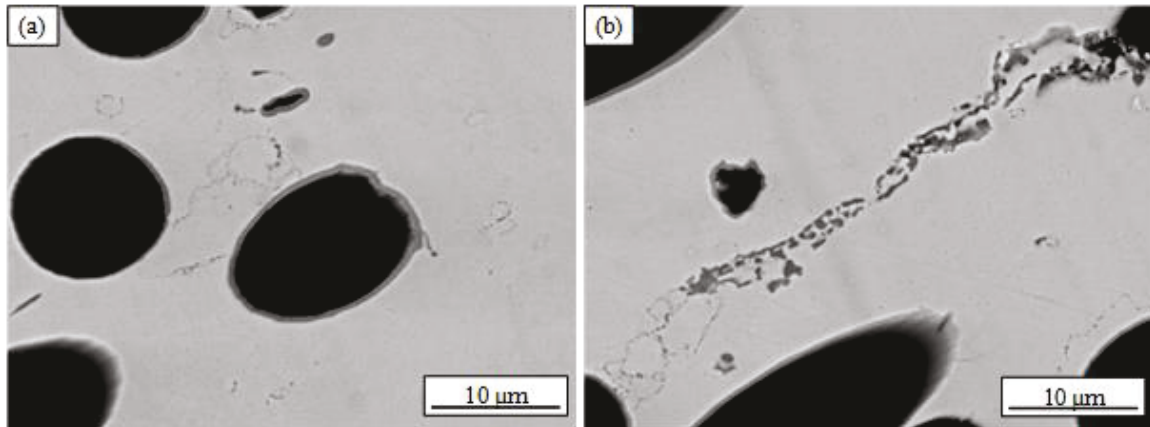


Figure 6.9. SEM micrographs of the cross-section of a composite synthesized with Cu-Ti and Cu-Si liquid phases.

Also, on Figure 6.9(b), the presence of residues in the Cu matrix were observed. To determine their and the interphase's composition, EDS line scans were carried out, and are given in Figure 6.10.

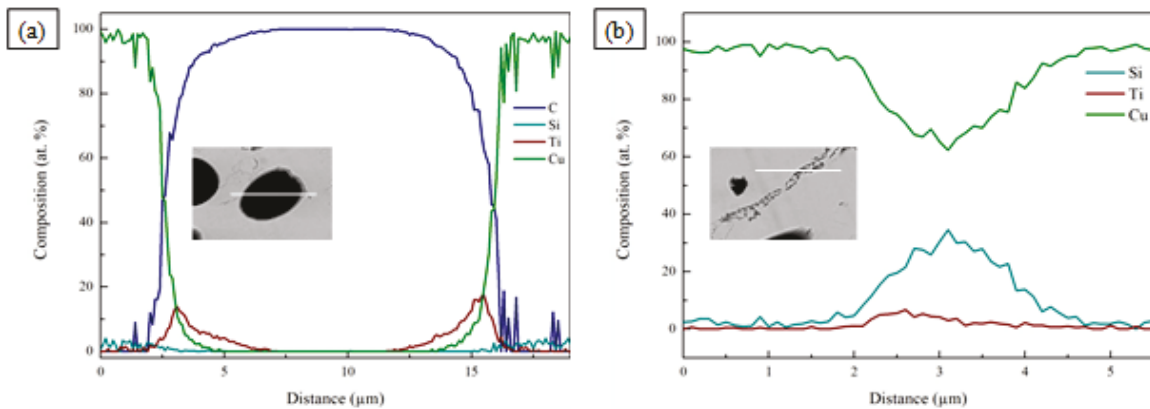


Figure 6.10. EDS line scans (a) across a carbon fiber, (b) across the residues in the matrix.

One can see that the interphase is primarily constituted of TiC which has also been confirmed through XRD (Figure 6.11). On the other hand, the line scan given in Figure 6.10(b) clearly shows the presence of Si in these traces in the matrix. Therefore, the diffusion of Si is limited within the Cu matrix. That could be due to oxygen which can be present around the initial powders under the form of oxides.

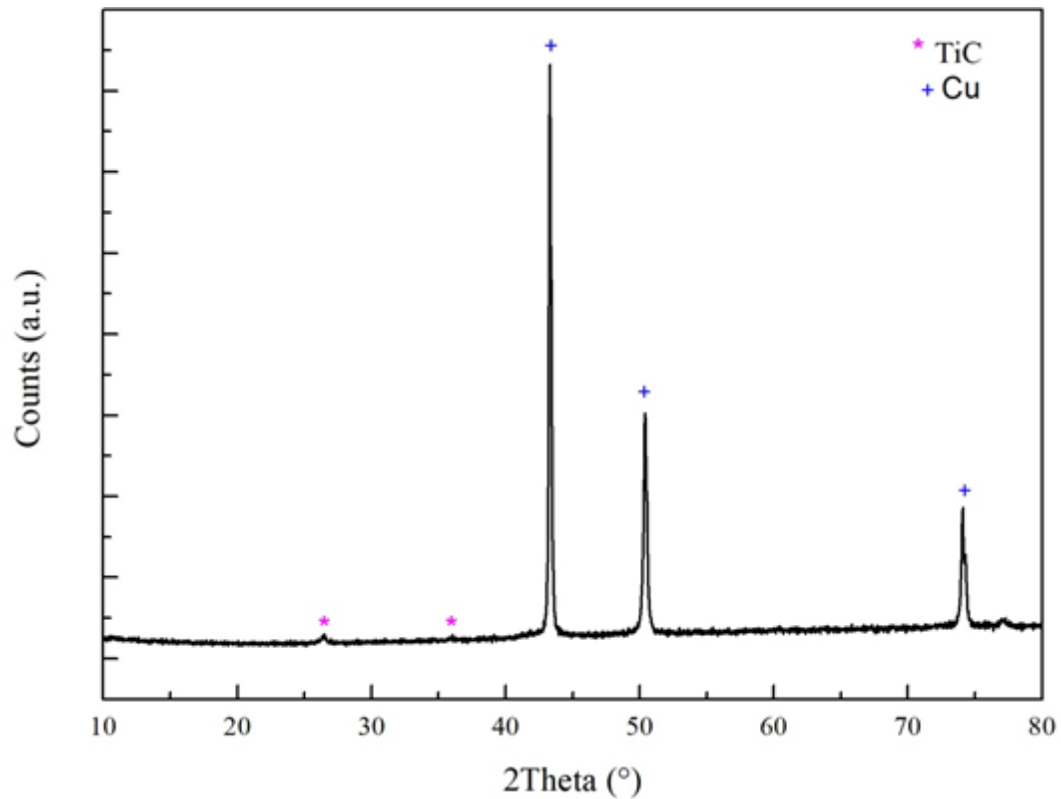


Figure 6.11. XRD pattern of a composite synthesized with Cu-Ti and Cu-Si liquid phases.

Further investigations should be carried out, where different compositions, sintering programs, and heat treatments are tested. Finally, thermal properties of the interphases and of the overall composite should be analyzed.

Finally, from an academic and human perspective, this French-American dual PhD initiative should be continued in order to maintain this strong partnership between our two universities, encourage sharing scientific knowledge and technical expertise from both sides, and develop exciting new projects for the future.

REFERENCES

- [1] International Energy Agency, World Energy Outlook, Paris, 2010. <http://www.worldenergyoutlook.org/media/weowebiste/2010/WEO2010.pdf>.
- [2] I. Ferain, C.A. Colinge, J.-P. Colinge, Multigate transistors as the future of classical metal–oxide–semiconductor field-effect transistors, *Nature*. 479 (2011) 310–316. doi:10.1038/nature10676.
- [3] G.E. Moore, Cramming more components onto integrated circuits (Reprinted from *Electronics*, pg 114-117, April 19, 1965), *Proc. Ieee*. 86 (1965) 82–85. doi:10.1109/N-SSC.2006.4785860.
- [4] M.M. Waldrop, The chips are down for Moore’s law, *Nature*. 530 (2016) 144–147. doi:10.1038/530144a.
- [5] T. Guillemet, Diamond -based heat spreaders for power electronic packaging applications, University of Nebraska-Lincoln/ University of Bordeaux, 2013.
- [6] M. Wang, UV LASER-ASSISTED DIAMOND DEPOSITION, University of Nebraska-Lincoln, 2014.
- [7] Z. Xie, Y. Zhou, X. He, Y. Gao, J. Park, H. Ling, L. Jiang, Y. Lu, Fast Growth of Diamond Crystals in Open Air by Combustion Synthesis with Resonant Laser Energy Coupling, *Cryst. Growth Des.* 10 (2010) 1762–1766. doi:10.1021/cg9014515.
- [8] T. Guillemet, A. Kusiak, L. Fan, J.M. Heintz, N. Chandra, Y. Zhou, J.F. Silvain, Y. Lu, J.L. Battaglia, Thermal characterization of diamond films through modulated photothermal radiometry, *ACS Appl. Mater. Interfaces*. 6 (2014) 2095–2102. doi:10.1021/am405188r.
- [9] J.-F. Silvain, A. Veillère, Y. Lu, Copper-Carbon and Aluminum-Carbon Composites Fabricated by Powder Metallurgy Processes, *J. Phys. Conf. Ser.* 525 (2014) 012015. doi:10.1088/1742-6596/525/1/012015.
- [10] J.-F. Silvain, A. Veillere, J.-M. Heintz, C. Vincent, T. Guillemet, G. Lacombe, Y. Lu, N. Chandra, The role of controlled interfaces in the thermal management of copper-carbon composites, *Emerg. Mater. Res.* 1 (2011) 75–88. doi:dx.doi.org/10.1680/emr11.0016.
- [11] W. Kaiser, W.L. Bond, Nitrogen, A Major Impurity in Common Type I Diamond, *Phys. Rev.* 115 (1959) 857–863. <https://link.aps.org/doi/10.1103/PhysRev.115.857>.

- [12] X. Liu, X. Jia, Z. Zhang, M. Zhao, W. Guo, G. Huang, H.A. Ma, Synthesis and characterization of new “bCN” diamond under high pressure and high temperature conditions, *Cryst. Growth Des.* 11 (2011) 1006–1014. doi:10.1021/cg100945n.
- [13] K. Lonsdale, Divergent-Beam X-Ray Photography of Crystals, *Philos. Trans. R. Soc. A Math. Phys. Eng. Sci.* 240 (1947) 219–250. doi:10.1098/rsta.1947.0002.
- [14] J. (John) Wilks, E. Wilks, *Properties and applications of diamond*, Butterworth-Heinemann, 1991.
- [15] M. Mertens, M. Mohr, K. Brühne, H.J. Fecht, M. Łojkowski, W. Świążkowski, W. Łojkowski, Patterned hydrophobic and hydrophilic surfaces of ultra-smooth nanocrystalline diamond layers, *Appl. Surf. Sci.* 390 (2016) 526–530. doi:10.1016/j.apsusc.2016.08.130.
- [16] J.R. Olson, R.O. Pohl, J.W. Vandersande, A. Zoltan, T.R. Anthony, W.F. Banholzer, Thermal conductivity of diamond between 170 and 1200 K and the isotope effect, *Phys. Rev. B.* 47 (1993) 14850–14856. doi:10.1103/PhysRevB.47.14850.
- [17] N. Takabatake, T. Kobayashi, D. Sekine, T. Izumi, Thermal characterization of CVD diamond film by photoacoustic method, *Appl. Surf. Sci.* 159 (2000) 594–598. doi:10.1016/S0169-4332(00)00062-3.
- [18] H.P. Ho, K.C. Lo, S.C. Tjong, S.T. Lee, Measurement of thermal conductivity in diamond films using a simple scanning thermocouple technique, *Diam. Relat. Mater.* 9 (2000) 1312–1319. doi:10.1016/S0925-9635(00)00231-4.
- [19] S.D. Wolter, D.A. Borca-Tasciuc, G. Chen, N. Govindaraju, R. Collazo, F. Okuzumi, J.T. Prater, Z. Sitar, Thermal conductivity of epitaxially textured diamond films, *Diam. Relat. Mater.* 12 (2003) 61–64. doi:10.1016/S0925-9635(02)00248-0.
- [20] T. Anthony, W. Banholzer, J. Fleischer, L. Wei, P. Kuo, R. Thomas, R. Pryor, Thermal diffusivity of isotopically enriched ¹²C diamond., *Phys. Rev. B. Condens. Matter.* 42 (1990) 1104–1111. doi:10.1103/PhysRevB.42.1104.
- [21] F.P. BUNDY, H.T. HALL, H.M. STRONG, R.H. WENTORF, Man-Made Diamonds, *Nature.* 176 (1955) 51–55. doi:10.1038/176051a0.
- [22] J. Asmussen, D.K. Reinhard, *Diamond films handbook.*, 2002. doi:10.1201/9780203910603.
- [23] S. Matsumoto, Y. Sato, M. Tsutsumi, N. Setaka, Growth of diamond particles from methane-hydrogen gas, *J. Mater. Sci.* 17 (1982) 3106–3112. doi:10.1007/BF01203472.

- [24] J.C. Angus, H.A. Will, W.S. Stanko, Growth of diamond seed crystals by vapor deposition, *J. Appl. Phys.* 39 (1968) 2915–2922. doi:10.1063/1.1656693.
- [25] P. Bachmann, D. Leers, D. Wiechert, P. Bachmann, D. Leers, D.W. Diamond, C. Vapour, *Diamond Chemical Vapour Deposition, J. Phys. IV Colloq.* 02 (1991) pp.C2–907–C2–913.
- [26] M. Sunkara, J.C. Angus, C.C. Hayman, F.A. Buck, Nucleation of diamond crystals, in: *Carbon N. Y.*, 1990: pp. 745–746. doi:10.1016/0008-6223(90)90265-Z.
- [27] M. Murakawa, S. Takeuchi, Y. Hirose, Diamond coating of a long substrate by use of a combustion flame, *Surf. Coatings Technol.* 39-40 (1989) 235–240. doi:10.1016/0257-8972(89)90057-1.
- [28] Y. Hirose, S. Amanuma, K. Komaki, The synthesis of high-quality diamond in combustion flames, *J. Appl. Phys.* 68 (1990) 6401–6405. doi:10.1063/1.346859.
- [29] T. Schubert, B. Trindade, T. Weißgärber, B. Kieback, Interfacial design of Cu-based composites prepared by powder metallurgy for heat sink applications, *Mater. Sci. Eng. A.* 475 (2008) 39–44. doi:10.1016/j.msea.2006.12.146.
- [30] K. Yoshida, H. Morigami, Thermal properties of diamond/copper composite material, *Microelectron. Reliab.* 44 (2004) 303–308. doi:10.1016/S0026-2714(03)00215-4.
- [31] T. Schubert, Ciupiński, W. Zieliński, A. Michalski, T. Weißgärber, B. Kieback, Interfacial characterization of Cu/diamond composites prepared by powder metallurgy for heat sink applications, *Scr. Mater.* 58 (2008) 263–266. doi:10.1016/j.scriptamat.2007.10.011.
- [32] O. Beffort, F.A. Khalid, L. Weber, P. Ruch, U.E. Klotz, S. Meier, S. Kleiner, Interface formation in infiltrated Al(Si)/diamond composites, *Diam. Relat. Mater.* 15 (2006) 1250–1260. doi:10.1016/j.diamond.2005.09.036.
- [33] H. GUO, Y. HAN, X. ZHANG, C. JIA, J. XU, Microstructure and thermophysical properties of SiC/Al composites mixed with diamond, *Trans. Nonferrous Met. Soc. China.* 25 (2015) 170–174. doi:10.1016/S1003-6326(15)63592-0.
- [34] R. Tavangar, J.M. Molina, L. Weber, Assessing predictive schemes for thermal conductivity against diamond-reinforced silver matrix composites at intermediate phase contrast, *Scr. Mater.* 56 (2007) 357–360. doi:10.1016/j.scriptamat.2006.11.008.
- [35] S. Kaciulis, A. Mezzi, R. Donnini, P. Deodati, R. Montanari, N. Ucciardello, M. Amati, M. KazemianAbyaneh, C. Testani, Microchemical characterisation of

- carbon-metal interface in Ti6Al4V-SiCf composites, *Surf. Interface Anal.* 42 (2010) 707–711. doi:10.1002/sia.3219.
- [36] G. Kumar, K.N. Prabhu, Review of non-reactive and reactive wetting of liquids on surfaces, *Adv. Colloid Interface Sci.* 133 (2007) 61–89. doi:10.1016/j.cis.2007.04.009.
- [37] K. Landry, S. Kalogeropoulou, N. Eustathopoulos, Wettability of carbon by aluminum and aluminum alloys, *Mater. Sci. Eng. A.* 254 (1998) 99–111. doi:10.1016/S0921-5093(98)00759-X.
- [38] Z.Y. Ma, S.C. Tjong, L. Gen, In-situ Ti-TiB metal-matrix composite prepared by a reactive pressing process, *Scr. Mater.* 42 (2000) 367–373. doi:10.1016/S1359-6462(99)00354-1.
- [39] Mortimer D. et Nicholas M., The wetting of Carbon and Carbides by Copper Alloy, *J. Mater. Sci.* 8 (1973) 640.
- [40] D.A. Mortimer, M. Nicholas, The wetting of carbon by copper and copper alloys, *J. Mater. Sci.* 5 (1970) 149–155. doi:10.1007/BF00554633.
- [41] A. Veillère, A. Sundaramurthy, J.M. Heintz, J. Douin, M. Lahaye, N. Chandra, S. Enders, J.F. Silvain, Relationship between interphase chemistry and mechanical properties at the scale of micron in Cu/Cr/CF composite, *Acta Mater.* 59 (2011) 1445–1455. doi:10.1016/j.actamat.2010.11.006.
- [42] Chung, Chih Yu, C.H. Chu, M.T. Lee, C.M. Lin, S.J. Lin, Effect of titanium addition on the thermal properties of diamond/Cu-Ti composites fabricated by pressureless liquid-phase sintering technique, *Sci. World J.* 2014 (2014). doi:10.1155/2014/713537.
- [43] H. Pal, V. Sharma, Thermal conductivity of carbon nanotube-silver composite, *Trans. Nonferrous Met. Soc. China (English Ed.)* 25 (2015) 154–161. doi:10.1016/S1003-6326(15)63590-7.
- [44] S. Volz, R. Carminati, *Microscale and nanoscale heat transfer*, 2007. doi:10.1007/11767862.
- [45] G. V Chester, A. Thellung, The Law of Wiedemann and Franz, *Proc. Phys. Soc.* 77 (1961) 1005–1013. doi:10.1088/0370-1328/77/5/309.
- [46] F.P. Incropera, D.P. DeWitt, T.L. Bergman, A.S. Lavine, *Fundamentals of Heat and Mass Transfer*, 2007. doi:10.1016/j.applthermaleng.2011.03.022.
- [47] P.L. Kapitza, Heat transfer and superfluidity of helium II, *Phys. Rev.* 60 (1941) 354–

355. doi:10.1103/PhysRev.60.354.
- [48] E.T. Swartz, R.O. Pohl, Thermal boundary resistance, *Rev. Mod. Phys.* 61 (1989) 605–668. doi:10.1103/RevModPhys.61.605.
- [49] M.L. Roukes, M.R. Freeman, R.S. Germain, R.C. Richardson, M.B. Ketchen, Hot electrons and energy transport in metals at millikelvin temperatures, *Phys. Rev. Lett.* 55 (1985) 422–425. doi:10.1103/PhysRevLett.55.422.
- [50] A. Majumdar, P. Reddy, Role of electron-phonon coupling in thermal conductance of metal-nonmetal interfaces, *Appl. Phys. Lett.* 84 (2004) 4768–4770. doi:10.1063/1.1758301.
- [51] J. TAO, X. ZHU, W. TIAN, P. YANG, H. YANG, Properties and microstructure of Cu/diamond composites prepared by spark plasma sintering method, *Trans. Nonferrous Met. Soc. China.* 24 (2014) 3210–3214. doi:10.1016/S1003-6326(14)63462-2.
- [52] A.G. Every, Y. Tzou, D.P.H. Hasselman, R. Raj, The effect of particle size on the thermal conductivity of ZnS/diamond composites, *Acta Metall. Mater.* 40 (1992) 123–129. doi:10.1016/0956-7151(92)90205-S.
- [53] D.P.H. Hasselman, L.F. Johnson, Effective Thermal Conductivity of Composites with Interfacial Thermal Barrier Resistance, *J. Compos. Mater.* 21 (1987) 508–515. doi:10.1177/002199838702100602.
- [54] A. Devpura, P.E. Phelan, R.S. Prasher, Size effects on the thermal conductivity of polymers laden with highly conductive filler particles, *Microscale Thermophys. Eng.* 5 (2001) 177–189. doi:10.1080/108939501753222869.
- [55] R.P. Kusy, Influence of particle size ratio on the continuity of aggregates, *J. Appl. Phys.* 48 (1977) 5301–5305. doi:10.1063/1.323560.
- [56] W.J. Kim, M. Taya, K. Yamada, N. Kamiya, Percolation study on electrical resistivity of SiC/Si₃N₄ composites with segregated distribution, *J. Appl. Phys.* 83 (1998) 2593. doi:10.1063/1.367020.
- [57] S.K.B.H.A.T. Yya, S. Basu, Effect of size, shape and oxide content of metal particles on the formation of segregated networks in pvc composites, (1978) 177–183.
- [58] a. Devpura, P.E. Phelan, R.S. Prasher, Percolation theory applied to the analysis of thermal interface materials in flip-chip technology, *Proc. of IThERM.* 1 (2000) 21–28. doi:10.1109/ITHERM.2000.866803.

- [59] Q. Liu, X.B. He, S. Bin Ren, T.T. Liu, Q.P. Kang, X.H. Qu, Fabrication and thermal conductivity of copper matrix composites reinforced with Mo₂C or TiC coated graphite fibers, *Mater. Res. Bull.* 48 (2013) 4811–4817. doi:10.1016/j.materresbull.2013.07.064.
- [60] W. Yang, L. Zhou, K. Peng, J. Zhu, L. Wan, Effect of tungsten addition on thermal conductivity of graphite/copper composites, *Compos. Part B Eng.* 55 (2013) 1–4. doi:10.1016/j.compositesb.2013.05.023.
- [61] J. Li, H. Zhang, Y. Zhang, Z. Che, X. Wang, Microstructure and thermal conductivity of Cu/diamond composites with Ti-coated diamond particles produced by gas pressure infiltration, *J. Alloys Compd.* 647 (2015) 941–946. doi:10.1016/j.jallcom.2015.06.062.
- [62] Q. Kang, X. He, S. Ren, L. Zhang, M. Wu, C. Guo, W. Cui, X. Qu, Preparation of copper-diamond composites with chromium carbide coatings on diamond particles for heat sink applications, *Appl. Therm. Eng.* 60 (2013) 423–429. doi:10.1016/j.applthermaleng.2013.05.038.
- [63] H. Bai, N. Ma, J. Lang, C. Zhu, Y. Ma, Thermal conductivity of Cu/diamond composites prepared by a new pretreatment of diamond powder, *Compos. Part B Eng.* 52 (2013) 182–186. doi:10.1016/j.compositesb.2013.04.017.
- [64] B. Dewar, M. Nicholas, P.M. Scott, The solid phase bonding of copper, nickel and some of their alloys to diamonds, *J. Mater. Sci.* 11 (1976) 1083–1090. doi:10.1007/BF00553116.
- [65] L. Weber, R. Tavangar, On the influence of active element content on the thermal conductivity and thermal expansion of Cu-X (X = Cr, B) diamond composites, *Scr. Mater.* 57 (2007) 988–991. doi:10.1016/j.scriptamat.2007.08.007.
- [66] Q.L. Che, J.J. Zhang, X.K. Chen, Y.Q. Ji, Y.W. Li, L.X. Wang, S.Z. Cao, L. Guo, Z. Wang, S.W. Wang, Z.K. Zhang, Y.G. Jiang, Spark plasma sintering of titanium-coated diamond and copper–titanium powder to enhance thermal conductivity of diamond/copper composites, *Mater. Sci. Semicond. Process.* 33 (2015) 67–75. doi:10.1016/j.mssp.2015.01.041.
- [67] G.A. López, E.J. Mittemeijer, The solubility of C in solid Cu, *Scr. Mater.* 51 (2004) 1–5. doi:10.1016/j.scriptamat.2004.03.028.
- [68] Q.L. Che, X.K. Chen, Y.Q. Ji, Y.W. Li, L.X. Wang, S.Z. Cao, Y.G. Jiang, Z. Wang, The influence of minor titanium addition on thermal properties of diamond/copper composites via in situ reactive sintering, *Mater. Sci. Semicond. Process.* 30 (2015) 104–111. doi:10.1016/j.mssp.2014.09.050.

- [69] K. Chu, C. Jia, H. Guo, W. Li, On the thermal conductivity of Cu-Zr/diamond composites, *Mater. Des.* 45 (2013) 36–42. doi:10.1016/j.matdes.2012.09.006.
- [70] C.Y. Chung, M.T. Lee, M.Y. Tsai, C.H. Chu, S.J. Lin, High thermal conductive diamond/Cu-Ti composites fabricated by pressureless sintering technique, *Appl. Therm. Eng.* 69 (2014) 208–213. doi:10.1016/j.applthermaleng.2013.11.065.
- [71] J. Li, X. Wang, Y. Qiao, Y. Zhang, Z. He, H. Zhang, High thermal conductivity through interfacial layer optimization in diamond particles dispersed Zr-alloyed Cu matrix composites, *Scr. Mater.* 109 (2015) 72–75. doi:10.1016/j.scriptamat.2015.07.022.
- [72] S. Ren, Q. Hong, J. Chen, X. He, X. Qu, The influence of matrix alloy on the microstructure and properties of (flake graphite + diamond)/Cu composites by hot pressing, *J. Alloys Compd.* 652 (2015) 351–357. doi:10.1016/j.jallcom.2015.08.191.
- [73] D. Arnaud, J. Barbery, R. Biais, B. Fargette, P. Naudot, *Propriétés du cuivre et de ses alliages*, 2008.
- [74] S.-J. Park, *Carbon Fibers*, 2015. doi:10.1361/asmhba0003354.
- [75] C. Van Nguyen, S.K. Sistla, S. Van Kempen, N.A. Giang, A. Bezold, C. Brockmann, F. Lange, A comparative study of different sintering models for Al₂O₃, *J. Ceram. Soc. Japan.* 124 (2016) 301–312. doi:10.1039/C5RA08965D.
- [76] J.-O. Andersson, T. Helander, L. Hoglund, P. Shi, B. Sundman, Thermo-Calc & DICTRA, computational tools for materials science., *CALPHAD Comput. Coupling Phase Diagrams Thermochem.* 26 (2002) 273–312. doi:10.1016/S0364-5916(02)00037-8.
- [77] N. Saunders, A.P. Miodownik, Editors., *Calculation of Phase Diagrams (CALPHAD): A Comprehensive Guide.*, Elsevier, 1998.
- [78] B.S. Hans Lukas, Suzana G. Fries, *Computational Thermodynamics The Calphad Method*, (2007) 324. doi:10.1017/CBO9780511804137.
- [79] J. Wang, C.-L. Liu, C. Leinenbach, U.E. Klotz, P.J. Uggowitzer, J.F. Löffler, Experimental investigation and thermodynamic assessment of the Cu-Sn-Ti ternary system., *CALPHAD Comput. Coupling Phase Diagrams Thermochem.* 35 (2011) 82–94. doi:10.1016/j.calphad.2010.12.006.
- [80] L.F.S. Dumitrescu, M. Hillert, Reassessment of the solubility of TiC and TiN in Fe., *ISIJ Int.* 39 (1999) 84–90. doi:10.2355/isijinternational.39.84.

- [81] L.F.S. Dumitrescu, M. Hillert, B. Sundman, A reassessment of Ti-C-N based on a critical review of available assessments of Ti-N and Ti-C., *Zeitschrift Fuer Met.* 90 (1999) 534–541.
- [82] R. Arroyave, T.W. Eagar, L. Kaufman, Thermodynamic assessment of the Cu-Ti-Zr system, *J. Alloys Compd.* 351 (2003) 158–170. doi:10.1016/S0925-8388(02)01035-6.
- [83] Y.Z. Wan, Y.L. Wang, H.L. Luo, X.H. Dong, G.X. Cheng, Effects of fiber volume fraction, hot pressing parameters and alloying elements on tensile strength of carbon fiber reinforced copper matrix composite prepared by continuous three-step electrodeposition, *Mater. Sci. Eng. A.* 288 (2000) 26–33. doi:10.1016/S0921-5093(00)00887-X.
- [84] L. Calmels, C. Mirguet, Y. Kihn, Evidence of alloying effects in $TiC_x N_{1-x}$ compounds from calculated and experimental electron energy loss spectra, *Phys. Rev. B - Condens. Matter Mater. Phys.* 73 (2006) 1–9. doi:10.1103/PhysRevB.73.024207.
- [85] Y. Kihn, C. Mirguet, L. Calmels, EELS studies of Ti-bearing materials and ab initio calculations, *J. Electron Spectros. Relat. Phenomena.* 143 (2005) 117–127. doi:10.1016/j.elspec.2004.02.170.
- [86] A.J. Scott, R. Brydson, M. MacKenzie, A.J. Craven, Theoretical investigation of the ELNES of transition metal carbides for the extraction of structural and bonding information, *Phys. Rev. B.* 63 (2001) 245105. doi:10.1103/PhysRevB.63.245105.
- [87] H.E. Swanson, R.K. Fuyat, G.M. Ugrinic, Standard X-ray diffraction powder patterns. IV. Data for 42 inorganic substances, 1955. papers2://publication/uuid/96D46134-3A54-4D50-BC04-D285C71513AC.
- [88] T. Jollivet, C. Peyrac, F. Lefebvre, Damage of composite materials, in: *Procedia Eng.*, 2013: pp. 746–758. doi:10.1016/j.proeng.2013.12.128.
- [89] C. Azina, M.M. Wang, E. Feuillet, L. Constantin, B. Mortaigne, P.-M. Geffroy, Y.F. Lu, J.-F. Silvain, Improved adhesion of polycrystalline diamond films on copper/carbon composite surfaces due to in situ formation of mechanical gripping sites, *Surf. Coatings Technology.* 321 (2017) 1–7. doi:http://dx.doi.org/10.1016/j.surfcoat.2017.04.037.
- [90] Y. Matsui, A. Yuuki, M. Sahara, Y. Hirose, Flame structure and diamond growth mechanism of acetylene torch, *Jpn. J. Appl. Phys.* 28 (1989) 1718–1724. doi:10.1143/JJAP.28.1718.

- [91] X. Jiang, C.P. Klages, Heteroepitaxial diamond growth on (100) silicon, *Diam. Relat. Mater.* 2 (1993) 1112–1113. doi:10.1016/0925-9635(93)90282-7.
- [92] X. Jiang, C.L. Jia, Diamond epitaxy on (001) silicon: An interface investigation, *Appl. Phys. Lett.* 67 (1995) 1197–1199. doi:10.1063/1.115005.
- [93] J.B. Donnet, D. Paulmier, H. Oulanti, T. Le Huu, Diffusion of cobalt in diamond films synthesized by combustion flame method, *Carbon N. Y.* 42 (2004) 2215–2221. doi:10.1016/j.carbon.2004.04.034.
- [94] T. Guillemet, Z.Q. Xie, Y.S. Zhou, J.B. Park, A. Veillere, W. Xiong, J.M. Heintz, J.F. Silvain, N. Chandra, Y.F. Lu, Stress and phase purity analyses of diamond films deposited through laser-assisted combustion synthesis, *ACS Appl. Mater. Interfaces.* 3 (2011) 4120–4125. doi:10.1021/am201010h.
- [95] K. Mallika, R. Komanduri, Diamond coatings on cemented tungsten carbide tools by low-pressure microwave CVD, *Wear.* 224 (1999) 245–266. doi:10.1016/S0043-1648(98)00337-8.
- [96] A. Veillère, T. Guillemet, Z.Q. Xie, C. a. Zuhlke, D.R. Alexander, J.F. Silvain, J.M. Heintz, N. Chandra, Y.F. Lu, Influence of WC-Co substrate pretreatment on diamond film deposition by laser-assisted combustion synthesis, *ACS Appl. Mater. Interfaces.* 3 (2011) 1134–1139. doi:10.1021/am101271b.
- [97] C. Wild, N. Herres, P. Koidl, Texture formation in polycrystalline diamond films, *J. Appl. Phys.* 68 (1990) 973–978. doi:10.1063/1.346663.
- [98] P. Smereka, X. Li, G. Russo, D.J. Srolovitz, Simulation of faceted film growth in three dimensions: microstructure, morphology and texture, *Acta Mater.* 53 (2005) 1191–1204. doi:10.1016/j.actamat.2004.11.013.
- [99] M. Chandran, C.R. Kumaran, S. Vijayan, S.S. Bhattacharya, M.S.R. Rao, Adhesive Microcrystalline Diamond Coating on Surface Modified Non-Carbide Forming Substrate Using Hot Filament CVD, *Mater. Express.* 2 (2012) 115–120. doi:10.1166/mex.2012.1061.
- [100] Y.X. Han, M. Zhao, J. Sun, H. Ling, T. Gebre, Y.F. Lu, Real-time monitoring of diamond nucleation and growth using field-enhanced thermionic emission current, *Appl. Surf. Sci.* 254 (2007) 1423–1426. doi:10.1016/j.apsusc.2007.06.064.
- [101] V. Elofsson, B. Lü, D. Magnfält, E.P. Münger, K. Sarakinos, Unravelling the physical mechanisms that determine microstructural evolution of ultrathin Volmer-Weber films, *J. Appl. Phys.* 116 (2014) 044302. doi:10.1063/1.4890522.
- [102] T. Guillemet, Diamond-based heat spreaders for power electronic packaging

applications, 2013.

- [103] F.P. Bundy, H.P. Bovenkerk, H.M. Strong, R.H. Wentorf, Diamond-Graphite Equilibrium Line from Growth and Graphitization of Diamond, *J. Chem. Phys.* 35 (1961) 383–391. doi:10.1063/1.1731938.
- [104] D.S. Knight, W.B. White, Characterization of diamond films by Raman spectroscopy, *J. Mater. Res.* 4 (1989) 385–393. doi:10.1557/JMR.1989.0385.
- [105] T.R. Anthony, J.L. Fleischer, J.R. Olson, D.G. Cahill, The thermal conductivity of isotopically enriched polycrystalline diamond films, *J. Appl. Phys.* 69 (1991) 8122–8125. doi:10.1063/1.347463.
- [106] G.W. Bak, K. Fabisiak, L. Klimek, M. Kozanecki, E. Saryga, Investigation of biaxial stresses in diamond films deposited on a silicon substrate by the HF CVD method, *Opt. Mater. (Amst.)* 30 (2008) 770–773. doi:10.1016/j.optmat.2007.02.034.
- [107] P.-M. Geffroy, J.-D. Mathias, J.-F. Silvain, Heat Sink Material Selection in Electronic Devices by Computational Approach, *Adv. Eng. Mater.* 10 (2008) 400–405. doi:10.1002/adem.200700285.
- [108] C.T. Kuo, C.R. Lin, H.M. Lien, Origins of the residual stress in CVD diamond films, *Thin Solid Films*. 290-291 (1996) 254–259. doi:10.1016/S0040-6090(96)09016-5.
- [109] Q. Fan, J. Gracio, E. Pereira, Residual stresses in chemical vapour deposited diamond films, *Diam. Relat. Mater.* 9 (2000) 1739–1743. doi:10.1016/S0925-9635(00)00284-3.
- [110] L.S. Fan, Y.S. Zhou, M.X. Wang, Y. Gao, L. Liu, J.F. Silvain, Y.F. Lu, Resonant vibrational excitation of ethylene molecules in laser-assisted diamond deposition, *Laser Phys. Lett.* 11 (2014) 076002. doi:10.1088/1612-2011/11/7/076002.
- [111] Y.H. Cheng, X.L. Qiao, J.G. Chen, Y.P. Wu, C.S. Xie, S.B. Muo, Y.B. Sun, B.K. Tay, Synthesis of carbon nitride films by direct current plasma assisted, 231 (2002) 225–231.
- [112] J. Grzonka, J. Kruszewski, M. Rosiński, Ł. Ciupiński, A. Michalski, K.J. Kurzydłowski, Interfacial microstructure of copper/diamond composites fabricated via a powder metallurgical route, *Mater. Charact.* 99 (2015) 188–194. doi:10.1016/j.matchar.2014.11.032.
- [113] C. Zhang, R. Wang, Z. Cai, C. Peng, Y. Feng, L. Zhang, Effects of dual-layer coatings on microstructure and thermal conductivity of diamond/Cu composites prepared by vacuum hot pressing, *Surf. Coatings Technol.* 277 (2015) 299–307.

doi:10.1016/j.surfcoat.2015.07.059.

- [114] Fricke, A Mathematical Treatment of the Electrical conductivity and Capacity of Disperse Systems, *Phys. Rev.* 24 (1924) 678–681. doi:10.1103/PhysRev.24.575.
- [115] T.B. Lewis, L.E. Nielsen, Dynamic mechanical properties of particulate-filled composites, *J. Appl. Polym. Sci.* 14 (1970) 1449–1471. doi:10.1002/app.1970.070140604.
- [116] D. Arnaud, J. Barbery, R. Biais, B. Fargette, P. Naudot, Propriétés du cuivre et de ses alliages, *Tech. L'ingénieur.* M4640 (2008) 1–45.
- [117] J. He, X. Wang, Y. Zhang, Y. Zhao, H. Zhang, Thermal conductivity of Cu-Zr/diamond composites produced by high temperature-high pressure method, *Compos. Part B Eng.* 68 (2015) 22–26. doi:10.1016/j.compositesb.2014.08.023.
- [118] R.M. Nicklow, G. Gilat, H.G. Smith, L.J. Raubenheimer, M.K. Wilkinson, Phonon frequencies in copper at 49 and 298??K, *Phys. Rev.* 164 (1967) 922–928. doi:10.1103/PhysRev.164.922.
- [119] J. Prakash, B.S. Semwal, P.K. Sharma, Phonon frequency distribution functions of copper, nickel and vanadium, *Acta Phys. Acad. Sci. Hungaricae.* 30 (1971) 231–240. doi:10.1007/BF03158174.
- [120] J.L. Warren, J.L. Yarnell, G. Dolling, R.A. Cowley, Lattice dynamics of diamond, *Phys. Rev.* 158 (1967) 805–808. doi:10.1103/PhysRev.158.805.
- [121] L. Pintschovius, W. Reichardt, B. Scheerer, Lattice dynamics of TiC, *J. Phys. C Solid State Phys.* 11 (1978) 1557–1562. doi:10.1103/PhysRevB.24.3048.
- [122] P. Jochym, K. Parlinski, Ab initio lattice dynamics and elastic constants of ZrC, *Eur. Phys. J. B.* 15 (2000) 265–268. doi:10.1007/s100510051124.
- [123] Z. Liang, H.L. Tsai, Reduction of solid-solid thermal boundary resistance by inserting an interlayer, *Int. J. Heat Mass Transf.* 55 (2012) 2999–3007. doi:10.1016/j.ijheatmasstransfer.2012.02.019.
- [124] M.W. Barsoum, The MAX Phases : A New Class of Solids, *Prog. Solid State Chem.* 28 (2000) 201–281. doi:10.1016/S0079-6786(00)00006-6.